Physics-Dynamics Coupling: Understanding Tropical Processes and Process Interactions in Weather and Climate Models

Submitted by

Susannah Nadine Hearn

to the University of Exeter as a thesis for the degree of

Doctor of Philosophy in Mathematics

In June 2022

I certify that all material in this thesis which is not my own work has been identified and that no material has previously been submitted and approved for the award of a degree by this or any other University.

Signed: .....

Abstract

The tropics are an important area of uncertainty in weather and climate models with variation between models in the tropics often being larger than in the extra-tropics for example due to a lack of strong geostrophic balance. In this thesis, we consider atmospheric behaviour in the tropics with a focus on understanding the long-term balance regimes that arise when drag and heating interact in the tropical atmosphere.

We will look at the dry and moist case as well as considering the adjustment to balance process. We outline a number of long-term balance regimes for the 2D dry and moist tropical atmosphere in the absence of Coriolis acceleration with heating and drag physics, deriving scalings for horizontal velocity, vertical velocity, potential temperature, Exner pressure, and where appropriate buoyancy frequency and total water. We then investigate the ability of a model to achieve or not achieve our hypothesised balances. We find in the dry case that the four regimes we outline are achievable within the model and produce distinct behaviours with scaling relationships that mostly match the theory. In the moist case however, only one balance regime can be achieved by the model, but the existence or not of long-term balance in the moist case has a notable effect on the triggering, sustaining and organisation of moist plumes.

We also look at numerical constraints affecting the development of long-term balance regimes and we find that the horizontal gridlength has a strong effect on which long-term balance regime the model finds itself in and whether the model can achieve balance at all. We also consider the effect of horizontal gridlength on adjustment processes such as gravity waves.

Acknowledgments

As I'm sure is often the case, writing my thesis has been a marathon effort and there are many people who have helped along the way. I would like to thank my supervisors Robert Beare and John Thuburn at the University of Exeter and Ben Shipway at the UK Met Office for their input and guidance throughout my PhD. I would also like to thank my family: my dog for being a bundle of joy; my wonderful partner Oliver Stoner for his thoughtfulness and support during the whole PhD process and especially at submission time when I needed to focus; and the rest of my family including my sisters for their continued moral support and letting me talk to them about my work even though they have no idea what I'm talking about most of the time.

Contents

List of Figures

List of Tables

Chapter 1

Preface

The tropics – defined as the region of the Earth in the immediate environ of the equator, usually between 23.5 degrees South and 23.5 degrees North – is an important part of the weather and climate system. Important processes in this region include radiative heating from the sun and consequently evaporation and precipitation and thereby the formation of clouds and large-scale circulation patterns such as the inter-tropical convergence zone (ITCZ) and the processes driving monsoon patterns. It is also the area of the Earth where the Coriolis acceleration has the least influence allowing processes such as surface drag to exhibit more control over the tropical circulation than in the extra-tropics or polar regions. Each of these processes does not operate in isolation, but in combination with other tropical processes to produce the weather and climate patterns we see on Earth.

In atmospheric models, performance is often worse in the tropics. Park et al. (2008) for example show that variation in lower atmospheric temperature in the tropics is much higher between models than in the extra-tropics where quasi-geostrophic balance is stronger. Likewise, forecast skill for precipitation in the tropics has been shown to be worse in the tropics (ECMWF-TIGGE-Skill-forecasts, 2022). Important features of the tropical circulation are also not fully understood. This includes large-scale patterns such as the Madden Julian Oscillation and tropical cyclone behaviour (Swinbank et al., 2016), as well as the more substantial presence of convection and cloud formation feedbacks in the tropics which causes significant uncertainty in weather and climate models (Bony et al., 2015). Better understanding the processes and process interactions in the tropics is therefore crucial to improving the representation of the tropics in General Circulation Models (or GCMs).

However, improving our understanding of weather and climate processes and process interactions is no trivial task. Substantial improvements in weather and climate prediction accuracy in the last few decades have been found by increasing resolution. Convection for example is better represented in higher resolution models (Lean et al., 2008). However increasing resolution is not always a perfect solution. In recent years, we have seen the emergence of grey-zones in models where some processes in models are only partially resolved and therefore increasing the resolution may lead to poorer model performance due to assumptions made within models about how to represent real-world weather and climate processes. The assumptions can provide good approximations to the real world in coarse resolution models, but may perform much worse when the model resolution is increased.

In order to improve the accuracy of the representation of real-world processes and process interactions in weather and climate models – including representation of the tropics – we must therefore understand the underlying physical processes better. Simplified models and theoretical frameworks provide a way to analyse processes and process interactions without the often overwhelming complexity of working with a full GCM. By returning to the fundamentals, researchers are able to challenge pre-existing assumptions that underpin current GCMs and provide new frameworks for understanding real-world processes.

In this thesis, we explore the problem of process interactions in the tropics by studying theoretical long-term balance regimes in the dry and moist cases with drag and heating physics. We will also look at the adjustment to balance processes in the dry case with the inclusion of drag and the excitement of gravity waves. Through the analysis of long-term balance in the tropics when multiple physics processes are included, we can identify atmospheric states towards which models might be expected to converge as well as provide greater insight into how each of the physics processes might impact model behaviour and long-term balance states where a long-term balance state is an atmospheric state in the absence of fast motions such as waves.

Chapter 2

An Overview of Physics-Dynamics Coupling in Atmospheric Models

Let us consider first the current landscape of weather and climate model development and how the various weather and climate processes and process interactions are represented and assessed within models. Though the focus of this thesis is the tropics and the long-term balance regimes that arise from interactions between surface drag, heating and moisture, questions about the representation and understanding of processes and process interactions can be found in all parts of the Earth system. Any discussion therefore necessitates an understanding of physics-dynamics coupling in weather and climate models and the challenges that arise when we attempt to understand real-world processes and capture their behaviour in finite models.

2.1 Introduction

Current operational weather and climate forecasting models (often called Earth System Models – or ESMs) are complex models which contain multiple coupled processes (Randall et al., 2019). Coupled processes here mean processes that are linked to each other, but for whatever reason, cannot be easily solved within the same set of equations. In the case of full ESMs, we might think initially of the coupling between different spheres of the Earth system – e.g. the land, the ocean, and the atmosphere – but there is also coupling of processes within each of the spheres. In this thesis, we consider primarily atmospheric models – sometimes called General Circulation Models (or GCMs) – which, like many of the individual Earth sphere

models, must themselves deal with internal coupled processes. In the case of GCMs, we can categorise the coupled processes into two distinct, but sometimes arbitrary types.

The first type – commonly called the *'dynamics'* – are the numerical discretizations used to solve the continuous governing equations for fluid motion in the atmosphere over a finite grid. The dynamics may also refer to only the governing equations and not their discretizations when referring to the theory that the dynamical core of a model is based on. The dynamics are often the first part of a GCM to be developed – firstly by choice of theoretical governing equations and then by their numerical implementation. The dynamics typically represents only processes that occur on lengthscales larger than the gridsize and timescales larger than the timestep (Gross et al., 2018). As such, processes represented by the dynamics are sometimes referred to as *'resolved'* processes.

The second type of process we find in GCMs is called the *'physics'* which encompasses all the processes that cannot be captured or 'resolved' by the dynamical core. This could be because the physics processes are diabatic forcing processes such as radiative heating which cannot be included in the dynamics as the governing equations are assumed to be in entropy-conserving equilibrium (although the numerical representation of the dynamics is not necessarily entropy-conserving due to dissipation). Or it could be because the physics processes are sub-dynamic processes i.e. processes which occur on scales too small or quick to be resolved by the dynamics such as surface drag or turbulence (Gross et al., 2018). The split between the dynamics and the sub-dynamic physics can be said to be arbitrary in that the split is determined by the timestep and grid resolution of any given model. As the resolution of the dynamical core increases, we would expect processes in the sub-dynamic physics category to be captured by the dynamics of the model.

However, increases in resolution are computationally expensive. Thus resolution cannot grow as fast as it has historically so the modelling community will have to contend with sub-dynamic processes for the foreseeable future. Additionally models must still contend with diabatic forcing physics processes regardless of grid resolution. So how we include – or couple – physics processes to dynamical cores is an important question for the atmospheric modelling community.

Indeed *Physics-Dynamics Coupling* is a field of increasing interest when it comes to improving model accuracy (Gross et al. (2018), Maher et al. (2019)). Histori-

cally, GCMs would often undergo two separate development stages. As previously mentioned, the models for the dynamics of the large scale circulation are usually developed first, followed by models for small-scale processes and diabatic processes which are developed to be included in the dynamical core via *'parameterizations'*. The dynamics and the physics might also be developed in parallel but separately.

However, much like real-world processes such as convection and the boundary layer for example, many physics parameterizations interact not only with the dynamics, but with each other as well. And yet the different physics parameterizations schemes are frequently developed in isolation and evaluation may be done without considering the effects of other physics processes in a model.

Problems in physics-dynamics coupling can arise from the separate development of the physics and dynamics. In most models, the physics parameterizations are developed for specific grid-lengths or time steps and may be nested within single columns in the dynamics (Maher et al., 2019). As computing power increases and modellers attempt to increase resolution, parameterization packages can require a complete rethink and remodelling of some processes as they become resolved or partially resolved. Separate development also causes inconsistencies in the physics and the dynamics such as relying on different governing equations or not allowing proper interactions between the dynamics and the physics.

Then of course, we come to the question of how to actually check if our parameterizations are effective and accurate representations of real-world problems and how we can know which parts of our complex GCMs have what effect on the model output.

2.2 GCMs: a Mix of Dynamics, Physics and Physics-Dynamics Coupling

Before we consider the challenges of physics-dynamics coupling, it is helpful to understand a little more about the physics and the dynamics separately and how they are implemented in GCMs. As previously stated, a given GCM will have separate dynamics and physics, but different GCMs can also have completely different numerical formulations for the dynamics, the physics, and the physics-dynamics coupling mechanisms. In this section, we will review a number of dynamics and physics

strategies and their implementation so as to begin to understand the complexity of the problem of analysing and improving the accuracy of GCMs when there are so many differences between individual GCMs and so many numerical schemes within them.

2.2.1 Differences in Dynamical Cores

First, let us consider the differences between the 'dynamics' used for models. We will give a fairly brief overview here as our main focus is processes and process interactions and therefore physics-dynamics and physics-physics coupling, but we cannot understand physics-dynamics and physics-physics coupling without first understanding the dynamics and the physics separately. Currently, dynamical cores tend to fall into a few categories based first on the choice of theoretical governing equations and then numerically on the choice of numerical solvers and grids.

With respect to the governing equations, some cores such as the Met Office Unified Model (UM) solve the compressible non-hydrostatic Euler equations (Wood et al., 2014), whilst others may use hydrostatic equations such as the ECMWF Integrated Forecasting System (IFS, 2021). Governing equations may be chosen to increase efficiency by reducing terms in the equations e.g. assuming hydrostatic balance, but equally a fuller but more computationally expensive set of equations may be preferred for the flexibility of being able to use the same model to run global simulations which provide global weather and climate predictions as well as higher resolution limited area simulations which provide local weather predictions (Walters et al., 2017). At higher resolutions, the assumption of hydrostatic balance would be a poor approximation to make since horizontal lengthscales may be closer to vertical lengthscales.

When it comes to differences in the numerical solvers used in dynamical cores, models might use spectral transform methods or gridpoint methods. Each method has advantages and disadvantages. The spectral transform method – which takes model fields from the grid representation to a spectral representation – can accurately and efficiently calculate derivatives. But for the spectral core, Randall et al. (2019) note that the computational cost increases faster than the degrees of freedom in calculations, meaning computational challenges if increasingly high horizontal resolutions are desired.

Gridpoint methods have become more popular in recent years since developments in parallel computing and increases in horizontal resolution, because when compared to the spectral method, the computational cost of gridpoint methods scales more slowly relative to the number of gridpoints. Thus it is estimated that spectral cores will become slower than gridpoint methods in future if increases in resolution continue. However, gridpoint method dynamical cores must also carefully consider variable staggering on the grid i.e. where in the grid each variable is calculated. Variables might be calculated at the same vertical and horizontal levels in a model or they might be calculated between levels for example. There is no universally preferred grid staggering. In the vertical, two main vertical grid-staggering methods are used in different weather and climate models: Charney-Phillips grid-staggering – where the horizontal velocities u and v are located at different vertical level to the thermodynamic variable (θ – or potential temperature) (Charney and Phillips, 1953); and the Lorenz grid-staggering – where u and v are co-located with θ (Lorenz, 1960). Each method contains its own advantages and challenges. The Charney-Phillips grid performs well at capturing hydrostatic and thermal wind balance, but poses challenges for energy conservation (Randall et al., 2019), whereas the Lorenz grid-staggering is more useful for energy conservation, but contains a computational mode which can disrupt model accuracy (Holdaway et al., 2013). In the horizontal, various grid-staggering methods have been investigated with Arakawa and Lamb (1977) showing that separation of the horizontal velocities in the horizontal performed better than co-location in a geostrophic adjustment study. Gridpoint methods may include finite volume or finite difference schemes which take the difference in space or time on the grid to solve the governing equations and these may be coupled with semi-Lagragian schemes which find a departure point from one or two timesteps ago for the trajectory of each fluid parcel arriving at a gridpoint to then calculate the current flow (Robert, 1982).

There has also been increasing interest in varying grid shapes. For example, cubed-spheres which use cubes instead of horizontal latitude-longitude grids or icosohedral grids which use triangles to construct the grid surface. Other options include a Yin-Yang grid which overlays two partially-banded grids, one that takes a band over the poles and another which takes a band around the equator and midlatitudes, or geodesic grids which use a combination of hexagons and pentagons. Choosing grids with sufficient accuracy is no trivial task and involves trying to balance com-

putational efficiency with the minimisation of spurious numerical issues such as growing computational modes. Additionally, regardless of the grid chosen, model solutions will likely contain noise caused specifically by the grid-shape which must be thoroughly understood before the grid can be used operationally (Staniforth and Thuburn, 2012). There has also been interest in grids with varying gridlengths where resolution can be increased in particular areas of the model, without needing to increase resolution globally. Variable resolution models can be useful in resolving parts of the weather and climate system which would otherwise need to be globally parameterized – for example, small-scale eddies or topographically-driven features that would be subgrid if resolution was not increased. Local increases in resolution in multi-resolution grids have also been shown to have little effect on errors with the dominant part of the solution error relating to the coarsest grid scale and not the section of the model with higher resolution (Ringler et al., 2011).

Any given model may combine different solvers or grids. A few examples of models include: the ICON model which uses an icosohedral triangular grid and finite volume solver (Zangl et al., 2015); FV^3 which uses a cubed-sphere grid with finite volume solver (Putman and Lin, 2007); GEM which uses a Yin-Yang grid with a finite difference solver (Qaddouri and Lee, 2011); DYNAMICO which uses a geodesic grid with a finite volume solver (Dubos et al., 2015); and CAM-SE which uses a cubed-sphere grid with a spectral element solver (Dennis et al., 2012).

Thus, it is clear that there is wide variation in dynamical cores used in current GCMs and the variety of solvers and grids is unlikely to reduce in coming years. For ensemble forecast analysis which uses multiple models or model formulations to determine the most likely atmospheric or climate states given certain parameters, variation is actually a good thing.

2.2.2 Differences in Physics Packages

We now move onto discussing the 'physics' side of GCMs in more detail with the 'physics' accounting for a large number of processes and process interactions in models. As previously noted, the physics may take many forms and comprises processes all across the globe. In GCMs, the physics includes radiation, convection, precipitation, the boundary layer, orography, gravity wave drag, land-surface fluxes, and cloud micro-physics (Walters et al., 2017). In turn, each of these processes

may be represented by a different numerical physics package or multiple numerical physics packages coupled to the dynamical core (e.g. deep and shallow convection are often treated separately). Some dynamical cores also include the option to use different numerical physics packages for the same real-world physics process. Often this serves to aid research. In PaiMazumder and Done (2016) for example, it is shown that drought features are robust to variation in the World Research and Forecasting (WRF) community model physics packages that deal with radiation, the boundary layer, cumulus and micro-physics.

Most physics parameterizations are based on similar theoretical results. One example is boundary layer formulations where nearly all atmospheric models use Monin-Obukhov similarity theory to determine surface fluxes (Randall et al., 2019). But even if the underlying theory is the same, the numerical implementation can still vary. Kalnay and Kanamitsu (1988) for example analysed performance of vertical diffusion and surface heat fluxes in boundary layer parameterizations. They found that for the same damping equation, the nonlinear terms caused excessive oscillations in boundary layer tendencies for multiple different numerical time schemes.

The physics packages also usually have to be formulated for a specific dynamical core and the implementation of any physics package is therefore dependent on choices made about the governing equations and the numerical solvers in the dynamical core although we will see later that the physics does not always consider the impact of both and vice-versa. Each physics package – or parameterization – may also be formulated for a specific gridlength and timestep range in the dynamical core and a given physics package may even become unneccesary or partially redundant as resolution increases. Convection is a notable example of this phenomenon. Previously in models with horizontal gridlengths around 10 km or more such as some of the Global Met Office UM setups used in Birch et al. (2015), the deep convection was handled entirely by a deep convection parameterization scheme as part of the model 'physics', but when the resolution is increased to 1.5 km as in the Met Office's UK variable resolution model (Lean et al., 2008), the deep convection can be handled more effectively by the dynamical core and indeed the use of a deep convective parameterization is of questionable validity at such scales.

Physics parameterizations can also pose additional challenges with respect to how they interact with and feedback on the dynamics. Again, using the example of convection: in many models, convection is parameterized within a single ver-

tical column and does not interact in the horizontal (Maher et al., 2019). Thus parameterizations may also fail to represent interactions between convection and the large-scale dynamic circulation (Birch et al. (2015)). How the physics interact with each other is also often difficult to accurately represent (Wan et al., 2013).

But perhaps the most important thing to take away is that we are dealing with lots of models with lots of different physics packages that need to interact with the dynamics. Physics also suffer from being less clearly defined than the dynamics in terms of which parts of a given parameterization are the theoretical basis and which parts are the numerics. This poses an additional challenge to understanding the physics.

2.2.3 Physics-Dynamics Coupling Challenges

Having reviewed the differences in the dynamics and some physics packages separately, we now consider the physics-dynamics and physics-physics coupling differences between models. In particular, we will look at the challenges arising from physics-dynamics and physics-physics coupling and how these complicate attempts to check and assess the accuracy of model behaviour. We break down the challenges into four key areas: time-stepping issues; spatial discretization issues and grey-zone issues; issues arising from the inconsistent formulations of physics and dynamics; and physics-physics and physics-dynamics feedback issues. These issues are not entirely independent of each other either so an issue may be classified as both a time-stepping issue and a feedback issue for example. We will see that many of the issues come from an incomplete understanding of the interactions between physics processes and dynamics processes and between multiple physics processes in the real world.

Time-stepping issues

Because of the interrelated nature of model processes and the overlap of time scales, it can be difficult to determine when to trigger physics processes within the dynamics and how often to compute them. There are generally two approaches to this problem: sequential splitting and parallel splitting. Sequential splitting involves calculating parameterized processes within a time-step one after the other. In sequential splitting, a model may compute tendencies from the behaviour of one physics process to

pass on to the next physics process, as well as also remembering the model state at the start of the time step. Or the model state may be updated and passed to the new process (Donahue and Caldwell, 2018). Parallel splitting involves allowing all parameterized physics processes to run on within the time step of the model using only the initial state of the model and not updating with any other processes until the next full time step where all the process tendencies computed within the time step are used to change the core model state.

The selection of a time-stepping approach can substantially impact how the physics-physics and physics-dynamics interactions work in a given model. If modellers choose a sequentially-split model, for example, the order in which physics processes are calculated becomes very important. Donahue and Caldwell (2018) showed that when the order of calculation for the physics parameterizations in the sequentially-split Energy Exascale Earth System Model (EESM) was changed, there were large differences in the reported climate sensitivity in the model. One solution to this is to group processes into fast or slow processes relative to the time-step and compute them accordingly in order (Beljaars et al., 2018), but difficulties still remain. In particular, problems can arise in sequential splitting when one physics process is a source or sink of a quantity needed by the next physics process. Through sequential splitting, it is possible for one quantity to be used up by the model before it is needed by the next process. For example, Wan et al. (2013) showed that the sulfuric acid condensation was substantially over-predicted when the sulfuric acid production physics process was calculated before the condensation in a sequentially split model even though the processes in the real world would occur simultaneously.

Parallel splitting can counteract some of these problems. Notably, in Wan et al. (2013), when sulfuric acid production and condensation were parallel split, the results were more accurate. However, Wan et al. (2013) also found the results of their model were then negatively biased because when the production and condensation processes for sulfuric acid were parallel split, they did not interact at all before the end of the timestep and therefore more extreme states were calculated by each process.

It has been suggested that going forwards, models might consider a combination of sequential and parallel splitting. Beljaars et al. (2018) argue that sequential splitting with some parallel splitting of interlinked processes with similar timescales may be the best strategy, although they had difficulty implementing such a strategy

in the ECMWF model due to constraints in the model i.e. vertical diffusion had to be called before convection, surface fluxes were needed by the convection scheme for closure.

It is clear therefore that any future formulations of parameterization schemes in models must pay close attention to understanding the underlying physics-dynamics and physics-physics interactions before decisions about how the time splitting of processes are made. If we fail to understand physics-physics and physics-dynamics interactions properly, we will end up with time-splitting processes that neglect important interactions in the real atmosphere.

Spatial Discretization Issues

Just as processes are split by timescale, they are also split by gridlength and spatial discretization issues can also impact the accuracy of models with coupled physics and dynamics processes.

One way is through the selection of spatial grids for the dynamics. Normally, selection of the spatial grid for a given model is about selecting the best performing grid for the dynamics. At first glance, this seems intuitive. However, not accounting for which spatial grid works best for both the dynamics and coupled physics processes could cause unnecessary inaccuracies in GCMs. The advantages of the Lorenz and Charney-Philips grids have already been discussed with respect to the dynamics, but the picture becomes more complicated when we consider the optimal grids for 'physics' processes as well. Holdaway et al. (2013) perform an analysis of the Lorenz and Charney grids using a dynamical core coupled to a planetary boundary layer. They find that in the boundary layer alone without the dynamics, the Lorenz grid is most accurate. However, when the boundary layer is coupled with the dynamics, the Charney-Philips grid is found to be more accurate provided the Richardson number is calculated without vertically averaging the shear. Given that grid-formulation occurs often at the dynamics stage mostly without necessarily considering the physics, this result is important.

The Grey-Zone: There is also the issue of the effect of increasing spatial resolution on parameterizations and how it affects traditional process splits into physics or dynamics processes. The 'grey-zone' is a term that has gained popularity in the last decade with large increases in model resolution and the grey-zone occurs when

the gridlength (or sometimes timestep) of a model is fine enough to resolve part of a weather or climate process, but not fine enough to resolve fully the entire process. In other words, a process that is in the grey-zone in a model cannot be handled by either the physics or the dynamics alone. These processes may be called 'grey-zone processes', though it should be noted that the grey-zone occurs at different resolutions for different processes so a given process will not always be a grey-zone process in all models. For example, the grey-zone of convection with respect to horizontal resolution is considered to be in the region of a few kilometres, whilst the grey-zone for turbulence is considered to be in the region of a few hundred metres (Honnert et al., 2020). As previously mentioned, physics parameterizations can be heavily dependent on the gridlength or timestep of a model and any changes to the gridlength or timestep can force a complete rethink of the physics.

Wyngaard (2004) showed that when the largest turbulence lengthscales in the the boundary layer are on the same scale as the model resolution then fundamental assumptions in common turbulence parameterizations no longer hold. Honnert et al. (2011) then showed that as the resolution approached the lengthscale of turbulence in the boundary layer, traditional Reynolds-averaged Navier-Stokes approaches led to underestimating subgrid thermals in a mesoscale hydrostatic model without parameterizaed mass flux. When a mass flux parameterization was used, the subgrid thermals were then over-estimated suggesting the existence of a grey-zone resolution range where neither resolved nor parameterized approaches were sufficiently accurate.

The presence of grey-zone processes can also exacerbate issues related to other aspects of physics-dynamics coupling such as the the choice of time-stepping schemes. In Williamson (2013), convection in the Community Atmosphere Model (CAM4) was handled partially by the physics and partially by the dynamics and this split led to competition for resources where they overlapped and a subsequent exacerbation of storms.

Inconsistent Formulation of the Physics and the Dynamics

Challenges in physics-dynamics coupling can also arise when there are inconsistencies in the formulation or numerical implementation of the physics and the dynamics.

On the numerical side, the physics and dynamics may be computed on different

spatial grids. In the ECMWF model for example, the radiation physics scheme is calculated on a coarser resolution grid compared to the dynamics and whilst Morcrette et al. (2008) showed the use of a coarser grid to be computationally efficient with results mostly free of systemic differences caused by any spatial interpolation needed to go from one grid to another, it also led to near-surface temperature errors at land-sea coastlines of up to 10 K due to substantial surface temperature and albedo horizontal gradients (Beljaars et al., 2018). Different processes may also require different numerical schemes with fast physics processes suggested to be manageable using explicit schemes whilst physics processes that depend on other physics processes are suggested to need implicit schemes for stability (Beljaars et al. (2018)). The use of implicit schemes is particularly important for strongly-linked physics processes.

Physics-Physics and Physics-Dynamics Feedbacks

For physics-physics feedbacks, we have already seen the example of Wan et al. (2013) where the sulfuric acid production had a substantial effect on condensation. How the physics and dynamics feedback on each other can also substantially affect model results. Birch et al. (2015) showed that the shallow and deep convection schemes in the Met Office UM did not accurately feedback to the large-scale circulation dynamics resulting in unrealistic diurnal cycles and weakened sea-breeze conditions. We might also consider the effect of the dynamical numerics on the physics. We have already seen that failure to account for the physics in model grid selection can lead to a grid being selected which is optimal for the dynamics, but not the coupled physics and dynamics, but problems also exist when choosing other parts of the numerical implementation of dynamical cores. For example, Diamantakis et al. (2006) note that the use of semi-implicit, semi-Lagrangian schemes and the corresponding increase in computationally permissable timesteps increased the likelihood of spurious oscillatory behaviour in the boundary layer turbulence physics scheme.

2.3 Evaluating and Improving Accuracy of Physics-Dynamics and Physics-Physics Coupling in GCMs

So with all the differences between models at all levels of development as well as high levels of complexity within each model, how do we even go about trying to effectively understand GCM behaviour in the context of improving accuracy? Dynamical cores on their own go through a number of standard tests for checking accuracy in the numerical solvers (Ullrich et al., 2017), but compared to full GCMs, analysis of dynamical core performance is fairly straightforward as there exists a clear split between the governing equations and the numerics used to solve them. When physics are coupled with the dynamical core, it is less clear how we should analyse model accuracy.

Of course, we can check operational models against real-world observations, but this is not always enough and sometimes data are insufficient or biased. For example, in the tropics, there is often uncertainty in precipitation observations with limited observations of shallow circulations in particular (Good et al., 2021). It is also clear that we cannot rely on increasing computational power and subsequent increasing resolution alone to improve accuracy. We need to understand the physics-dynamics coupling mechanisms better. And we need to understand interactions between physics-dynamics and physics-physics processes in the real world better as well.

This is clear from a number of time-step convergence studies. In fluid dynamics convergence studies, we should theoretically be able to use time-stepping analysis to check model convergence towards the 'true solution', where the 'true solution' can be found by considering the behaviour of the system in the limit of the time step and the gridlength going to zero (Gross et al., 2018). However, this is infeasible for complex GCMs as the parameterizations for many physics processes are specified for specific time-step and grid-length ranges and will not function correctly beyond the scale for which they were defined. An example is given in Williamson (2013), where the CAM4 model is faster to diverge away from an atmosphere-like state when the timestep of the model is decreased, because the time-scales of the deep and shallow parameterizations which are already longer than the timestep become far too slow as the time step is decreased to allow the model to return to an atmosphere-like state within a single time step. So in Williamson (2013), decreasing the time step

actually made the model solution *less* reliable. And even when the model isn't behaving counter-intuitively, the convergence towards a solution may be weak. Wan et al. (2015) performed a time step analysis on the CAM5 model and found that the actual convergence rate of the temperature field in the full model was less than half the convergence rate of the reduced physics version with stratiform cloud schemes causing the largest time-stepping errors, though Wan et al. (2015) did produce a reference state of a kind, against which convergence can be measured. However, such reference states should be treated with caution, especially if the converged state requires parameterizations to be used outside of the spatio-temporal range for which they were defined in as the model in the converged state could be violating core assumptions in the initial formulation of the physics parameterizations.

As such, it is difficult to determine how full models should behave and what criteria or reference to use for a convergence study and it can be more helpful to break the problem down into more manageable chunks, which brings us to the idea of a hierarchy of models and test cases.

2.3.1 Development of Test Case and Model Hierarchies

In light of the challenges of attempting to evaluate GCM and physics-dynamics coupling performance, there have been many calls to establish a hierarchy of models and test cases for GCM analysis (Gross et al. (2018); Thatcher and Jablonowski (2016); Maher et al. (2019)). The reason for establishing a hierarchy of models is that given the complexity of the problem, it is reasonable that the solution might also be complex. When it comes to analysing the performance of GCMs with a view to increasing accuracy, using a hierarchy of models allows greater breadth and depth of analysis. Any test cases and testing methods will have shortcomings at any level of complexity, but by using test cases or testing methods at multiple levels of complexity, we can mitigate some of those shortcomings. In particular, we can use simplified models to isolate and understand processes and mechanisms and the hierarchy can be useful for tracing the processes and mechanisms back up to their relevance or not in more complex models which are closer representations of the real-world atmosphere.

We will now consider a few stages of complexity in model testing approaches and the advantages and disadvantages of each and therefore why they cannot stand

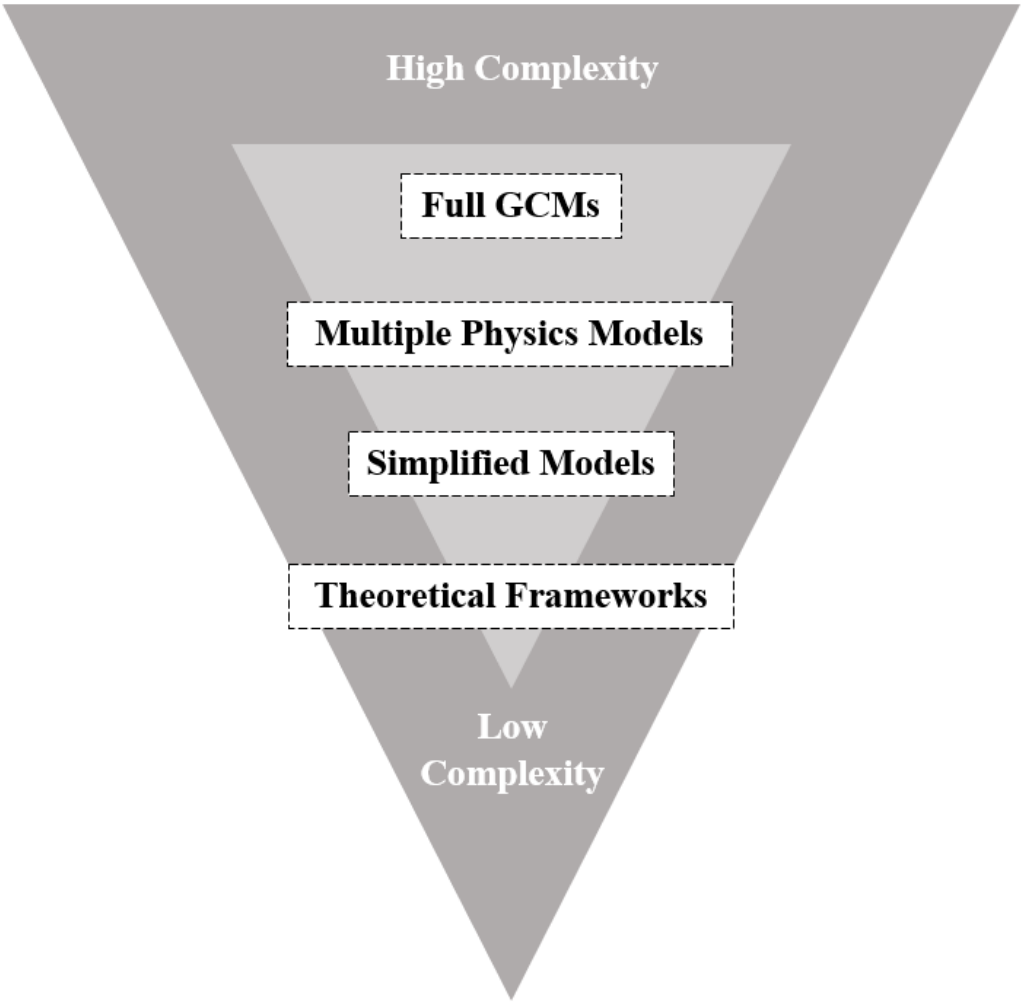

Figure 2.1: Model Hierarchy with increasing complexity going up

alone. We will also consider how test cases at different levels of model complexity mitigate the disadvantages of tests at other levels of complexity.

Full Model Test Cases

Full-physics tests of the dynamical core are towards the higher complexity end of the test case hierarchy and use minimal simplifications whilst preserving the physics of the full model. One example of a full-physics test case is Neale and Hoskins (2000), where sea-surface temperature (SST) forcings are applied to the bottom boundary of the model to induce circulation in an aqua-planet context (i.e. no land surface). Gross et al. (2018) build on this approach to make an aqua-planet assessment of four different dynamical cores in CAM5, all of which show similar precipitation

rates when set up with the same parameterization schemes for boundary layer and mass-flux. Gross et al. (2018) suggest the potential for an average reference solution obtained from their simulations which might represent a 'true' solution, however such a reference state may not hold for models outside of CAM5 and there is no guarantee that the average state will be the 'true solution' as models can have similar biases. In Gross et al. (2018), they acknowledge that the single-peak Inter-Tropical Convergence Zone (ITCZ) which comes out as an average reference solution is highly contested as a number of model runs showed a double peak ITCZ instead.

It is also very difficult to determine the cause of discrepancies between reference solutions and model results or even between observations and model results with so many variables affecting performance, though sometimes by varying the physics package within a dynamical core, it is possible to identify the cause of spurious behaviour within a model. Birch et al. (2015) for example vary the deep and shallow convection parameterizations between parameterized and explicit within the Met Office UM as well as varying the boundary layer between two different formulations to identify convection and boundary layer feedbacks on sea-breeze activity where the Met Office UM has consistently shown inaccuracies. Their results clarify the cause of a shifted diurnal cycle of sea-breeze activity over a particular region in the model. However, improving the parameterizations that led to the problem in the first case would require better understanding of the physics processes and their formulations.

Multiple Physics Test Cases

A step down from full model tests are multiple physics tests cases. In multiple physics tests, at least 2 physics processes are included in the model test runs. This category of test cases is broad and can range from the very simple to the more complex.

On the simple end of the spectrum, we have test cases such as Held and Suarez (1994) which imposes heating processes and linear drag on the dynamical core. The simplified heating and drag formulations in Held and Suarez (1994) serve as simple proxies for much more complex parametrization schemes, including convective and radiative heating and the boundary layer. However, Held and Suarez (1994) do not provide an expected reference solution or 'true solution' for their test which means dynamical core behaviour can only be compared with reference to other models such

as high resolution LES simulations.

The reference solution problem also manifests on the more complex end of the multiple physics test cases. Thatcher and Jablonowski (2016) developed a more complex physics-dynamics test which takes account of moisture and so allows investigation of model condensation and boundary layer mixing. However, the test case they propose contains splitting of processes – large-scale condensation is computed first, then surface moisture, then temperature flux, and finally boundary layer mixing and friction (Thatcher and Jablonowski, 2016). This means that the formulation of the test case between dynamical cores must be carefully thought out and reference solutions may vary widely because of differences in physics-dynamics coupling. Furthermore, we do not know which reference state is accurate. Reference states mostly only help us to understand where models differ, not to understand which model is most accurate.

With multiple physics test cases such as Thatcher and Jablonowski (2016) where the splitting of processes is imposed, there is also the danger of imposing the numerics of the model. A test case should be applicable to multiple formulations if it is based on governing equations. Imposing numerics muddies the waters between whether we are testing the ability of the model to represent a theoretical state accurately or whether we are testing for implementation of a particular parameterization. Both are useful to a degree, but only the former is about representing the process as opposed to the implementation.

Simplified Models

The next level we discuss – the use of simplified models – is perhaps the first test level to diverge away from using the GCM framework itself. Simplified models are models which may focus on a single or a limited number of processes. Examples include Beare and Cullen (2019) and moist boundary layer-convection interactions or Muller and Bony (2015) and radiation-convection feedbacks. Simplified models aren't exactly test cases for more complex models, however they do provide a method of analysing full model behaviour so should not be neglected in the discussion of understanding and improving the accuracy of physics-dynamics coupling in GCMs.

Simplified models are particularly useful for analysing model behaviour in three ways: better understanding underlying real-world physical processes; understanding

cause and effect between physics processes; and acting as validation experiments or providing reference solutions for more complex models.

Understanding Underlying Physical Processes It almost goes without saying that accurately representing the weather and climate relies on a thorough understanding of the underlying physical processes in the real-world. Attempting to understand the behaviour of a single process using only a GCM can be challenging and even futile given the number of processes feeding back on each other.

Likewise, as previously noted, GCMs may be subject to the same biases due to reliance on the same underlying theory, similar finite resolutions or similar formulations in the dynamical core. PaiMazumder and Done (2016) for example show that even when the radiation, cumulus, microphysics and boundary layer parameterizations in the WRF model are varied between different formulations, the WRF model still produces a peak in precipitation that occurs too early in the diurnal cycle in every single case suggesting a bias in the dynamical core. By removing the complexity from the problem of evaluating GCMs – and sometimes the need for a functional forecasting model – researchers can more thoroughly interrogate their assumptions about their understanding of a given process or set of processes.

Beare and Cullen (2019) use a simplified model to better understand interactions between the boundary layer and moist convective activity showing how increases in drag in the boundary layer lead to a horizontally thinner region of convection. And single-column models are often used to test physics parameterizations and understand how they work with other physics parameterizations in a given model. Lock et al. (2000) for example test a turbulent mixing scheme for a boundary layer parameterization in a single column version of the Met Office UM to understand how it interacts with other physics processes before implementation in the full model.

Clarifying Cause and Effect: As previously noted, GCMs can be extremely complex and therefore it can be difficult to distinguish cause and effect between individual processes. Likewise, the wide range of parameterizations available can make it difficult to understand how all the processes affect each other both in the model and in the real world. Simplified models allow for better understanding of physics-physics and physics-dynamics process interactions and can help clarify which parts of the system force other parts and which processes are closely tied.

Simple models are often designed to investigate the behaviour of a particular process, or set of processes that likely affect each other. One example involves an attempt to clarify the relationship between sea surface temperature (SST), low-level winds in the boundary layer and convergence in the tropics in Back and Bretherton (2009), where the authors use a mixed layer model (MLM) to investigate the problem and compare the results to observational data. They propose that boundary layer convergence is most likely a cause of deep convection and a function of the SST gradients – a finding similar to that obtained by Lindzen and Nigam (1987), although the latter uses a different model formulation. Thus, some features of the climate system are robust, through minor variations in model formulations or parameterizations, though there are still significant differences in results. The Lindzen-Nigam model contains a representation of 'back pressure' from the free troposphere which is found to be an unrealistic assumption, when compared to observations and the slightly more complicated MLM of Back and Bretherton (2009).

The simplified models used in both papers allow the authors to determine certain properties of SST driven boundary layer convergence and Back and Bretherton (2009) highlight that variations in the amount of rainfall in GCMs may be associated with the different representation of boundary layer convergence within the models. Such a conclusion would be significantly more difficult to diagnose in a full GCM and the result is important when considering the interplay of parameterizations within a full model. We have seen that splitting problems are exacerbated by failing to compute processes that are heavily reliant on each other simultaneously, and this is visible in the differences between the Lindzen-Nigam model and the Back and Bretherton MLM, where the first neglects free-tropospheric effects in its model and so neglects an important process in SST driven convergence patterns in the boundary layer. Simplified models provide the ability to clarify which processes should form part of the same parameterization package and may allow for better compartmentalization of processes and more justifiable splitting regimes in large GCMs.

Further examples of how simplified models have been used to understand weather and climate processes include trying to understand convective aggregation (e.g. Muller and Bony (2015) use a cloud resolving model to clarify the effects of longwave radiative feedbacks and find the convective aggregation can be triggered when below-cloud downdrafts are weak) and propagation of important large-scale weather

systems (e.g. Vallis (2021) which uses a simplified model to propose that the Madden-Julian Oscillation Eastward propagation scales with the strength of convective heating as opposed to gravity wave speed).

Convergence Reference Solutions: Another use for simple models is in the validation of process implementation in larger GCMs. By using a simplified version of the governing equations and focusing on a particular process, it is possible to determine which parameterizations will potentially cause stability issues in larger scale models. This can be done by checking model results against long-term balances that we might expect from atmospheric and fluid dynamic theory, even if such an analysis would not be possible in the full model.

Beare and Cullen (2012) look at the behaviour of the boundary layer in a simplified model. They find that including an Ekman balanced term in the formulation of boundary layer drag in a semi-geotriptic model reduces instabilities associated with a typical, non-Ekman component drag scheme and they advocate for a variant of a semi-geotriptic model as it is more stable and closer to results produced by the Shallow Water Equations. This analysis in a simplified setting allows testing of potential parameterization schemes against the theory, even though the full model cannot be tested in such a way. It also demonstrates that convergence studies can be performed early on in the development of parametrizations and can provide useful information, even if a time-step analysis of the full model may be questionable.

However, simplified models are not always useful. They are often criticised for their simplicity and for the fact that just because a simple model attains a balance or shows a clear relationship may not mean that such a relationship exists in the real weather or climate system and it can sometimes be difficult to implement findings in large scale models (Donahue and Caldwell, 2018). Simplified models can end up neglecting important factors such as Lindzen and Nigam (1987) neglecting free-troposphere effects, but they can easily be re-investigated and checked. For example, Back and Bretherton (2009) build on the Lindzen and Nigam (1987) framework for their investigation of SST-driven convergence in the boundary layer.

It should also be noted that the purpose of a simplified model is to clarify interactions between processes. Simplified formulations may not be directly relevant to the real world, but they might at least provide some conceptual understanding of the processes involved and allow better informed judgement when it comes to

implementing a set of parameterizations in a full model.

Theoretical Frameworks

And finally, one step down from simplified models are theoretical frameworks. The line between theoretical frameworks and simplified models is not always clear, but let us say here that theoretical frameworks require results to be obtained from analytical or theoretical analysis of equations alone.

Theoretical frameworks often form the underpinning of more complex models and have similar usefulness when evaluating model behaviour to simplified models. That is to say theoretical frameworks can also help us better understand underlying physical processes, provide convergence reference solutions and clarify cause and effect between real-world processes. But theoretical frameworks can also be useful in two other ways: by causing re-evaluation of previously held theoretical assumptions which form the basis of dynamical cores or physics packages; and by providing an understanding of theoretical regimes models can inhabit which increases our understanding of the effect of real-world procesess and process interactions.

Re-evaluation of Theoretical Assumptions: In the past, advances in our understanding of processes and process interactions have often come from insights from theoretical frameworks. Examples include Held and Hou (1980) who analysed axially symmetric circulations in a stably stratified, differentially heated, rotating Boussinesq fluid on a sphere to show how Hadley cell behaviour in the tropics behaved in a sufficiently inviscid fluid. They noted substantial differences and improved performance under the new assumptions compared to the previously more common viscous axisymmetric flows used to study tropical atmospheric behaviour. More recently, Hartmann and Larson (2002) showed that emission temperatures of upper tropospheric water vapour and tropical anvil clouds are mostly independent of changes to the planet surface temperature.

Understanding Theoretical Regimes: Theoretical frameworks are also very useful for situating model-states within the wider context. It is sometimes easy to forget that Earth-like atmospheric states are only a select number of states arising from a constrained set of equations. We make assumptions about gravity for example, or a stably stratified atmosphere. For a broader understanding of phenomena,

it can be very useful to understand how one state fits with another one even if that state is difficult to obtain in the real-world Earth System. Such theoretical frameworks are fairly common and well-documented on the dynamics side of the equation – geostrophic balance for example – with attempts to go as far as to outline a unifying mathematical approach for the dynamics (Klein, 2005). Extending the theoretical framework to include physics processes is more complicated, though notable physics-dynamics balance frameworks where at least one physics process is included would encompass work such as the Weak Temperature Gradient Approximation (Sobel et al., 2001) and geotriptic or semi-geostrophic balance (Beare and Cullen, 2012). Klein (2005) also deal briefly with source terms on the right hand side of the dynamical governing equations, though mostly in reference to other works such as the Weak Temperature Gradient (WTG) Approximation. There are relatively few theoretical frameworks that consider more than one physics process. Sobel et al. (2001) do include Rayleigh drag in their equations, but it is not treated in any serious capacity as the focus is on the free tropospheric WTG regime where drag is not very important.

The use of theoretical frameworks has similar advantages to the use of simplified models in analysing GCM behaviour, but with the added advantage of being theories and not models and therefore not subject to numerical complications in results. But just as theoretical frameworks have similar advantages to simplified models, theoretical frameworks also suffer from similar criticisms – namely of being too simple to be of much use when analysing GCMs. Theoretical frameworks in particular might be accused of being too simple to have much bearing on full GCMs at all, though the usefulness of theoretical frameworks in providing reference solutions should not be discounted.

As Maher et al. (2019) argue, simplified models – and by extension – theoretical frameworks will usually connect to GCMs through a series of models of increasing complexity. In Bretherton and Sobel (2003), the WTG framework for example is found to provide a reasonable approximation to the simplified Gill Model (Gill, 1980). And we have seen that simple single-column models are used to test physics parameterizations before their implementation in full models (Lock et al., 2000). Though sometimes the link between theoretical frameworks and full models is more direct such as Cullen (2018), where semi-geostrophic theory is used to analyse the performance of the full Met Office Unified Model.

We argue that theoretical frameworks combined with simplified models are probably some of the most important tools available to researchers when it comes to understanding physical processes and thereby understanding physics-physics and physics-dynamics interactions. And regardless of simplifications, more understanding of physical processes should filter up to GCMs.

2.4 Conclusions

This review has examined Physics-Dynamics coupling in the context of atmospheric models. The interactions of small-scale processes in large-scale models can be complex and difficult to analyse. Through this chapter, we have identified issues with separate dynamics, separate physics formulations, and separate physics-dynamics coupling schemes.

It has been established that many of the traditional analyses are difficult to use for physics-dynamics coupling analysis in full GCMs, with time step convergence tests proving problematic in full models. We showed that although there may not be a simple solution to the problem of improving accuracy in weather and climate models, there are nonetheless still many ways to approach the problem. In particular, the development of a model and test case hierarchy allows us to analyse model accuracy at multiple levels from complex full model test runs to using simplified models and theoretical frameworks to better understand real-world processes and process interactions.

The remainder of this thesis focuses on outlining theoretical frameworks to help us better understand process behaviour and process interactions in the tropics. In particular, we will look at interactions between the surface drag and convective heating in the dry and moist tropical atmosphere and specifically within the boundary layer since surface drag and convective heating are significant processes in the boundary layer and boundary layer convergence and surface drag have been shown to affect convective behaviour in the tropics (e.g. Back and Bretherton (2009), Park et al. (2018)). We will approach the problem via attempting to better understand the theoretical long-term balance regimes or a lack thereof in the tropics when heating and drag physics are present and we will also look at how adjustment to balance after a heating event may be affected by damping.

We will define a long-term balanced state to be an atmospheric state where fast

modes such as gravity waves are filtered out although fast processes will have an effect on the development or existence of long-term balanced states.

The advantage of looking at theoretical long-term balance states when it comes to understanding processes and process interactions in the tropics is that theoretical long-term balance states give us the expected long-term behaviour of a model. Thus, we can use theoretical long-term balance states as reference solutions of a kind against which full models can be tested. Looking at which long-term balance states occur when we vary the parameters for various physical processes such as drag and heating also allows us to identify which features of the long-term circulation might be caused by or impacted by which processes or process interactions.

We also want to investigate the sensitivity of long-term balance states to the choice of input parameters, especially the horizontal resolution of a given model. Given concerns around the grey-zone in atmospheric modelling, it is important to understand how the existence or non existence of theoretical regimes is affected by actual model restraints and in particular whether any processes in particular can cause model results to be strongly affected by changes in resolution.

More specifically, in chapter 3, we will outline four theoretical long-term balance regimes in the 2D dry Euler equations for the tropical atmosphere with heating and drag physics which can form the theoretical reference solutions for balance scalings that should hold in 2D Held-Suarez-like test cases for the near-equator region. We will show that each regime is dependent on the strength of heating and drag parameters and that each regime produces notably different behaviour in the Thuburn (2017) model.

In chapter 4, we will outline moist versions of the long-term balance regimes in chapter 3 as well as additional regimes supported in the moist case. We will show not only that a long-term balance regime is achievable in the moist boundary layer, but also that the existence or not of long-term balance in the boundary layer substantially affects the triggering, sustaining and organisation of moist convective plumes.

In the dry experiments in chapter 3 and the moist experiments in chapter 4, we will see that results are often dependent on the choice of input parameters, but also on how the model circulation interacts with the the input parameters such as resolution to determine which long-term regime a model run finds itself in – if a long-term balance regime exists at all.

Then in chapter 5, we will consider adjustment to balance looking specifically at the effect of drag on gravity waves in a weak temperature gradient adjustment setup similar to geostrophic or hydrostatic adjustment problems. We will show that there is a critical value of drag above which waves cannot be supported in the drag-damped part of the model and that the critical drag value is dependent on the resolution and the background temperature profile.

Finally, in chapter 5, we also ask how the drag-damping might affect adjustment to balance in the dry model runs and whether the balance timescales for the regimes outlined in chapter 3 are affected by drag-damping of gravity waves.

Chapter 3

Dry Balance Regimes in 2D Tropical Dynamics with Heating and Drag Physics

In this chapter, we use scale analysis of the 2D (vertical slice) dimensionless dry Euler equations for fluid motion in the atmosphere to derive four distinct long-term balance regimes that highlight interactions between heating and drag in the tropics. Our scale analysis provides scalings for response variables such as horizontal and vertical velocity and perturbations to pressure and potential temperature, which can be used as ground truths in 2D Held-Suarez-like near-equator test cases for the development of more complex weather and climate models. We also derive timescales for balance in each balance regime and critical parameter values for transitions between regimes. Theoretical results are then tested in a 2D semi-Lagrangian, semi-implicit dynamical core with heating and Rayleigh drag physics. We find that model results broadly match theoretical expectations, though there are discrepancies caused by uncertainties in variable scales, especially the horizontal length scale.

3.1 Introduction

We begin our analysis of weather and climate processes and process interactions in the tropics by considering the effect of drag and heating in an idealised setup of the dry tropical atmosphere.

Heating and drag are two important physics processes at play in the tropical

atmosphere, especially in the boundary layer where surface drag is strongest and heating can be said to a first order approximation to be driven by convective heating or clouds. We choose to start by looking at the dry equations as even though moisture is an important process in the tropics, it is useful for our understanding of heating and drag interactions in the tropics to study first how drag and heating interact in the absence of moisture. We can then use any understanding gleaned from drag and heating interactions in the dry case to inform our understanding of the moist case later on in chapter 4. The dry case also provides an interesting test case on its own and when it comes to the boundary layer, convection can often be dry anyway (Honnert et al., 2020).

In this chapter, we present a theoretical framework based on scale analysis of the dimensionless 2D Euler Equations for a dry compressible atmosphere without Coriolis acceleration to investigate long-term balance regimes, transitions and timescales in tropical dynamics when heating and drag are included.

We use Rayleigh drag for the drag term in the horizontal momentum equation and we use a specified elliptical heating rate in the thermodynamic equation for the heating. Scale analysis then provides us with a number of dimensionless parameters including, crucially, one parameter based on the drag timescale and one parameter based on the heating rate. By varying the dimensionless drag and heating parameters independently, we obtain four possible long-term physics-dynamics balance regimes where either the drag, the heating, or both are leading order terms in the governing equations.

It is of particular importance that we consider both heating and drag as, whilst scale analysis of dynamics-only balance regimes is a long-established and well-studied field (e.g. Klein (2005), Vallis (2017) among many others), balance regimes which include physics components have received less attention. Some notable examples include the Weak Temperature Gradient approximation – or WTG (Sobel et al., 2001) which considers the effect of heating on the free troposphere, and Darcy's balance which considers the effect of drag on circulation in the boundary layer (Beare and Cullen, 2012). Both are examples of single physics balance analysis. Multiple physics balance analysis has received even less attention than single physics balance analysis, possibly due to increasing complexity of the equations when more physics components are added. Here, we build on both WTG and Darcy's balance to consider the multiple long-term balance regimes which emerge from the inclusion

of multiple physics – notably drag and heating – in the 2D dry Euler equations.

In general, broadening the analysis of long-term balance regimes to include physics processes should help us better understand physics interactions in GCMs. Test cases based on physics-dynamics balance regimes can be developed to highlight areas where the numerical representations of parameterizations in GCMs are failing and the balance regimes themselves might be used as asymptotic limits towards which GCMs should converge. Analysis of long-term balance regimes can also provide theoretical solutions for already developed test cases which rely on 'reference solutions'. For example, particularly relevant to this chapter are Held-Suarez like test cases. Held and Suarez (1994) developed an idealised test case which imposed drag and heating on GCMs. The test case was used to highlight the differences between dynamical core performance with a focus on extra-tropical eddies as results in the tropics can be sensitive to numerical treatments such as diffusion. However, Held and Suarez (1994) provided no theoretical solutions to their test case.

Here, we provide theoretical solutions for a 2D Held-Suarez like test case for the near-equator tropics. The long-term balance regimes derived in this chapter can be used to test models in two ways. Firstly, for each of our identified balance regimes, the theory predicts the scaling of typical response variables (e.g. horizontal velocity, vertical velocity, perturbations to the background Exner pressure profile, and perturbations to the background potential temperature profile) based on variables that are often model inputs and can be more easily imposed on models (e.g. heating rate, drag strength etc.) Secondly, the theory also predicts where transitions between regimes occur. We can use both the response variable scalings and transition predictions as 'ground truths' for weather and climate models with appropriate setups and input variables, though choosing the correct horizontal and vertical length scales in particular is no trivial task. Changes to the horizontal lengthscale driven by the flow itself choosing its own lengthscales impact the transitions between regimes as the heating rate is increased and the horizontal lengthscale is required to shrink in order for two of the four balance regimes outlined in this chapter to be achievable.

Predictions based on the physics-dynamics heating and drag long-term balance regime theory are tested initially in a 2D semi-Lagrangian, semi-implicit model (Thuburn, 2017). We find that the model is able to achieve the long-term balance regimes in the theory and many features are well-predicted, although substantial discrepancies between predictions and model results still remain. More model com-

parisons are required to check whether the discrepancies between prediction and results are replicated across models.

3.2 Dry Equation Framework

3.2.1 2D system of equations

Consider a set of 2D equations for a simplified version of the tropics at the equator. These are the 2D equations for a dry, compressible atmosphere, neglecting Coriolis and variations with latitude:

$$\frac{\partial \rho}{\partial t} + \nabla\cdot(\rho \mathbf{u}) = 0; \tag{3.1}$$

$$\frac{D\theta}{Dt} = q; \tag{3.2}$$

$$\frac{D\mathbf{u}}{Dt} + c_p\theta\nabla\pi + \nabla\phi = \left(-\frac{u}{\tau}, 0\right); \tag{3.3}$$

$$\pi = \left(\frac{\rho R\theta}{p_{ref}}\right)^{\frac{\kappa}{1-\kappa}}. \tag{3.4}$$

These equations provide a mass conservation equation (3.1), a thermodynamic equation with a physics heating component (3.2), a momentum equation with a drag component in the horizontal (3.3), and an equation of state, here for dry air (3.4). Equations (3.1)-(3.4) provide a system of 5 equations for 5 prognostic variables. Notation is mostly standard with p pressure, p_{ref} a constant reference pressure, $\mathbf{u} = (u(x,z,t), w(x,z,t))$ velocity in the horizontal (x) and vertical (z) directions only, with temporal dependence where t is time. Here θ is potential temperature, q is a heating rate, ρ is density, c_p is the specific heat capacity at constant pressure for dry air, R is the gas constant for dry air, ϕ is geopotential and u/τ is a linear Rayleigh drag term, where $\tau(x,z)$ is a drag timescale. We also have dimensionless parameter $\kappa = R/c_p$. The Exner pressure π is related to pressure p by the following equation: $\pi = \left(\frac{p}{p_{ref}}\right)^{\kappa}$. As the equations are 2D, the operator ∇ takes the form $\nabla a = \partial_x a + \partial_z a$ and the operator D/Dt likewise takes the form $D(a)/Dt = d_t a + x\partial_x a + z\partial_z a$.

3.2.2 Scaled variables

In order to identify leading order terms in equations (3.1)-(3.4) and therefore long-term balance regimes where heating and drag are of leading order, we scale the variables as follows. Firstly, let

$$\theta = \theta_0(z) + \Theta\hat{\theta}(x, z, t), \tag{3.5}$$

where a hat ($\hat{}$) denotes a dimensionless variable of $O(1)$. The variable θ has two parts: a background mean θ_0 which varies only with height z, and a perturbation to the mean $\Theta\hat{\theta}$; the dimensionless perturbation $\hat{\theta}$ depends on height and horizontal location and can vary in time, while Θ is a constant dimensional scale for the perturbation. Variables π and ρ are similarly split:

$$\pi = \pi_0(z) + \Pi\hat{\pi}(x, z, t); \quad \rho = \rho_0(z) + P\hat{\rho}(x, z, t). \tag{3.6}$$

We will also assume the background thermodynamic variables are in hydrostatic balance i.e.

$$\frac{\partial \pi_0}{\partial z} = -\frac{g}{c_p\theta_0}. \tag{3.7}$$

where $g = \partial\phi/\partial z$. Throughout this chapter, we will also use the Brunt-Vaisala frequency (e.g. Emmanuel (1994), Vallis (2017) etc.) which is defined as

$$N^2 = \frac{g}{\theta_0}\frac{\partial \theta_0}{\partial z} \tag{3.8}$$

We will use a zero mean for the velocities. The remaining scaled quantities include:

$$\begin{aligned} &u = U\hat{u}, \quad w = W\hat{w}, \quad q = Q\hat{q} \quad \tau = \tau_0\hat{\tau} \\ &x = L\hat{x}, \quad z = H\hat{z}, \quad t = T\hat{t}. \end{aligned}$$

3.2.3 Non-Dimensional Equations

We now scale equations (3.1)-(3.4) to obtain non-dimensional equations with dimensionless parameters.

Mass conservation

From equation (3.1):

$$\frac{P}{T}\frac{\partial\hat{\rho}}{\partial\hat{t}}+P\hat{\rho}\left(\frac{U}{L}\frac{\partial\hat{u}}{\partial\hat{x}}+\frac{W}{H}\frac{\partial\hat{w}}{\partial\hat{z}}\right)+\rho_0\left(\frac{U}{L}\frac{\partial\hat{u}}{\partial\hat{x}}+\frac{W}{H}\frac{\partial\hat{w}}{\partial\hat{z}}\right)+W\frac{\partial\rho_0}{\partial z}\hat{w}+\frac{UP}{L}\hat{u}\frac{\partial\hat{\rho}}{\partial\hat{x}}+\frac{WP}{H}\hat{w}\frac{\partial\hat{\rho}}{\partial\hat{z}}=0. \tag{3.9}$$

Non-dimensionalising gives

$$\frac{L}{UT}\frac{\partial\hat{\rho}}{\partial\hat{t}}+\frac{\rho_0}{P}\frac{\partial\hat{u}}{\partial\hat{x}}+\frac{\rho_0}{P}\frac{LW}{UH}\frac{\partial\hat{w}}{\partial\hat{z}}+\hat{\rho}\frac{\partial\hat{u}}{\partial\hat{x}}+\frac{LW}{UH}\hat{\rho}\frac{\partial\hat{w}}{\partial\hat{z}}+\frac{\rho_0 WL}{PUH_\rho}\hat{w}+\hat{u}\frac{\partial\hat{\rho}}{\partial\hat{x}}+\frac{LW}{UH}\hat{w}\frac{\partial\hat{\rho}}{\partial\hat{z}}=0. \tag{3.10}$$

Rewriting in terms of dimensionless parameters gives

$$St\frac{\partial\hat{\rho}}{\partial\hat{t}}+\frac{1}{\rho_r}\left(\frac{\partial\hat{u}}{\partial\hat{x}}+\frac{A_s}{V_s}\frac{\partial\hat{w}}{\partial\hat{z}}\right)+\hat{\rho}\left(\frac{\partial\hat{u}}{\partial\hat{x}}+\frac{A_s}{V_s}\frac{\partial\hat{w}}{\partial\hat{z}}\right)-\frac{1}{\rho_r}\frac{A_s}{V_s}\frac{H}{H_\rho}\hat{w}+\hat{u}\frac{\partial\hat{\rho}}{\partial\hat{x}}+\frac{A_s}{V_s}\hat{w}\frac{\partial\hat{\rho}}{\partial\hat{z}}=0. \tag{3.11}$$

where $St=\frac{L}{UT}$ is the Strouhal number representing the ratio of the advection timescale $\frac{L}{U}$ to the transience timescale T and $\rho_r=\frac{P}{\rho_0}$. We also have the scale height for density $\frac{1}{H_\rho}=-\frac{1}{\rho_0}\frac{\partial\rho_0}{\partial z}$, the aspect ratio $A_s=\frac{L}{H}$, and the ratio of horizontal to vertical velocity $V_s=\frac{U}{W}$.

Thermodynamic equation

From equation (3.2), and letting $\frac{\partial\theta_0}{\partial z}=\frac{N^2}{g}\theta_0$ by definition of the Brunt-Vaisala frequency, we get a non-dimensionalised equation:

$$\frac{L}{UT}\frac{\partial\hat{\theta}}{\partial t}+\hat{u}\frac{\partial\hat{\theta}}{\partial x}+\hat{w}\frac{WLN^2\theta_0}{U\Theta g}+\frac{LW}{UH}\hat{w}\frac{\partial\hat{\theta}}{\partial z}=\frac{QL}{\Theta U}\hat{q}. \tag{3.12}$$

Now we rewrite for dimensionless parameters:

$$St\frac{\partial\hat{\theta}}{\partial t}+\hat{u}\frac{\partial\hat{\theta}}{\partial x}+\hat{w}\left(\frac{A_s}{V_s}\right)\frac{N^2H}{g\theta_r}+\frac{A_s}{V_s}\hat{w}\frac{\partial\hat{\theta}}{\partial z}=\lambda\hat{q}, \tag{3.13}$$

where $\theta_r=\frac{\Theta}{\theta_0}$ is the ratio of the potential temperature perturbations to the background profile, $\lambda=\frac{QL}{\Theta U}$ is the ratio of the advection timescale to the heating timescale, similar to the dimensionless number obtained in the shallow water system in Sobel et al. (2001).

Equation of state

We use the equation of state to derive the speed of sound. Following the example given in Thuburn (2017), we say

$$\left.\frac{\partial\rho}{\partial p}\right|_{\eta} = \frac{1}{c^2}. \tag{3.14}$$

Letting $\eta = c_p \log(\theta)$ (Emanuel et al., 1987) and re-arranging equation 3.4, we get

$$\left.\frac{\partial\rho}{\partial p}\right|_{\eta} = \left.\frac{\partial\rho}{\partial p}\right|_{\theta} = \left.\frac{\partial}{\partial p}\right|_{\theta}\left[\frac{(p_{ref})^{\kappa}}{R\theta}p^{(1-\kappa)}\right] \tag{3.15}$$

which gives

$$\left.\frac{\partial\rho}{\partial p}\right|_{\theta} = \frac{(p_{ref})^{\kappa}}{R\theta}(1-\kappa)p^{-\kappa}. \tag{3.16}$$

Substituting π back in, we get

$$\left.\frac{\partial\rho}{\partial p}\right|_{\theta} = \frac{1-\kappa}{R\theta\pi} = \frac{1-R/c_p}{R\theta\pi}. \tag{3.17}$$

If we now acknowledge that specific heat capacities at constant volume (c_v) and pressure (c_p) are linked via $c_p - c_v = R$, we obtain

$$\left.\frac{\partial\rho}{\partial p}\right|_{\theta} = \frac{c_p - c_v}{c_p R\theta\pi} = \frac{c_v}{c_p R\theta\pi} = \frac{1}{\gamma R\theta\pi} \tag{3.18}$$

where $\gamma = c_p/c_v$ is a dimensionless constant here. Using our scaled variables, we extract the speed of sound $c(z)$ for the background state of the atmosphere at rest: $c^2(z) = \gamma R\pi_0\theta_0$. The speed of sound varies here as a function of height, temperature and pressure. We use $c(z)$ later for the Mach number – the ratio of a typical flow velocity to the speed of sound.

In terms of non-dimensionalising the equation of state, we take logarithms of equation (3.4), substitute in equations (3.5) and (3.6) and rearrange to give:

$$\log(\pi_0 + \Pi\hat{\pi}) = \frac{\kappa}{1-\kappa}\Big(\log(\rho_0 + P\hat{\rho}) + \log(\theta_0 + \Theta\hat{\theta}) + \mathsf{constant}\Big) \tag{3.19}$$

Then we differentiate and linearise to obtain:

$$\frac{\Pi}{\pi_0}\hat{\pi} = \frac{\kappa}{1-\kappa}\left(\frac{P}{\rho_0}\hat{\rho} + \frac{\Theta}{\theta_0}\hat{\theta}\right). \tag{3.20}$$

Re-arranging gives

$$\gamma R\pi_0\theta_0\hat{\rho} = \frac{1}{\rho_r}\left(\kappa R\Pi\theta_0\hat{\pi} - \gamma R\pi_0\Theta\hat{\theta}\right) \implies \rho_r\hat{\rho} = \frac{1}{\kappa\gamma}\pi_r\hat{\pi} - \theta_r\hat{\theta}. \tag{3.21}$$

Momentum equation - x component

From the x-component of equation (3.3), assuming no geopotential derivative in the horizontal:

$$\frac{\partial u}{\partial t} + u\frac{\partial u}{\partial x} + w\frac{\partial u}{\partial z} + c_p\theta\frac{\partial \pi}{\partial x} = -\frac{u}{\tau}. \tag{3.22}$$

We then scale and non-dimensionalise to give:

$$\frac{L}{UT}\frac{\partial \hat{u}}{\partial \hat{t}} + \hat{u}\frac{\partial \hat{u}}{\partial \hat{x}} + \frac{WL}{UH}\hat{w}\frac{\partial \hat{u}}{\partial \hat{z}} + \frac{c_p\theta_0\Pi}{U^2}\frac{\partial \hat{\pi}}{\partial \hat{x}} + \frac{c_p\Theta\Pi}{U^2}\hat{\theta}\frac{\partial \hat{\pi}}{\partial \hat{x}} = -\frac{L}{U\tau_0}\frac{\hat{u}}{\hat{\tau}}. \tag{3.23}$$

In terms of dimensionless parameters:

$$St\frac{\partial \hat{u}}{\partial \hat{t}} + \hat{u}\frac{\partial \hat{u}}{\partial \hat{x}} + \frac{A_s}{V_s}\hat{w}\frac{\partial \hat{u}}{\partial \hat{z}} + \frac{\pi_r}{\kappa\gamma M^2}\frac{\partial \hat{\pi}}{\partial \hat{x}} + \frac{\pi_r\theta_r}{\kappa\gamma M^2}\hat{\theta}\frac{\partial \hat{\pi}}{\partial \hat{x}} = -D\frac{\hat{u}}{\hat{\tau}}, \tag{3.24}$$

where M is the Mach number such that $M^2 = \frac{U^2}{c^2}$, and $D = \frac{L}{U\tau_0}$ is the ratio of the advection timescale to the drag timescale.

Momentum equation - z component

From the z-component of equation (3.3):

$$\frac{W}{T}\frac{\partial \hat{w}}{\partial \hat{t}} + \frac{UW}{L}\hat{u}\frac{\partial \hat{w}}{\partial \hat{x}} + \frac{W^2}{H}\hat{w}\frac{\partial \hat{w}}{\partial \hat{z}} + c_p\theta\frac{\partial \pi}{\partial z} + \frac{\partial \phi}{\partial z} = 0. \tag{3.25}$$

Non-dimensionalising, we obtain:

$$\frac{L}{UT}\frac{\partial \hat{w}}{\partial \hat{t}} + \hat{u}\frac{\partial \hat{w}}{\partial \hat{x}} + \frac{WL}{UH}\hat{w}\frac{\partial \hat{w}}{\partial \hat{z}} + \frac{Lc_p\theta_0}{WU}\frac{\partial \pi_0}{\partial z} + \frac{Lc_p\Theta}{WU}\frac{\partial \pi_0}{\partial z}\hat{\theta} + \frac{Lc_p\theta_0\Pi}{WUH}\frac{\partial \hat{\pi}}{\partial \hat{z}} + \frac{Lc_p\Theta\Pi}{WUH}\hat{\theta}\frac{\partial \hat{\pi}}{\partial \hat{z}} + \frac{Lg}{WU} = 0. \tag{3.26}$$

Recalling that we assumed a hydrostatic base-state where $\frac{\partial \pi_0}{\partial z} = -\frac{g}{c_p\theta_0}$ we then have that $\frac{Lc_p\theta_0}{WU}\frac{\partial \pi_0}{\partial z} + \frac{Lg}{WU} = 0$. We now define the remaining terms with dimensionless parameters:

$$St\frac{\partial \hat{w}}{\partial \hat{t}} + \hat{u}\frac{\partial \hat{w}}{\partial \hat{x}} + \frac{A_s}{V_s}\hat{w}\frac{\partial \hat{w}}{\partial \hat{z}} - \frac{Lg}{WU}\theta_r\hat{\theta} + A_sV_s\frac{\pi_r}{\kappa\gamma M^2}\frac{\partial \hat{\pi}}{\partial \hat{z}} + A_sV_s\frac{\pi_r\theta_r}{\kappa\gamma M^2}\hat{\theta}\frac{\partial \hat{\pi}}{\partial \hat{z}} = 0. \tag{3.27}$$

Both momentum equations contain the Mach number on the denominator for pres-

sure terms, as we might expect (Klein, 2005).

3.2.4 Dimensionless parameters

Below is a list of all 14 dimensionless parameters obtained from this analysis:

$$\lambda = \frac{QL}{\Theta U}, \quad A_s = \frac{L}{H}, \quad St = \frac{L}{UT}, \quad D = \frac{L}{U\tau_0}, \quad M^2 = \frac{U^2}{\gamma R\theta_0\pi_0}, \quad \frac{N^2H}{g}, \quad \theta_r = \frac{\Theta}{\theta_0}$$
$$\gamma = \frac{c_p}{c_v}, \quad \kappa = \frac{R}{c_p}, \quad \pi_r = \frac{\Pi}{\pi_0}, \quad \frac{Lg}{WU}, \quad \frac{H}{H_\rho}, \quad \rho_r = \frac{P}{\rho_0}, \quad V_s = \frac{U}{W}.$$

This is expected from Buckingham's Π theorem where the number of dimensionless parameters in a given equation set is the total number of parameters minus the number of base dimensions (Buckingham, 1914). Here, we have 19 variables: ρ_0, P, T, U, L, W, H, H_ρ, θ_0, Θ, N^2, g, Q, τ_0, π_0, Π, c_p, c_v, R. These variables contain 4 base dimensions, which we might write K, m, s, kg and so we should expect 15 dimensionless parameters. However, as Π and π_0 are already dimensionless, and can be represented in the equations by their ratio, we can reduce to 14 dimensionless parameters only as above.

The choice of dimensionless parameters chosen here is not unique, but we have attempted to define parameters that will be most useful in the regime analyses in Section 3.4, as well as choosing, where possible, recognised dimensionless parameters such as the Mach and Strouhal numbers and trying to obtain similar parameters across equations for easier comparison. We will use the dimensionless parameters to determine dominant balances and regimes. We will do this by reducing the 'free' or varying dimensionless parameters through systematic assumptions.

3.3 Simplifying Parameter Assumptions and Impacts

The scope of equations (3.1)-(3.4) is very broad. In this chapter, we consider a subcategory of the full framework that exposes the relationship between drag and heating in the equations. In the following section, we lay out the assumptions that provide us with a narrow enough region of parameter space to obtain 4 separate balance regimes, which will be explored in Section 3.4, with predictions used to test a model in Section 3.6. We start with 14 dimensionless parameters. As γ and κ are constant, taking typical values for dry air, we are down to 12 dimensionless parameters.

3.3.1 Timescales

For our balances, we consider the long term behaviour of the system, when the Strouhal number satisfies $St \ll O(1)$, i.e. the transience timescale is much larger than the advection timescale $T \gg \frac{L}{U}$. This reduces the 'free' dimensionless parameters to 11 and removes the time derivatives from our equations when considering balance states.

3.3.2 Perturbation sizes

We then assume the perturbation part of each thermodynamic variable is much smaller than the mean state such that

$$\theta_r = \frac{\Theta}{\theta_0} \ll O(1); \quad \pi_r = \frac{\Pi}{\pi_0} \ll O(1); \quad \rho_r = \frac{P}{\rho_0} \ll O(1) \tag{3.28}$$

This is a reasonable assumption if the forcing on the right-hand side of the thermodynamic equation is not too strong as is reasonable for virtually all atmospheric flows. We now have 8 'free' dimensionless parameters.

3.3.3 Mass conservation and advection scales

We now consider the scaled mass conservation equation (3.11), neglecting products of small quantities i.e. perturbation multiples:

$$St\frac{\partial\hat{\rho}}{\partial\hat{t}} + \frac{1}{\rho_r}\left(\frac{\partial\hat{u}}{\partial\hat{x}} + \frac{A_s}{V_s}\frac{\partial\hat{w}}{\partial\hat{z}}\right) + \frac{1}{\rho_r}\frac{A_s}{V_s}\frac{H}{H_\rho}\hat{w} = 0. \tag{3.29}$$

Now, either $St\rho_r \geq O(1)$, which would allow acoustic waves, or $St\rho_r \ll O(1)$ and we have an anelastic atmosphere, where $\nabla\cdot(\rho_0\mathbf{u}) \approx 0$. We have established already that we are interested in long timescale and therefore we neglect the time derivative. This allows for 2 balances, dependent on parameter $\frac{H}{H_\rho}$. Either $\frac{H}{H_\rho} \sim O(1)$ for the compressible anelastic case, or $\frac{H}{H_\rho} \ll O(1)$ for the Boussinesq case where the density scale height can be considered infinite (Dukowicz, 2013). $\frac{H}{H_\rho} \gg O(1)$ is not allowed as there would be no term to balance it, though it is possible in an acoustic wave scenario when the time derivative has not been discarded.

Both $\frac{H}{H_\rho} \ll O(1)$ and $\frac{H}{H_\rho} \sim O(1)$ give a balance of the form:

$$\frac{A_s}{V_s} \sim O(1) \implies \frac{U}{L} \sim \frac{W}{H}. \tag{3.30}$$

This implies horizontal velocity over horizontal scales is similar to vertical velocity over vertical scales, with the caveat that in the compressible case, all three remaining advection terms balance, as opposed to only the $\nabla \cdot \mathbf{u}$ terms as in the Boussinesq approximation. For our purposes, this does not affect our analysis and we are down to 6 'free' dimensionless parameters.

3.3.4 Hydrostatic balance - perturbations

In the z-momentum equation, if we assume $St \ll O(1)$, and that perturbations to the mean state for θ and π are much smaller than the mean state, we are left with

$$\hat{u}\frac{\partial \hat{w}}{\partial \hat{x}} + \frac{A_s}{V_s}\hat{w}\frac{\partial \hat{w}}{\partial \hat{z}} - \frac{Lg}{WU}\theta_r\hat{\theta} + A_s V_s \frac{\pi_r}{\kappa\gamma M^2}\frac{\partial \hat{\pi}}{\partial \hat{z}} = 0. \tag{3.31}$$

For L sufficiently large, and $\frac{Lg}{WU} >> \frac{1}{\theta_r}$, the $\frac{Lg}{WU}\theta_r\hat{\theta}$ term cannot be balanced by the advection terms, which are both $O(1)$, due to anelasticity. Therefore, we expect hydrostatic balance to hold not only for the background thermodynamic terms, but also for the perturbation terms:

$$\frac{Lg}{WU}\theta_r \sim A_s V_s \frac{\pi_r}{\kappa\gamma M^2} \implies \Theta\frac{g}{\theta_0} \sim \frac{c_p\theta_0\Pi}{H} \implies \Theta \sim \frac{c_p\theta_0^2\Pi}{Hg}. \tag{3.32}$$

In the atmosphere, M^2 is often assumed to be small (Klein, 2005), and this is implied by the balance in equation (3.32). It should also be noted that although we have hydrostatic balance in the perturbation terms here, the equations allow for non-hydrostatically balanced regimes if L is sufficiently small and Θ perturbations sufficiently large. This fixes another dimensionless parameter, leaving us with only 5 'free' dimensionless parameters remaining – a much more tractable regime space.

3.3.5 Boundary layer and the free troposphere

In the x-momentum equation, we consider the separation between boundary layer and free troposphere to be determined by the strength of the drag i.e. the size of the dimensionless parameter $D = \frac{L}{U\tau_0}$. In the free troposphere, we might expect drag

to be small enough that it is close to zero, i.e. $D \ll O(1)$, whereas in the boundary layer, we assume $D \geq O(1)$ (see figure 3.1).

3.3.6 Drag-Heating Regime Space

Applying the assumptions above, we are left with the following set of equations and dominant balances:

$$\frac{WL}{UH} \sim O(1) \tag{3.33}$$

$$\Theta \sim \frac{c_p \theta_0^2 \pi}{Hg} \tag{3.34}$$

$$\hat{u}\frac{\partial \hat{\theta}}{\partial \hat{x}} + \hat{w}\left(\frac{WL}{UH}\right)\frac{N^2 H}{g\theta_r} + \frac{WL}{UH}\hat{w}\frac{\partial \hat{\theta}}{\partial \hat{z}} = \lambda \hat{q}, \tag{3.35}$$

$$\hat{u}\frac{\partial \hat{u}}{\partial \hat{x}} + \frac{WL}{UH}\hat{w}\frac{\partial \hat{u}}{\partial \hat{z}} + \frac{\pi_r}{\kappa\gamma M^2}\frac{\partial \hat{\pi}}{\partial \hat{x}} = -D\frac{\hat{u}}{\hat{\tau}}, \tag{3.36}$$

From these equations, we can determine long-term balance regimes where drag and/or heating are of leading order.

3.4 Regimes

We now consider the four regimes determined primarily by differences in the magnitudes of drag parameter D and heating parameter λ. These are the Weak Temperature Gradient, the Boundary Layer Pseudo-Weak Temperature Gradient, the Advection Dominated Boundary Layer, and the Advection Dominated Free Troposphere. The latter three are novel at least in the formulation in this thesis e.g. 2D Euler equations with Rayleigh drag and constant heating rate and so the regime names have been chosen accordingly and are not taken from existing literature. The regime space we outline is presented in figure 3.1 with four regimes where heating and drag parameters are of leading order. There is also an area of the regime space when $\lambda < O(1)$ which we determine to have no circulation as when forced heating is present, $\lambda \geq O(1)$ because the other variables should adjust to the forcing. Thus the portion of the regime space where $\lambda < O(1)$ is inaccessible when forced heating is present and would correspond to unforced dynamics only.

3.4.1 Weak Temperature Gradient

We will start by looking at the balance regime called the Weak Temperature Gradient approximation (WTG), because it is a well-known regime associated with the tropical free troposphere. WTG assumes a dominant balance in the thermodynamic equation between heating and vertical velocity. The regime has been explored in the Shallow Water Equation system (Sobel et al., 2001) and in 3D equations (Romps, 2012). The WTG approximation is often used as a supra-domain-scale parameterization for the free troposphere to establish a background balanced state that can be forced by the boundary layer or other heating processes and has been tested in various contexts (Bretherton and Sobel (2003), Romps (2012)). Here we demonstrate how the regime fits into the parameter space governed by variations in the dimensionless heating parameter λ and the dimensionless drag parameter D. Figure 3.1 shows the regime space.

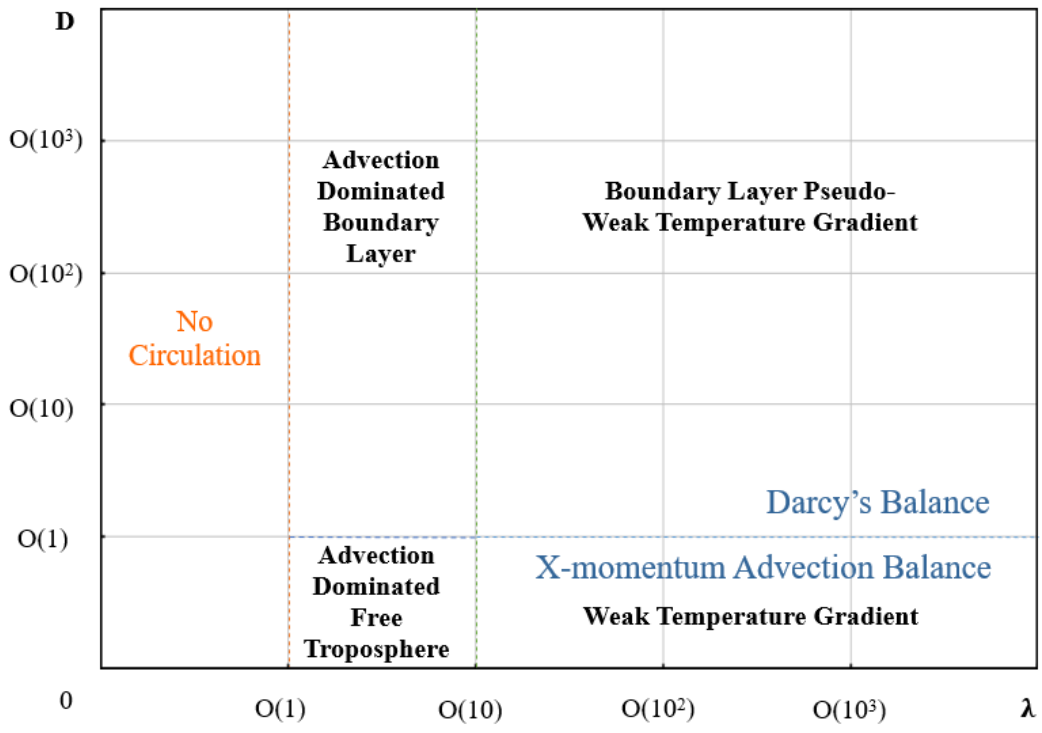

Figure 3.1: Hypothesised regimes obtained by varying dimensionless parameters D and λ, where D represents a drag parameter and λ a heating parameter.

The WTG regime is easily derived from the 2D equations (3.33)-(3.36) with the further assumptions that $\lambda > O(1)$ and $D \ll O(1)$ i.e. the heating term is of leading order and drag term is negligeable as we are dealing with the free troposphere. This

leaves us with a set of balances in our equations. From the thermodynamic equation, with $\mathrm{St} \ll O(1)$, we have

$$\left(\frac{LW}{UH}\right)\frac{N^2 H}{g\theta_r} \sim \lambda. \tag{3.37}$$

Noting that due to anelasticity, $\frac{LW}{UH} \sim O(1)$, we can simplify the balance and obtain W in terms of the other variables:

$$\frac{N^2 H\theta_0}{g\Theta} \sim \frac{QH}{\Theta W} \implies W \sim \frac{Qg}{N^2\theta_0}. \tag{3.38}$$

The remaining unknowns U, Θ and Π can then be determined from balances in the z-momentum, x-momentum and mass conservation equations:

$$\Theta \sim \frac{c_p\theta_0^2\Pi}{gH}; \quad \frac{\pi_r}{\kappa\gamma M^2} \sim O(1); \quad \frac{WL}{UH} \sim O(1). \tag{3.39}$$

We can then rearrange to give U, Π and Θ in terms of quantities that can be imposed in model tests:

$$U \sim \frac{LW}{H} \sim \frac{gQL}{N^2\theta_0 H}; \tag{3.40}$$

$$\Pi \sim \pi_0\kappa\gamma M^2 \sim \frac{U^2}{c_p\theta_0} \sim \frac{g^2Q^2L^2}{N^4\theta_0^3H^2c_p}; \tag{3.41}$$

$$\Theta \sim \frac{\theta_0 U^2}{gH} \sim \frac{gQ^2L^2}{H^3N^4\theta_0}. \tag{3.42}$$

Using the predictions for the scales of the output variables, we can also predict the size of all the dimensionless parameters. Notably, we can predict D and λ.

For WTG, D is negligible as the drag timescale τ_0 can be interpreted as being very large. By substituting the scalings for U and Θ in the WTG regimes into $\lambda = QL/(U\Theta)$, we obtain:

$$\lambda \sim \left(\frac{N^3H^2\theta_0}{QLg}\right)^2. \tag{3.43}$$

Using our output variable and dimensionless parameter predictions, we can check whether model behaviour corresponds with the scales suggested by the theory and thus whether assumptions about which regime a model finds itself in are valid. We check this in the model in Section 3.6.

We might also want to extract a timescale at which we assume balance has been

achieved. We can do this by remembering that St $< O(1)$ in the balanced state. Thus, we expect the system to approach a WTG balance when

$$T > \frac{L}{U} \implies T > \frac{QgL^2}{N^2\theta_0 H}. \tag{3.44}$$

3.4.2 Boundary Layer Pseudo-Weak Temperature Gradient

We call the next regime we derive the boundary layer pseudo-weak temperature gradient regime (BLWTG). BLWTG is derived from equations (3.33)-(3.36) with the further assumptions that $\lambda > O(1)$ and $D > O(1)$. From the thermodynamic equation, we have the same balance as WTG and the velocity scales W and U are obtained in the same way as for WTG, given $\frac{WL}{UH} \sim O(1)$:

$$W \sim \frac{Qg}{N^2\theta_0}; \quad U \sim \frac{QLg}{N^2 H\theta_0}. \tag{3.45}$$

The remaining unknowns Θ and Π can be determined from the balances in the z-momentum, x-momentum and mass conservation equations again:

$$\Theta \sim \frac{c_p\theta_0^2\Pi}{gH}; \quad \frac{\pi_r}{\kappa\gamma M^2} \sim D; \quad \frac{WL}{UH} \sim O(1). \tag{3.46}$$

The key difference between the boundary layer pseudo-WTG and the WTG is the balance in the x-momentum equation. In the WTG regime, we had the pressure gradient term balanced by advection as $D \ll O(1)$. In the BLWTG regime, $D > O(1)$ which means the dominant balance in the x-momentum equation is between drag and pressure i.e. Darcy's balance (Beare and Cullen, 2012). We can now rearrange our balances to obtain Π and Θ in terms of imposed quantities using the new x-momentum balance:

$$\Pi \sim \pi_0 \frac{L}{U\tau_0}\frac{U^2}{\gamma R\theta_0\pi_0}\kappa\gamma \sim \frac{QL^2 g}{N^2 H\theta_0^2 c_p\tau_0}; \tag{3.47}$$

$$\Theta \sim \frac{c_p\theta_0^2\Pi}{gH} \sim \frac{QL^2}{N^2H^2\tau_0}. \tag{3.48}$$

For BLWTG λ is given by

$$\lambda \sim \frac{N^4H^3\tau_0^2\theta_0^2 cp}{Qg}, \tag{3.49}$$

and for D, we have:

$$D \sim \frac{N^2 H \theta_0}{g Q \tau_0}. \tag{3.50}$$

We can also predict the relationship between D and λ, if we say

$$\frac{L}{U} \sim \frac{\lambda \Theta}{Q} \implies D \sim \lambda \frac{\Theta}{Q \tau_0} \tag{3.51}$$

Using our scaling for Θ in equation 3.48, we can then find the relationship between D and λ which will be linear if N^2, L and τ_0 are assumed constant:

$$D \sim \lambda \frac{L^2}{N^2 H^2 \tau_0} \tag{3.52}$$

Again, we can use this relationship to check whether model behaviour corresponds with the scales suggested by the theory and whether the model produces a linear trend between D and λ.

Note that as the scaling for U is the same in WTG and BLWTG, both regimes are expected to reach balance states over the same timescale.

3.4.3 Advection Dominated Boundary Layer

We call our next regime the advection dominated boundary layer (ADBL) regime. We derive ADBL from equations (3.33)-(3.36) with the further assumptions that $\lambda \sim O(1)$ and $D > O(1)$. From the thermodynamic equation, with $\mathrm{St} \ll O(1)$, we have the following balance:

$$\lambda \sim O(1) \implies \frac{QL}{U} \sim \Theta \tag{3.53}$$

The x-momemtum, z-momentum and mass conservation balances are the same as for the Boundary Layer pseudo-WTG regime. If we re-arrange and solve for unknowns W, U, Π and Θ, we get:

$$W \sim \frac{H}{L} \left(\frac{QHg\tau_0}{\theta_0} \right)^{\frac{1}{2}}; \tag{3.54}$$

$$U \sim \left(\frac{QHg\tau_0}{\theta_0} \right)^{\frac{1}{2}}; \tag{3.55}$$

$$\Pi \sim \frac{L}{c_p \theta_0} \left(\frac{QgH}{\tau_0 \theta_0} \right)^{\frac{1}{2}}; \tag{3.56}$$

$$\Theta \sim L\theta_0 \left(\frac{Q}{gH\tau_0\theta_0} \right)^{\frac{1}{2}}. \tag{3.57}$$

Note that any transition between BLWTG and ADBL regimes will occur when the perturbation potential temperature derivative with respect to height exceeds the background potential temperature derivative with respect to height:

$$\Theta \frac{\partial \hat{\theta}}{\partial z} > \frac{\partial \theta_0}{\partial z}. \tag{3.58}$$

If we non-dimensionalise and re-arrange, we find unsurprisingly that this condition is met when

$$\frac{\Theta}{H} > \frac{\theta_0 N^2}{g} \implies O(1) > \frac{N^2 H \theta_0}{\Theta g}. \tag{3.59}$$

In other words, when the vertical advection of the perturbation potential temperature Θ in the thermodynamic equation (strictly O(1) in an anelastic regime) exceeds the vertical advection of the background potential temperature θ_0. ADBL is almost certainly a regime present in the well-mixed boundary layer when N^2 is very small, or in fact zero.

The condition in equation (3.59) can be expressed in terms of input parameters to give the following requirement for heating rate Q for BLWTG to transition to ADBL:

$$Q > \frac{N^4 H^3 \tau_0 \theta_0}{gL^2}. \tag{3.60}$$

In theory, it should be straightforward to find the transition point of the flow, but we will see in section 3.6 that predicting the transition can be complicated if the flow lengthscales change.

As with BLWTG, we can also predict the scales of D and λ:

$$D \sim L \left(\frac{\theta_0}{QHg\tau_0^3} \right)^{\frac{1}{2}}; \quad \lambda \sim 1. \tag{3.61}$$

Heating parameter λ is independent of all input variables when we are in the ADBL regime, as $\lambda \sim O(1)$. Thus there is no relationship between D and λ and D is simply inversely proportional to the square root of the heating.

The balance timescale for ADBL differs from WTG and BLWTG. For ADBL balance to be achieved, it is sufficient that

$$T \gg L \left(\frac{\theta_0}{QHg\tau_0} \right)^{\frac{1}{2}}. \tag{3.62}$$

If we compare the balance timescale for ADBL to WTG, we find that if

$$\frac{Q^3 g^3 L^3}{N^4 \theta_0^3 H} > O(1), \tag{3.63}$$

then ADBL reaches balance faster than WTG. For likely values of N, θ_0, g, and H, equation (3.63) should hold if $L > Q^{-1}$.

3.4.4 Advection Dominated Free Troposphere

We have termed our final regime the advection dominated free troposphere (ADFT) where we take equations (3.33)-(3.36) and further assume $\lambda \sim O(1)$ and $D < O(1)$. In the ADFT regime, even though drag may be present, it is not one of the dominant terms in the x-momentum equation; the x-momentum balance is the same as in the WTG free troposphere regime. By contrast, the thermodynamic balance is the same as in the advection dominated boundary layer. Anelasticity and hydrostatically balanced perturbations are also part of ADFT. This gives us the following output scaling relationships:

$$W \sim \frac{H}{L} \left(\frac{QLgH}{\theta_0} \right)^{\frac{1}{3}}; \tag{3.64}$$

$$U \sim \left(\frac{QLgH}{\theta_0} \right)^{\frac{1}{3}}; \tag{3.65}$$

$$\Pi \sim \frac{1}{c_p \theta_0} \left(\frac{QLgH}{\theta_0} \right)^{\frac{2}{3}}; \tag{3.66}$$

$$\Theta \sim \left(\frac{Q^2 L^2 \theta_0}{gH} \right)^{\frac{1}{3}}. \tag{3.67}$$

As with BLWTG and ADBL, we expect there to be a transition between WTG and ADFT when

$$O(1) > \frac{N^2 H \theta_0}{g\Theta} \implies Q > \frac{N^3 H^2 \theta_0}{gL}. \tag{3.68}$$

It should also be possible for ADBL to transition to ADFT if

$$O(1) > D \implies O(1) > \frac{L}{\tau_0}\left(\frac{\theta_0}{QHg\tau_0}\right)^{1/2} \implies Q > \frac{L^2\theta_0}{Hg\tau_0^3}. \tag{3.69}$$

In other words, the relationship between drag, horizontal lengthscale and heating are key in determining the transition from ADBL to ADFT. For ADFT, there will also be no relationship between D and λ.

The timescale required to ensure ADFT balance is reached should be:

$$T \gg L\left(\frac{\theta_0}{QLgH}\right)^{\frac{1}{3}} \tag{3.70}$$

Again, we compare the timescale for balance for ADFT to WTG and we find that if

$$\frac{Q^4g^4L^4}{N^6\theta_0^4H^2} > O(1), \tag{3.71}$$

then ADFT reaches balance faster than WTG. For likely values of N, θ_0, g, and H, equation (3.71) should hold again if $L > Q^{-1}$. If

$$\frac{\theta_0}{QLgH} > O(1), \tag{3.72}$$

then ADBL reaches balance faster than ADFT. For likely values of N, θ_0, g, and H, equation (3.72) should hold if $L > Q^{-1} \times 10^{-2}$.

3.5 Model Setup

In this section we investigate whether a numerical model can reproduce the theoretical long-term balance regimes of section 3.4 and therefore whether predictions based on the theoretical long-term balance regimes can realistically form the basis for ground truths for a test case. There are often challenges when attempting to match model results to theoretical results. These can arise because the assumptions behind the theory do not hold, or because the model fails to capture accurately the relevant physics. In testing scaling predictions there can also be challenges in diagnosing the scales of the quantities involved; we have attempted to mitigate this where possible and we will discuss this further in section 3.6.

For our study, we use the model described by Thuburn (2017). It solves the compressible Euler equations in a two-dimensional (horizontal-vertical slice) domain.

Model variables are stored with a C-grid staggering in the horizontal and a Charney-Phillips staggering in the vertical for accurate wave propagation. Semi-Lagrangian advection of variables, with a conservative formulation in the case of density, and a semi-implicit time stepping scheme ensure stability even for large time steps. The model has been extended to include the drag and heating terms needed for the present study and we modify the Thuburn (2017) model in the following ways:

3.5.1 Temperature stratification

In the initial conditions, we include a background temperature stratification of the form:

$$T(z) = T_s + \Gamma z, \tag{3.73}$$

where $\Gamma = -6.5 \times 10^{-3}$ K/m is a lapse rate and T_s is the surface temperature. This translates to a background potential temperature which increases with height.

Since we are interested in interactions between heating and drag, we also include a drag term and a heating rate. For all runs, both the drag term and the heating rate are only non-zero in the boundary layer of the model (or the lowest 1 km).

3.5.2 Boundary layer drag

The drag term is strongest at the bottom of the model and decreases linearly with height, until the top of the boundary layer ($h_{bl} = 1,000$ m). Above h_{bl}, in the free troposphere space, the drag term is zero.

$$\frac{1}{\tau} = \begin{cases} \frac{h_{bl}-z}{h_{bl}\times\tau_s} & z \leq h_{bl}, \\ 0 & z > h_{bl}. \end{cases} \tag{3.74}$$

The value of constant τ_s determines the strength of the drag and will vary between model setups. A similar formulation but with τ as a function of pressure was given in Held and Suarez (1994).

3.5.3 Heating rates

The heating rate term is also confined to the boundary layer (or lowest 1 km) and is strictly zero at the bottom boundary to prevent unphysical behaviour at

the surface. This is a necessary requirement as the model of Thuburn (2017) sets the vertical velocity to be zero at the bottom boundary and therefore the semi-Lagrangian scheme cannot advect heat away from the boundary. Model runs where the heating rate is non-zero at the bottom boundary cause the model to collapse due to unreasonably large pressure gradients at the centre of the heating. For the model runs in this study, we set the heating rate up with the following elliptically-shaped formulation:

$$H_*(x,z) = H_{max} \times 10^a \cos^2\left[\frac{(z-z_0)\pi}{h_{bl}}\right] \cos^2\left[\frac{(x-x_0)\pi}{0.25 \times L_D}\right], \tag{3.75}$$

where x_0 is the centre of the x-domain and z_0 is half the boundary layer height ($z_0 = h_{bl}/2$), and $H_{max} = 3$ K/s. Thus H_* is roughly 3 K per day at the centre of the heating when $a = -5$. As we intend to run the model with multiple heating rates to check the validity of the scale analysis over multiple heating scales, a will take values from the set $a = [-8, -7, -6, -5, -4, -3]$ such that the heating rate ranges between approximately $q \sim 10^{-8}$ K/s and $q \sim 10^{-3}$ K/s.

To the horizontally-centred heating, we add compensating cooling of the form:

$$S(z) = \frac{1}{L_D}\int_0^{L_D} H_*(x,z)dx, \tag{3.76}$$

where L_D is the size of the x-domain, to ensure that the horizontal mean heating is zero. Depending on the model run, either $L_D = 1,000$ km, $L_D = 5,000$ km, or $L_D = 50,000$ km. Of greatest interest is perhaps regimes with $L_D = 5,000$ km which is the most applicable to real world convection as $5,000$ km is approximately an eighth of the Earth's circumference and should allow for tropical convection up to its largest characteristic scales (Muller et al., 2018).

Our final heating rate on the right hand side of the thermodynamic equation is then:

$$q(x,z) = H_* - S. \tag{3.77}$$

The Thuburn (2017) model is formulated in terms of entropy η not potential temperature, so heating has been implemented by taking $\theta_{ref} = 300$ K and assuming $\eta = c_p \ln\theta$ which gives:

$$\frac{D\theta}{Dt} = q; \quad \frac{D\eta}{Dt} = \frac{c_p}{\theta_{ref}}q. \tag{3.78}$$

Our heating rate has been formulated to ensure no net change in entropy over the full domain, i.e.

$$\int_D \frac{c_p}{\theta_{ref}} q(x,z) dx dz = 0. \tag{3.79}$$

Examples of what the drag and heating look like are shown in figure 3.2, though the magnitude of the drag and heating will vary depending on the run and the imposed variables.

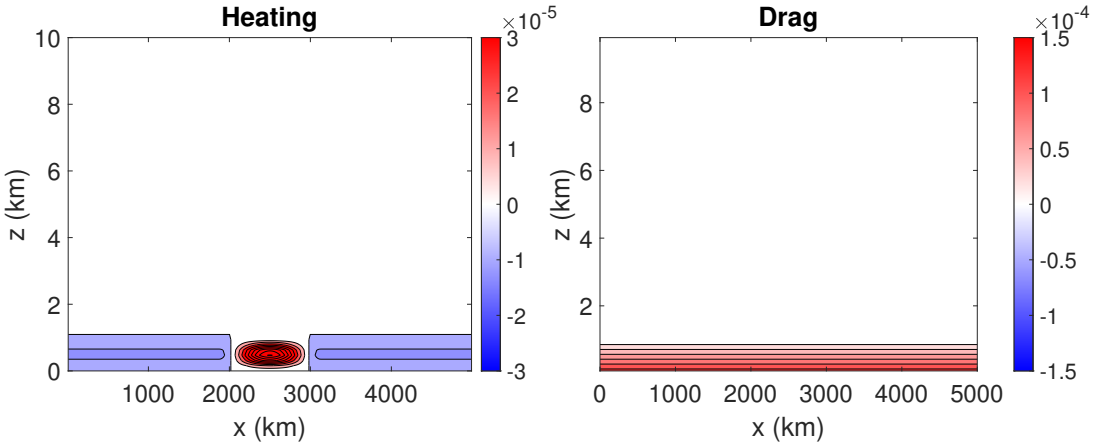

Figure 3.2: Examples of heating shape and drag shape in the model runs. Here we have drag timescale $\tau_0 \sim 10^4$ s and heating rate $Q \sim 10^{-5}$ K/s.

3.5.4 Imposed scales

For all model runs herein, we will use a vertical gridlength of $\Delta z \sim 150$ m and a timestep of $\Delta t \sim 20$ s to minimise numerical issues arising from unresolved time-dependent processes. The horizontal gridlength Δx varies with domain size such that $\Delta x \sim L_D/250$.

Table 3.1 lists the scales of all the imposed variables at the initial model timestep.

Imposed Variable	ρ_0	**H**	θ_0	$\mathbf{N^2}$	**g**	π_0	$\mathbf{c_p}$
Scale	1	10^3	10^2	10^{-4}	10	1	10^3
Units	kg/m^3	m	K	s^{-2}	m/s^2	–	m^2·s^{-2}·K^{-1}

Table 3.1: Table of imposed variables and their scales in the 2D model setup.

In our model runs, we will vary predominantly the drag timescale τ_s [s] and the heating rate q [K/s]. The corresponding scales will be referred to as τ_0 and Q. We will also vary the horizontal lengthscale L_D – scale L [m] as it is a factor in both

our drag parameter D and our heating parameter λ. Note also that the structure of the drag means τ varies with height, and therefore we specify τ_0 to be the scale of the value of τ_0 over the majority of the boundary layer or approximately $\tau_s \times 10$ where we recall τ_s is the value of the drag timescale at the surface.

It should also be noted that imposed lengthscales for H and L may not hold when balance is reached. Initially, L and H are taken to be the scales of the horizontal and vertical domains respectively, but in many cases, we might expect H and L to become smaller than suggested by the model domain size owing to the structure of the flow forced by the heating.

3.6 Test Results

We now move onto testing the model against the theory. The results in this section serve two functions. Firstly, we want to check the ability of a model to achieve the theoretical balance regimes from section 3.4 and secondly, we want to identify which diagnostics might be used for a test case based on the theory. Therefore, we begin by running forty-two model runs with varying drag timescales, heating rates and horizontal lengthscales. We will look at how these runs fit within the regime space in figure 3.1. Then, using the theory in section 3.4, we will then look at extracting scaling laws for the output parameters U, W, Π and Θ based on the heating rate and the regime. And finally we will look more in depth at examples of each of the regimes – WTG, ADBL, BLWTG, and ADFT – to examine the behaviour features of each long-term balance regime and how each regime differs from the others.

3.6.1 Regime Diagram

We begin by running all of the model setups in table 3.2, varying the drag timescale, heating rate and horizontal lengthscale to ascertain where each model run should theoretically fall within the regime space. The various scales of τ_0, Q and L used in the model setups are listed in table 3.2 alongside the name of the run. The scales cover ranges we are likely to see on earth as well as scales larger and smaller.

In particular, we will vary the horizontal lengthscale over the range $L \sim 10^5$ m to $L \sim 10^7$ m. Drag timescale will vary over the range $\tau_0 \sim 10^3$ s to $\tau_0 \sim 10^6$ s as well as $\tau_0 \sim \infty$ and the heating rate will vary over the range $Q \sim 10^{-8}$ K/s to

Test Run	τ_0	**L**	**q**
L105drag720	10^3	10^5	10^{-8} to 10^{-3}
L105drag7200	10^4	10^5	10^{-8} to 10^{-3}
L105drag72000	10^5	10^5	10^{-8} to 10^{-3}
L106drag720	10^3	10^6	10^{-8} to 10^{-3}
L106drag7200	10^4	10^6	10^{-8} to 10^{-3}
L106drag72000	10^5	10^6	10^{-8} to 10^{-3}
L107drag7200	10^4	10^7	10^{-8} to 10^{-3}
Units	s	m	K/s

Table 3.2: Table of prescribed scales for drag, heating rate and horizontal lengthscale terms in the 2D model setup.

$Q \sim 10^{-3}$ K/s. We diagnose our results at approximately 7 days or $t = 600,000$ s – a timescale chosen to ensure T is greater than the required timescales for balance outlined in section 3.4 for each regime such that St $< O(1)$.

Figure 3.3 shows how the model runs are distributed based on the regime space in figure 3.1. We have excluded runs where the drag timescale is infinite from figure 3.3, because for runs where $\tau_0 \sim \infty$, the drag parameter D is necessarily zero and it is difficult to plot a zero on a loglog scale. Were we to plot the runs where $\tau_0 \sim \infty$, they would form a line along the bottom of the diagram in figure 3.3 – all within either the ADFT or the WTG space.

From figure 3.3, we can see immediately that three of the runs fall into an area which should have no circulation. These runs however are likely ADBL as there is definitely circulation when we inspect the outputs by eye. We can also see that there are some runs where the drag $(1/\tau_0)$ is non-zero which fall into the WTG regime space. This is not unexpected as these runs have weak drag (τ_0 large) compared to the advection timescale L/U of the run and thus the magnitude of D for these runs is small.

Similarly, runs which fall into the ADFT portion of the regime diagram are runs where the drag is again small compared to horizontal lengthscale. The key difference being that the heating rate is stronger. It should also be noted that in figure 3.3, a larger λ seems to correspond to a smaller Q in the BLWTG and WTG regimes. This is expected from the theory as equation (3.43) also tells us that in the WTG regime, λ scales with Q^{-2} and equation (3.52) tells us that in the BLWTG regime,

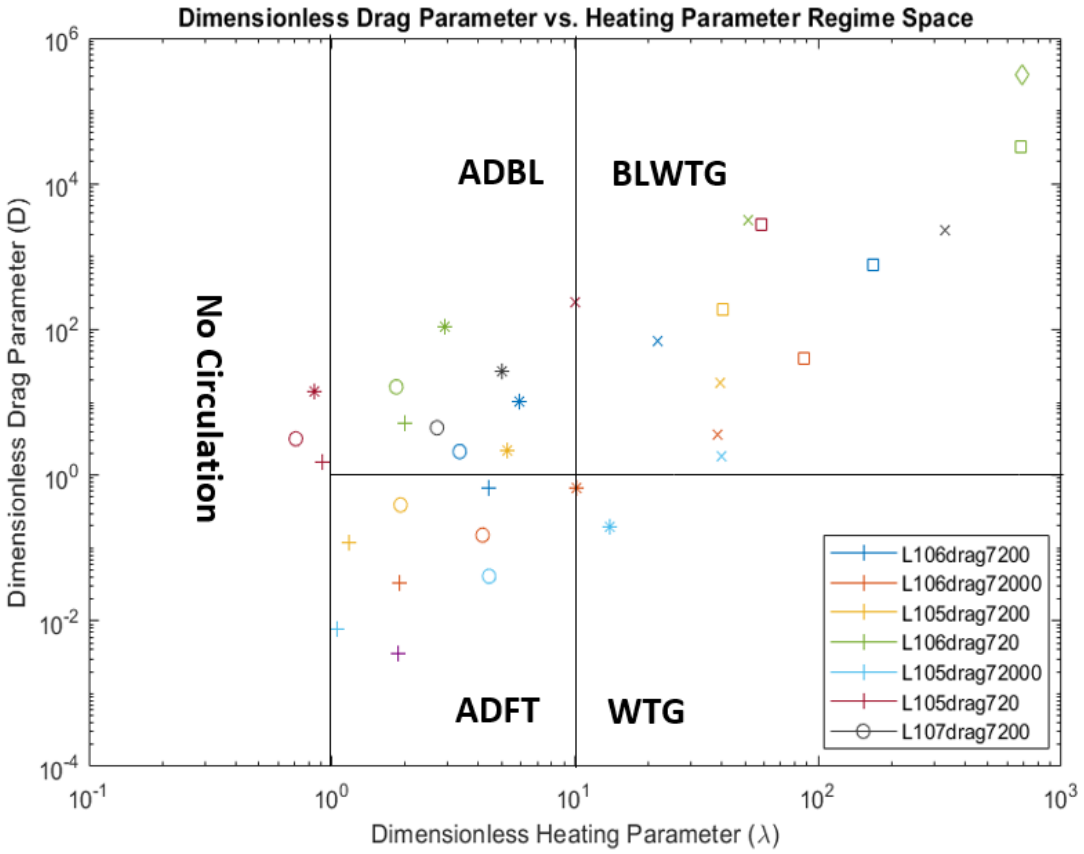

Figure 3.3: Dimensionless parameters D and λ for each setup in table 3.2 after ~ 7 days. Heating rates are represented in descending order with $Q = [3\times10^{-3}, 3\times10^{-4}, 3\times10^{-5}, 3\times10^{-6}, 3\times10^{-7}, 3\times10^{-8}]$ K/s corresponding to $[+, \circ, *, \times, \square, \diamond]$. The horizontal length scale used to calculate D and λ was the lengthscale of the domain.

λ should scale with Q^{-1}.

For the ADBL or ADFT regimes, $\lambda \sim O(1)$ and therefore we do not expect any clear relationship between Q and λ. In figure 3.3, we can see in the ADBL regime space that $Q \sim 10^4$ K/s runs seem to consistently have lower λ values than the $Q \sim 10^3$ K/s runs whilst the $Q \sim 10^4$ K/s runs seem to consistently have lower λ values than the $Q \sim 10^5$ K/s runs. The exact relationship between Q and λ will depend on how Θ, U and L change. Here, Θ and U are diagnosed from the model flow as their flow maximums in the heated layer i.e. $\Theta = \Theta_{max}$ and $U = U_{max}$ in the lowest 1 km of the model.

3.6.2 Scaling Laws and Regime Transitions

There is reasonable evidence in figure 3.3 that four different model regimes are achievable in the model, but we can introduce another diagnostic to verify this further via reference to trend line diagrams for heating rate Q vs. output variables where the trend lines will be the lines obtained from plotting on the loglog scale our four output variables against heating rate Q across multiple heating rates. Here, we consider all the model runs including those where $\tau_0 \sim \infty$.

For the trend line plots, we will present a few different drag/horizontal length-scale setups as examples which should match different regimes based on the points in the regime diagram in figure 3.3. We choose to look at L106nodrag as this run should change only between WTG and ADFT over the range of heating rates considered and then we choose to look at L106drag720, L106drag7200 and L106drag72000 as these model setups should only be either BLWTG or ADBL.

In every regime, for each of the output variables we can write the output variable predictions in the form:

$$V_{out} = Q^a \times 10^b, \tag{3.80}$$

where V_{out} represents any of horizontal velocity U, vertical velocity W, Exner pressure perturbation Π, or potential temperature perturbation Θ. The index b is determined by imposed scales for the input variables whilst a is the power of Q in our predictions in section 3.4.

Taking logs of both sides, we can obtain a linear relationship between the log of the heating rate and the log of the predicted output variables:

$$\log\left(V_{out}\right) = a\log\left(Q\right) + b\log\left(10\right) \tag{3.81}$$

When we plot our model results against our predictions, we should expect the gradients to match well as Q is an imposed variable that should not adjust during model runs. The heating rate Q is also particularly useful for distinguishing between the regimes as aside from WTG and BLWTG having the same predicted scales for U and W, the predictions for all the other output variables have different powers of Q depending on regime. BLWTG variables all scale with Q, WTG variables apart from U and W scale with Q^2, ADBL variables scale with $Q^{1/2}$, and ADFT variables

scale with $Q^{1/3}$ or $Q^{2/3}$.

Thus, for sufficient model runs, we should be able to check which regime a model run finds itself in by how well the runs match the gradient of the prediction trend line. We should also be able to determine at what value of Q the model run switches from one regime to another by observing any changes in the gradient of the trend line. The transition should match with the predictions from the theory in section 3.4, provided we are able to correctly identify the scales of the imposed variables that determine the transition. The horizontal and vertical lengthscales L and H are particularly critical for determining the transition point, as well as the background potential temperature θ_0 and the buoyancy frequency N^2.

For each trend line plot, we will use heating rates from approx $Q \sim 10^{-8}$ K/s to $Q \sim 10^{-3}$ K/s as laid out in Section 3.5. This gives us a total of six runs for each model setup in table 3.2, a space which should also account for transitions between regimes suggested in figure 3.1.

We use the scaling relationships in Section 3.4 to predict the scale of output variables U,W, Θ, and Π over our chosen setups in table 3.2 and all six heating rates. We then compare the predicted scales to the actual scales of output variables in the model tests.

No Drag Predictions vs. Model Runs

We look first at a model run without drag – L106nodrag. In the absence of drag, we can only obtain predicted scales for WTG and ADFT regimes as $\tau_0 \sim \infty$ is not feasible for BLWTG and ADBL predictions. Therefore, in figure 3.4, we plot only the log of our predicted output variable scales from WTG and ADFT against the log of the heating rate. We also plot the log of the output variable scales returned by the model against the log of the heating rate on the same plot. This allows us to check whether our regime output variable predictions are in agreement with the model output variables as well as whether our regime transition predictions from Section 3.4 match well with the model results.

In figure 3.4, horizontal and vertical velocity are well-predicted by the WTG scalings at low heating rates. At higher heating rates, the vertical velocity doesn't seem well-predicted by either WTG or ADFT, though horizontal velocity seems to tend towards the gradient predicted by ADFT at higher heating rates. This

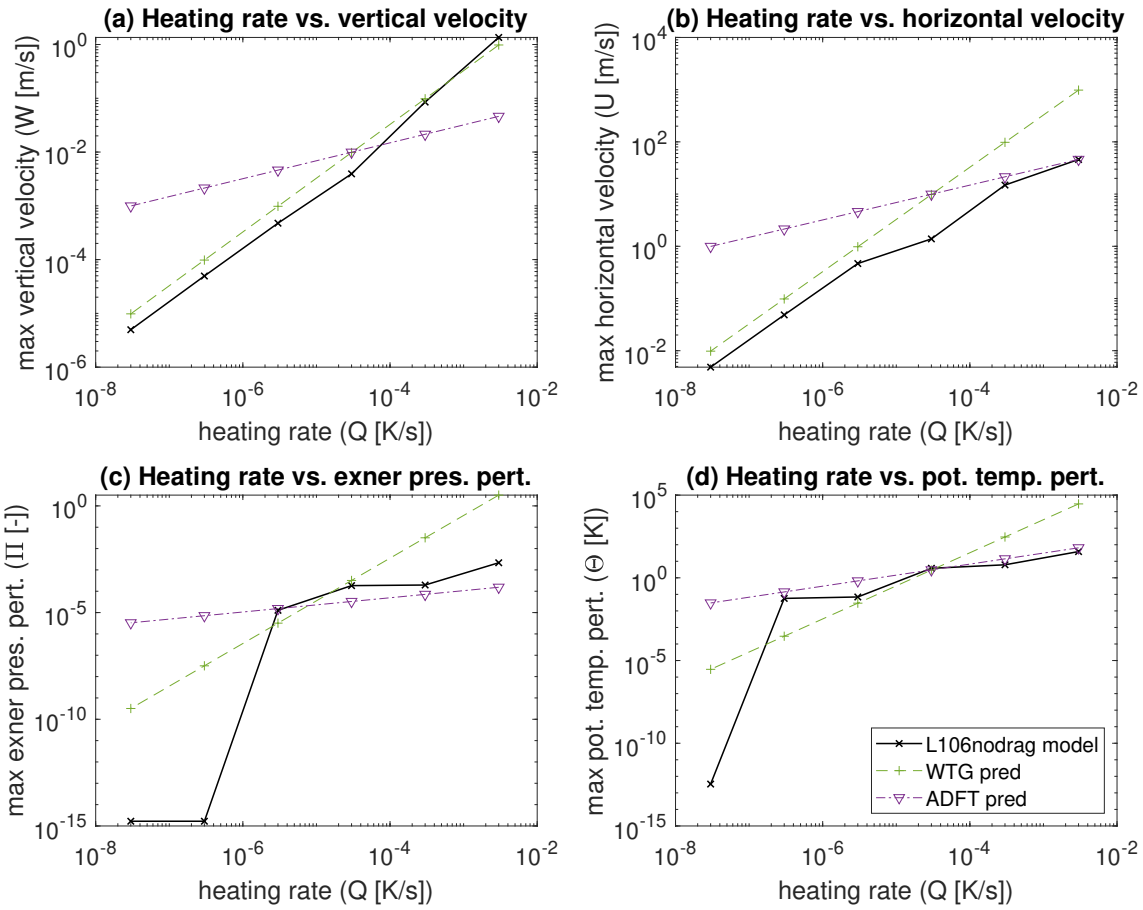

Figure 3.4: Log-log plots of the relationship between output variables and heating rate extracted from scaling relationships in Section 3.4. Results from model runs with the L106nodrag setup are in black. Regime predictions based on the theory are also given for the WTG regime (green) and the ADFT regime (purple). Model variables are taken at approximately 7 days.

makes sense as from equation (3.68), we expect WTG to transition to ADFT for L106nodrag when

$$Q > \frac{N^3 H^2 \theta_0}{gL} \implies Q > 10^{-5} \text{ K/s}. \tag{3.82}$$

In figure 3.4, there is a clear transition in the vertical velocity at $Q > 10^{-5}$ K/s as well as the perturbation Exner pressure, though the perturbation Exner pressure is poorly predicted across all the heating rates with a sudden drop in magnitude and a flattening of the gradient at lower heating rates. We believe this is due to the magnitude of Π dropping below the round off error scale in the diagnostic output of the model.

Potential temperature perturbation Θ also performs similarly at low heating

rates, though this is unsurprising as Exner pressure and potential temperature perturbations are linked via hydrostatic balance. Across the heating rates, the mismatch in theoretical predictions for Π and Θ compared to the model results is likely due to the model failing to fully satisfy the assumptions in section 3.4. An extended transition also occurs in horizontal velocity U.

Drag Included Predictions vs. Model Runs

We next consider model runs where we expect to get BLWTG, ADBL, or possibly ADFT regimes dependent on the magnitude of the heating.

As previously stated, the examples we will look at here are L106drag720, L106drag7200 and L106drag72000 from table 3.2. For each of these model setups, we plot the output variables against the heating rate as we did for L106nodrag, except now we plot all possible prediction lines for WTG, BLWTG, ADBL and ADFT. Results for L106drag720 are in figure 3.5, results for L106drag7200 are in figure 3.6, and results for L106drag72000 are in figure 3.7.

We start by looking at model setup L106drag720 in figure 3.5. In figure 3.5, we observe a clear transition in the horizontal and vertical velocities from BLWTG to ADBL as heating rate Q increases. For vertical velocity W, the transition seems to occur for Q between 10^{-6} K/s and 10^{-5} K/s, whilst the horizontal velocity gradient does not match the ADBL prediction until $Q > 10^{-4}$ K/s. Transitions in the Exner pressure perturbation, Π and the potential temperature perturbation, Θ seem to occur around $Q > 10^{-6}$ K/s and $Q > 10^{-5}$ K/s respectively. If we plug the L106drag720 input scales in table 3.2 into equation (3.60) from the theory, we would expect the transition from BLWTG to ADBL to start to occur when

$$Q > \frac{N^4 H^3 \tau_0 \theta_0}{gL^2} \implies Q > 10^{-7} K/s. \tag{3.83}$$

However, in figure 3.5, we see that the model does not start to transition until $Q > 10^{-6}$ K/s and doesn't seem to finish transitioning until $Q > 10^{-4}$ K/s or $Q > 10^{-3}$ K/s depending on the variable examined.

We explain the discrepancy between the predicted transition and the actual transition by considering the lengthscales in the problem. As previously noted, the horizontal and vertical lengthscales imposed on the model are not necessarily the scales seen by the model as both horizontal and vertical lengthscale can adjust

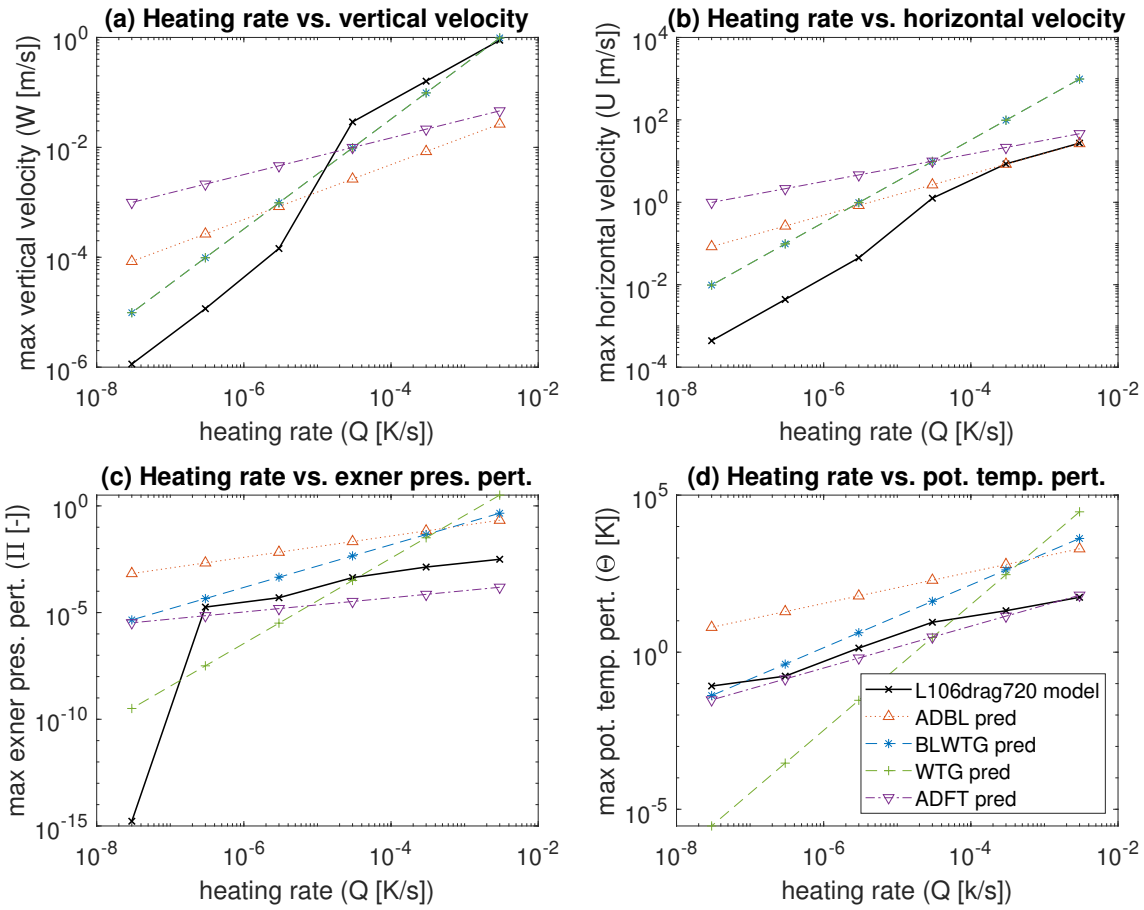

Figure 3.5: Log-log plots of the relationship between output variables and heating rate extracted from scaling relationships in Section 3.4. Results from model runs with the L106drag720 setup are in black. Regime predictions based on the theory are also given for the ADBL regime (red), the BLWTG regime (blue), the WTG regime (green) and the ADFT regime (purple). Model variables are taken at approximately 7 days.

depending on how the model reacts to the heating forcing. The flow will attain its own lengthscales and the lengthscales may change as the heating or regimes change when the model stratification becomes unstable due to the structure of the heating. Provided the regime the model adjusts to is anelastic, the flow lengthscales will still have to satisfy equation (3.11).

In figure 3.8, we plot the imposed lengthscales (i.e. domain sizes) against the lengthscales returned by the model flow in the lowest 1 km of the model. Lengthscales returned by the model are calculated as

$$L = \frac{u_{max}}{(du/dx)_{max}} \quad \text{and} \quad H = \frac{w_{max}}{(dw/dz)_{max}}. \tag{3.84}$$

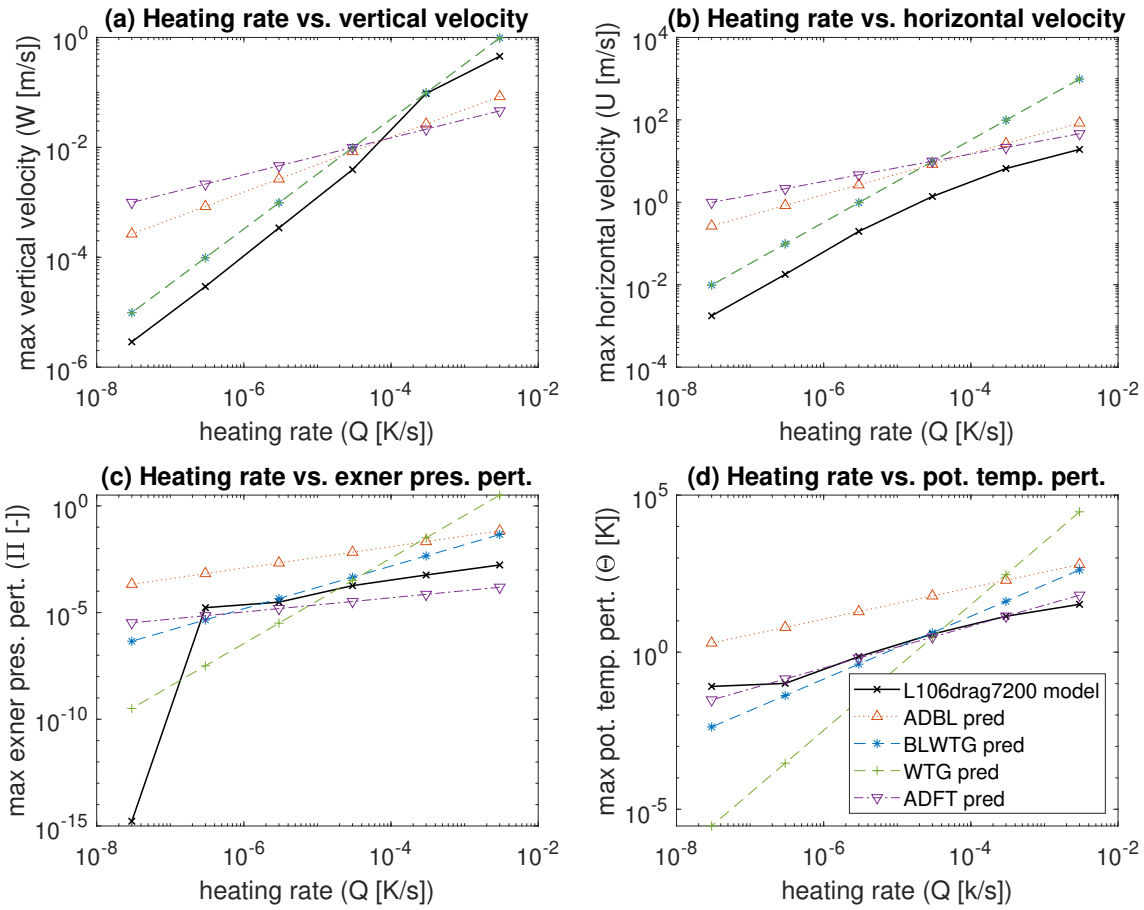

Figure 3.6: Log-log plots of the relationship between output variables and heating rate extracted from scaling relationships in Section 3.4. Results from model runs with the L106drag7200 setup are in black. Regime predictions based on the theory are also given for the ADBL regime (red), the BLWTG regime (blue), the WTG regime (green) and the ADFT regime (purple). Model variables are taken at approximately 7 days.

We use the maximum as opposed to the mean of the magnitudes or an L2 norm as using the maximum avoids the scales of variables being artificially lowered by the lower values of variables in the majority of the boundary layer where the heating is marginally negative since the region in which Q is positive accounts for only a fifth of the horizontal domain.

At low heating rates, the horizontal lengthscale returned by the model seems to be of a similar magnitude to the width of the positively heated air, which is roughly $L_Q = 0.2 \times L_D$. At higher heating rates, vertical and horizontal lengthscales shrink. This is not unique to $L \sim 10^6$ m cases and likely corresponds to regime shifts.

However, when the lengthscales change, so too does the magnitude of Q required for transition from BLWTG to ADBL. Notably, when the horizontal lengthscale L

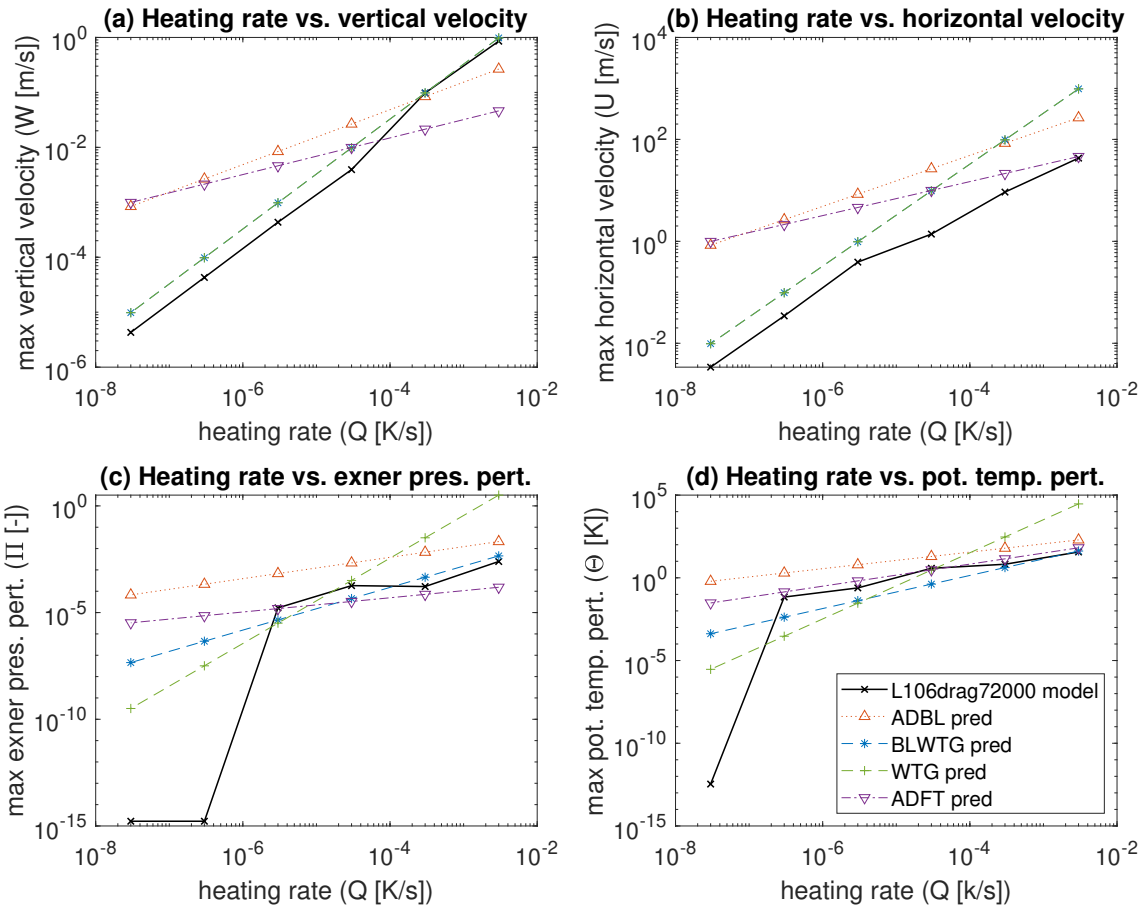

Figure 3.7: Log-log plots of the relationship between output variables and heating rate extracted from scaling relationships in Section 3.4. Results from model runs with the L106drag72000 setup are in black. Regime predictions based on the theory are also given for the ADBL regime (red), the BLWTG regime (blue), the WTG regime (green) and the ADFT regime (purple). Model variables are taken at approximately 7 days.

decreases, the minimum heating rate required for transition increases. This may explain why we witness extended transition regions in figure 3.5. For L106drag720, if the horizontal lengthscale shrinks to $L \sim 10^4$ m, we would require $Q > 10^{-3}$ K/s for transition from BLWTG to ADBL. This seems consistent with the point at which the model output gradients seem to match up with the ADBL predictions.

Extended transitions also occur in figures 3.6 and 3.7. Although for L106drag7200 and L106drag72000, the model doesn't quite reach the gradients predicted by ADBL at $Q \sim 10^{-3}$ K/s. This is because when the horizontal lengthscale L shrinks to $L \sim 10^4$ m, the minimum required Q for full transition from BLWTG to ADBL is $Q > 10^{-2}$ K/s for L106drag7200 and $Q \sim 10^{-1}$ K/s for L106drag72000.

It is quite interesting that if we set the heating parameter to fit a regime most

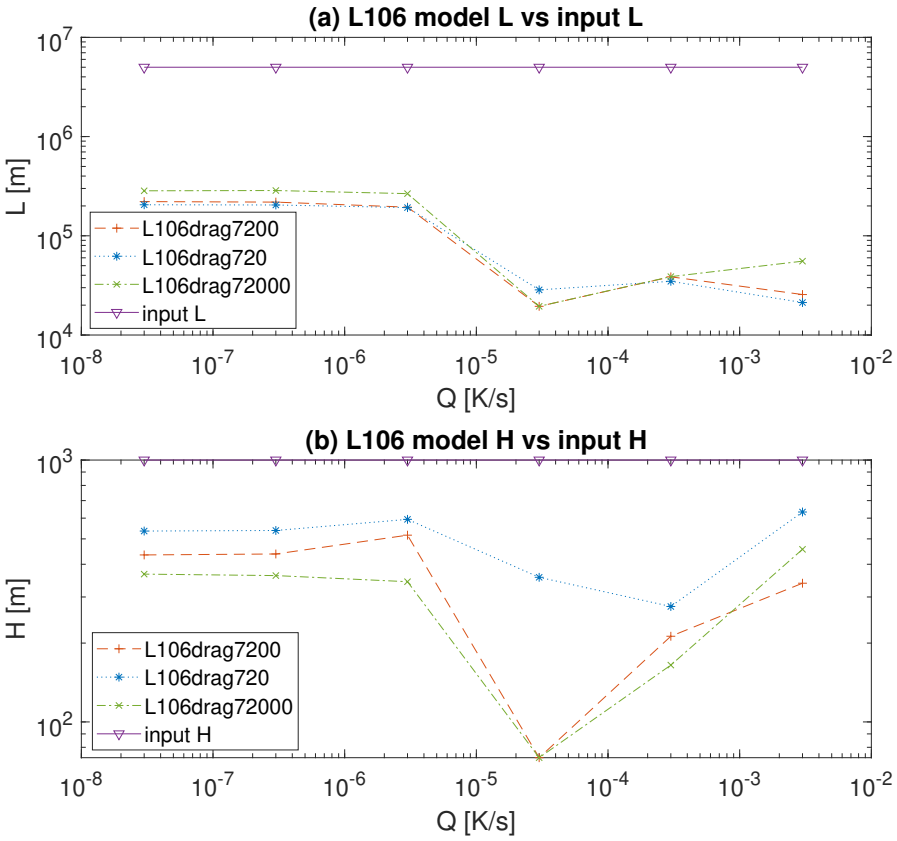

Figure 3.8: Sizes of horizontal lengthscale L and vertical lengthscale H, as predicted by the model flow in equation (3.84) for model runs L106drag720 (blue), L106drag7200 (red) and L106drag72000 (green) compared to the lengthscales of the horizontal and vertical domain sizes (purple). Horizontal lengthscale comparisons are in subplot (a). Vertical lengthscales comparisons are in subplot (b).

similar to heating on Earth ($Q \sim 10^{-5}$ K/s or approximately 3 K per day), we find ourselves on the edge of 2 long-term regimes in the L106 cases. A transition seems to occur in both drag and non-drag cases at around $Q > 10^{-5}$ K/s.

At this stage, it is worth plotting each drag-horizontal lengthscale setup for D and λ using the flow lengthscales determined by the model from equation (3.84). Figure 3.9 is a plot of D and λ for each model run using flow lengthscales instead of imposed ones as in figure 3.3 to check if flow lengthscales are better choices for L and H when determining D and λ for a given model run. Although H is unimportant for predicting D and λ, L is present in both quantities so mispredicting L will lead to mispredicting both D and λ. In figure 3.3 , we plot the same model runs that we previously plotted using $L = L_D$ using the horizontal flow lengthscale for comparison.

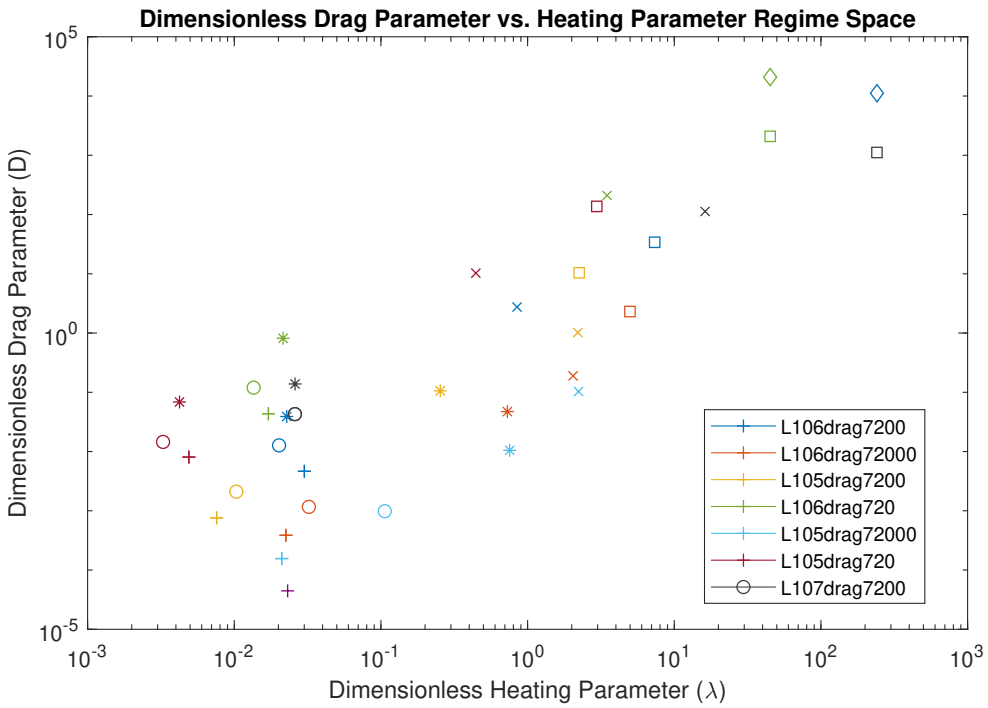

Figure 3.9: Dimensionless parameters D and λ for each setup in tables 3.2 after $\sim$ 7 days. Heating rates are represented in descending order with $Q = [3 \times 10^{-3}$, 3×10^{-4}, 3×10^{-5}, 3×10^{-6}, 3×10^{-7}, $3 \times 10^{-8}]$ K/s corresponding to [+, $\circ$, $*$, $\times$, $\square$, $\diamond$]. The horizontal length scale used to calculate D and λ was the size of the horizontal lengthscale returned by the flow using equation 3.84.

There is a much clearer distinction in figure 3.9 between ADBL and BLWTG regimes when compared to figure 3.3. Similarly, there is a clearer distinction between ADFT and WTG regimes in figure 3.9 as well. However, in figure 3.9, regimes that were previously classified as ADBL by virtue of having drag parameter $D > O(1)$, now appear to be mostly ADFT, though it is unlikely that this is the case for all the runs since there is no evidence for the ADBL regimes in figure 3.3 being ADFT from the trend line plots. As such, the results for D and λ seem more realistic in figure 3.3 than in figure 3.9.

3.6.3 Example regime behaviour

Having seen evidence that the model runs seem to fall into four different regimes in the trend line diagrams and in the regime diagram, it remains now to demonstrate that the regimes not only represent different spaces on the regime diagram, but also represent different behaviours. We will look at example model behaviour

in four runs – each of which will represent one of the regimes outlined in section 3.4. Figures 3.11 and 3.10 show contours for the vertical and horizontal velocities for L105drag7200, L106drag7200, L106drag72000 and L106nodrag at approximately 7 days with identical colour bars so differences between regime velocity magnitudes are clear. Wherever possible, we have chosen runs which correspond to horizontal lengthscales, heating rates and drag timescales that are not infeasible for Earth. Some scales are also comparable to experiments by other researchers. Drag timescales of $\tau_0 \sim 10^4$ s and $\tau_0 \sim 10^5$ s for example are comparable to experiments carried out in a 3D model by Wu et al. (2000). We will see some of the behaviours they observed are replicated in our 2D model cases.

We will now discuss each case with reference to the theory.

WTG Test

We start by considering the behaviour of the well-recognised weak temperature gradient regime, where the drag timescale τ_0 can be assumed to be infinite, so $D \ll O(1)$. When $L \sim 10^6$ m, $Q \sim 10^{-5}$ K/s and $\tau_0 \sim \infty$, the model produces $U \sim O(1)$ and $\Theta \sim O(10^{-1})$, giving $\lambda \sim O(10^2)$. $\lambda \sim O(10^2)$ and $D \ll O(1)$ satisfy the requirements for the long-term WTG balance in section 3.4.1.

In the model, this means heat is advected away in the horizontal – as we can see in subplot (d) of figures 3.11 and 3.13 – and the vertical velocity due to the heating does not extend above the vertical layer being heated. This is evidenced by weak vertical velocities above the boundary layer in subplot (d) of figure 3.10 and in subplot (d) of figure 3.12 where we can see most of the circulation forced by the heating stays within the boundary layer.

The following scales are what we expect from the WTG theory:

$$W \sim \frac{Qg}{N^2\theta_0} \sim 10^{-3}; \quad U \sim \frac{QgL}{N^2\theta_0 H} \sim O(1); \tag{3.85}$$

$$\Pi \sim \frac{g^2Q^2L^2}{N^4\theta_0^3H^2c_p} \sim 10^{-6}; \quad \Theta \sim \frac{gQ^2L^2}{N^2\theta_0H^3} \sim 10^{-2}. \tag{3.86}$$

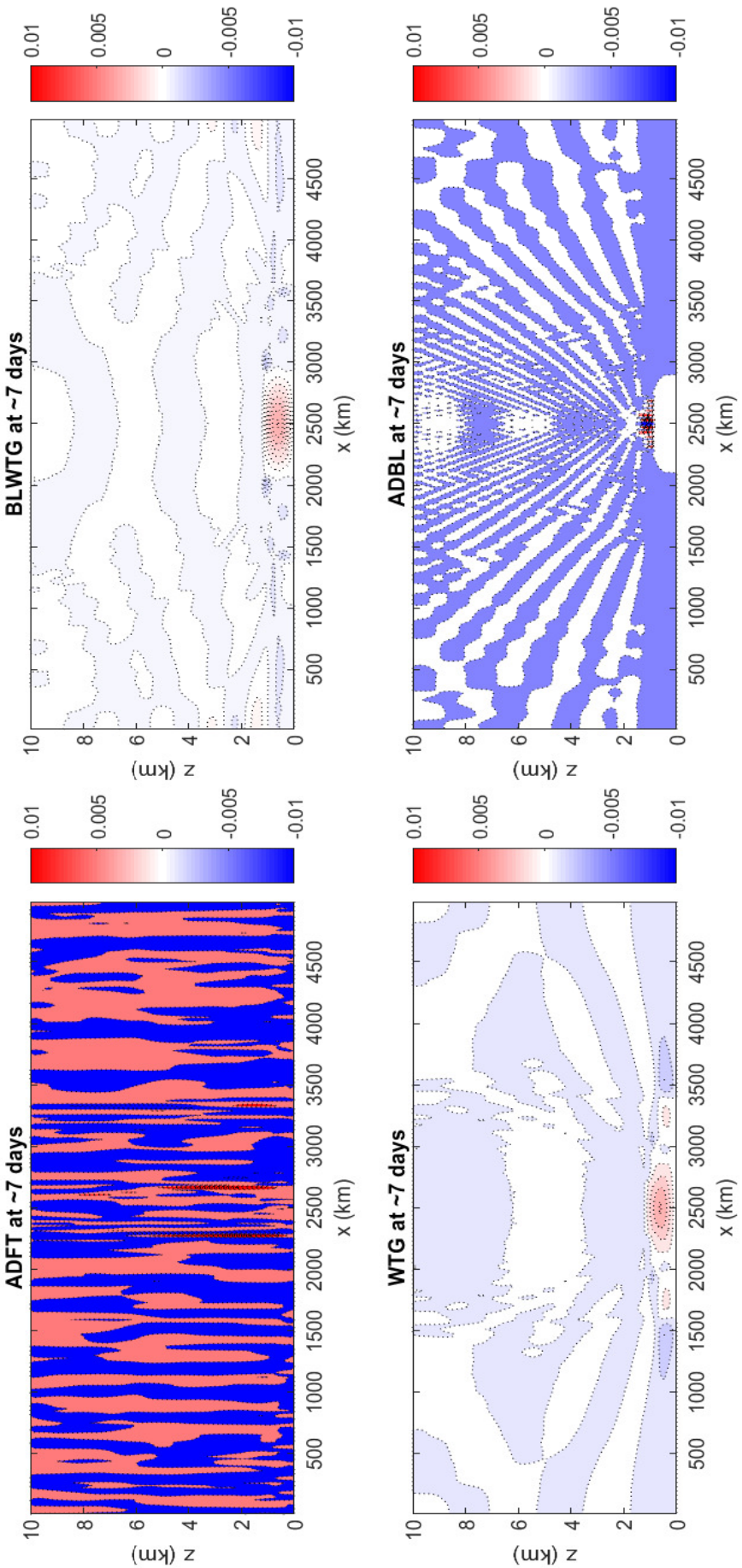

Figure 3.10: Vertical velocity (w) x-z cross sections for test cases outlined in table 3.2 after approximately 7 days. Each test case is classified into a regime based on the scale of D and λ: (a) is advection dominated boundary layer – ADBL; (b) is boundary layer pseudo weak temperature gradient – BLWTG; (c) is advection dominated free troposphere – ADFT; and (d) is weak temperature gradient – WTG. All four test cases are presented with the same colour bar scale ranging from -0.01 m/s to 0.01 m/s for comparison of magnitude.

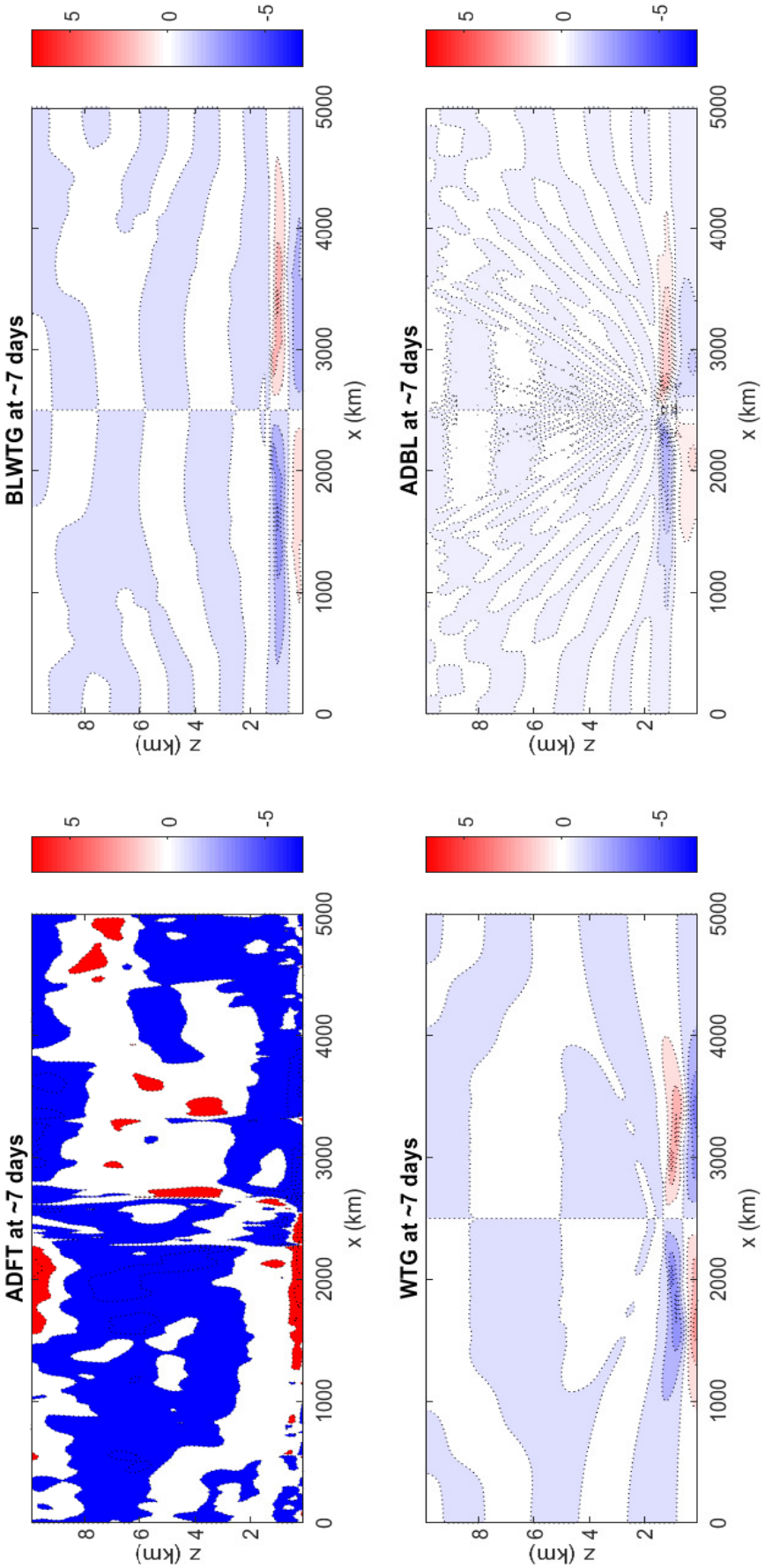

Figure 3.11: Horizontal velocity (u) x-z cross sections for test cases outlined in table 3.2 after approximately 7 days. Each test case is classified into a regime based on the scale of D and λ: (a) is advection dominated boundary layer – ADBL; (b) is boundary layer pseudo weak temperature gradient – BLWTG; (c) is advection dominated free troposphere – ADFT; and (d) is weak temperature gradient – WTG. All four test cases are presented with the same colour bar scale ranging from -6 m/s to 6 m/s for comparison of magnitude.

The scales returned by the model for the WTG test are as predicted for the horizontal and vertical velocities. However, both Π and Θ are under-predicted by O(10). In the model $\Pi \sim O(10^{-5})$ and $\Theta \sim 0(10^{-1})$ K. The disagreement between theory and results in the thermodynamic variables could be attributed to difficulties determining the variable scales. However, since the thermodynamic variables do not contain any variable scales except c_p that are not found in the velocity prediction, it is also possible that the presence of gravity waves is affecting the model results or that the model does not sufficiently satisfy the thermodynamic assumptions.

Advection Dominated Free Troposphere Test

The next regime we test is ADFT. Again τ_0 is assumed to be infinite so we have $D \ll O(1)$. For $L \sim 10^6$ m, $Q \sim 10^{-3}$ K/s and $\tau_0 \sim \infty$, the model produces $U \sim O(10)$ and $\Theta \sim O(10)$ giving $\lambda \sim O(10)$. Although this does not satisfy the requirement of ADFT when $L \sim 10^6$ m, it is possible that the imposed L is too large and horizontal lengthscale in the model may be effectively smaller (see section 3.6.2 and figure 3.9). Assuming the flow horizontal lengthscale satisfies $L < 10^5$ m, D and λ satisfy the requirements for long-term ADFT balance in Section 3.4.4.

In the model, the ADFT regime seems to translate to multiple thin bands of convection across the whole width of the model domain, with the strongest vertical velocities occurring above the centre of the heating (figure 3.12, subplot (c) and figure 3.10, subplot (c)). The horizontal velocity seems to extend the full width of the horizontal domain as well in figure 3.11 subplot (c) and figure 3.13 subplot (c) as with WTG, though symmetry is not very well-preserved. This is likely due to the strength of the heating and the strength of the model response to the heating. Note that in this ADFT example, both horizontal velocity u and vertical velocity w are an order of magnitude greater than for the other example cases.

The scales expected from the theory for the response variables are below:

$$W \sim \frac{H}{L}\left(\frac{QLgH}{\theta_0}\right)^{\frac{1}{3}} \sim 10^{-2}; \quad U \sim \left(\frac{QLgH}{\theta_0}\right)^{\frac{1}{3}} \sim 10; \tag{3.87}$$

$$\Pi \sim \frac{1}{c_p\theta_0}\left(\frac{QLgH}{\theta_0}\right)^{\frac{2}{3}} \sim 10^{-2}; \quad \Theta \sim \left(\frac{Q^2L^2\theta_0}{gH}\right)^{\frac{1}{3}} \sim 10. \tag{3.88}$$

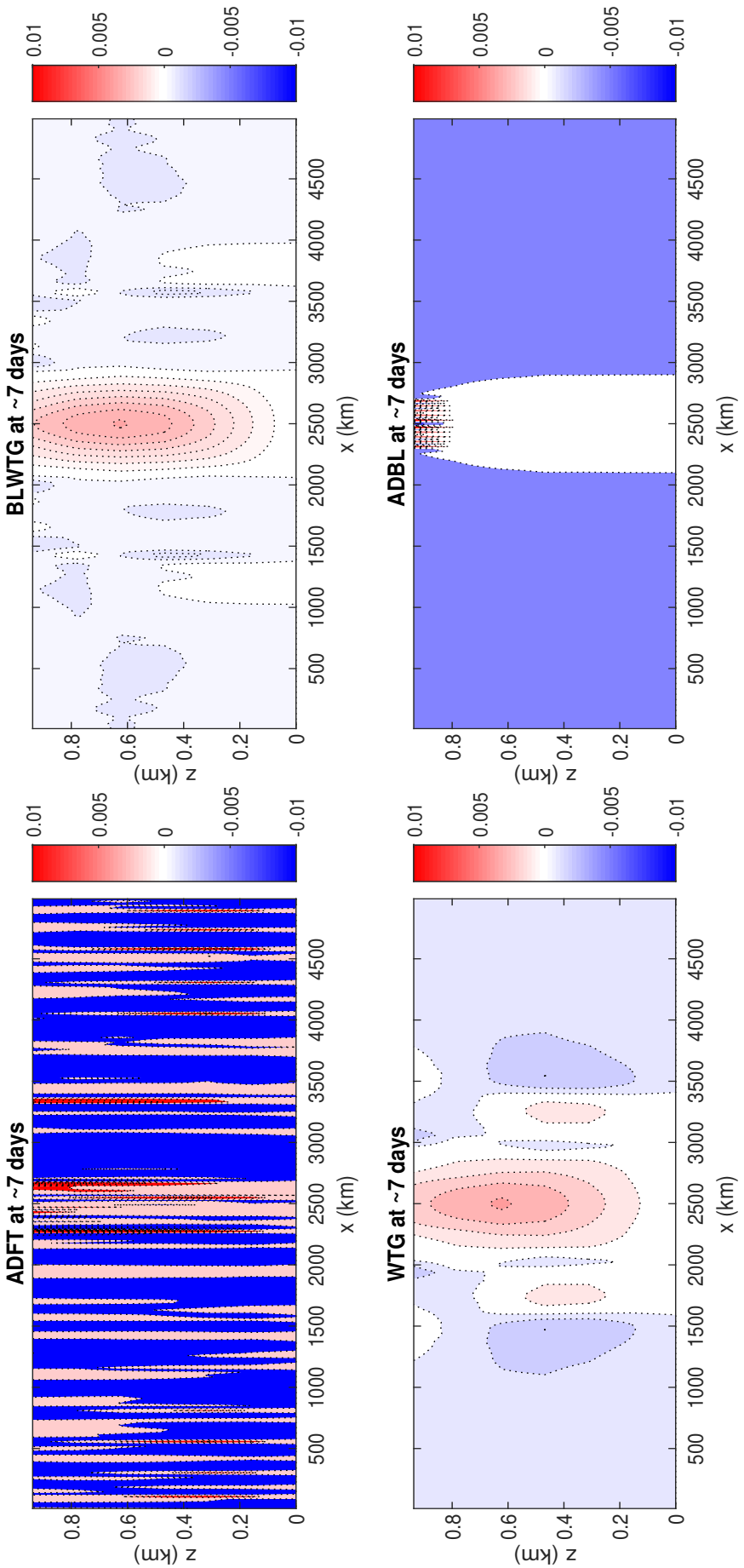

Figure 3.12: Boundary layer only x-z cross sections of vertical velocity (w) for test cases outlined in table 3.2 after approximately 7 days. Each test case is classified into a regime based on the scale of D and λ: (a) is advection dominated boundary layer – ADBL; (b) is boundary layer pseudo weak temperature gradient – BLWTG; (c) is advection dominated free troposphere – ADFT; and (d) is weak temperature gradient – WTG. All four test cases are presented with the same colour bar scale ranging from -0.01 m/s to 0.01 m/s for comparison of magnitude.

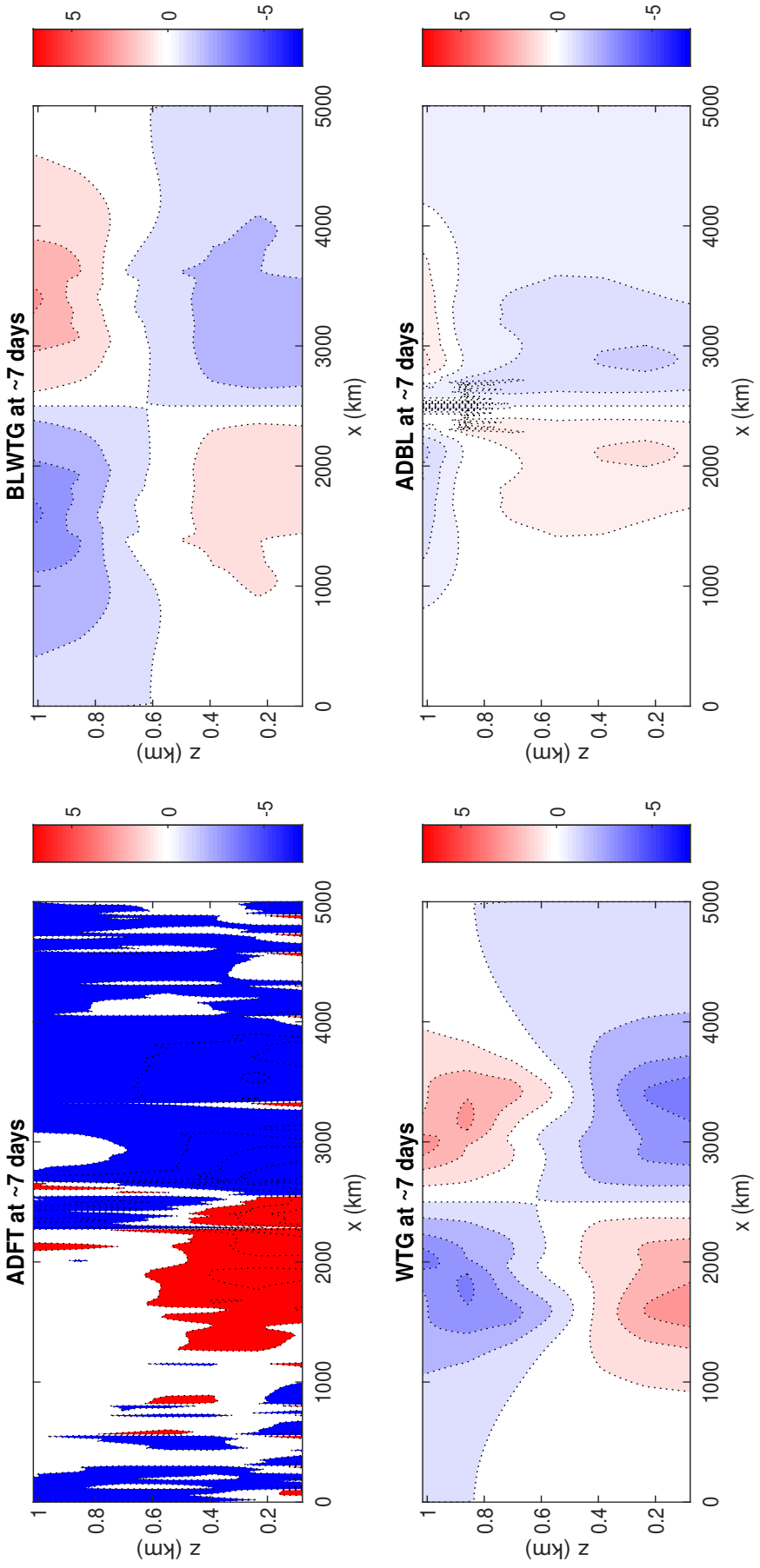

Figure 3.13: Boundary layer only x-z cross sections of horizontal velocity (u) for test cases outlined in table 3.2 after approximately 7 days. Each test case is classified into a regime based on the scale of D and λ: (a) is advection dominated boundary layer – ADBL; (b) is boundary layer pseudo weak temperature gradient – BLWTG; (c) is advection dominated free troposphere – ADFT; and (d) is weak temperature gradient – WTG. All four test cases are presented with the same colour bar scale ranging from -6ms^{-1} to 6ms^{-1} for comparison of magnitude.

Here, U is the only well-predicted variable. Π and Θ are over-predicted by an order of magnitude and W is two orders of magnitude larger in the model than suggest by the theory. Considering this, it is possible the heating is too strong and this test case does not satisfy the assumptions on the thermodynamic variables in terms of backgrounds and perturbations and so the model may not satisfy a long-term balance at all leading to gravity waves in the model output.

Boundary Layer Pseudo-WTG Test

The next regime we test is the Boundary Layer pseudo-WTG regime (BLWTG). For this regime, using $L \sim 10^6$ m, $Q \sim 10^{-5}$ K/s, and $\tau_0 \sim 10^5$ s, a drag timescale comparable to experiments such as Wu et al. (2000), the scales returned by the model for U and Θ are $U \sim O(1)$ and $\Theta \sim 10^{-1}$ K. Thus $D > O(1)$ and $\lambda > O(1)$ in the model, which means the model is in the BLWTG regime.

Darcy's balance should therefore be the dominant balance in the x-momentum equation. We also have a WTG balance in the thermodynamic equation.

The scales expected from the BLWTG theory are below:

$$W \sim \frac{Qg}{N^2\theta_0} \sim 10^{-3}; \quad U \sim \frac{QgL}{N^2\theta_0 H} \sim O(1); \tag{3.89}$$

$$\Pi \sim \frac{QL^2g}{N^2H\theta_0^2c_p\tau_0} \sim 10^{-3}; \quad \Theta \sim \frac{QL^2}{N^2H^2\tau_0} \sim O(1). \tag{3.90}$$

Similar to WTG, the scales returned by the model for the horizontal and vertical velocity scales are accurate whilst Π and Θ are out by an order of magnitude.

In the BLWTG regime, heat is removed in the horizontal by an advective horizontal wind circulation and the vertical velocity structure in the boundary layer is similar to WTG, but weaker (figure 3.12, subplot(b)). We also see in figure 3.11 subplot (b) and 3.13 subplot (b) that the horizontal circulation extends to almost the entire horizontal domain. The vertical circulation does not extend much beyond the heated layer in the vertical, as evidenced by a lack of significant vertical velocity above the boundary layer in figure 3.10 subplot (b). Wu et al. (2000) also found heating is not advected much in the vertical when $\tau_0 \sim 10^{-5}$ s (and $L \sim 10^6$ m). Some small circulations do seem to develop just above the boundary layer in figure 3.10 although they do not seem to have a significant impact on the model.

Advection Dominated Boundary Layer Test

The final regime we test is the Advection Dominated Boundary Layer regime (ADBL). For this regime, we need $\lambda \sim O(1)$ and $D > O(1)$, however this is difficult to impose on the model from the outset and here ADBL develops from an initial BLWTG setup after a transition due to the size of the vertical gradient of the perturbation potential temperature. The transition is driven by the model itself adjusting its horizontal flow lengthscale as seen in section 3.6.2.

In this regime, imposing the scales $L \sim 10^6$ m, $Q \sim 10^{-5}$ K/s and $\tau_0 \sim 10^4$ s, the model returns $U \sim O(1)$, $\Theta \sim O(1)$ and we get $D > O(1)$ and $\lambda \sim O(10)$. Similar to the ADFT test we ran, we know from section 3.6.2 that the horizontal lengthscale shrinks so if we apply that here, we get $\lambda \sim O(1)$ and we are in the ADBL regime.

For ADBL, the drag is strong enough to inhibit horizontal advection of heat, which means the model cannot efficiently move heat away from the heat source in the horizontal (see figure 3.11 subplot (a) and 3.13 subplot (a)). Thus, we witness multiple thin bands of convection above the heat source in figure 3.10 subplot (a) and figure 3.12 subplot (a). Width of convection has been associated with drag strength in the past in an even more simplified model setting (Beare and Cullen, 2019) and likely has an effect in 'heat island' experiments where substantial convection is observed over the 'heat island' due to strong convergence of horizontal wind and therefore upward motion at the top of the boundary layer (Cullen, 2018). Thorpe and Guymer (1977) give observations that put land drag around 10^{-3} s (the surface drag value for this model run when $\tau_0 \sim 10^{-4}$ s) and drag values over the water between 10^{-3} s and 10^{-4} s (which would correspond to the BLWTG test we looked at), so drag increases over a 'heat island' when a 'heat island' corresponds to a real-world island and should have an impact on convective behaviour above the boundary layer.

Here, confining heating in the horizontal means the vertical potential temperature gradient for the perturbations increases and exceeds the vertical potential temperature gradient for the background state and thus N^2 becomes very small, less than 10^{-4} s^{-2} and the O(1) advection terms must balance the heating.

As with the other results, we check our solutions against the theory:

$$W \sim \frac{H}{L}\left(\frac{QHg\tau_0}{\theta_0}\right)^{\frac{1}{2}} \sim 10^{-2}; \quad U \sim \left(\frac{QHg\tau_0}{\theta_0}\right)^{\frac{1}{2}} \sim 1; \tag{3.91}$$

$$\Pi \sim \frac{L}{c_p\theta_0}\left(\frac{QgH}{\tau_0\theta_0}\right)^{\frac{1}{2}} \sim 10^{-4}; \quad \Theta \sim L\theta_0\left(\frac{Q}{gH\tau_0\theta_0}\right)^{\frac{1}{2}} \sim 10^{-1}. \tag{3.92}$$

U, W and Π in the model are well-predicted, however Θ is predicted to be too small. In the model $\Theta \sim O(1)$.

Note that in ADBL, there seems to be strong and sustained production of gravity waves in the free troposphere part of the model (figure 3.10, subplot (a)). Air above the boundary layer cannot be assumed to fall into any of the long-term balance regimes in Section 3.4 as $\lambda < O(1)$ owing to $Q = 0$ K above the boundary layer. And so if the circulation penetrates the free troposphere via vertical advection, we might expect $\frac{N^2H}{g\theta_r} > O(1)$. The only term in the thermodynamic equation able to balance the vertical velocity is the time derivative so the free troposphere must be in a state of continuous waves. We also see the waves in BLWTG and WTG cases though less dramatically (figure 3.10, subplots (b) and (d)).

3.7 Conclusions

We have presented a theoretical dimensionless parameter-based framework to investigate interactions between drag and heating physics in the dry tropical atmosphere and their representation in dynamical cores.

Using this framework we have shown that model behaviour should differ depending on drag and heating separately. Building on previous work in this area such as Sobel et al. (2001) and Beare and Cullen (2012), we have outlined scaling for four possible long-term balance regimes of which three are novel in the formulations presented in this chapter e.g. 2D Euler equations with Rayleigh drag and constant heating rate. The balance regimes presented include one well-recognised free tropospheric regime (WTG), as well as two boundary layer regimes (BLWTG and ADBL), and one other regime (ADFT), which differ from each other by orders of magnitude in the drag and heating parameters. Each regime should produce different behaviour when observed in models e.g. convection vs. no convection and each regime also provides different response variable scalings based on heating rate and drag timescale. We suggest that the theoretical scalings for the balance regimes can be used as ground truths for physics-dynamics coupling test cases – particularly 2D Held-Suarez like test cases for the near-equator region of the tropics – and we have tested the regimes in a 2D dynamical core. We have examined the usefulness of these

theoretical scalings for testing models by comparing them with the results from a 2D dynamical core, highlighting discrepancies in model thermodynamic variables and adjustments in the model horizontal lengthscale when regimes transition.

The dimensional analysis and scaling relationships explain many features of model behaviour in the test case results, including the existence of convection above the boundary layer and the importance of advection in some of the drag-influenced regimes – an aspect that is often neglected in analysis of Ekman balanced boundary layer behaviour (for example Stevens et al. (2002), Lindzen and Nigam (1987)).

We find imperfect agreement between the scalings from any given model run and the theoretical scalings, mainly due to the fact that some of the scales we impose on the model may change depending on regime evolution – particularly the horizontal and vertical lengthscales.

As such, we suggest that trend line analysis over multiple heating rates should form the backbone of test cases based on the regimes outlined in this paper. The trend lines analysis in section 3.6 takes gradients based solely on the power of heating rate Q and as Q has no time dependency and therefore cannot change in our setup, the results of the trend line analysis are robust to changes in all imposed model variable scales except Q itself.

There are limitations of this study. Firstly, we have only considered a set of 2D equations. Whilst the analysis is unlikely to be complicated by the addition of a third dimension alone, in reality we would also need to include rotational effects since Coriolis acceleration quickly becomes significant within a few degrees of the equator. Although, it shoud be noted that Wu et al. (2000) studied a 3D problem with heating and friction forcing on a β-plane and found behaviours that match well with the balance regimes outlined in this chapter.

And secondly, the absence of moisture is a further limitation since mositure forms an important part of tropical circulations, however the regimes explored here provide a good framework for analysing model behaviour in dry dynamical cores and the regime behaviours highlighted in this chapter may help to provide further insight into moist dynamics and particularly how moisture specifically changes model behaviour compared to the dry case.

Chapter 4

Moist Balance Regimes in 2D Tropical Dynamics with Heating and Drag Physics

When discussing the tropics, no analysis is complete without considering atmospheric water and moist processes. In this chapter, we expand on the results of chapter 3 where we looked at the case of the dry tropical atmosphere with heating and drag physics and we now consider the addition of moisture to the problem which complicates the picture considerably. The presence of latent heat introduces new feedbacks which mean that the flow chooses its own lengthscales rather than any externally imposed ones. Similarly, substantial latent heating can lead to instabilities or transient behaviour which means the model may also choose its own timescales and the buoyancy frequency N^2 (or N_m^2 now in the moist case) is no longer able to be imposed since $N_m^2 = 0$ can be 'chosen' by the model.

In this chapter, we will look at a number of behaviours in tropical dynamics when drag and externally imposed heating interact with moist processes and dynamics. We will consider long-term balance regimes for the moist case with heating and drag physics as well as the effect of interactions between drag, heating and moisture on the formation, sustaining and organisation of moist plumes in a 2D setup. Specifically, we will show that balance is achievable in the moist boundary layer for a strong enough drag and that variation in the formation, sustaining, and organisation of moist plumes is more dependent on whether the boundary layer satisfies a long-term balanced regime than the strength of the drag alone. We also show a stronger

dependence on model resolution compared to the dry case results.

4.1 Introduction

As previously noted, the tropics is a region where strong amounts of convective heating driven by moist processes – such as evaporation and condensation – interact with boundary layer surface drag. In weather and climate models, the representation of moist processes is a key source of variation in model accuracy in the tropics and cloud feedbacks for example are a leading source of uncertainty in climate models (Bony et al., 2015). As such, it is important to understand the effect moisture, heating, surface drag and their respective interactions might have on long-term balance regimes in the tropics. Likewise, it is also helpful to identify specific behaviours associated with each regime. Here, we are particularly interested in the effect of the boundary layer long-term balance regime on the formation, sustaining and organisation of moist convective plumes in the free troposphere. We hypothesise how long-term balance in the boundary layer affects the flow via convergence and modifying the vertical stability.

One of the shortfalls of chapter 3 was that we did not consider the effect of moisture on tropical dynamics even though moisture has a large impact on atmospheric circulation in the tropics owing to the effect of latent heat release and absorption associated with a change in water phase during convection and cloud formation (Sukhatme et al., 2012). In chapter 3, the model heating was fixed, but in reality it should interact with the other processes in the model as well.

Thus, in this chapter, we will build on the results in the dry regimes chapter to understand not only how the moist regimes differ from the dry ones – and thus the effect of moisture on circulation – but also how features distinct to the moist case present themselves depending on interactions between drag, heating and moisture in the boundary layer.

Similarly to the dry framework in chapter 3, we will again use scale analysis of the 2D Euler equations in the absence of rotation to define a parameter space from which we can identify long-term moist balance regimes where either heating, drag or moisture sources/sinks are of leading order. However, we do make some modifications to the equations from chapter 3 to facilitate the inclusion of moisture. Notably, we will use a buoyancy equation instead of the potential temperature equation to

avoid the complication of finding an adequate and informative representation of latent heat using the potential temperature equation. We will also include a water equation to represent the moisture itself.

Otherwise, the equation sets are very similar and the dry case from chapter 3 can be seen as a special case of the moist case in this chapter, requiring simply that we set the moist buoyancy frequency N_m^2 to be the dry buoyancy frequency N^2 from chapter 3 and assume total water q^t to be zero (for a definition of N_m^2, see section 4.2 of this chapter which uses the derivation of Emanuel et al. (1987)). By using very similar sets of equations, we can more easily compare behaviour in the moist and dry cases. We can also more easily establish how moisture is affecting the circulation and use insights from behaviour in the dry case to better understand behaviour in the moist case. This is particularly useful given the additional complications in the moist case and extra behaviours not observed in the dry case such as moist convective plumes and latent heating which can sustain plumes above the boundary layer for longer and higher up than the dry case could.

In order to compare with the dry case, we will also use a similar 2D semi-Lagrangian, semi-implicit model setup (Thuburn, 2017) to test our theoretical ideas and provide further insight into moist processes and how those processes differ from the dry case. In particular, how the existence or non-existence of long-term balance regimes in the boundary layer may impact circulations in the tropics.

There have been a number of studies of forced circulation in the moist tropics which attempt to understand the existence or not of balance states. Sukhatme et al. (2012) for example use a heat source due to condensation and evaporation to attempt to define an asymptotic balance state within the confines of a strongly stratified 2D Boussinesq system with rapid condensation and evaporation. Sobel et al. (2001) outline a moist variant of the Weak Temperature Gradient approximation alongside the dry case and in Bretherton and Sobel (2002), the weak temperature gradient (WTG) approximation is applied to an idealized model of the Walker circulation in the tropics without a boundary layer where it is found that small differences in the sea-surface temperature (SST) across the domain cause convection everywhere, whereas large differences in the SST across the domain result in no steady-state solution.

Thus far, the role of boundary layer drag in achieving a balance state in moist forced tropical circulations has not been widely studied. In a simplified model setup,

Beare and Cullen (2019) demonstrate that drag has an effect on the total convective region with stronger drag leading to thinner convection, and they also show that very strong drag can inhibit the ability of their simplified model to maintain a convective boundary layer. Increases in surface drag have also been shown to have an effect on convective organisation in large eddy-simulations (Park et al., 2018). In their geostrophic model with drag, Lindzen and Nigam (1987) highlight the importance of horizontal convergence acting to redistribute mass and thereby reduce horizontal pressure gradients arising from low-level temperature gradients forced by SST anomalies in the near-equator region. Lindzen and Nigam (1987) find that increasing the drag decreases the horizontal velocity and convergence. In Lindzen and Nigam (1987), they use a steady state model so balance is essentially imposed and thus, there is little investigation of how the drag interacts with existence or non-existence of long-term balance regimes. In this chapter, we will show that the increase of drag alone does not have a substantial effect on our model results except when the drag increases enough that the model boundary layer can be considered to be in a balanced state.

We will begin our investigation by first defining the possible long-term balances from the 2D moist Euler equations and then we will investigate if any of them can be achieved in numerical simulations and what the impact of the existence or non existence of long-term balance regimes is on model behaviour.

There are four main findings from this work. Firstly, we find that balance is possible in the moist boundary layer of the model when drag is strong enough – in particular, we find clear evidence of Darcy's balance in the horizontal momentum equation. Only one of the moist variants of the long-term dry balance regimes seen in chapter 3 appears to be obtainable in our experiments with the moist variant of the advection dominated boundary layer (ADBL) appearing to be the only balance regime we are able to replicate in the moist case. Attempts to force the others were unsuccessful, suggesting that either our $\sim$10-day model runs were not long enough to establish balance or that the other balance regimes simply do not exist in the moist case or are unstable. One of the new moist regimes based on the vertical stability is also achievable and has a similar formulation to ADBL in that the new moist regime also has strong drag in the boundary layer.

Secondly, we find that there is a clear distinction in model behaviour between model runs we consider to be balanced and those where balance is not evident. In

particular, whether or not the boundary layer is in Darcy's balance has a strong effect on the strength, timing and organisation of convective plumes.

Thirdly, we find that the strength and number of convective plumes across the horizontal domain is also partially dependent on the drag strength. This holds both for the case of a continuously externally heated boundary layer and for the case of the boundary layer externally heated only at the initial timestep and mirrors results such as Park et al. (2018) who find that increasing surface drag in an LES simulation changes convective behaviour from predominantly convective cells to predominantly convective rolls. However, we find here that the effect of drag alone is less strong than the effect of a change in balance regime in the continuously heated case. That is to say, changing the boundary layer drag alone does not substantially affect the model results unless the boundary layer also changes to satisfy a balance regime. In particular, whether or not the boundary layer satisfies Darcy's balance (e.g. a long-term balance in the horizontal momentum equation between pressure and drag (Beare and Cullen, 2012)) has more effect than just changing the drag parameter. The presence of moisture and latent heating means the circulations will also be subject to further 'internal' heating, but we do not quantify this effect here except via the change in the moist buoyancy frequency.

Finally, we find that the horizontal lengthscale L is more strongly dependent on horizontal gridlength Δx compared to the dry case. In the dry case, the model results only become dependent on the gridlength L in certain balance regimes (notably ADBL and ADFT, but not BLWTG or WTG). In the moist case, the dependence is clear for the unbalanced model runs and for balanced model runs that appear to satisfy the ADBL regime. Due to the stronger dependence on gridlength, the transition between regimes is also partially determined by the gridlength. Whilst this dependence on gridlength makes it difficult to determine which balance regime a model truly finds itself in, it does highlight how model regimes can switch based both on externally imposed parameters and parameters determined internally by the model. In effect, both the governing equations and the model can impact observed balance regimes in the model. This is particularly significant as it demonstrates that important parameters that determine regime changes are determined by the resolution and not any 'true' value when the real physics are not properly captured.

In chapter 2, we saw that increases in model resolution can lead to problems with the validity of parameterizations of physics processes at smaller gridlengths.

As such, it is important to acknowledge that the regimes we see in models may not be fully accurate regimes and that model resolution can obscure the relationship between parameters and regimes i.e. a regime that exists at a particular resolution may not exist at another one. It also highlights the importance of determining which processes might force dependence on gridlength e.g. the dry case was not dependent on gridlength in many model runs whilst the moist case has a stronger dependence on gridlength – at least in the range of drag, heating and moisture parameters explored in this chapter and in the dry case in chapter 3.

4.2 Moist Equation Framework

We now move on to discussing the theoretical framework we will use for our moist analysis. As previously stated, in order to understand the effect of adding moisture to the dry problem in chapter 3, we use the same base 2D Euler equations with heating and drag physics, but with two changes. The potential temperature equation is replaced by a buoyancy equation to allow for a better representation of moist adiabats and latent heat, and we also add a water equation to consider balances between moist sources and sinks and the drag and heating balances we have already obtained from the dry case.

This gives us the following set of equations:

$$\frac{\partial \rho}{\partial t} + \nabla\cdot(\rho \mathbf{u}) = 0; \tag{4.1}$$

$$\frac{Db}{Dt} + wN_m^2 = \beta \tag{4.2}$$

$$\frac{D\mathbf{u}}{Dt} + c_p\theta\nabla\pi + \nabla\phi = \left(-\frac{u}{\tau}, 0\right); \tag{4.3}$$

$$\frac{Dq^t}{Dt} = m_s \tag{4.4}$$

$$\pi = \left(\frac{\rho R\theta}{p_{ref}}\right)^{\frac{\kappa}{1-\kappa}}. \tag{4.5}$$

These equations provide a mass conservation equation (4.1), a thermodynamic equation with a physics component (4.2), a momentum equation with a drag component in the horizontal (4.3), a water equation with a physics component (4.4), and an equation of state (4.5), with p pressure, p_{ref} a constant reference pressure, $\mathbf{u} = (u(x,z), w(x,z))$ velocity in the horizontal (x) and vertical (z) directions only.

Variable b is the buoyancy, β a buoyancy forcing term, q^t total water, π the Exner pressure, ρ density, c_p the specific heat capacity at constant pressure for dry air, R the gas constant for dry air, ϕ geopotential and u/τ a linear Rayleigh drag term, where $\tau(x, z)$ is a drag timescale. Variable m_s can represent either a moisture source or a moisture sink. We also have dimensionless parameter $\kappa = R/c_p$. The Exner pressure π is still related to pressure p by the following equation: $\pi = \left(\frac{p}{p_{ref}}\right)^{\kappa}$. The m_s term represents a moisture source or sink that can either be externally imposed or internally determined. Moisture sources and sinks could include precipitation or condensation or surface evaporation. We use the dry air values of R and c_p for the theory as they do not vary much with moisture (Emmanuel, 1994), though they will be variable when implemented in the model.

In the thermodynamic equation, the buoyancy and buoyancy forcing relate to the potential temperature and heating from the dry chapter via

$$b = \frac{g\theta}{\theta_0}, \quad \beta = \frac{gQ}{\theta_0}, \tag{4.6}$$

where θ_0 is the background potential temperature and g is of course gravity. We make some approximations on buoyancy b. Notably by using the dry potential temperature θ, we neglect the effect of water vapour and liquid water loading on b, but this should not have a substantial impact on the scaling relations. Heating Q is an externally imposed heating source used to excite and maintain the dynamics circulation whilst any latent heating and dynamics feedbacks are accounted for by changes in the N_m^2 term. In reality, separating the two is not easy, but for our purposes, we expect the effect of the latent heating to be substantially larger than the imposed heating Q – although Q may still have an effect if it is strong enough.

The definition of N_m^2 follows Emanuel et al. (1987) such that

$$N_m^2 = g\frac{\Gamma_m}{\Gamma_d}\frac{\partial \log(\theta_e)}{\partial z}, \tag{4.7}$$

where the factor Γ_m/Γ_d is the ratio of the moist adiabatic lapse rate Γ_m to the dry adiabatic lapse rate Γ_d. When the relative humidity is zero, we take N_m^2 to be the dry buoyancy frequency $N^2 = \frac{g}{\theta}\frac{\partial \theta}{\partial z}$. θ_e is the equivalent potential temperature.

4.2.1 Non-dimensionalised Equations

In order to discuss the similarities and differences between the dry regime and the moist regime, we again non-dimensionalise our equation set. For our moist analysis, we use the same non-dimensionalisations of equations (4.1), (4.3), and (4.5) for the mass conservation equation, x and z-momentum equations, and equation of state as in the dry chapter, but we also add non-dimensionalisations of the buoyancy equation (4.2) and the water equation (4.4).

Buoyancy Equation

The buoyancy equation can be expanded to give:

$$\frac{\partial b}{\partial t} + u\frac{\partial b}{\partial x} + w\frac{\partial b}{\partial z} + wN_m^2 = \beta. \tag{4.8}$$

Non-dimensionalising our variables, such that:

$$b = B\hat{b}; \quad w = W\hat{w}; \quad u = U\hat{u}; \quad \beta = \beta\hat{\beta}; \quad t = T\hat{t}, \tag{4.9}$$

we can rewrite equation (4.2) as a dimensionless equation:

$$\frac{B}{T}\frac{\partial \hat{b}}{\partial \hat{t}} + \frac{UB}{L}\hat{u}\frac{\partial \hat{b}}{\partial \hat{x}} + \frac{WB}{H}\hat{w}\frac{\partial \hat{b}}{\partial \hat{z}} + W\hat{w}N_m^2 = \beta\hat{\beta}. \tag{4.10}$$

Rewriting as an equation in terms of dimensionless parameters from the dry regimes chapter, we get:

$$St\frac{\partial \hat{b}}{\partial \hat{t}} + \hat{u}\frac{\partial \hat{b}}{\partial \hat{x}} + \frac{WL}{UH}\hat{w}\frac{\partial \hat{b}}{\partial \hat{z}} + \frac{WLN_m^2}{UB}\hat{w} = \lambda, \tag{4.11}$$

where our dimensionless parameters for the potential temperature equation in the dry regimes chapter are equivalent to those in the buoyancy equation here. Notably

$$\lambda = \frac{\beta L}{UB} = \frac{gQ}{\theta_0}\frac{L}{U}\frac{\theta_0}{g\Theta} = \frac{QL}{U\Theta}, \tag{4.12}$$

and provided anelasticity holds,

$$\frac{WLN_m^2}{UB} = \frac{WLN_m^2}{U}\frac{\theta_0}{g\Theta} = \frac{N_m^2 H\theta_0}{g\Theta}. \tag{4.13}$$

Water Equation Scalings

Next, we non-dimensionalise the water equation. Firstly, we expand equation (4.4) to give:

$$\frac{\partial q^t}{\partial t} + u\frac{\partial q^t}{\partial x} + w\frac{\partial q^t}{\partial z} = m_s. \tag{4.14}$$

Then we non-dimensionalise our variables such that

$$m_s = M_s \hat{m}_s, \quad q^t = Q_t \hat{q}^t, \tag{4.15}$$

and consider the non-dimensionalised equation:

$$St\frac{\partial \hat{q}^t}{\partial \hat{t}} + \hat{u}\frac{\partial \hat{q}^t}{\partial \hat{x}} + \frac{WL}{UH}\hat{w}\frac{\partial \hat{q}^t}{\partial \hat{z}} = \mu \hat{m}_s, \tag{4.16}$$

where $\mu = \frac{M_s L}{U Q^t}$. From this, it might be said that μ is similar to λ – but for moisture forcing – as it represents the ratio of the water adjustment timescale compared to the advection timescale. In this framework, the externally imposed buoyancy forcing and water forcing are independent of each other. However, despite the independence in the forcings, the moist parameter μ and heating/buoyancy parameter λ are not completely independent of each other as they are both dependent on the horizontal advection timescale L/U and μ is dependent on water Q^t. Variables U and Q^t will be determined by the flow and L may also be determined by the flow. The internal buoyancy forcing accounted for by N_m^2 is not necessarily independent of the water forcing.

We also consider one further equation relating to water in the model which we will refer to as the moisture flux equation. Since we anticipate substantial exchanges of water between the boundary layer and the free troposphere, it is helpful to define an equation which can quantify these effects.

For the moisture flux equation, we combine the density with the water equation:

$$\frac{\partial(\rho q^t)}{\partial t} + \nabla \cdot \rho q^t \mathbf{u} = \rho m_s. \tag{4.17}$$

Then we integrate over a volume of interest, here the model boundary layer such that

$$\frac{\partial}{\partial t}\int_V \rho q^t \partial V + \int_V \rho q^t \mathbf{u}\cdot n \partial A = \int_V \rho m_s \partial V, \tag{4.18}$$

where V is the boundary layer volume and n is the unit normal going outwards from the surface of the boundary layer volume. In a model, this would mean the 'surface' between the boundary layer and the free troposphere.

We can then write equation (4.18) more simply as

$$\frac{\partial I}{\partial t} + F = S, \tag{4.19}$$

where I is the total mass of water in the volume, F is the net flux of water out of the water, and S is the net source of water into the volume.

When moist plumes are triggered, I decreases and F is non-zero as water is being advected from the boundary layer into the free troposphere. S will be zero initially when plumes are triggered or small as it captures only water returning to the boundary layer. For balance to occur, total water in the boundary layer I will decrease to the minimum amount permissable whilst F and S should balance each other i.e. no more water is leaving the boundary layer than returns over the full balance timescale. In any given model run, it is unlikely that both F and S will be zero.

We can then also non-dimensionalise equation (4.19) to give:

$$\frac{I}{T} + F = S. \tag{4.20}$$

4.2.2 Parameter Assumptions

In this moist heating and drag investigation, we will again make assumptions about some of the dimensionless parameters which match assumptions made in the dry chapter. In short, we assume a long timescale T so $St \ll O(1)$, anelasticity so $\frac{WL}{UH} \sim O(1)$ and hydrostatically balanced perturbations so $\Theta \sim \frac{c_p\theta_0^2\Pi}{Hg}$ or $B \sim \frac{c_p\theta_0\Pi}{H}$ with $B \ll b$ to follow the thermodynamic convention from chapter 3 (since $\Theta \ll \theta_0$ and given equation (4.6), we have $\frac{g\Theta}{\theta_0} \ll g$). This leaves us with the following equation set with multiple possible balances:

$$\frac{WL}{UH} \sim O(1); \tag{4.21}$$

$$\Theta \sim \frac{c_p \theta_0^2 \Pi}{Hg} \implies B \sim \frac{c_p \theta_0 \Pi}{H}; \tag{4.22}$$

$$\hat{u}\frac{\partial \hat{u}}{\partial \hat{x}} + \frac{WL}{UH}\hat{w}\frac{\partial \hat{u}}{\partial \hat{z}} + \frac{\pi_r}{\kappa\gamma M^2}\frac{\partial \hat{\pi}}{\partial \hat{x}} = -D\frac{\hat{u}}{\hat{\tau}}; \tag{4.23}$$

$$\hat{u}\frac{\partial \hat{b}}{\partial \hat{x}} + \frac{WL}{UH}\hat{w}\frac{\partial \hat{b}}{\partial \hat{z}} + \frac{WLN_m^2}{UB}\hat{w} = \lambda; \tag{4.24}$$

$$\hat{u}\frac{\partial \hat{q}^t}{\partial \hat{x}} + \frac{WL}{UH}\hat{w}\frac{\partial \hat{q}^t}{\partial \hat{z}} = \mu \hat{m}_s. \tag{4.25}$$

From this base, we analyse two new moist regimes and four moist variants of the dry regimes outlined in chapter 3.

4.3 Moist Regimes

In this section, we now outline the moist regimes. It should be noted that some of the regimes will be applicable in the boundary layer only where some amount of drag is feasible whilst other regimes may also be applicable in the free troposphere. In model runs, it is very likely that the boundary layer and the free troposphere are in different regimes as we saw in the dry case in chapter 3 where the boundary layer could satisfy one of the long-term balance regimes even whilst the free troposphere could not. In particular, we will outline a new moist regime for the free troposphere where previously in the dry case, we only had gravity waves and no long-term balance in the free troposphere. With the presence of latent heating, long-term balances may exist in the free troposphere part of a model as well as in the boundary layer in the absence of continuous forcing from the externally imposed heating term q in the thermodynamic equation (4.2). A second long-term balance regime without continuous externally imposed heating is presented here too.

It should be noted that it can often be difficult from the theory alone to figure out what a regime might look like in the real-world and it is also possible that regimes that should be able to exist in theory may not exist in the real-world or be achievable in models.

We will also outline requirements on the moist buoyancy frequency N_m^2 at the boundary layer top where we expect any boundary layer regimes to change to free troposphere regimes and therefore what this means for required relative humidity

levels in each regime.

4.3.1 New Regimes

Moist Unheated Free Troposphere

The first of the new moist regimes we consider is the moist unheated free troposphere (MUFT). This is a regime that occurs in a moist unheated free troposphere where transient motions such as the dispersal of moist plumes has decreased sufficiently that N_m^2 can be part of a leading order term in the horizontal velocity equation. In order to obtain MUFT, we must make a few key assumptions. Adding to assumptions of long-term, anelastic, and hydrostatic balance from section 4.2.2, we also assume a free troposphere pressure balance in the X-momentum equation, and a long-term balance in the buoyancy equation between horizontal advection and the buoyancy frequency term of the vertical advection:

$$\frac{WLN_m^2}{UB} \sim O(1). \tag{4.26}$$

We will call this the moist advection buoyancy frequency balance and such a balance might occur for example a the top of the moist plumes – where horizontal advection carries away any unstable negative buoyancy created by overshooting plumes – or at the base of the plumes in the boundary layer of a model when drag is set to zero. Within the plumes themselves, $N_m^2 = 0$ is required so MUFT cannot be a regime within the plumes.

In the dry case, we saw a lot of wave activity in the model results forced by the break from a heated boundary layer to a non-heated free troposphere which necessarily resulted in a balance between the background potential temperature term and the time derivative in the free troposphere. In the moist case, we might expect that when substantial vertical velocity exists (as it does when plumes forced by externally imposed heating and internal moist processes escape the boundary layer), the buoyancy frequency term might be balanced by the vertical and horizontal velocities and we might expect to see fewer waves above the plumes.

We also include the relationship between buoyancy and equivalent potential temperature to give the following set of balances:

$$\frac{WLN_m^2}{UB} \sim O(1); \quad \frac{\pi_r}{\kappa\gamma M^2} \sim O(1); \quad \frac{c_p\theta_0^2\Pi}{gH} \sim \Theta; \quad \frac{WL}{UH} \sim O(1); \quad B \sim \frac{g\Theta}{\theta_0}. \tag{4.27}$$

These might also be written:

$$W \sim \frac{UB}{LN_m^2}; \quad \Pi \sim \frac{U^2}{c_p\theta_0}; \quad \Theta \sim \frac{c_p\theta_0^2\Pi}{gH}; \quad U \sim \frac{WL}{H}; \quad B \sim \frac{g\Theta}{\theta_0}. \tag{4.28}$$

From these balances, we extract our output predictions for 5 variables U, W, Π, Θ, and B.

$$W \sim \frac{H^2N_m}{L}; \quad U \sim HN_m; \quad \Pi \sim \frac{H^2N_m^2}{c_p\theta_0}; \tag{4.29}$$

$$\Theta \sim \frac{\theta_0 HN_m^2}{g}; \quad B \sim HN_m^2. \tag{4.30}$$

Here, N_m^2 is the moist buoyancy frequency.

Additionally, if we include a moisture source or sink, we get a balance between the moisture source/sink term and the $O(1)$ advection terms in the water equation. Hence, we get the following long-term balance in the water equation:

$$\mu \sim O(1) \implies Q^t \sim \frac{M_sL}{U}, \tag{4.31}$$

and therefore

$$Q^t \sim \frac{M_sL}{HN_m^2}. \tag{4.32}$$

Furthermore, if we are also interested in the total water remaining in the boundary layer of the model, then we might consider again equation 4.20. When the model is balanced, we expect that the total flux of water out of the boundary layer over the balance timescale is equal to the total water flux into the boundary layer over the same timescale. And so, we have the following inequality for total water in the boundary layer I:

$$\frac{I}{T} < O(1) \implies I < T. \tag{4.33}$$

The timescale for balance in the moist unheated free troposphere regime will be when the Strouhal number satisfies $St < O(1)$. So when

$$\frac{L}{U} < T \implies \frac{L}{HN_m} < T. \tag{4.34}$$

And so we expect the minimum value of T for equation (4.33) to be satisfied is $T = \frac{L}{HN_m}$ and so we can say that at the minimum balance timescale,

$$I \leq \frac{L}{HN_m}. \tag{4.35}$$

We should note here that as we are dealing with moisture, the magnitude of the horizontal lengthscale L may be impacted by the tendency of plumes triggering to behave as a delta function in the absence of turbulent processes which limit the collapse of scale (Emmanuel, 1994). In other words, in our model runs which don't account for turbulent processes, the horizontal lengthscale L is likely to collapse to the smallest possible lengthscale, i.e. the horizontal gridlength Δx. Thus for the MUFT regime, we might assume that $L \sim \Delta x$ in any model.

Due to the requirement for long-term balance $\mathrm{St} = \frac{L}{UT} < O(1)$ being dependent on horizontal lengthscale L, plumes in any given model run might be expected to develop (or dissipate) on smaller timescales for smaller Δx (or higher resolution). Such is in keeping with classic stability analysis which shows faster growth rate for narrower modes in the absence of viscosity (Emmanuel, 1994).

Moist Unheated Boundary Layer

Our second new moist regime is the moist unheated boundary layer (MUBL). This regime would occur in an unheated boundary layer where the drag parameter is of leading order in the x-momentum equation and the air contains moisture. Heating in the boundary layer would be driven predominantly by latent heating. The MUBL regime is a balance regime we might expect to find once transient behaviours such as plume triggering have decreased the relative humidity in the boundary layer to the point where N_m^2 is large enough to be a leading order term in the thermodynamic equation. MUBL may also be a regime we expect in the boundary layer beneath convective rolls due to the importance of drag.

For this regime, adding to assumptions of long-term, anelastic, hydrostatic balance, we also assume Darcy's balance in the X-momentum equation, moist buoyancy

frequency balance in the buoyancy equation and a relationship between buoyancy and equivalent potential temperature. The balances are as follows:

$$\frac{WLN_m^2}{UB} \sim O(1); \quad \frac{\pi_r}{\kappa\gamma M^2} \sim D; \quad \frac{c_p\theta_0^2\Pi}{gH} \sim \Theta; \quad \frac{WL}{UH} \sim O(1); \quad B \sim \frac{g\Theta}{\theta_0}. \quad (4.36)$$

These might also be written:

$$W \sim \frac{UB}{LN_m^2}; \quad \Pi \sim \frac{UL}{c_p\theta_0\tau_0}; \quad \Theta \sim \frac{c_p\theta_0^2\Pi}{gH}; \quad U \sim \frac{WL}{H}; \quad B \sim \frac{g\Theta}{\theta_0}. \quad (4.37)$$

We then extract our output predictions in the MUBL regime for 5 variables: U, W, Π, Θ, and B. Note that we could remove the prediction for Θ and only use B, but we keep it in order to compare with the dry case.

$$W \sim \frac{\tau_0 H^2 N_m^2}{L^2}; \quad U \sim \frac{\tau_0 H N_m^2}{L}; \quad \Pi \sim \frac{H N_m^2}{c_p\theta_0}; \quad (4.38)$$

$$\Theta \sim \frac{N_m^2\theta_0}{g}; \quad B \sim N_m^2. \quad (4.39)$$

If we include the effect of a moisture source or sink, we also find that

$$Q^t \sim \frac{M_s L^2}{\tau_0 H N_m^2}. \quad (4.40)$$

If we compare the scalings for the MUBL regime to the scaling for the MUFT regime, we see that the buoyancy and perturbation thermodynamic terms have the same scalings in both and that the inclusion of drag primarily affects the horizontal and vertical velocity. The horizontal and vertical velocity scalings for the MUBL and MUFT regimes differ by a factor of $\frac{N_m\tau_0}{L}$. For likely values of N_m, τ_0 and L, we have:

$$\frac{N_m\tau_0}{L} < 1. \quad (4.41)$$

This suggests that we should expect to see weaker horizontal and vertical advection in the MUBL regime and therefore, we expect MUBL will have more, but weaker plumes being triggered with individual plumes drawing on smaller horizontal

pools of moisture to sustain themselves.

The timescale for balance in the moist unheated boundary layer regime will be when the Strouhal number satisfies $St < O(1)$. So when

$$\frac{L}{U} < T \implies \frac{L^2}{\tau_0 H N_m^2} < T, \tag{4.42}$$

and the minimum total water I therefore satisfies:

$$I \leq \frac{L^2}{\tau_0 H N_m^2}. \tag{4.43}$$

Compared with the moist unheated free troposphere regime, this means the difference in the timescale for balance for the two new regimes is the inverse of the same factor as in equation (4.41): $\frac{L}{\tau_0 N_m}$. Since we expect $\frac{L}{\tau_0 N_m} > O(1)$, this would imply that the moist unheated free troposphere regime should reach balance faster than the moist unheated boundary layer. As the relative humidity increases and therefore, N_m decreases, we expect the differences to become more pronounced. Likewise, as drag is increased and therefore τ_0 decreases.

Also, if L does not shrink to the gridlength lengthscale, it is possible the required balance timescale for balance for each regime is very large.

4.3.2 Moist Versions of the Dry Regimes

We now consider moist versions of the four dry balance regimes outlined in chapter 3. The variable scalings here are identical to the dry case, simply with different notation and using buoyancy instead of potential temperature in the thermodynamic equation. There are two reasons we outline the moist variants of the dry cases. Firstly, we want to check if balance – or a state resembling balance – similar to the dry balances can be achieved with the inclusion of moisture. And secondly we want to look at the effect various balances in the moist heated layer might have on the development, sustaining and organisation of moist plumes in the unheated layer above. Or to put it in atmospheric terms, we want to look at the effect various balances in the heated boundary layer might have on the development, sustaining and organisation of moist plumes in the free troposphere.

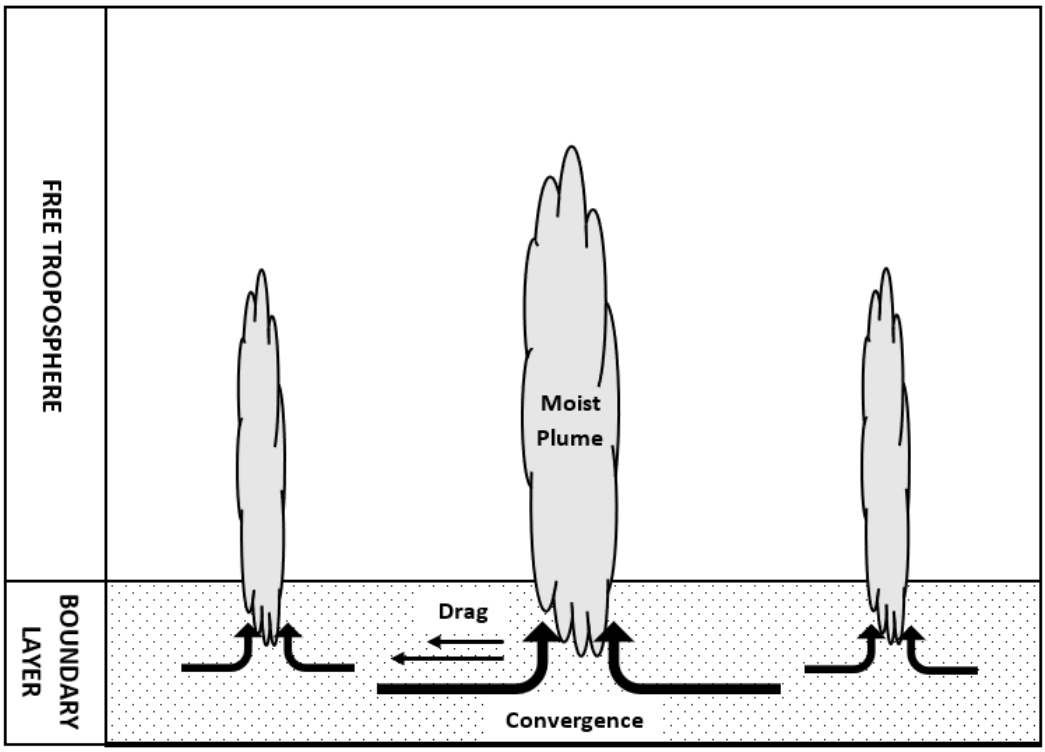

Figure 4.1: A diagram of forces interacting in a moist boundary layer setup and hypothesised model behaviour.

Moist Advection Dominated Boundary Layer

The first of the dry regimes we translate to the moist case is the ADBL regime, which we will now refer to rather unimaginatively as the Moist Advection Dominated Boundary Layer (or MADBL). We recalculate scalings for the 5 variables U, W, Π, Θ, and B in terms of the moist buoyancy frequency and the buoyancy and derive a scaling for the moist buoyancy frequency N_m^2 at the regime transition between MADBL and the new regime MUFT. This is important for the moist variant of ADBL because if a plume is triggered, the value of N_m^2 will determine the transition from the boundary layer buoyancy balance in the buoyancy equation ($\lambda \sim O(1)$) to the moist buoyancy frequency balance in the free troposphere ($\frac{WLN_m^2}{UB} \sim O(1)$).

As in the dry case, we assume long-term, anelastic, hydrostatic balance. We also assume Darcy's balance between pressure and drag in the x-momentum equation. We also assume any externally forced heating is balanced by the O(1) advection terms in the buoyancy equation as in the dry case.

$$\lambda \sim O(1); \quad \frac{\pi_r}{\kappa\gamma M^2} \sim D; \quad \frac{c_p\theta_0^2\Pi}{gH} \sim \Theta; \quad \frac{WL}{UH} \sim O(1); \quad B \sim \frac{g\Theta}{\theta_0}. \tag{4.44}$$

These might also be written:

$$U \sim \frac{L\beta}{B}; \quad \Pi \sim \frac{UL}{c_p\theta_0\tau_0}; \quad \Theta \sim \frac{c_p\theta_0^2\Pi}{gH}; \quad U \sim \frac{WL}{H}; \quad B \sim \frac{g\Theta}{\theta_0}. \tag{4.45}$$

From these balances, we extract our output predictions for 5 variables U, W, Π, Θ, and B.

$$W \sim \left(\frac{H^3\tau_0\beta}{L^2}\right)^{\frac{1}{2}}; \quad U \sim (H\tau_0\beta)^{\frac{1}{2}}; \quad \Pi \sim \frac{L}{c_p\theta_0}\left(\frac{H\beta}{\tau_0}\right)^{\frac{1}{2}}; \tag{4.46}$$

$$\Theta \sim \frac{\theta_0 L}{g}\left(\frac{\beta}{\tau_0 H}\right)^{\frac{1}{2}}; \quad B \sim \left(\frac{L^2\beta}{H\tau_0}\right)^{\frac{1}{2}}. \tag{4.47}$$

These scalings are identical to those in the dry chapter with the addition now of a buoyancy scaling and with the other variables predicted from buoyancy forcing β instead of potential temperature forcing Q.

In this chapter, we now extend our analysis to consider how this regime interacts with the added moisture element of the model. When moisture is present, this means considering N_m^2 instead of N^2 for the dry case. And specifically, we might ask how we determine N_m^2.

Where the heated boundary layer transitions to the unheated free troposphere, there will be a value of N_m^2 where we start to get a three-way balance between the previously $O(1)$ advection terms, the $O(1)$ heating parameter λ, and the vertical velocity buoyancy term in the buoyancy equation. In other words, the moist advection buoyancy frequency balance from equation (4.26):

$$\frac{WLN_m^2}{UB} \sim O(1). \tag{4.48}$$

If we use the values of W, U and B from the moist advection dominated boundary layer, we can obtain a scaling for the buoyancy frequency N_m^2 which is dependent on the drag strength τ_0:

$$N_m^2 \sim \frac{UB}{WL} \sim \left(\frac{L^2\beta}{H^3\tau_0}\right)^{\frac{1}{2}}. \tag{4.49}$$

In the event that part of the boundary layer could be considered a moisture source (e.g. surface evaporation), we might also assume we have a source term in the moisture equation of leading order. This would lead to the balance in equation (4.31) and we would have:

$$Q^t \sim \frac{M_s L}{(H\tau_0\beta)^{1/2}}. \tag{4.50}$$

In the boundary layer, precipitation might serve as a moisture sink though the occurence of precipitation is much more likely in the free troposphere than the boundary layer.

Given that the timescale for balance is

$$\frac{L}{U} < T \implies \frac{L}{(H\tau_0\beta)^{\frac{1}{2}}} < T, \tag{4.51}$$

we have a requirement on the total water in the boundary layer of

$$I < \frac{L}{(H\tau_0\beta)^{\frac{1}{2}}}. \tag{4.52}$$

Moist Advection Dominated Free Troposphere

We next obtain the moist saturated version of the advection dominated free troposphere (MADFT) we outlined in chapter 3. As we did with the MADBL regime, we are expecting to be able to determine the N_m^2 value for a transition from the MADFT regime to the MUFT regime. But also, we hope to determine the moisture content in the MADFT regime.

Again as in the dry case, we assume long-term, anelastic, hydrostatic balance. We also assume a balance between pressure and the advection terms in the x-momentum equation and we assume a relationship between buoyancy and potential temperature. We also assume any externally forced heating is balanced by the O(1) advection terms in the buoyancy equation.

Our balances for MADFT are then:

$$\lambda \sim O(1); \quad \frac{\pi_r}{\kappa\gamma M^2} \sim O(1); \quad \frac{c_p\theta_0^2\Pi}{gH} \sim \Theta; \quad \frac{WL}{UH} \sim O(1); \quad B \sim \frac{g\Theta}{\theta_0}. \tag{4.53}$$

These might also be written:

$$U \sim \frac{L\beta}{B}; \quad \Pi \sim \frac{U^2}{c_p\theta_0}; \quad \Theta \sim \frac{c_p\theta_0^2\Pi}{gH}; \quad U \sim \frac{WL}{H}; \quad B \sim \frac{g\Theta}{\theta_0}. \tag{4.54}$$

From these balances, we then extract our output predictions for 5 variables U, W, Π, Θ, and B, which are again identical to those in the dry chapter for the ADFT regime, except for the addition of the buoyancy scaling:

$$W \sim \left(\frac{\beta H^4}{L^2}\right)^{\frac{1}{3}}; \quad U \sim (L\beta H)^{\frac{1}{3}} \quad \Pi \sim \frac{1}{c_p\theta_0}(L\beta H)^{\frac{2}{3}}; \tag{4.55}$$

$$\Theta \sim \frac{\theta_0}{gH}(L\beta H)^{\frac{2}{3}}; \quad B \sim \frac{1}{H}\left(\frac{L\beta}{H}\right)^{\frac{2}{3}}. \tag{4.56}$$

Using these scalings, we can now extract a scaling for N_m^2 in the MADFT regime at the transition between the heated boundary layer and the unheated free troposphere – assuming again that the regime trends towards $\frac{WLN_m^2}{UB} \sim O(1)$. This gives us:

$$N_m^2 \sim \frac{UB}{WL} \sim \left(\frac{L\beta^3}{H^3}\right)^{\frac{1}{3}}. \tag{4.57}$$

If we compare the scalings for N_m^2 from MADBL and MADFT, we find that if

$$\frac{1}{\tau_0} > \frac{\beta^3}{H^3L^2}, \tag{4.58}$$

as is most likely the case for probable values of H, τ_0, L and β in the tropics, we would expect the value of the moist buoyancy frequency N_m^2 required for moist plumes to trigger in MADBL to be larger than the moist buoyancy frequency required for MADFT. Thus, the inclusion of drag means that a lower relative humidity is required in the boundary layer for moist plumes to develop and begin ascending into the free troposphere. This makes sense if we consider the behaviour of the dry case ADBL regime compared to the dry ADFT regime. In the dry ADBL regime, increasing the drag appeared to force the collapse of scale in the horizontal velocity at a lower heating rate. For model runs with identical setups except for the drag parameter,

a higher heating rate was required to force a collapse of scales when the drag term was not included. When a moist model setup has a lower relative humidity, it will most likely behave similarly to the dry case.

When it comes to the moisture content of the MADFT regime, in the event that part of the free troposphere could be considered a moisture sink, we might assume we have a source term in the moisture equation of leading order. This would lead again to the balance in equation (4.31). Note that it makes no difference to the scalings whether M_s represents a source or a sink. And we have:

$$Q^t \sim \frac{M_s L^{2/3}}{(\beta H)^{1/3}}. \tag{4.59}$$

Given that the timescale for balance for MADFT is

$$\frac{L}{U} < T \implies \frac{L}{(L\beta H)^{\frac{1}{3}}} < T, \tag{4.60}$$

we have a requirement on the total water in the boundary layer of

$$I < \frac{L}{(L\beta H)^{\frac{1}{3}}}. \tag{4.61}$$

In comparison with the MADBL scaling for total water, the minimum total water in the boundary layer under an MADFT regime may be higher or lower than in the MADBL regime depending on values of L, τ_0, β and H,

$$\text{If} \begin{cases} \beta H \tau_0^3 > L^2 & \text{MADBL has a lower minimum total water than MADFT,} \\ \beta H \tau_0^3 < L^2 & \text{MADFT has a lower minimum total water than MADBL.} \end{cases} \tag{4.62}$$

For likely values of β, H, τ_0, and L, both of these outcomes are possible.

Moist Weak Temperature Gradient

For the moist variant of the Weak Temperature gradient, we re-derive variable scalings for the moist version under the same assumptions as the dry case, except with moisture included. Again as in the dry case, we assume long-term, anelastic, hydrostatic balance. We also assume a balance between pressure and the advection terms in the x-momentum equation, a relationship between buoyancy and poten-

tial temperature and a balance between the heating rate and the vertical advection term which includes the buoyancy N_m^2 in the buoyancy equation. The balances in the equations are then given by:

$$\lambda \sim \frac{WLN_m^2}{UB}; \quad \frac{\pi_r}{\kappa\gamma M^2} \sim O(1); \quad \frac{c_p\theta_0^2\Pi}{gH} \sim \Theta; \quad \frac{WL}{UH} \sim O(1); \quad B \sim \frac{g\Theta}{\theta_0}. \tag{4.63}$$

From these balances, we extract our output predictions for 5 variables U, W, Π, Θ, and B:

$$W \sim \frac{\beta}{N_m^2}; \quad U \sim \frac{L\beta}{HN_m^2} \quad \Pi \sim \frac{\beta^2L^2}{c_p\theta_0N_m^4H^2}; \tag{4.64}$$

$$\Theta \sim \frac{\beta^2L^2\theta_0}{N_m^4gH^3}; \quad B \sim \frac{\beta^2L^2}{N_m^4H^2}. \tag{4.65}$$

And so, we can once again determine N_m^2 required for transition to MUFT now for the WTG regime:

$$N_m^2 \sim \frac{UB}{WL} \sim \left(\frac{L^2\beta^2}{H^4}\right)^{\frac{1}{3}}. \tag{4.66}$$

When comparing to the scaling for N_m^2 taken from the MADFT regime, we find that for likely values of L, β, and H,

$$\frac{1}{c_p\theta_0} < \frac{L^5\beta^5}{H^3} \implies \left(\frac{\beta^3L^3}{c_p\theta_0H^5}\right)^{\frac{1}{4}} < \frac{L^2\beta^2}{H^2}. \tag{4.67}$$

So MWTG has a larger N_m^2 than MADFT and therefore MWTG requires a lower relative humidity level for plumes to trigger. If we also compare MWTG results with the MADBL scaling for N_m^2 at the free troposphere transition, we find that neither is uniformly larger than the other for likely values of L, β, τ_0, and H. On a case by case basis:

$$\text{If} \begin{cases} \beta > \frac{L^2}{H\tau_0} & \text{MWTG requires a lower relative humidity than MADBL,} \\ \beta < \frac{L^2}{H\tau_0} & \text{MADBL requires a lower relative humidity than MWTG.} \end{cases} \tag{4.68}$$

This is interesting given that in the dry case, the WTG regime had no collapse of scale and little evidence of activity above the heated boundary layer or vertical

ascent caused by boundary layer processes.

If we now look at the total water content, for the MWTG regime with a moisture source/sink in the governing equations, we get from equation (4.31):

$$Q^t \sim \frac{M_s H N_m^2}{\beta}. \tag{4.69}$$

Given that the timescale for balance for MWTG is

$$\frac{L}{U} < T \implies \frac{H N_M^2}{\beta} < T, \tag{4.70}$$

we have a requirement on the total water in the boundary layer of

$$I < \frac{L}{(L\beta H)^{\frac{1}{3}}}. \tag{4.71}$$

Comparing the total water scalings for MADBL (equation (4.52)), MADFT (equation ((4.61)) and MWTG (equation (4.71)), we find that if N_m^2 is very small ($N_m < 10^{-3}$ s^{-1}), then for likely values of H, L, and τ_0, the total water in the MWTG regime should be less than the total water in the MADBL and MADFT regimes.

Moist Boundary Layer Pseudo-Weak Temperature Gradient

The final regime we consider is the moist variant of the Boundary Layer Pseudo-Weak Temperature gradient; we derive the scalings for the moist version under the same assumptions as the dry case, except with moisture. Again as in the dry case, we assume long-term, anelastic, hydrostatic balance. We also assume Darcy's balance between pressure and drag in the x-momentum equation, a relationship between buoyancy and equivalent potential temperature and a balance between the heating rate and the vertical advection term which includes the buoyancy N_m^2 in the buoyancy equation. The balances in the equations are given by:

$$\lambda \sim \frac{W L N_m^2}{U B}; \quad \frac{\pi_r}{\kappa \gamma M^2} \sim D; \quad \frac{c_p \theta_0^2 \Pi}{g H} \sim \Theta; \quad \frac{W L}{U H} \sim O(1); \quad B \sim \frac{g \Theta}{\theta_0}. \tag{4.72}$$

From these balances, we extract our output predictions for 5 variables U, W, Π, Θ, and B:

$$W \sim \frac{\beta}{N_m^2}; \quad U \sim \frac{L\beta}{HN_m^2} \quad \Pi \sim \frac{L\beta}{HN_m^2 c_p \theta_0 \tau_0}; \tag{4.73}$$

$$\Theta \sim \frac{L\beta\theta_0}{gHN_m^2\tau_0}; \quad B \sim \frac{L\beta}{H^2 N_m^2 \tau_0}. \tag{4.74}$$

For MBLWTG, the moist buoyancy frequency at the transition is given by

$$N_m^2 \sim \frac{UB}{WL} \sim \left(\frac{L\beta}{H^3\tau_0}\right)^{\frac{1}{2}}. \tag{4.75}$$

If we compare the MBLWTG moist buoyancy frequency scaling to the MADBL scaling, and we assume that $L > O(1)$ for all our likely runs, we have

$$\left(\frac{L\beta}{H^3\tau_0}\right)^{\frac{1}{2}} < \left(\frac{L^2\beta}{H^3\tau_0}\right)^{\frac{1}{2}}, \tag{4.76}$$

and so the relative humidity required for plumes is higher for MBLWTG than for MADBL.

In the case of a moisture source/sink, Q^t is given by the same scaling relationship as MWTG, because MBLWTG has the same scaling for the horizontal velocity U. The same is true for the minimum total water after the balance timescale is reached.

We now move onto testing the theory in a model. We will look at two sets of runs, one set with externally imposed initial heating only in the boundary layer of the model and one set of runs with continuous imposed heating.

4.4 Model Setup

The model setup for the moist tests is similar to the setup for the dry case. We use again the fully compressible 2D semi-Lagrangian, semi-implicit model of Thuburn (2017), this time including moisture. We specifically choose to use a similar setup to the dry experiments in chapter 3 to allow comparisons to be drawn and to allow us to better understand interactions between moisture, drag and heating.

As such, we again take a domain of $5,000$ km $\times$ 10 km in the horizontal and the vertical respectively. And we again use a vertical resolution of $\Delta z \sim 150$ m, whilst the horizontal resolution will vary depending on the model setup. The drag is again linearly decreasing with height over the boundary layer:

$$\frac{1}{\tau} = \begin{cases} \frac{h_{bl}-z}{h_{bl}\times\tau_s} & z \leq h_{bl}, \\ 0 & z > h_{bl}. \end{cases} \tag{4.77}$$

Here $h_{bl} = 1000$ m is again the height of the boundary layer and τ_s is a drag timescale.

The heating rate is the same cosine-squared formulation in the boundary layer as in the dry case, which can be translated to a buoyancy forcing by equation (4.6) i.e.

$$H_*(x,z) = H_{max} \times 10^a \cos^2\left[\frac{(z-z_0)\pi}{h_{bl}}\right] \cos^2\left[\frac{(x-x_0)\pi}{0.25\times L_D}\right], \tag{4.78}$$

where x_0 is the centre of the x-domain and z_0 is half the boundary layer height ($z_0 = h_{bl}/2$), and $H_{max} = 3$ K/s. Thus H_* is roughly 3 K per day at the centre of the heating when $a = -5$. As we intend to run the model with multiple heating rates to check the validity of the scale analysis over multiple heating scales, a will again take values from the set $a = [-8, -7, -6, -5, -4, -3]$ such that the heating rate ranges between approximately $q \sim 10^{-8}$ K/s and $q \sim 10^{-3}$ K/s or in terms of the buoyancy forcing, between approximately $\beta \sim 10^{-9}$ m/s^3 and $\beta \sim 10^{-4}$ m/s^3 .

To the horizontally-centred heating, we add compensating cooling of the form:

$$S(z) = \frac{1}{L_D}\int_0^{L_D} H_*(x,z)dx, \tag{4.79}$$

where L_D is the size of the x-domain, to ensure that the horizontal mean heating is zero. The heating then takes the form:

$$Q = H_* - S \implies \beta = \frac{g}{\theta_0}(H_* - S). \tag{4.80}$$

The moist experiments in this chapter are split by runs which are externally heated at each timestep and runs which are only heated at the initial timestep to excite the circulation. Equation (4.78) applies for both the continuously heated case and the initially heated case, though in the initially heated case, the heating is applied only at the initial timestep.

4.4.1 Boundary Layer Moisture Profile

With the addition of moisture to the model, a few changes are required to the background stratification for the equivalent potential temperature and the buoyancy frequency. In the boundary layer we set the background profile for the equivalent potential temperature to take account of water in the boundary layer. In the free troposphere, relative humidity is used.

The boundary layer moisture content is set up to be stable, i.e. if the model is unheated, no vertically advected air should escape the boundary layer owing to the moisture alone. We use a boundary layer depth of $1,000$ m with an approximate boundary layer potential temperature of $\theta \approx 300$ K to match the dry case, however the addition of moisture does change the initial θ profile notably. In the boundary layer, for most runs, we set the dimensionless quantity of total specific humidity to 0.01 kg/kg or 10 g/kg, although for some experiments we set the total specific humidity as low as 0.003 kg/kg.

We also have an inversion layer of depth 100 m with a change in θ across the inversion of 1 K. Above this, the tropospheric water profile is set by the relative humidity and a change in θ in the vertical of -4 K/km with increasing height. For our runs, we use a starting relative humidity in the free troposphere of 1% i.e. very dry. Increases to the relative humidity percentage in the free troposphere did not seem to have a large impact on results. The model code for the boundary layer background moisture profile is modified from code provided by Fenntun Sternberg.

4.4.2 Moisture Sources and Sinks

In the current set of experiments, we do not outline any imposed moisture sources or sinks. Precipitation as a moisture sink will be set by the internal flow characteristics of the model alone as we do not impose any set precipitation level. Currently, the model has pseudo-precipitation in the dynamics where water is removed from the model when it condenses.

However, there is also the problem of a potential numerical moisture source in the boundary layer. Due to using a semi-Lagrangian scheme, the water in the lowest model level cannot be advected vertically and so stays in the bottom layer of the model regardless of the moisture profile in the rest of the boundary layer. Thus, even when moisture is vertically advected out of the boundary layer, the boundary

layer will never fully dry out because the lowest level will continue to have the same total specific water as it had at the start of the model run. Similarly, if the bottom layer were to have zero total specific water, the boundary layer would dry out faster than it might otherwise, because the model boundary layer would be forced towards being dry.

To check how significant the effect of the numerical moisture source is in the boundary layer, we tracked the change in total water over time in the model, and found the change in water was small, but to counteract any effects, we applied a water fixer across the whole domain of the model to check how much of an effect the moisture source would have. The water fixer takes the form:

$$(q^t)^{n+1} = \frac{q_m^{n-1}}{q_m^n} * (q^t)^n \tag{4.81}$$

such that we calculate the percentage change in water mass q_m across the whole domain for a given timestep and counteract any numerically-forced change in total water at the beginning of the next timestep by multiplying the model water by a uniform factor across the domain. The water mass q_m is the global integral of water in the model such that:

$$q_m = \int_D q^t dxdz. \tag{4.82}$$

The formulation in equation (4.81) is reasonable with the drawback being that it is a global fixer and therefore the total water in each grid cell is multiplied by the same factor at each timestep which does not completely counteract the effect of the numerical moisture source in the lowest level of the model, but should mitigate spurious continuous increases in total water in the model. When applied to the model, we find no significant differences in regime obtained or behaviour observed over the timescale of the model runs we looked at. Therefore, we conclude that the numerical moisture source does not substantially impact the results. We do not include any other externally imposed moisture source/sink effects in our experiments in this chapter, though we do attempt to quantify the effect of the exchange of moisture between the boundary layer and the free troposphere which is part of the transient moisture response and which should account for most drying in the boundary layer in model runs before balance is reached. The exchange of moisture between the boundary layer and the free troposphere does not form part of M_s, but

instead is accounted for by the flux terms $F$and S from the water flux equation (4.20).

Table 4.1 lists the scales of the imposed variables at the initial model timestep.

Imposed Variable	ρ_0	**H**	θ_0	**g**	π_0	$\mathbf{c_p}$
Scale	1	10^3	10^2	10	1	10^4
Units	$\mathrm{kg/m^3}$	m	K	$\mathrm{m/s^2}$	–	$\mathrm{kg{\cdot}m^2{\cdot}s^{-2}{\cdot}K^{-1}}$

Table 4.1: Table of imposed variables and their scales in the 2D moist model setup.

4.5 Results

We will look at three different sets of results relating to the moist regimes outlined in section 4.3. Firstly, we consider a comparison between the two new moist regimes which we expect to obtain in the absence of a continuously heated boundary layer. We will then look at whether the moist versions of the dry boundary layer balances can be achieved when water is included in the model and how behaviours in the moist case differ from the behaviours we observed in the dry case. And finally, we will consider some of the constraints on triggering, sustaining and organisation of moist plumes observed in the model from the effect of drag strength to the effect of moist long-term boundary layer balance regimes.

4.5.1 New Moist Regimes

We look first at the initially externally heated boundary layer experiments. For this, we will compare the behaviour of the model for four drag values – the same four we used in the dry experiments e.g. $\tau_0 \sim 10^3$ s, $\tau_0 \sim 10^4$ s, $\tau_0 \sim 10^5$ s, $\tau_0 \sim \infty$ (or no drag). The specifications for all the runs we look at in the initial externally heated runs are in table 4.2.

Test Run	τ_0	Δx	q^t (BL)	r_h (FT)
ini qtbl01tr1 Δx104 drag720	10^3	10^4	0.01	1%
ini qtbl01tr1 Δx104 drag7200	10^4	10^4	0.01	1%
ini qtbl01tr1 Δx104 drag72000	10^5	10^4	0.01	1%
ini qtbl01tr1 Δx104 nodrag	∞	10^4	0.01	1%
ini qtbl005tr1 Δx104 drag720	10^3	10^4	0.005	1%
ini qtbl005tr1 Δx104 drag7200	10^4	10^4	0.005	1%
ini qtbl005tr1 Δx104 drag72000	10^5	10^4	0.005	1%
ini qtbl005tr1 Δx104 nodrag	∞	10^4	0.005	1%
ini qtbl003tr1 Δx104 drag720	10^3	10^4	0.003	1%
ini qtbl003tr1 Δx104 nodrag	∞	10^4	0.003	1%
Units	s	m	kg/kg	-

Table 4.2: Table of prescribed scales for drag, horizontal gridlength, boundary layer specific water and free troposphere relative humidity terms in the 2D moist model setup with initial heating only.

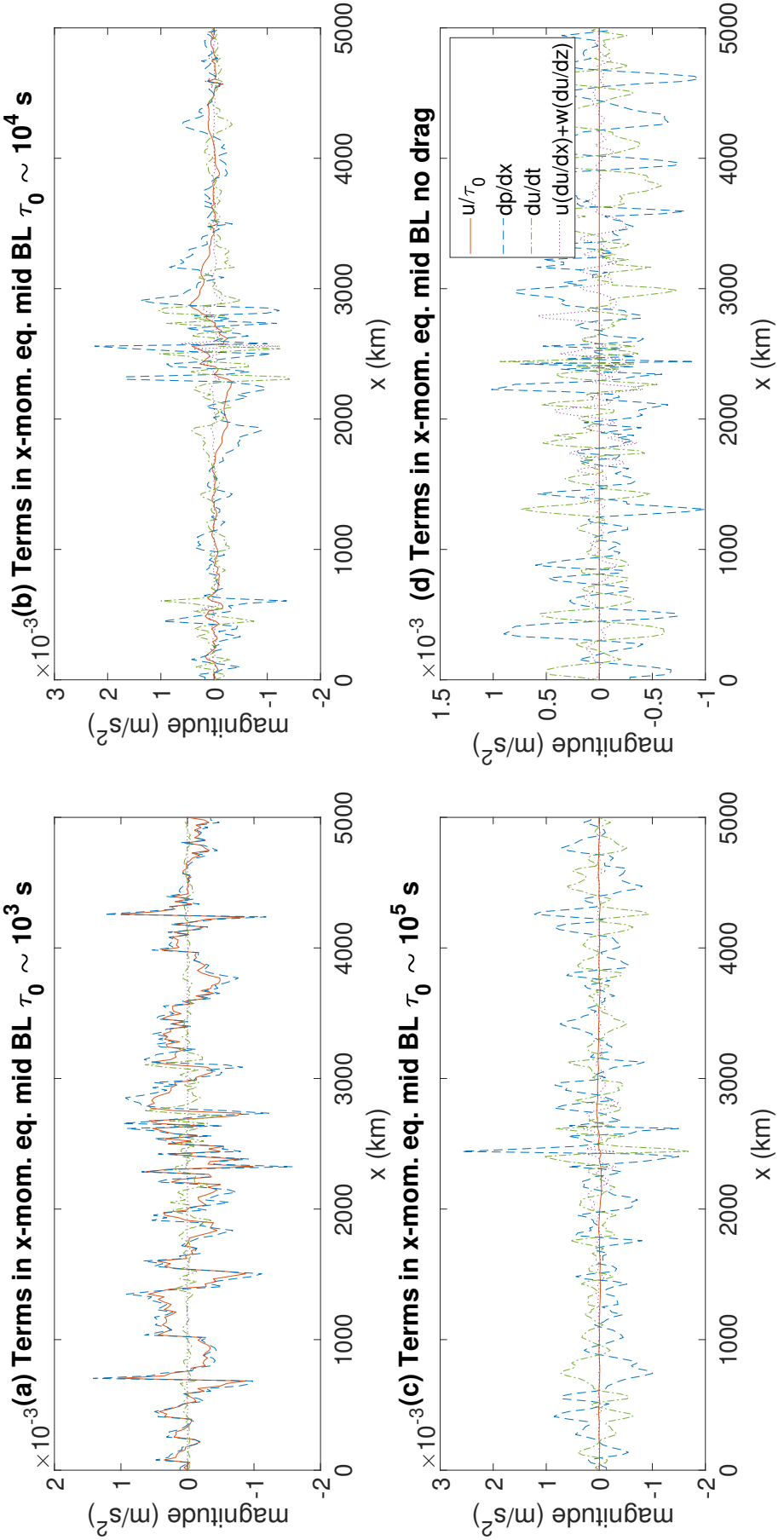

Figure 4.2: Magnitude of terms in the horizontal velocity equation taken from a horizontal slice in the middle of the boundary layer after approximately 7 days with $\Delta x \sim 10^4$ m. Terms shown include the drag term $-u/\tau_0$ (red), the horizontal pressure gradient term dp/dx (blue), the time derivative term $\partial u/\partial t$ (green), and the advection terms $u\frac{\partial u}{\partial x} + w\frac{\partial w}{\partial z}$ (purple).

In this section, we aim to test whether or not the MUFT and MUBL regimes are achievable in our model runs and then whether any aspects of model behaviour can be explained by the theory. Neither MUFT nor MUBL were achievable in the dry case due to absence of latent heating, but are potential long-term balance regimes in the moist case. We start therefore by looking for evidence of balance in our initial external heating only runs. Figure 4.2 shows the horizontal velocity equation terms in the model at 7 days. Due to the presence of N_m^2 in the requirement for balance timescales for MUFT and MUBL, it is difficult to determine a specific timescale for balance in advance.

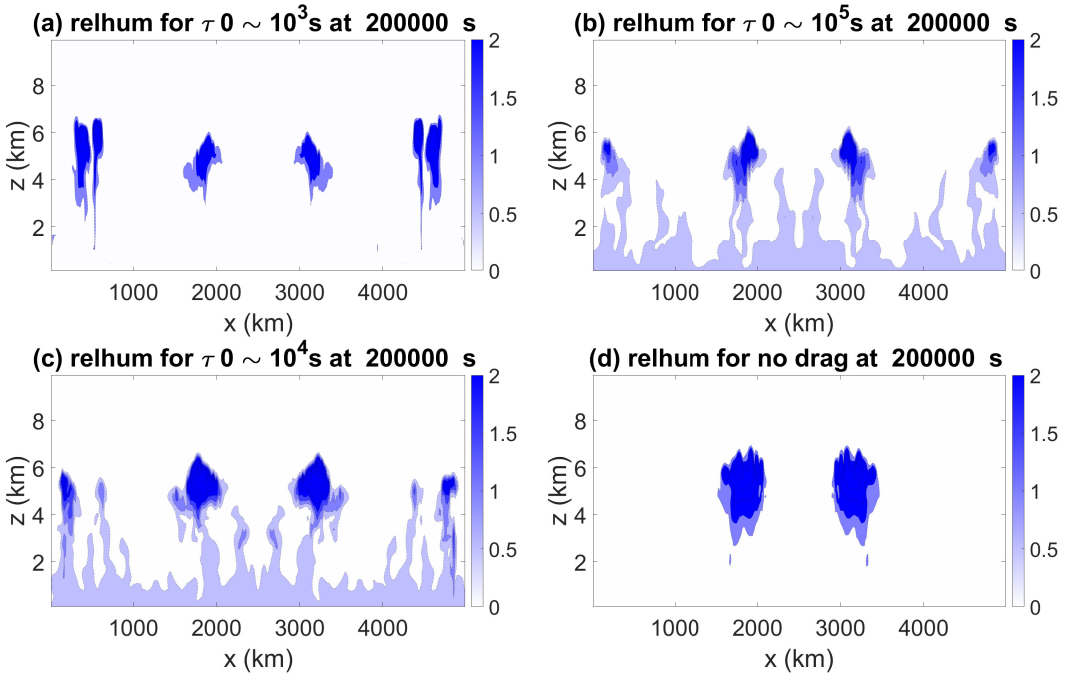

Figure 4.3: Relative humidity x-z cross sections at $t = 200,000$ s for (a) $\tau_0 \sim 10^3$ s, (c) $\tau_0 \sim 10^4$ s, (b) $\tau_0 \sim 10^5$ s and (d) no drag with initial specific humidity in the boundary layer 0.01 kg/kg and horizontal grid length $\Delta x \sim 10^4$ m. Initial heating only.

However, from the theory we expect the no drag case to reach balance before the drag cases for the same relative humidity – with increases in the drag corresponding to longer required timescales for balance. In figure 4.2, we see that the highest drag run ($\tau_0 \sim 10^3$ s) appears to be balanced whilst every other run has a dominant time derivative term in the horizontal velocity equation. Specifically, if we assume $L \sim \Delta x$, then the $\tau_0 \sim 10^3$ s run is the only case that satisfies Darcy's balance and therefore MUBL. In the other runs, the fact that the time derivative term and the

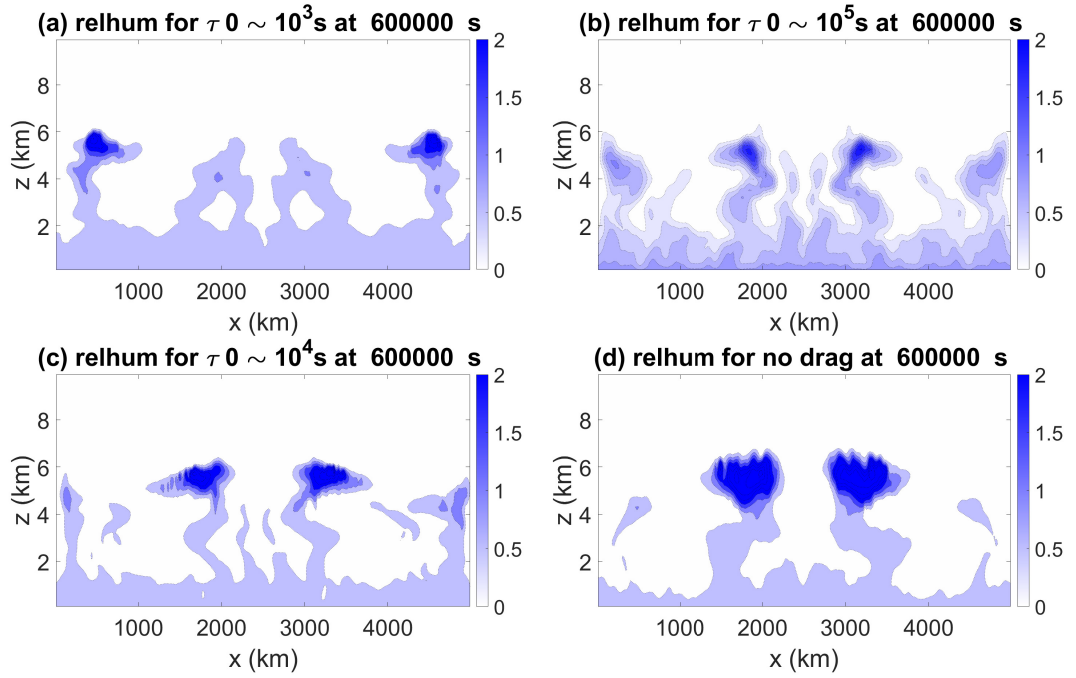

Figure 4.4: Relative humidity x-z cross sections at $t = 600,000$ s for (a) $\tau_0 \sim 10^3$ s, (c) $\tau_0 \sim 10^4$ s, (b) $\tau_0 \sim 10^5$ s and (d) no drag with initial specific humidity in the boundary layer 0.01 kg/kg and horizontal grid length $\Delta x \sim 10^4$ m. Initial heating only.

pressure gradient term are both of leading order suggests gravity waves are present and therefore there is no evidence that MUBL or MUFT or any kind of long-term balance is present or achievable in the other runs even though the theory suggests MUFT should be achievable at lower timescales than MUBL for the same relative humidity.

Further evidence for differences in model circulations between the highest drag run ($\tau_0 \sim 10^3$ s) and the other runs can be seen in figure 4.8 which shows x-z cross-sections of the horizontal velocities for each of the runs in the boundary layer at ~7 days. The $\tau_0 \sim 10^3$ s run has very little horizontal circulation in the boundary layer compared to the other runs with the $\tau_0 \sim 10^3$ s having a circulation which is concentrated at the top of the boundary layer where the drag is weakest.

In the initially heated only experiments, we find that the plumes seem much more concentrated in the horizontal in the no drag case with two larger plumes emerging by ~7 days in the free troposphere. When drag is included, the plumes occur at multiple locations in the boundary layer (figure 4.4). The difference in the layout is even more evident at ~3 days where the drag runs have substantially more

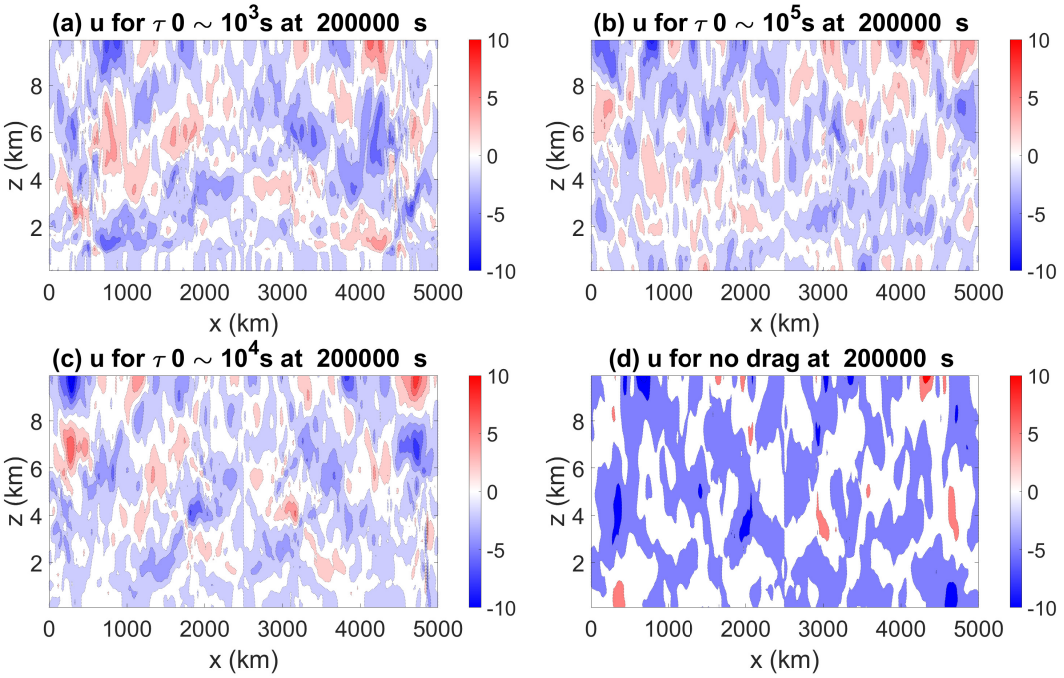

Figure 4.5: Horizontal velocity (u) x-z cross sections at $t = 200,000$ s for drag strengths (a) $\tau_0 \sim 10^3$ s, (c) $\tau_0 \sim 10^4$ s, (b) $\tau_0 \sim 10^5$ s and (d) no drag with initial specific humidity in the boundary layer 0.01 kg/kg and horizontal grid length $\Delta x \sim 10^4$ m. Initial heating only.

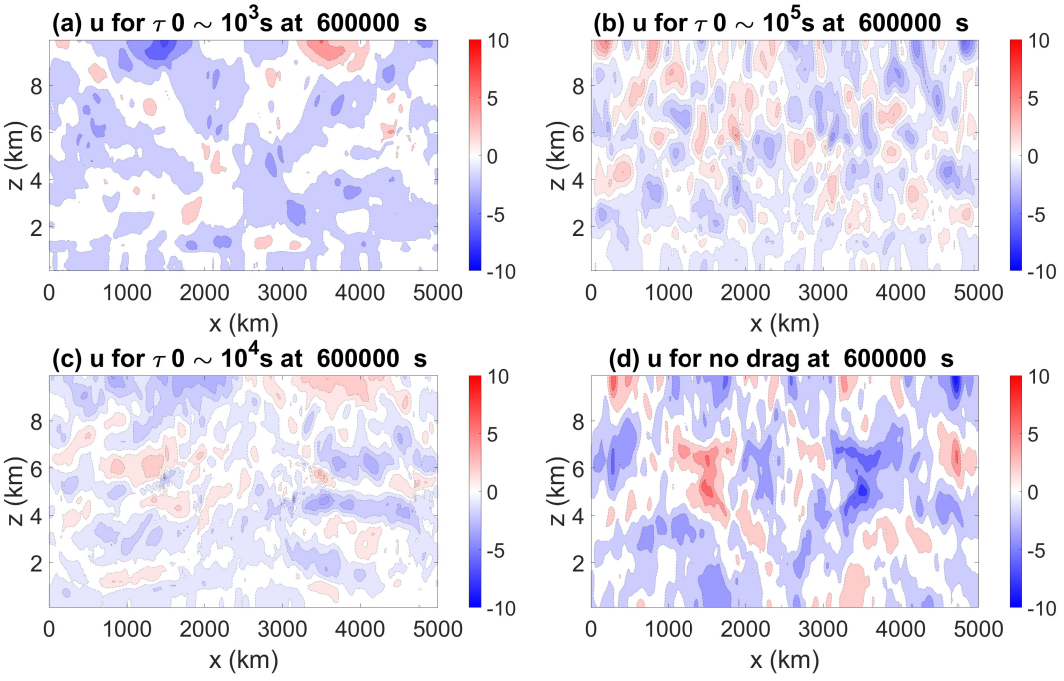

Figure 4.6: Horizontal velocity (u) x-z cross sections at $t = 600,000$ s for drag strengths (a) $\tau_0 \sim 10^3$ s, (c) $\tau_0 \sim 10^4$ s, (b) $\tau_0 \sim 10^5$ s and (d) no drag with initial specific humidity in the boundary layer 0.01 kg/kg and horizontal grid length $\Delta x \sim 10^4$ m. Initial heating only.

plumes triggered in the horizontal (figure 4.3). It has also been shown in large-eddy simulations that when surface drag is increased, convective rolls dominate over convective cells i.e. plumes are more spread out and numerous and may be shallower instead of forming fewer larger, deep cells (Park et al., 2018). We can explain this behaviour by considering interactions between relative humidity and drag in the boundary layer of the model.

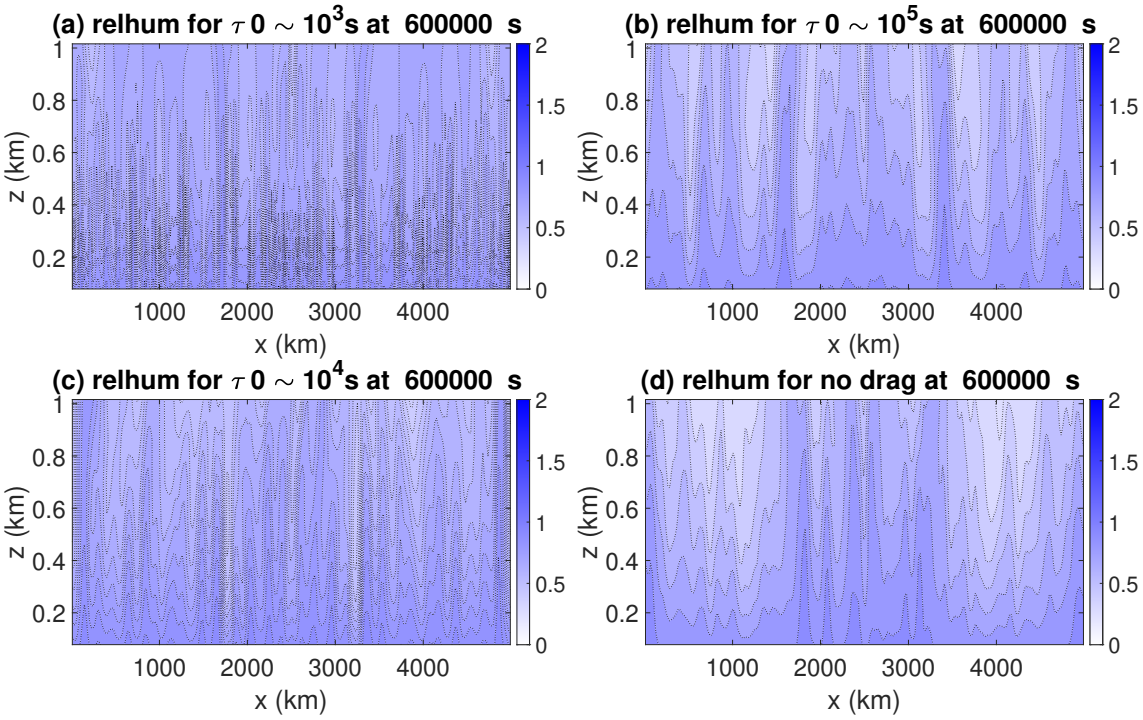

Figure 4.7: Relative humidity x-z cross sections at $t = 600,000$ s in the boundary layer only for drag strengths (a) $\tau_0 \sim 10^3$ s, (c) $\tau_0 \sim 10^4$ s, (b) $\tau_0 \sim 10^5$ s and (d) no drag with initial specific humidity in the boundary layer 0.01 kg/kg and horizontal grid length $\Delta x \sim 10^4$ m. Initial heating only.

A relative humidity of 100% is required for saturation and therefore for plumes to trigger, however this can occur in multiple ways. If the air in the boundary layer is not already saturated, then local external heating in the boundary layer will of course lead to air being lifted to a height where the surrounding air is cooler and therefore increase the relative humidity at its new height. Provided the air at the new height has a sufficiently high relative humidity for the lifting to cause the relative humidity to exceed 100%, a plume will be triggered. Similarly, drag in the boundary layer can also cause lifting since drag promotes horizontal convergence. Though unlike the heating, the drag also confines the horizontal velocity more effectively so plumes are more numerous in the horizontal when they are triggered as heat will

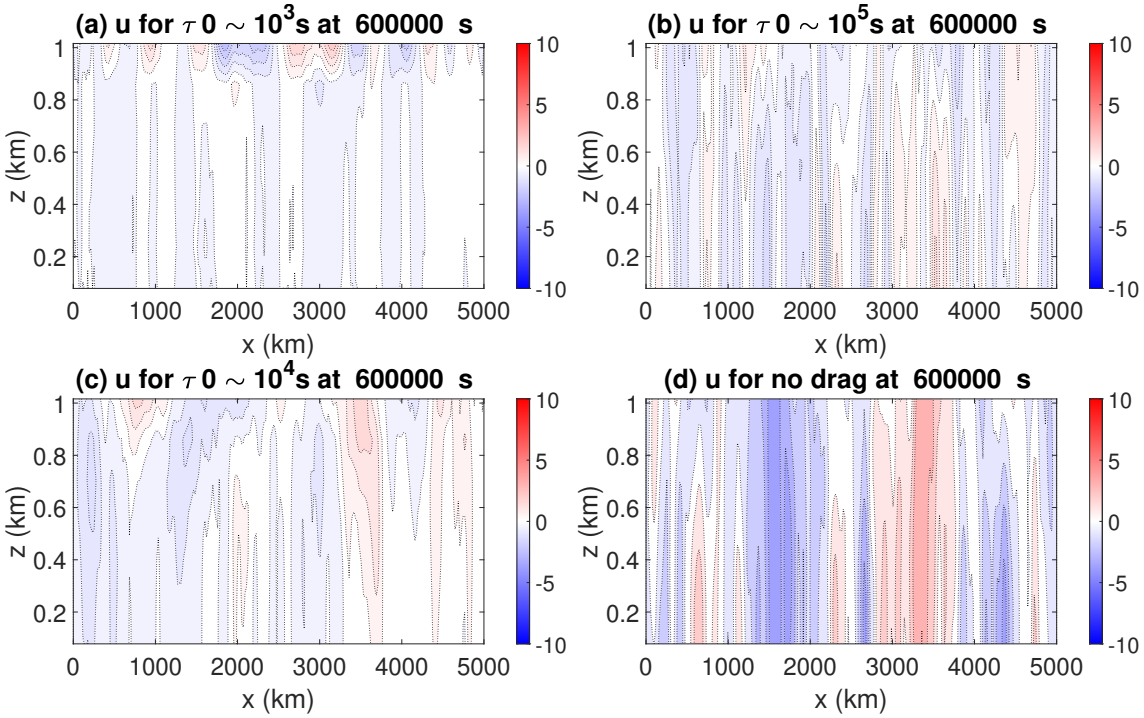

Figure 4.8: Horizontal velocity (u) x-z cross sections at $t = 600,000$ s in the boundary layer only for drag strengths (a) $\tau_0 \sim 10^3$ s, (c) $\tau_0 \sim 10^4$ s, (b) $\tau_0 \sim 10^5$ s and (d) no drag with initial specific humidity in the boundary layer 0.01 kg/kg and horizontal grid length $\Delta x \sim 10^4$ m. Initial heating only.

not be effectively discharged by horizontal velocity in the boundary layer. Weaker horizontal velocities for each increase in magnitude of the drag strength in the boundary layer can be seen in figure 4.8.

The importance of the effect of drag strength on horizontal convergence and therefore lifting and plume triggering is particularly pronounced at lower values of relative humidity in the boundary layer. For example, if we run the model with half the relative humidity in the boundary layer compared to previous runs (0.005 kg/kg), moist plumes only develop above the heating for the high drag case. In other words drag strength plays an important part in the horizontal layout of plumes and as the relative humidity in the boundary layer decreases, the drag becomes increasingly responsible for whether or not plumes are triggered at all. When relative humidity in the boundary layer is high enough, no externally imposed heating is necessary to trigger plumes and the role of drag in triggering plumes is less important.

Returning to the question we posed at the start of this chapter, it is clear that in the case of an initially externally heated boundary layer, moisture, heating and drag interactions are most significant when the relative humidity is low enough that

horizontal convergence has a significant effect on plume triggering.

4.5.2 Moist Dry Comparison

Existence or Non-Existence of Long-term Moist Balance Regimes

In section 4.3, we outlined the moist versions of the long-term dry balance regimes from chapter 3. Here we examine their validity and whether we can obtain long-term balance regimes in the model boundary layer for the moist case, or whether balance is infeasible. Note that balance in the boundary layer does not require balance in the free troposphere and indeed the free tropospheric behaviour of model runs may look very similar even though the boundary layer behaviour is different.

We will also look at the effect of the drag strength and model resolution on model results. The model runs considered in this section are listed in table 4.3 and include varying drag timscales, varying heating rates, and varying horizontal resolutions.

Test Run	τ_0	Δx	q	$\mathbf{q^t}$ (BL)	$\mathbf{r_h}$ (FT)
qtbl01tr1 Δx104 drag720	10^3	10^4	10^{-8} to 10^{-3}	10	1%
qtbl01tr1 Δx104 drag7200	10^4	10^4	10^{-8} to 10^{-3}	10	1%
qtbl01tr1 Δx104 drag72000	10^5	10^4	10^{-8} to 10^{-3}	10	1%
qtbl01tr1 Δx104 nodrag	∞	10^4	10^{-8} to 10^{-3}	10	1%
qtbl01tr1 Δx105 drag720	10^3	10^5	10^{-8} to 10^{-3}	10	1%
qtbl01tr1 Δx105 drag7200	10^4	10^5	10^{-8} to 10^{-3}	10	1%
qtbl01tr1 Δx105 drag72000	10^5	10^5	10^{-8} to 10^{-3}	10	1%
qtbl01tr1 Δx103 nodrag	∞	10^3	10^{-8} to 10^{-3}	10	1%
Units	s	m	K/s	m^{-3}	-

Table 4.3: Table of prescribed scales for drag, heating rate, horizontal gridlength, boundary layer specific water and free troposphere relative humidity terms in the 2D moist model setup with continuous heating.

Scaling Laws

We begin by looking at whether any of the moist variants of the dry balance regimes are achievable in the model. Our first test of the existence or validity of the moist variants of the dry balance regimes is to plot log-log plots of the scaling relationships between heating rate and horizontal velocity U, vertical velocity W, potential

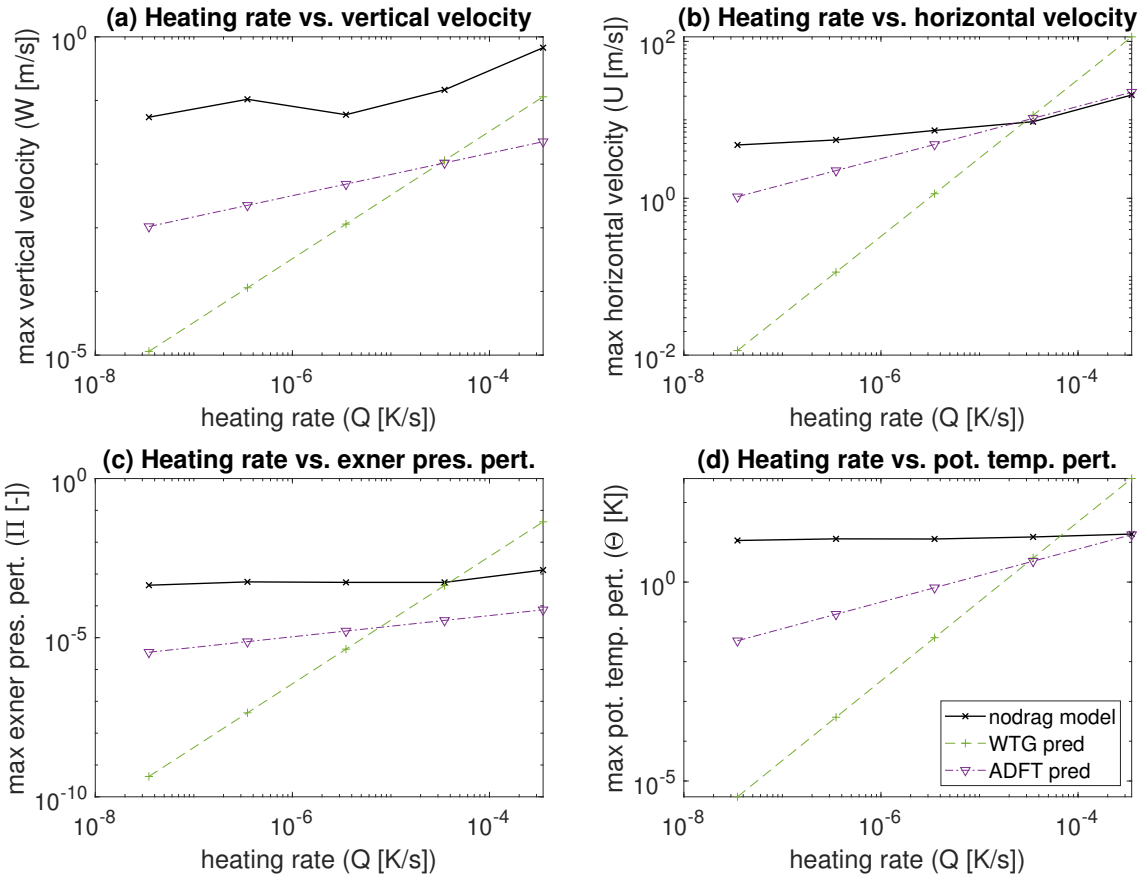

Figure 4.9: Log-log plots of the relationship between output variables and heating rate extracted from scaling relationships in Section 4.3. Results from model runs with the 'qtbl01tr1 Δx104 nodrag' setup are in black. Regime predictions based on the theory are also given for the WTG regime (green) and the ADFT regime (purple). Model variables are taken at approximately 7 days.

temperature perturbation Θ, potential Exner pressure perturbation Π for a number of runs where the buoyancy forcing is of a similar magnitude to the potential temperature forcings in chapter 3, i.e.

$$\beta \sim [10^{-9}, 10^{-8}, 10^{-7}, 10^{-6}, 10^{-5}] \implies Q \sim [10^{-8}, 10^{-7}, 10^{-6}, 10^{-5}, 10^{-4}] \quad (4.83)$$

We consider differing values of the drag timescale τ_0. In figure 4.9, we have $\tau_0 \sim \infty$ or no drag. In figure 4.10, $\tau_0 \sim 10^3$ s. In figure 4.11, we have $\tau_0 \sim 10^4$ s. And in figure 4.12, we have $\tau_0 \sim 10^5$ s. We plot each of U, W, Θ and Π again for comparison to the dry case.

The log-log plots in figure 4.9 appear to suggest most of the no drag model runs fall into the MADFT regime in the lowest kilometre of the model with no evidence of gradients in the variable trendlines across heating rates matching a WTG regime.

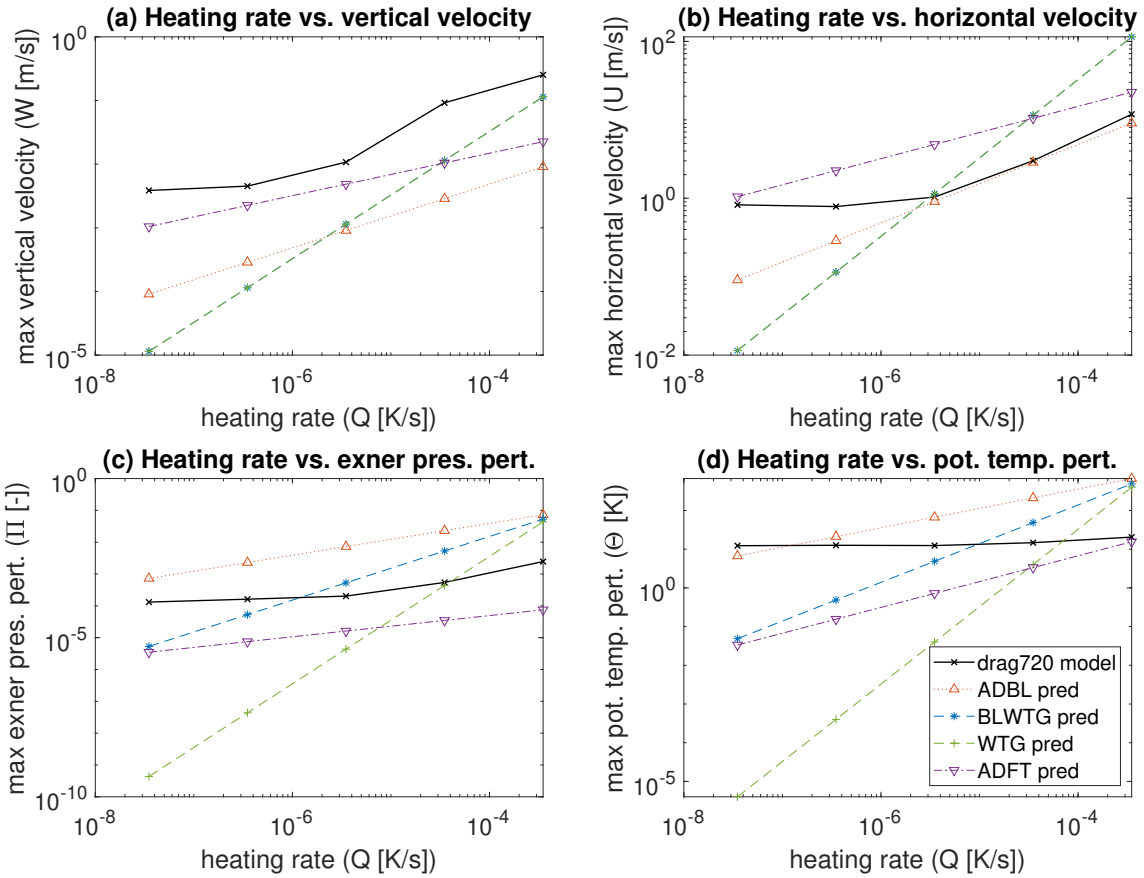

Figure 4.10: Log-log plots of the relationship between output variables and heating rate extracted from scaling relationships in Section 4.3. Results from model runs with the 'qtbl01tr1 Δx104 drag720' setup are in black. Regime predictions based on the theory are also given for the ADBL regime (red), the BLWTG regime (blue), the WTG regime (green) and the ADFT regime (purple). Model variables are taken at approximately 7 days.

For figures 4.10, 4.11, 4.12, the results are less conclusive with ADFT and ADBL both appearing to be possibilities at different heating values. There is very little evidence of the BLWTG regime in all the drag-included runs – even at lower heating rates where the regime was so prominent in the dry case. However gradients for W and U show very inconsistent behaviour from one heating rate to another which makes it hard to draw any serious conclusions from the log-log plots. This is quite different to the dry case where there were clear transition points.

X-momentum Balance Check

Since the results of the loglog plots are too inconsistent to draw any conclusions about balance over a range of heating rates, we take a closer look at some of the runs

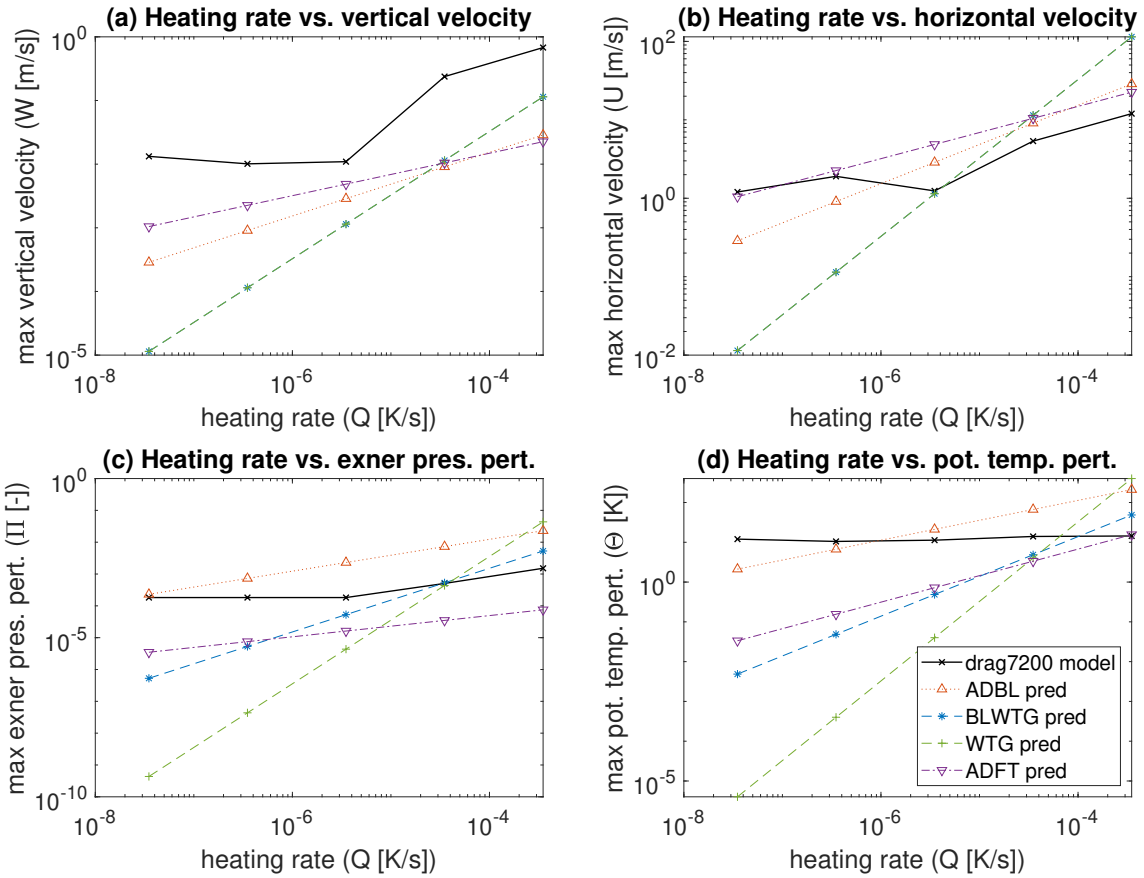

Figure 4.11: Log-log plots of the relationship between output variables and heating rate extracted from scaling relationships in Section 4.3. Results from model runs with the 'qtbl01tr1 Δx104 drag7200' setup are in black. Regime predictions based on the theory are also given for the ADBL regime (red), the BLWTG regime (blue), the WTG regime (green) and the ADFT regime (purple). Model variables are taken at approximately 7 days.

to ascertain if they are actually balanced. In particular, we look at the horizontal velocity equation in the boundary layer as we did with the initial externally imposed heating only runs.

Figure 4.13, subplot (b) shows the terms in the horizontal velocity equation for $\tau_0 \sim 10^3$ s, and for $\Delta x \sim 10^4$ m and $Q \sim 10^{-5}$ K/s ($\beta \sim 10^{-6}$ m/s^3). Here, we can clearly see the boundary layer is in Darcy's balance since the pressure gradient balances the drag and both terms are larger than the remaining horizontal velocity terms. Though not shown here, this is the case for all the $\tau_0 \sim 10^3$ s runs in figure 4.10 with $\Delta x \sim 10^4$ m.

If we look at the weaker drag values, we find that none of the other runs are in Darcy's balance. Figure 4.14 shows the $\tau_0 \sim 10^4$ s and $\tau_0 \sim 10^5$ s runs in subplots

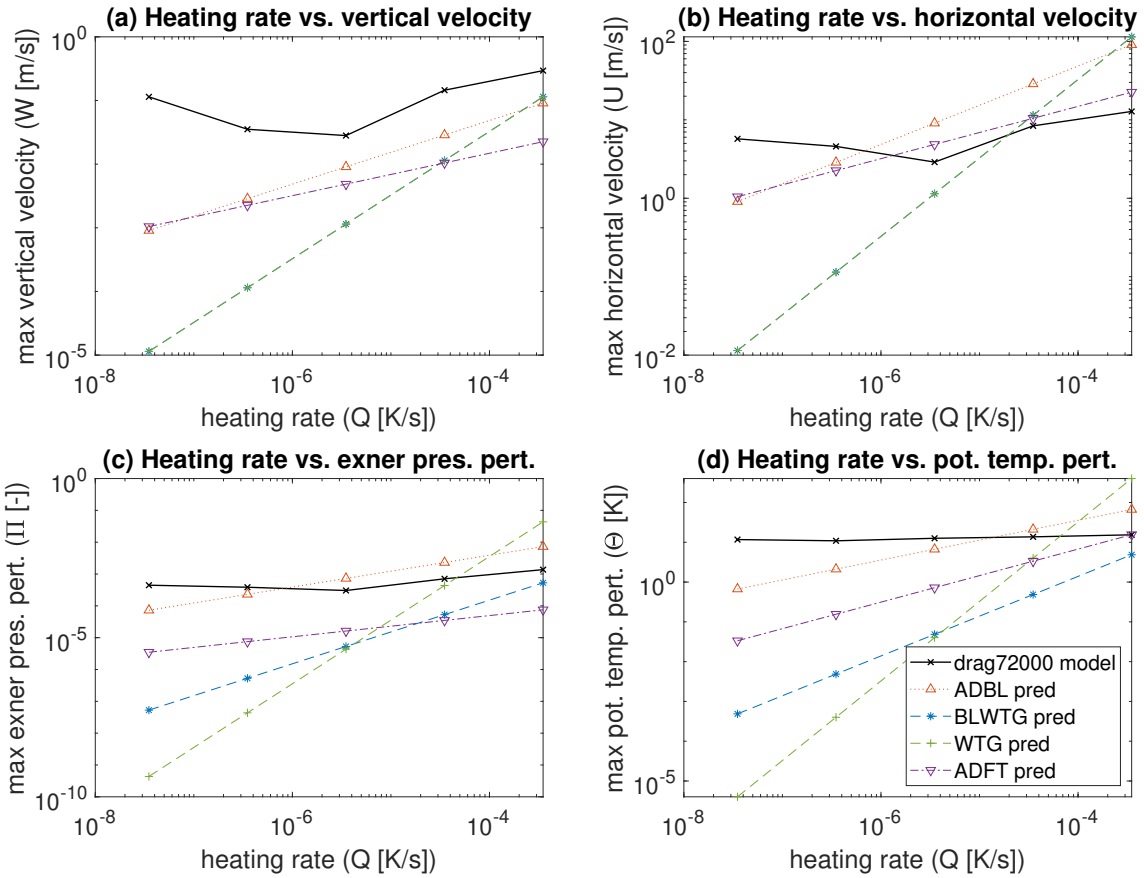

Figure 4.12: Log-log plots of the relationship between output variables and heating rate extracted from scaling relationships in Section 4.3. Results from model runs with the 'qtbl01tr1 Δx104 drag72000' setup are in black. Regime predictions based on the theory are also given for the ADBL regime (red), the BLWTG regime (blue), the WTG regime (green) and the ADFT regime (purple). Model variables are taken at approximately 7 days.

(a) and (b) respectively with $\Delta x \sim 10^4$ m and $Q \sim 10^{-5}$ K/s. We can see that the drag term u/τ is larger comparatively in the $\tau_0 \sim 10^4$ s run compared to the $\tau_0 \sim 10^5$ s run, but not enough to be a dominant balance term in either case. Indeed, the magnitude of the time derivative term suggests the runs are not balanced at all and the fact that the pressure gradient term is also of leading order suggests gravity waves are again present.

Sukhatme et al. (2012) similarly found that even though their theoretical analysis of the 2D stably stratified Boussinesq equations in the absence of drag suggested a slow mode consistent with a balance state, the numerical simulations only oscillated around the balance state whilst remaining turbulent. The Sukhatme et al. (2012) case corresponds most closely to the weaker drag and no drag cases here.

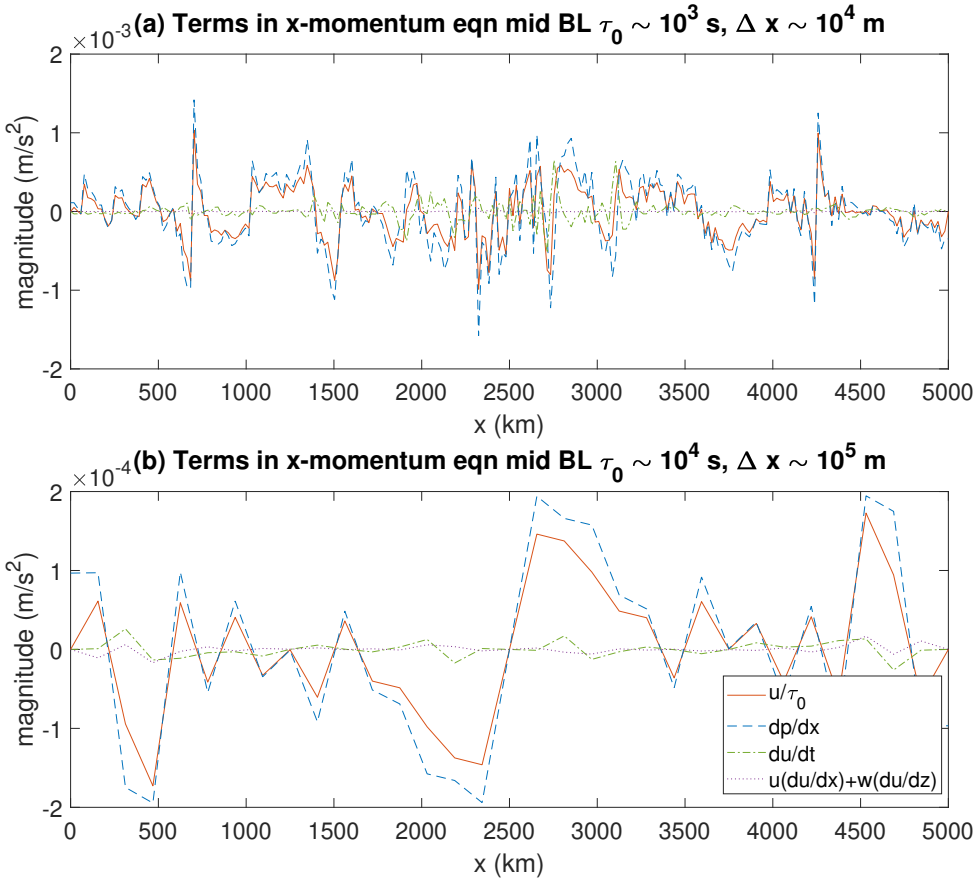

Figure 4.13: Magnitude of terms in the horizontal velocity equation taken from a horizontal slice in the middle of the boundary layer after ∼7 days with heating rate $Q \sim 10^{-5}$ K/s and with (a) $\tau_0 \sim 10^3$ s, $\Delta x \sim 10^4$ m, and then (b) $\tau_0 \sim 10^4$ s, $\Delta x \sim 10^5$ m. Terms shown include the drag term $-u/\tau_0$ (red), the horizontal pressure gradient term dp/dx (blue), the time derivative term $\partial u/\partial t$ (green), and the advection terms $u\frac{\partial u}{\partial x} + w\frac{\partial w}{\partial z}$ (purple).

In our experiment, $\tau_0 \sim 10^4$ s is a particularly interesting case here since we can see the drag term is on the same scale as the dominant time derivative and pressure terms at points in the domain. With this in mind, it is possible that the regime would satisfy the MADBL regime scalings without being fully balanced. This might explain some of the inconsistency in the log-log plots.

We should note here that our results do not hold across gridlength changes. In fact, if we run the model with $\Delta x \sim 10^5$ m, we find that the $\tau_0 \sim 10^4$ s runs as well as the $\tau_0 \sim 10^3$ s runs appear to be in Darcy's balance as in figure 4.13, subplot (b).

This is likely because for Darcy's balance to achieved, we must have $\frac{L}{U\tau_0} > O(1) \implies \tau_0 < L/U$. In other words, if the drag timescale is too large as is the

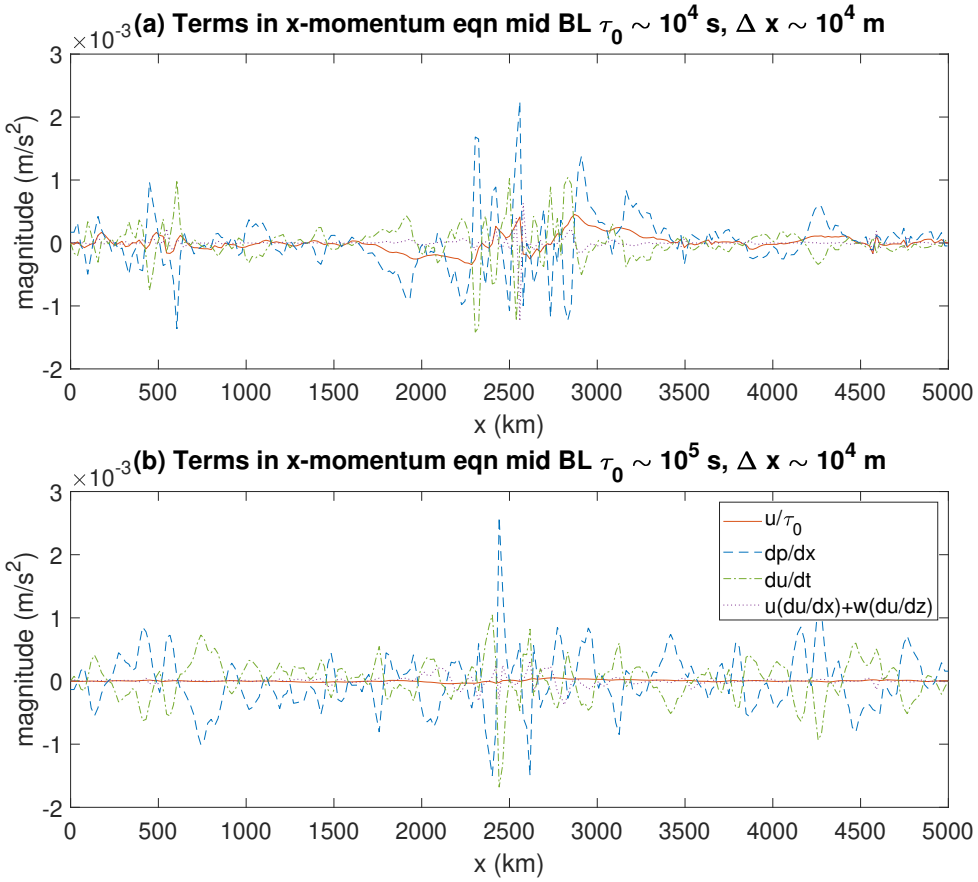

Figure 4.14: Magnitude of terms in the horizontal velocity equation taken from a horizontal slice in the middle of the boundary layer after ∼7 days with heating rate $Q \sim 10^{-5}$ K/s and $\Delta x \sim 10^4$ m and with drag strength (a) $\tau_0 \sim 10^4$ s and (b) $\tau_0 \sim 10^5$ s. Terms shown include the drag term $-u/\tau_0$ (red), the horizontal pressure gradient term dp/dx (blue), the time derivative term $\partial u/\partial t$ (green), and the advection terms $u\frac{\partial u}{\partial x} + w\frac{\partial w}{\partial z}$ (purple).

case with the weaker drag cases, the drag may not be able to act sufficiently on the horizontal velocity in the moist case due to flow horizontal lengthscales shrinking to the grid scale (figure 4.15). Although we saw similar shrinking of the lengthscale in the dry case, balance was still achieved in most cases. In the moist case, it seems Darcy's balance and subsequently MADBL cannot be achieved unless $\tau_0 < \Delta x/U$.

This also suggests the drag is not causing the collapse of the horizontal lengthscale to the gridlength in the moist case, whereas it did seem to be the cause (or a substantially contributing factor) in the dry case where an increase in drag for the same heating rate could cause a shrinking of lengthscale in model boundary layer circulations. For the moist case, the most significant effect of increasing the drag

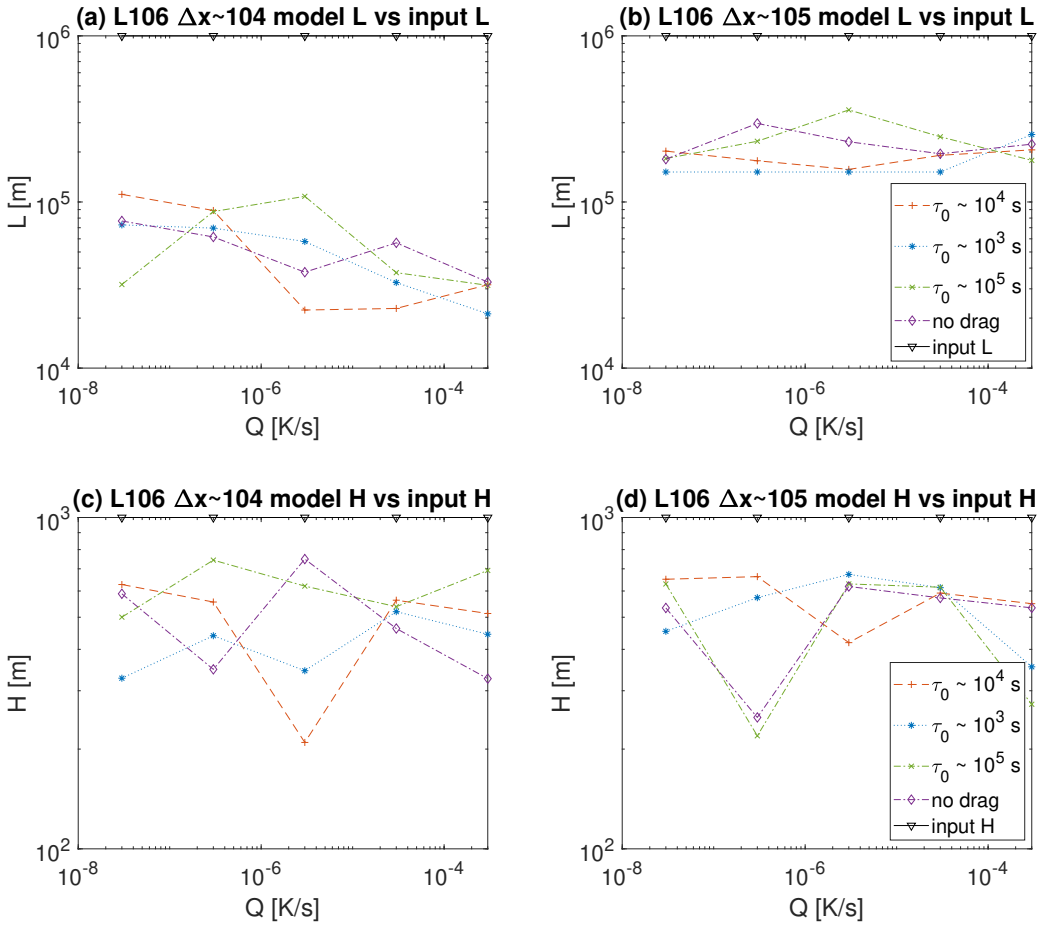

Figure 4.15: Horizontal and vertical lengthscales in the boundary layer for horizontal grid size $\Delta x \sim 10^4$ m and $\Delta x \sim 10^5$ m after approximately 7 days with initial boundary layer specific water 0.01 kg/kg and heating rate $Q \sim 10^{-5}$ K/s. Input horizontal and vertical domain lengthscales (black) are compared to lengthscales returned by the flow for $\tau_0 \sim 10^3$ s (blue), $\tau_0 \sim 10^4$ s (red), $\tau_0 \sim 10^5$ s (green) and no drag (purple).

seems to be that it allows balance to form in the boundary layer.

4.5.3 Triggering, Sustaining and Organisation of Convective Plumes

Having established that long-term balance regimes in the boundary layer in the moist case are possible in some cases, we now turn to discussing how drag strength and boundary layer regime affect model behaviour when it comes to the triggering, sustaining and organisation of moist convective plumes in the continuously heated moist case.

Effect of Drag Strength and Boundary Layer Regime on Triggering of moist plumes

We consider first the triggering of moist convective plumes. Or in other words, how long the model takes to develop plumes and how strong those plumes are.

To analyse when plumes are triggered, we use a mass flux and a relative humidity time series with values taken at the first model level above the boundary layer. The mass flux is calculated by

$$M_w = \int_{D_x} w_{bl+1} dx. \tag{4.84}$$

where M_w is the mass flux and $bl + 1$ represents the first vertical layer above the boundary layer. We only consider positive values of w_{bl} where $w_{bl} > 0$. In the model, the massflux in equation (4.84) is calculated as a sum:

$$M_w = \frac{1}{n_x} \sum_{i=1}^{n_x} w(i)_{bl+1} \tag{4.85}$$

where n_x is the total number of model points in the horizontal domain.

By considering when there are spikes in the mass flux time series and also when the relative humidity exceeds 100% (i.e. when the air is saturated), we can ascertain when plumes are triggered.

Again, we look at cases with no drag and cases with drag timescales $\tau_0 \sim 10^3$ s, $\tau \sim 10^4$ s, and $\tau_0 \sim 10^5$ s to understand if changing the drag strength affects the triggering of plumes and if the boundary layer regimes identified in the dry case still dominate the model behaviour in the presence of moisture. We choose an example here using $\beta \sim 10^{-6}$ m/s^3 or equivalent to $Q \sim 10^{-5}$ K/s as this corresponds most closely to real-world Earth heating rates.

In figure 4.16, we see that there isn't much difference initially between the no drag and the $\tau_0 \sim 10^5$ s case in the moist runs. $\tau_0 \sim 10^5$ s has slightly weaker mass flux, but it is a fairly small difference. In the $\tau_0 \sim 10^4$ s case, the maximum vertical velocity in the boundary layer is somewhat weaker at the first peak and the plume triggering seems to occur at a later time, albeit not much later. This is the case for both the first and second peak. The very minor effects of increases in drag for the no drag, $\tau_0 \sim 10^5$ s and $\tau_0 \sim 10^4$ s cases mirror results in Lindzen and Nigam (1987) where they find little difference between moist model results when drag is increased

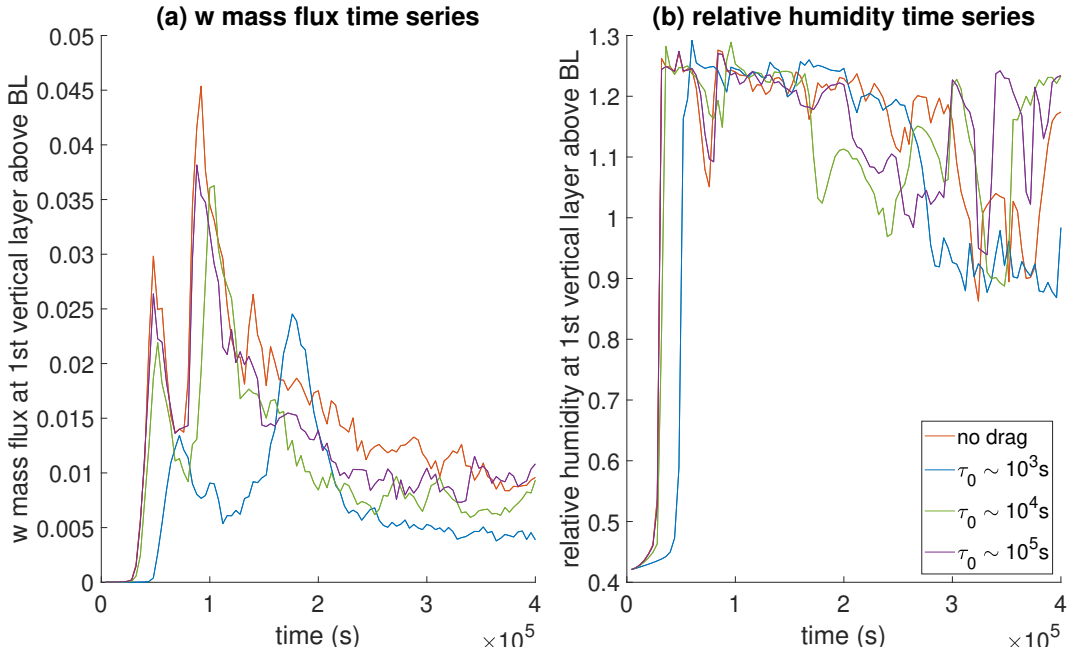

Figure 4.16: Comparison by drag strength of time series for (a) mass flux and (b) relative humidity at the first layer above the boundary layer. All runs have initial specific humidity in the boundary layer 0.01 kg/kg, grid length $\Delta x \sim 10^4$ m and continuous heating $Q \sim 10^{-5}$ K/s. Drag strengths shown are $\tau_0 \sim 10^3$ s (blue), $\tau_0 \sim 10^4$ s (green), $\tau_0 \sim 10^5$ s (purple), and no drag (red).

up to a certain threshold, after which drag does affect the model behaviour.

Indeed, in the $\tau_0 \sim 10^3$ s case, we observe that plume triggering seems to be delayed significantly compared to the other cases. The delay is evident in the mass flux and relative humidity times series in figure 4.16. The relative humidity cross-sections in figure 4.18, taken at approx $t = 44,000$ s, show that at the timing of the first peak for the no drag, $\tau \sim 10^5$ s, and $\tau_0 \sim 10^4$ s runs, there is no evidence of plumes forming in the $\tau_0 \sim 10^3$ s case.

However, in figure 4.19 at $t = 72,000$ s, despite substantially weaker mass flux at time of triggering, we can see that the $\tau_0 \sim 10^3$ s run does trigger plumes. The plumes produced are also much more horizontally confined than the other cases which appear to trigger plumes first at the edges of the heating. Indeed, in figure 4.19, the $\tau_0 \sim 10^3$ s case seems less dominated by the edges of the heating triggering initial plumes. In figure 4.19, we can also see a number of differences between the other model runs. For example, $\tau_0 \sim 10^4$ s has fewer plumes than $\tau_0 \sim 10^5$ s and the no drag case. The plumes in the $\tau_0 \sim 10^4$ s case are also slightly more uniform and the middle two plumes are stronger. This behaviour can be explained by drag

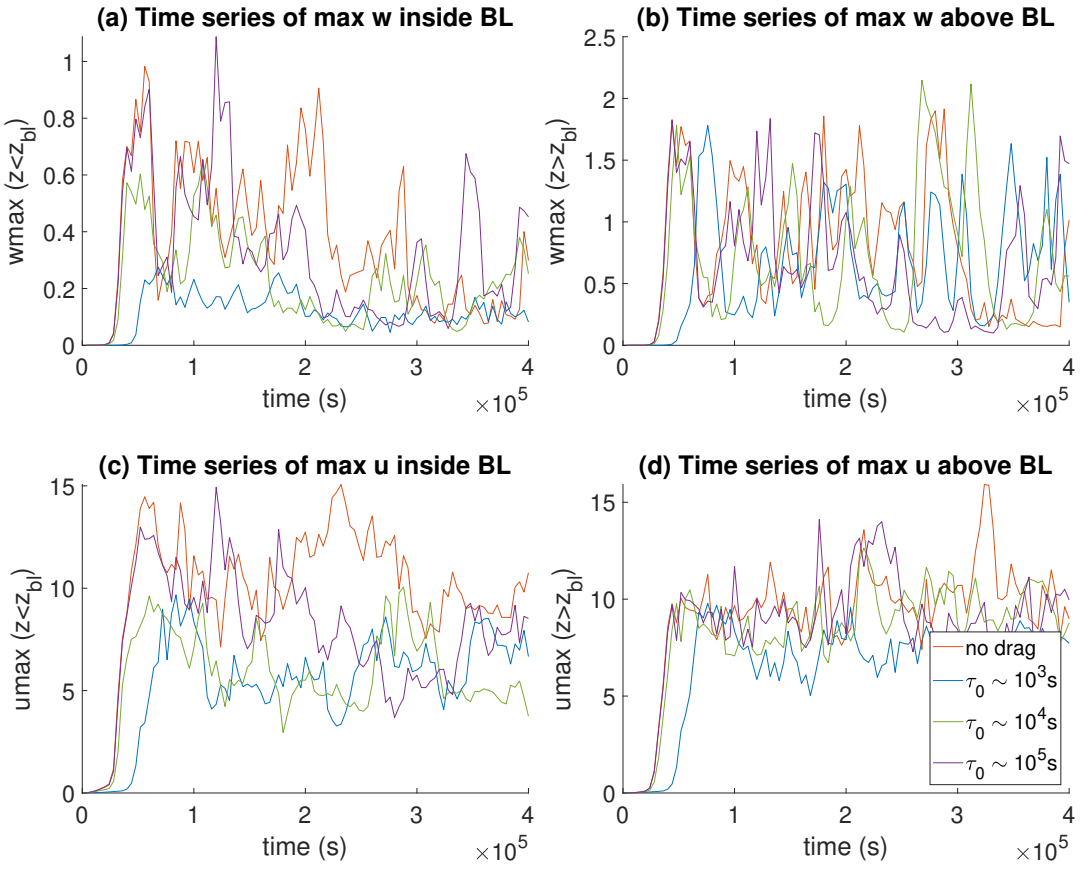

Figure 4.17: Comparison by drag strength of time series for (a) maximum vertical velocity inside the boundary layer, (b) maximum vertical velocity above the boundary layer, (c) maximum horizontal velocity inside the boundary layer, (d) maximum horizontal velocity above the boundary layer. All runs have initial specific humidity in the boundary layer 0.01 kg/kg, continuous heating $Q \sim 10^{-5}$ K/s, and grid length $\Delta x \sim 10^4$ m with drag strengths $\tau_0 \sim 10^3$ s (blue), $\tau_0 \sim 10^4$ s (green), $\tau_0 \sim 10^5$ s (purple), and no drag (red).

causing a slight delay in plume triggering and a consistently weaker massflux through the effect of the drag on the horizontal pressure gradients.

In figures 4.13 subplot (a) and 4.14 subplots (a) and (b), we can see clear signs of pressure gradients pushing air into the centre of the horizontal domain in the boundary layer, opposed by the drag. The pressure gradients are strongest in the highest drag case – maximum at approximately 1.5×10^{-3} compared to maximums on the order of 10^{-4} for the other cases – suggesting that the drag strength determines how strong the pressure gradient has to be to overcome the drag. This will in turn mean that stronger drag will lead to weaker mass flux and will also delay the

triggering of a plume, due to the need for a larger pressure gradient. Though again, this effect is only substantial when the boundary layer is balanced. If the drag is insufficient to reach balance in the boundary layer, we have seen the effect is marginal at best.

It should also be re-iterated that we do not expect substantially different behaviour between runs once plumes ascend into the free troposphere since in the free troposphere, there is no difference between the model run setups. Therefore it is the triggering of plume events and their strength which is most likely to differ because of increases in drag or externally imposed heating in the boundary layer.

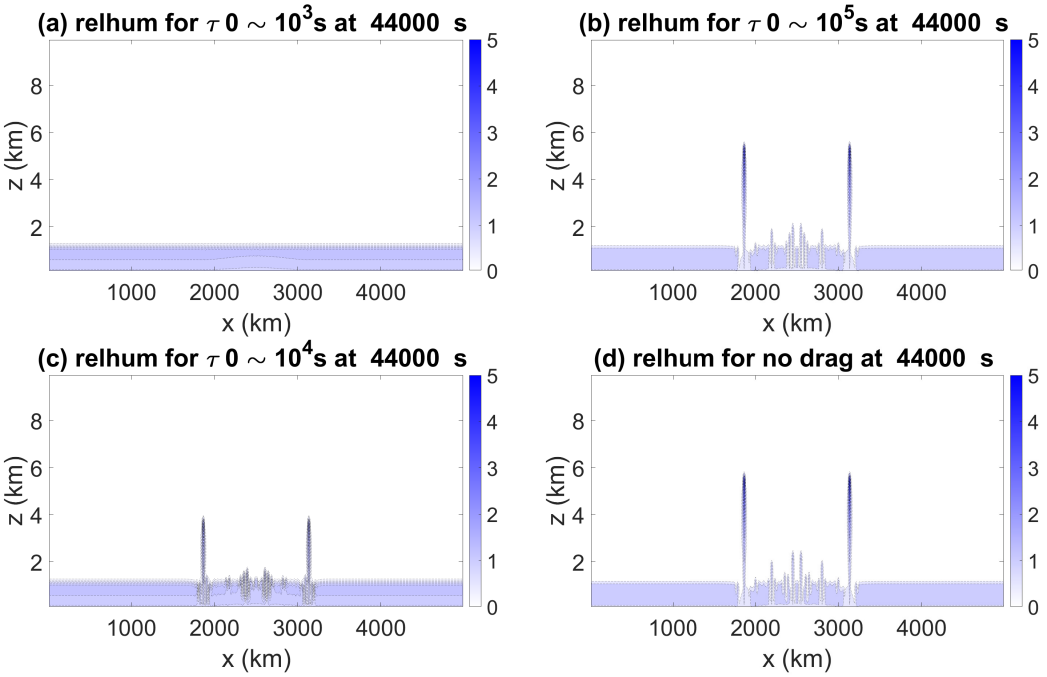

Figure 4.18: Relative humidity x-z cross sections at $t = 44,000$ s for drag strengths (a) $\tau_0 \sim 10^3$ s, (c) $\tau_0 \sim 10^4$ s, (b) $\tau_0 \sim 10^5$ s and (d) no drag with initial specific humidity in the boundary layer 0.01 kg/kg, grid length $\Delta x \sim 10^4$ m, and continuous heating $Q \sim 10^{-5}$ K/s.

For this reason, it is unsurprising that although the magnitude of vertical velocity above the boundary layer does not appear to differ substantially for the $\tau_0 \sim 10^3$ s run compared with all the other runs in figure 4.17, the vertical velocity in the boundary layer is substantially weaker. The mass flux in 4.16 is thus also correspondingly weaker for the $\tau_0 \sim 10^3$ s run.

Differences in drag strength alone may account for the very minor differences between the no drag run, the $\tau_0 \sim 10^5$ s and the $\tau_0 \sim 10^4$ s runs, but they do not

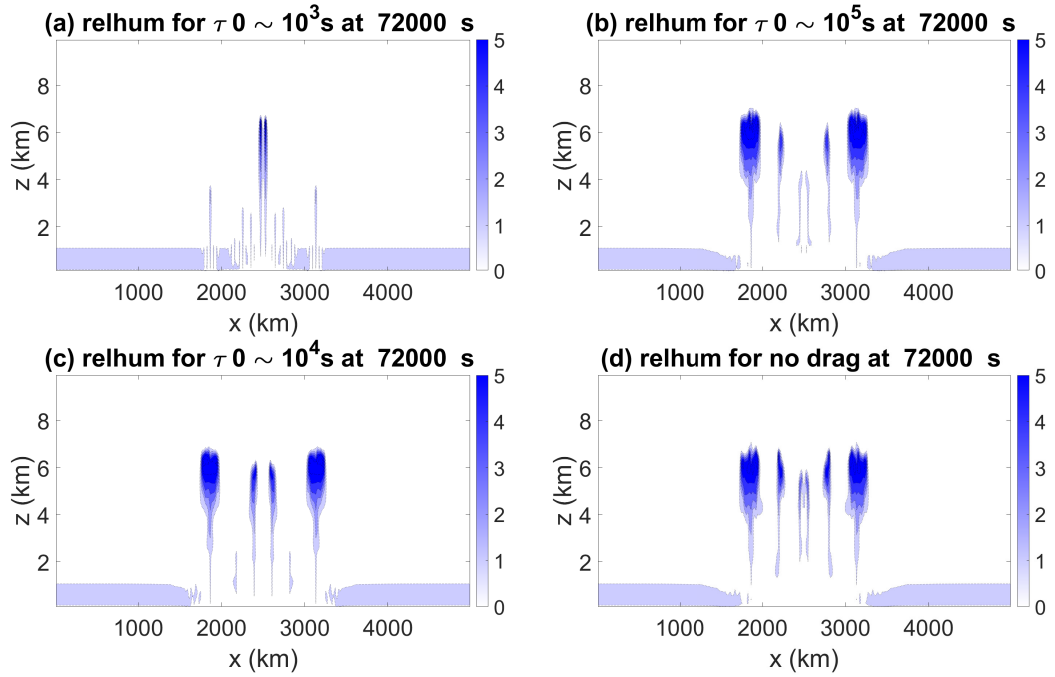

Figure 4.19: Relative humidity x-z cross sections at $t = 72,000$ s for drag strengths (a) $\tau_0 \sim 10^3$ s, (c) $\tau_0 \sim 10^4$ s, (b) $\tau_0 \sim 10^5$ s and (d) no drag with initial specific humidity in the boundary layer 0.01 kg/kg, grid length $\Delta x \sim 10^4$ m, and continuous heating $Q \sim 10^{-5}$ K/s.

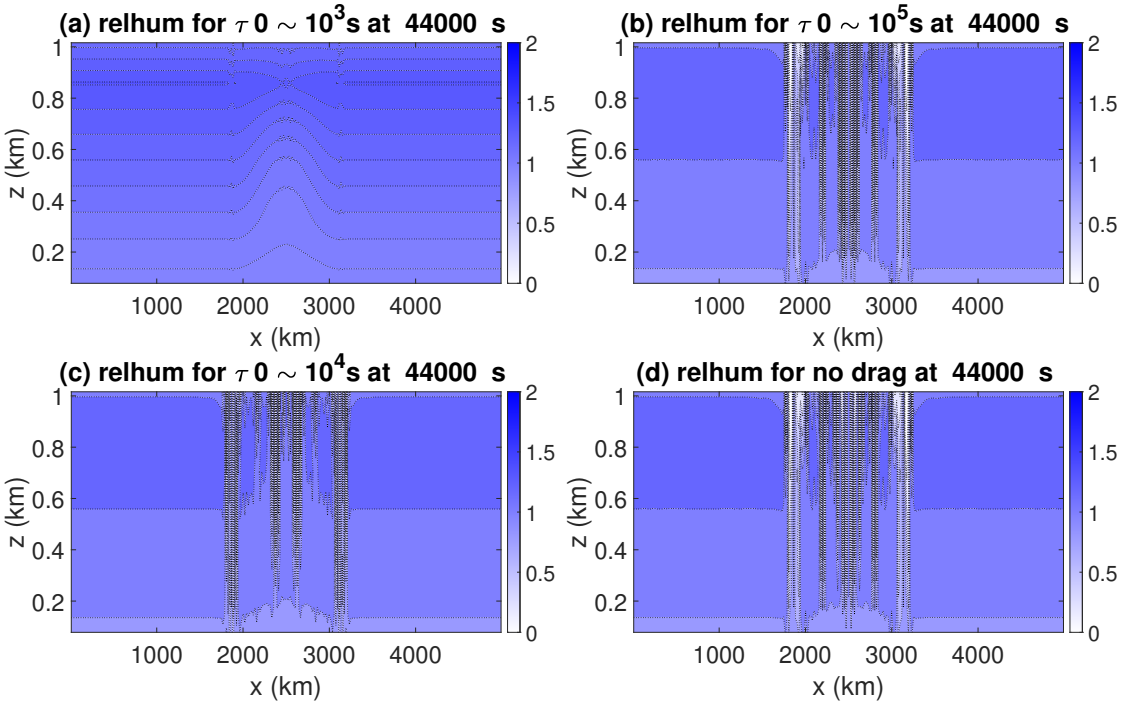

Figure 4.20: Relative humidity x-z cross sections at $t = 44,000$ s in the boundary layer only for drag strengths (a) $\tau_0 \sim 10^3$ s, (c) $\tau_0 \sim 10^4$ s, (b) $\tau_0 \sim 10^5$ s and (d) no drag with initial specific humidity in the boundary layer 0.01 kg/kg, grid length $\Delta x \sim 10^4$ m, and continuous heating $Q \sim 10^{-5}$ K/s.

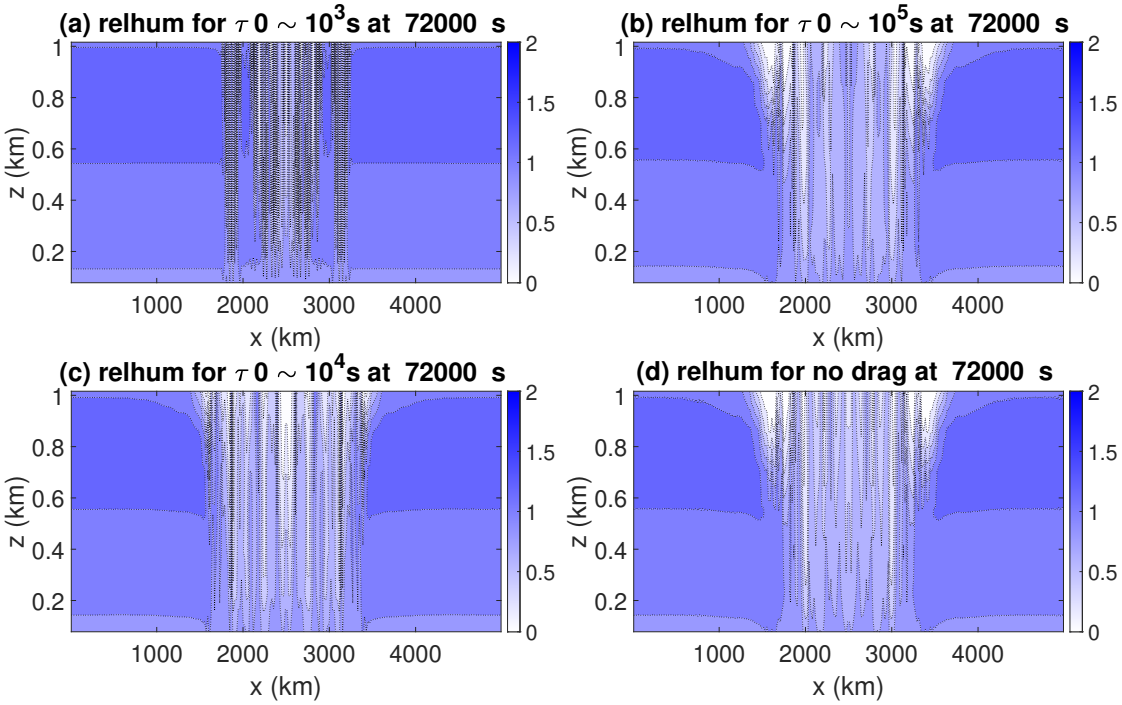

Figure 4.21: Relative humidity x-z cross sections at $t = 72,000$ s in the boundary layer only for drag strengths (a) $\tau_0 \sim 10^3$ s, (c) $\tau_0 \sim 10^4$ s, (b) $\tau_0 \sim 10^5$ s and (d) no drag with initial specific humidity in the boundary layer 0.01 kg/kg, grid length $\Delta x \sim 10^4$ m, and continuous heating $Q \sim 10^{-5}$ K/s.

account for the substantially larger difference between the $\tau_0 \sim 10^3$ s run and the other runs with weaker drag. Looking at figure 4.10, we can see the $\tau_0 \sim 10^3$ s run appears to be on the edge of the moist ADBL regime when $Q \sim 10^{-5}$ K/s, whereas the other runs seem to be more consistent with no long-term balance regime (figures 4.9, 4.11, and 4.12). Lindzen and Nigam (1987) similarly observed the effect of the increase in drag, but did not make a connection to a possible long-term balance regime in the boundary layer that might explain the change in model behaviour for increased drag.

Thus, when the model is not balanced in the boundary layer, drag strength accounts for some delay in the triggering of plumes – and the strength of the plumes triggered. However, larger differences in model behaviour are more likely driven by whether the boundary layer is in a long term balance regime and which regime that is, though it should be noted that the boundary layer balance regime itself will of course be a function of drag strength as well as other variables.

We ran the model for multiple heating rates and found that the externally imposed continuous heating does have an effect on the triggering of moist plumes in

the model as well with higher heating rates corresponding to earlier onset of plumes in all model setups. This is unsurprising as stronger externally imposed heating would lead to parcels of air being lifted faster and reaching saturation faster.

Effect of Drag Strength and Boundary Layer Regime on Sustaining of moist plumes

Interestingly, there does not seem to be much connection between drag strength and how long convective plumes are sustained. Here, we measure a plume being sustained (or multiple plumes being sustained) as the period in which the relative humidity in the first layer above the boundary layer exceeds 100% continuously.

When the relative humidity in the first layer above the boundary layer drops below 100%, we consider that to be a break in convective plumes possibly owing to insufficient moisture to maintain one or more plumes. If the relative humidity in the first layer above the boundary layer then exceeds 100% again, we consider that to be the triggering of a new plume event. Note that even if multiple plumes are triggered during the period when the relative humidity in the first layer above the boundary layer exceeds 100%, it will be counted as a single moist convective plume event.

How well a plume event is sustained and how long it takes the model to trigger a new plume event after one finishes is likely due to two factors: the amount of total water available in the boundary layer and the magnitude of the horizontal velocity. Both of these quantities will be affected by the drag strength and the boundary layer balance regime – if it exists. The presence of gravity waves may also have an effect, though we do not look at this in this chapter.

Considering both the effect of drag and boundary layer regime, we expect first of all that drag will weaken the horizontal velocity, meaning less moisture can be advected into plumes. Higher drag would therefore imply moist convective events of shorter duration. However, if we also consider the boundary layer total water content, the picture is a little more complicated. A higher drag case may be unable to advect as much moisture into the plumes, but it may also have more moisture left after a moist convective plume event if it falls into the ADBL regime as opposed to the ADFT or WTG regime with the ADFT and WTG regimes being able to sustain moist plumes at a lower relative humidity and therefore a lower boundary layer total

water content.

In figure 4.16, the relative humidity drops faster for $\tau_0 \sim 10^4$ s than the other cases and the relative humidity in the no drag case drops below 100% faster than the $\tau_0 \sim 10^5$ s case. It makes sense that $\tau_0 \sim 10^4$ s run drops below 100% faster than the $\tau_0 \sim 10^5$ s and no drag runs. Since the horizontal velocity is weaker because of drag and a stronger horizontal pressure gradient is needed to force horizontal convergence, it is expected that moisture cannot be advected in the horizontal as efficiently and thus the plumes are able to access less moisture in the horizontal to feed their ascent. Ultimately this might mean that less moisture ends up leaving the boundary layer in each plume and therefore, the moisture level recovers more quickly. However, the same reasoning does not hold for why the no drag case dips below 100% relative humidity faster than the $\tau_0 \sim 10^5$ s case. A possible explanation is that the moisture is advected too efficiently in the no drag case, depleting the boundary layer moisture more quickly which suppresses the model's ability to sustain plumes.

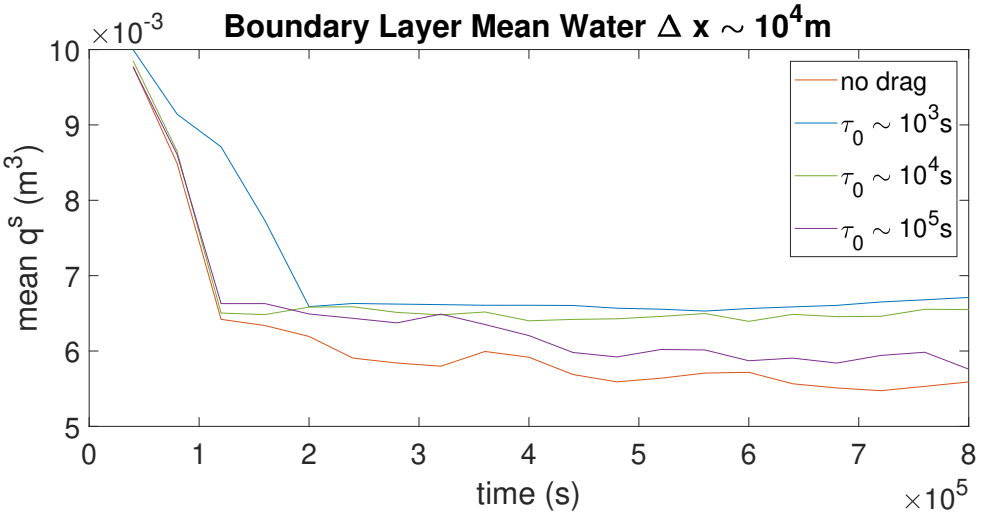

Figure 4.22: Time series for average water in the boundary layer for $\tau_0 \sim 10^3$ s (blue), $\tau_0 \sim 10^4$ s (green), $\tau_0 \sim 10^5$ s (purple) and no drag (red) with initial specific humidity in the boundary layer 0.01 kg/kg, grid length $\Delta x \sim 10^4$ m and continuous heating $Q \sim 10^{-5}$ K/s.

The $\tau_0 \sim 10^3$ s case takes the longest of all the runs to fall below 100% relative humidity. It is possible we can explain this with reference to the boundary layer balance regime. Since $\tau_0 \sim 10^3$ s seems to fall into the ADBL regime, we expect plumes can be sustained longer since the regime is likely to lose less moisture initially, but also recover faster to trigger further plumes. The regime loses less moisture because

of Darcy's balance inhibiting the horizontal velocity and therefore the horizontal advection of boundary layer moisture into plumes, but recovers faster since ADBL should be unable to sustain plumes for a lower boundary layer relative humidity or larger N_m^2. Thus when the boundary layer total water drops below a certain threshold, the plumes also stop, but there is more water remaining in the boundary layer than for other balance regimes or for regimes that have not yet reached balance.

In figure 4.22, we see that the boundary layer mean water in the $\tau_0 \sim 10^3$ s case stabilises above the other runs. Given the evidence from figure 4.13 subplot (a) that the $\tau_0 \sim 10^3$ s run is balanced, we would expect the boundary layer water to stabilise once there is no longer sufficient moisture in the boundary layer to feed the transient plume response.

Curiously, the $\tau_0 \sim 10^4$ s run stabilises around the same value, despite not being balanced in the horizontal velocity equation in figure 4.14 subplot (a), although the drag term is of leading order in parts of the domain so the scalings for total water etc from the ADBL regime may still hold since it would still be true that the drag parameter is the same order as the pressure gradient term.

The similarity between the $\tau_0 \sim 10^3$ s run and the $\tau_0 \sim 10^4$ s run is also borne out in the magnitude of the maximum horizontal velocity in the boundary layer in figure 4.17. The no drag case maintains a maximum horizontal velocity fairly consistently larger than the three drag cases whilst $\tau_0 \sim 10^3$ s and $\tau_0 \sim 10^4$ s appear to maintain approximately the same magnitude over the run time.

We note again here that the strength of the externally imposed heating rate also has an effect on the organisation of plumes. At lower heating rates, the model develops two plumes at the edges of the externally imposed heating whereas for higher heating rates, a central plumes also emerges. This could be a flaw in the experimental design as the downdraft-updraft motion being forced at the edges of the externally imposed heating due to the change from a positive to a negative heating rate may be driving the formation of plumes more efficiently than the most strongly positive part of the externally imposed heating or the centre of the heating. We saw some of this behaviour in the dry case, but in the moist case it is more noticeable and appears to have a larger impact on the model results since where plumes are first triggered has a larger effect on how and where moisture is advected out of the boundary layer. Note also that the pattern of which drag strength cases fall below 100% relative humidity fastest is replicated across almost all externally

imposed continuous heating rates explored in this chapter.

Effect of Drag Strength and Boundary Layer Regime on Organisation of moist convective plumes

Organisation of the convective plumes also seems to be related to the horizontal velocity and boundary layer total water. However, the organisation of plumes is also highly dependent on the gridlength Δx.

Let us consider cross sections from our four drag strength runs at $t = 72,000$ s where the $\tau_0 \sim 10^3$ s case has its first peak in relative humidity at the first model level above the boundary. The relative humidity cross section we already saw in figure 4.19 where we observed a few differences between the model runs. For example, $\tau_0 \sim 10^4$ s has fewer plumes than $\tau_0 \sim 10^5$ s and the no drag case. In figure 4.21, we can see that around the plume triggering location in white, there is a much steeper gradient for the total water at the top of the boundary layer in the $\tau_0 \sim 10^3$ s case. The gradient gets less steep as the drag decreases. This suggests the more drag increases, the less water is being pulled into the plumes in the horizontal.

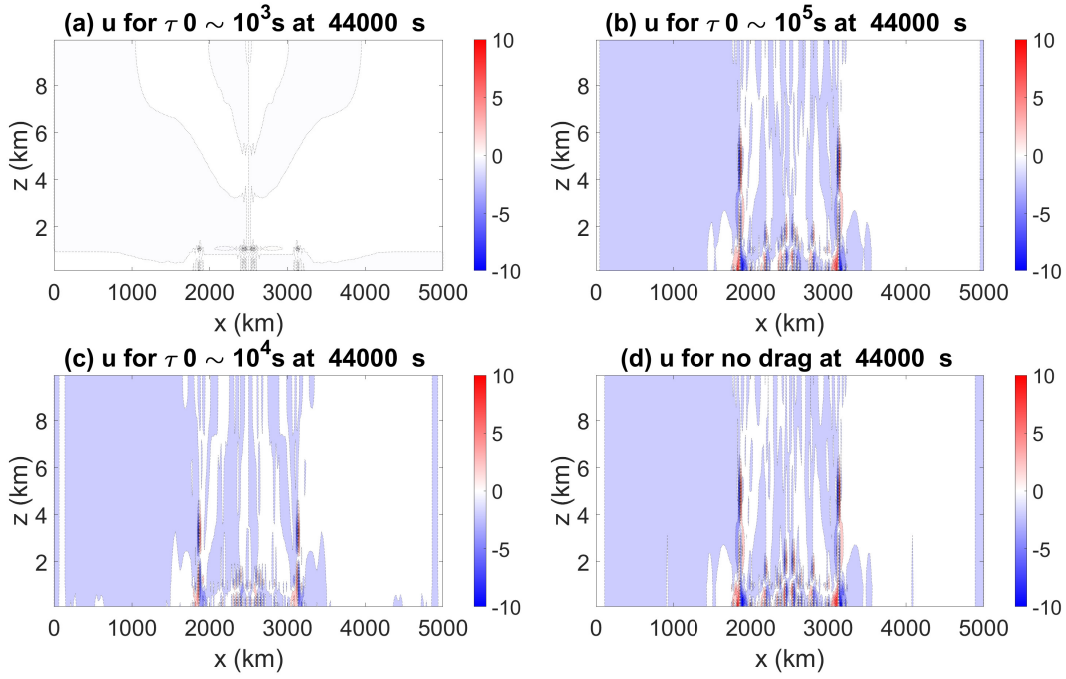

Figure 4.23: Horizontal velocity (u) x-z cross sections at $t = 44,000$ s for drag strengths (a) $\tau_0 \sim 10^3$ s, (c) $\tau_0 \sim 10^4$ s, (b) $\tau_0 \sim 10^5$ s and (d) no drag with initial specific humidity in the boundary layer 0.01 kg/kg, grid length $\Delta x \sim 10^4$ m, and continuous heating $Q \sim 10^{-5}$ K/s.

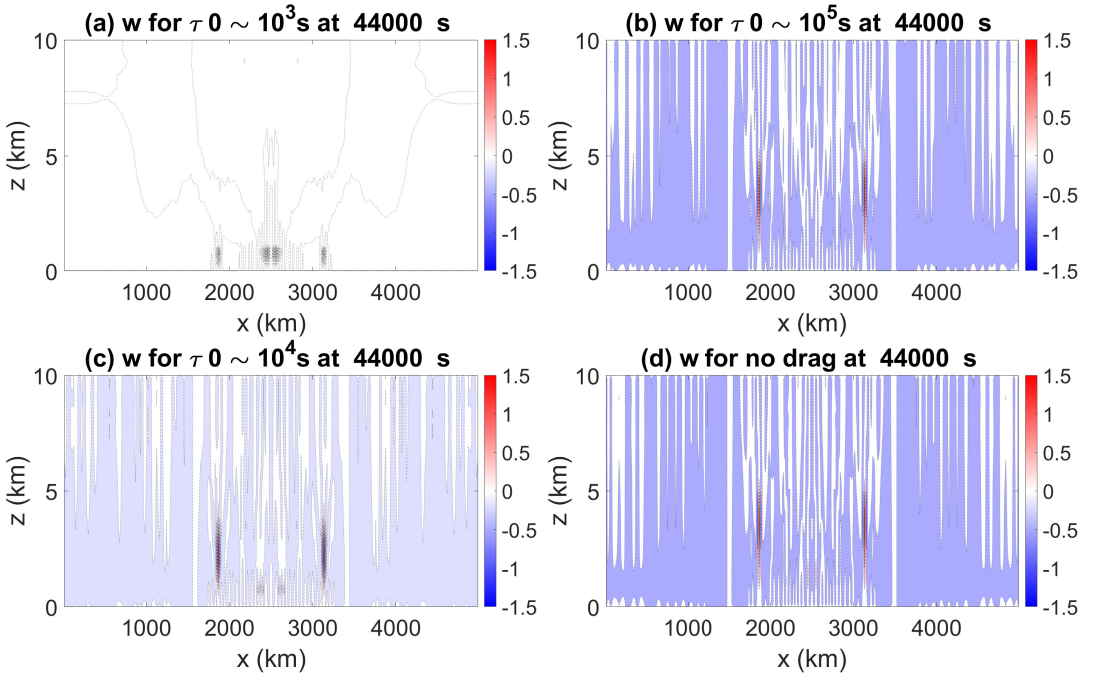

Figure 4.24: Vertical velocity (w) x-z cross sections at $t = 44,000$ s for drag strengths (a) $\tau_0 \sim 10^3$ s, (c) $\tau_0 \sim 10^4$ s, (b) $\tau_0 \sim 10^5$ s and (d) no drag with initial specific humidity in the boundary layer 0.01 kg/kg, grid length $\Delta x \sim 10^4$ m, and continuous heating $Q \sim 10^{-5}$ K/s.

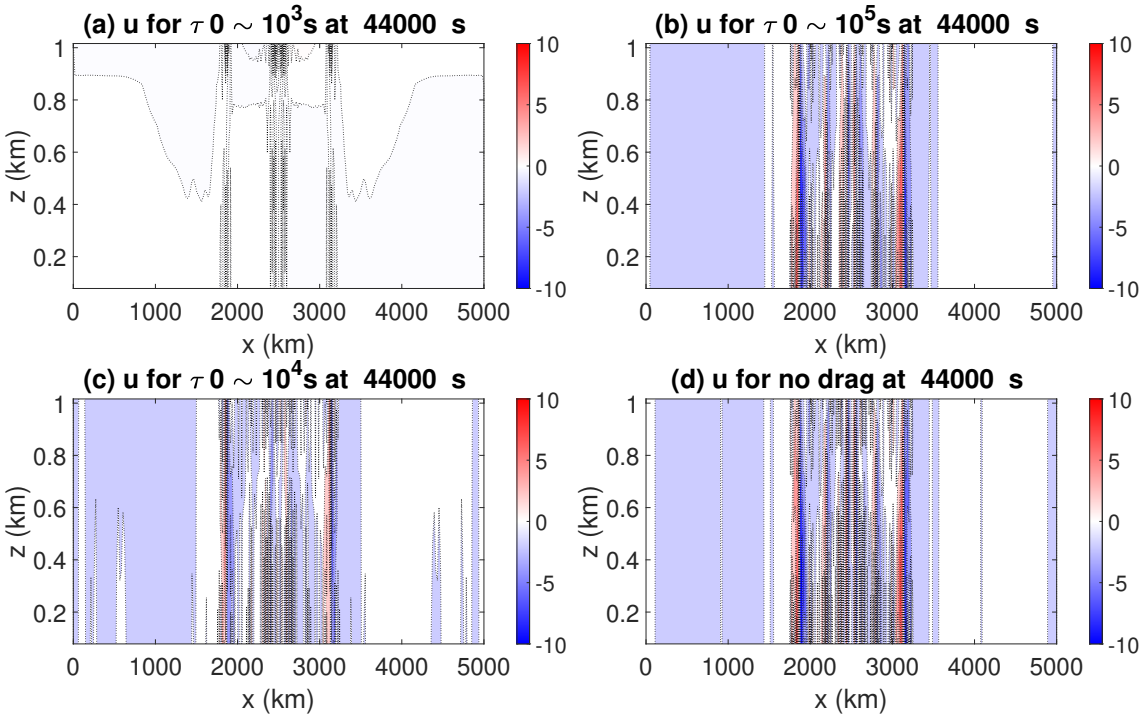

Figure 4.25: Horizontal velocity (u) x-z cross sections at $t = 44,000$ s in the boundary layer only for drag strengths (a) $\tau_0 \sim 10^3$ s, (c) $\tau_0 \sim 10^4$ s, (b) $\tau_0 \sim 10^5$ s and (d) no drag with initial specific humidity in the boundary layer 0.01 kg/kg, grid length $\Delta x \sim 10^4$ m, and continuous heating $Q \sim 10^{-5}$ K/s.

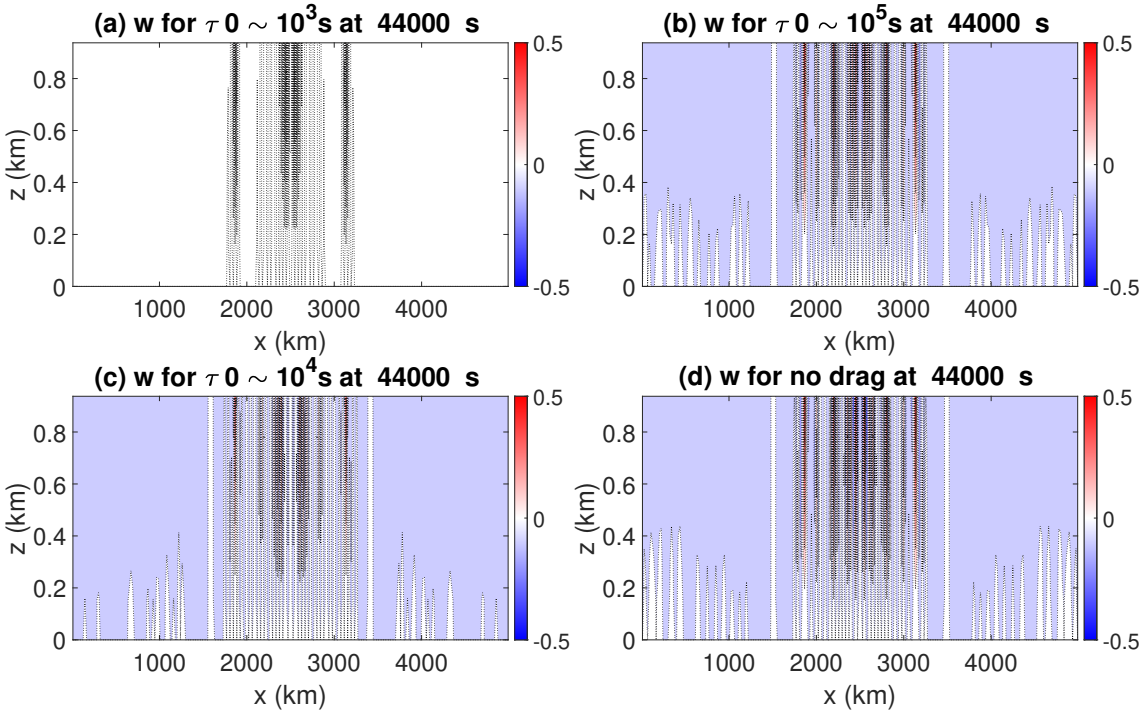

Figure 4.26: Vertical velocity (w) x-z cross sections at $t = 44,000$ s in the boundary layer only for (a) $\tau_0 \sim 10^3$ s, (c) $\tau_0 \sim 10^4$ s, (b) $\tau_0 \sim 10^5$ s and (d) no drag with initial specific humidity in the boundary layer 0.01 kg/kg, grid length $\Delta x \sim 10^4$ m, and continuous heating $Q \sim 10^{-5}$ K/s.

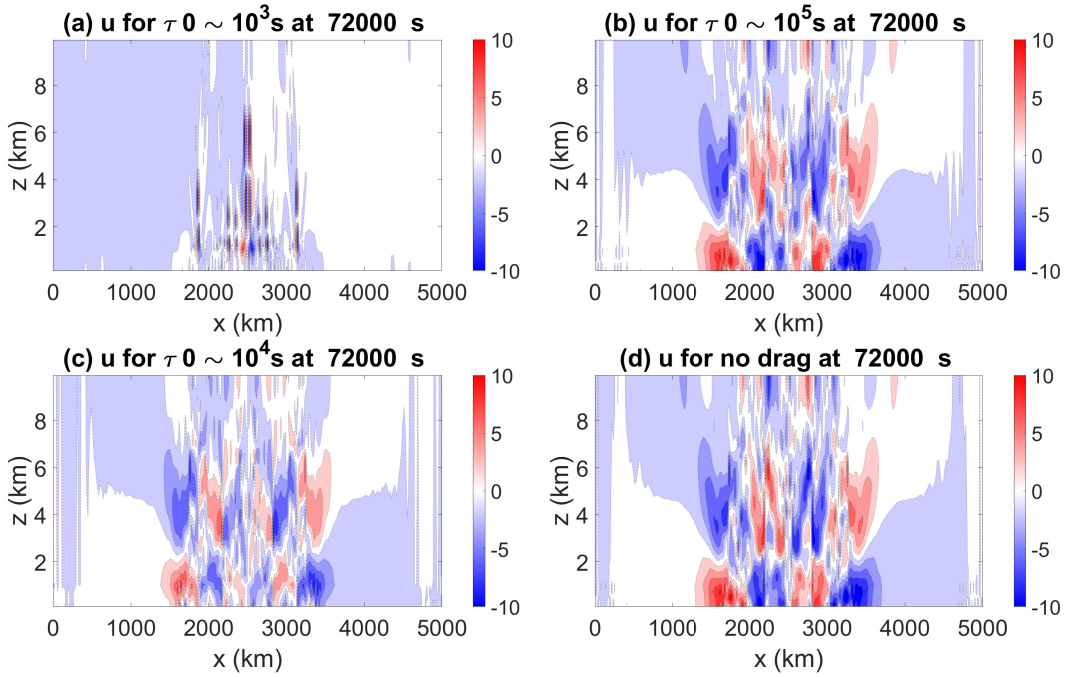

Figure 4.27: Horizontal velocity (u) x-z cross sections at $t = 72,000$ s for drag strengths (a) $\tau_0 \sim 10^3$ s, (c) $\tau_0 \sim 10^4$ s, (b) $\tau_0 \sim 10^5$ s and (d) no drag with initial specific humidity in the boundary layer 0.01 kg/kg, grid length $\Delta x \sim 10^4$ m, and continuous heating $Q \sim 10^{-5}$ K/s.

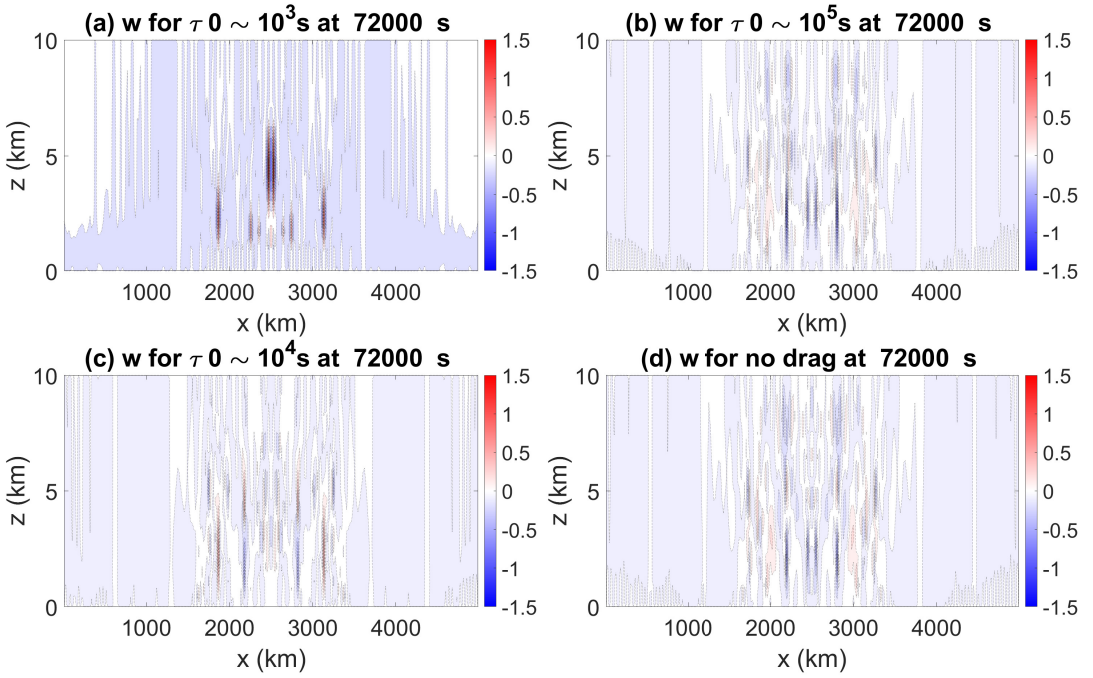

Figure 4.28: Vertical velocity (w) x-z cross sections at $t = 72,000$ s for drag strengths (a) $\tau_0 \sim 10^3$ s, (c) $\tau_0 \sim 10^4$ s, (b) $\tau_0 \sim 10^5$ s and (d) no drag with initial specific humidity in the boundary layer 0.01 kg/kg, grid length $\Delta x \sim 10^4$ m, and continuous heating $Q \sim 10^{-5}$ K/s.

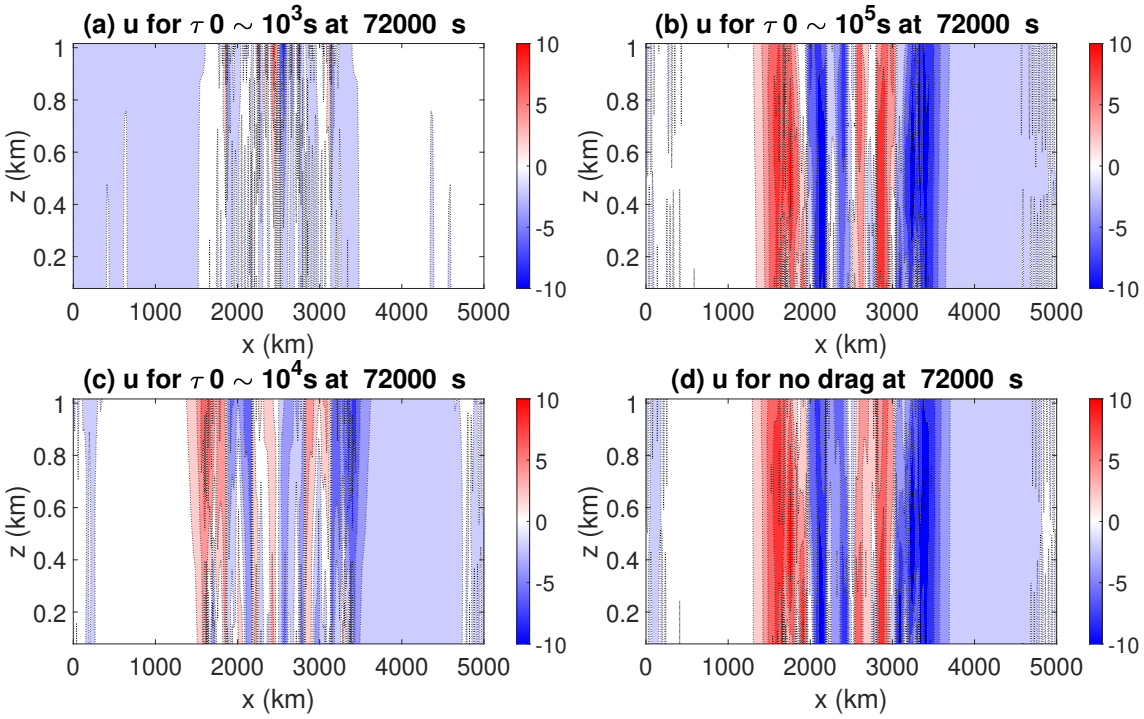

Figure 4.29: Horizontal velocity (u) x-z cross sections at $t = 72,000$ s in the boundary layer only for drag strengths (a) $\tau_0 \sim 10^3$ s, (c) $\tau_0 \sim 10^4$ s, (b) $\tau_0 \sim 10^5$ s and (d) no drag with initial specific humidity in the boundary layer 0.01 kg/kg, grid length $\Delta x \sim 10^4$ m, and continuous heating $Q \sim 10^{-5}$ K/s.

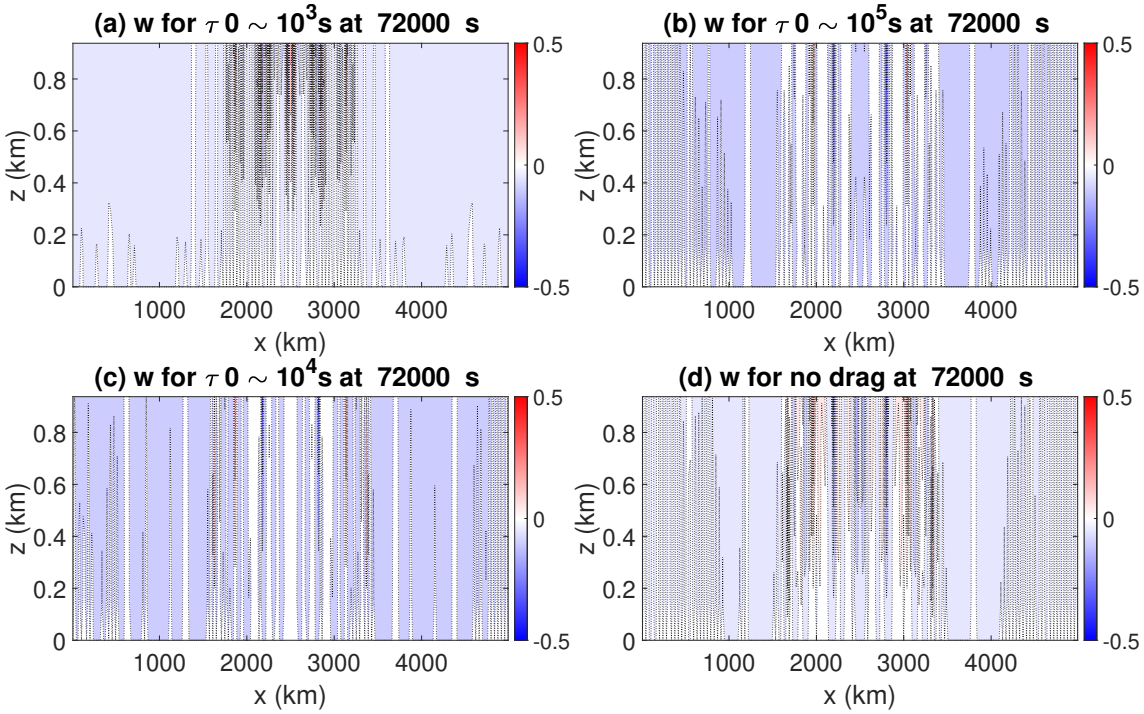

Figure 4.30: Vertical velocity (w) x-z cross sections at $t = 72,000$ s in the boundary layer only for drag strengths (a) $\tau_0 \sim 10^3$ s, (c) $\tau_0 \sim 10^4$ s, (b) $\tau_0 \sim 10^5$ s and (d) no drag with initial specific humidity in the boundary layer 0.01 kg/kg, grid length $\Delta x \sim 10^4$ m, and continuous heating $Q \sim 10^{-5}$ K/s.

If we look at the corresponding horizontal velocity cross section in figure 4.27 and the corresponding boundary layer cross sections in figure 4.29, we see an even clearer example of the weaker drag cases being able to draw from wider moisture sources in the horizontal as the horizontal velocity circulation for the $\tau_0 \sim 10^3$ s case is much more confined than the others. And the $\tau_0 \sim 10^4$ s case is more horizontally confined than the $\tau_0 \sim 10^5$ s and the no drag case whilst $\tau_0 \sim 10^5$ s is marginally more confined than the no drag case. In the dry case, this led to vertical velocity advecting air out of the boundary layer most strongly in the high drag cases. However the inclusion of moisture seems to almost reverse the conclusions from the dry case where weaker and no drag cases in the dry experiments struggled to show vertical velocity above the boundary layer at all. In the moist case, the extra complication of plumes needing to be able to draw on wide moisture reserves horizontally in the boundary layer to maintain themselves means that it is the weaker drag and no drag cases which maintain more substantial vertical velocity above the boundary layer with initial plumes triggering more easily above the imposed continuous heating. In Bretherton and Sobel (2002) the low-tropospheric wind is predominantly responsible

for advecting moisture and here, the boundary layer horizontal velocity is the most affected by drag and thus slower advection of moisture should lead to more plumes. In the real world, the picture is likely more complicated as wind direction may also play a part (Chen et al., 1996).

A Note on the Effect of Grid Size on Organisation of moist convective plumes

One further important point on the organisation of the moist convective plumes is that horizontal extent seems closely tied to grid size. Figure 4.15 shows us straight away that the horizontal lengthscale of the flow in the boundary layer is set by the horizontal gridlength Δx. Although, at weaker heating rates, it seems at least one of the model runs has a larger lengthscale than the gridlength (drag72000). We also saw that gridlength has an effect on boundary layer balance regimes with an increase in Δx allowing model runs that were previously unbalanced to become balance (e.g. figure 4.13 subplot (b) vs. 4.14 subplot (a)).

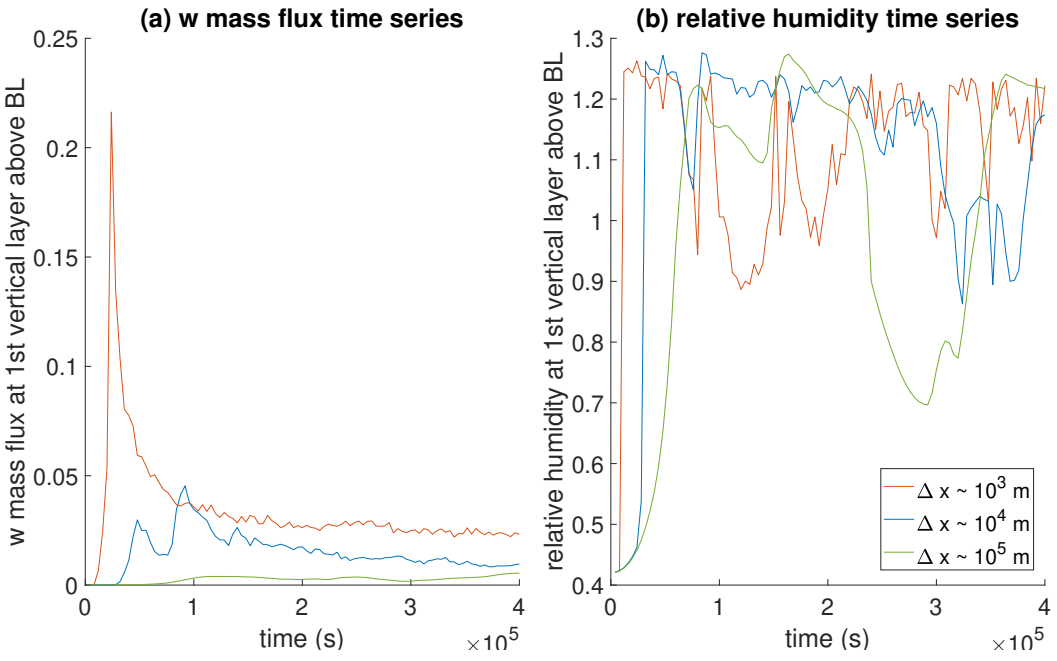

Figure 4.31: Comparison by horizontal gridlength of time series for (a) mass flux and (b) relative humidity at the first layer above the boundary layer. All runs have initial specific humidity in the boundary layer 0.01 kg/kg, drag strength $\tau_0 \sim 10^4$ m and continuous heating $Q \sim 10^{-5}$ K/s. Horizontal gridlengths shown include $\Delta x \sim 10^3$ m (red), $\Delta x \sim 10^4$ m (blue), and $\Delta x \sim 10^3$ m (green).

Thus, we vary the gridlength in the model to see how large the effect is. Once

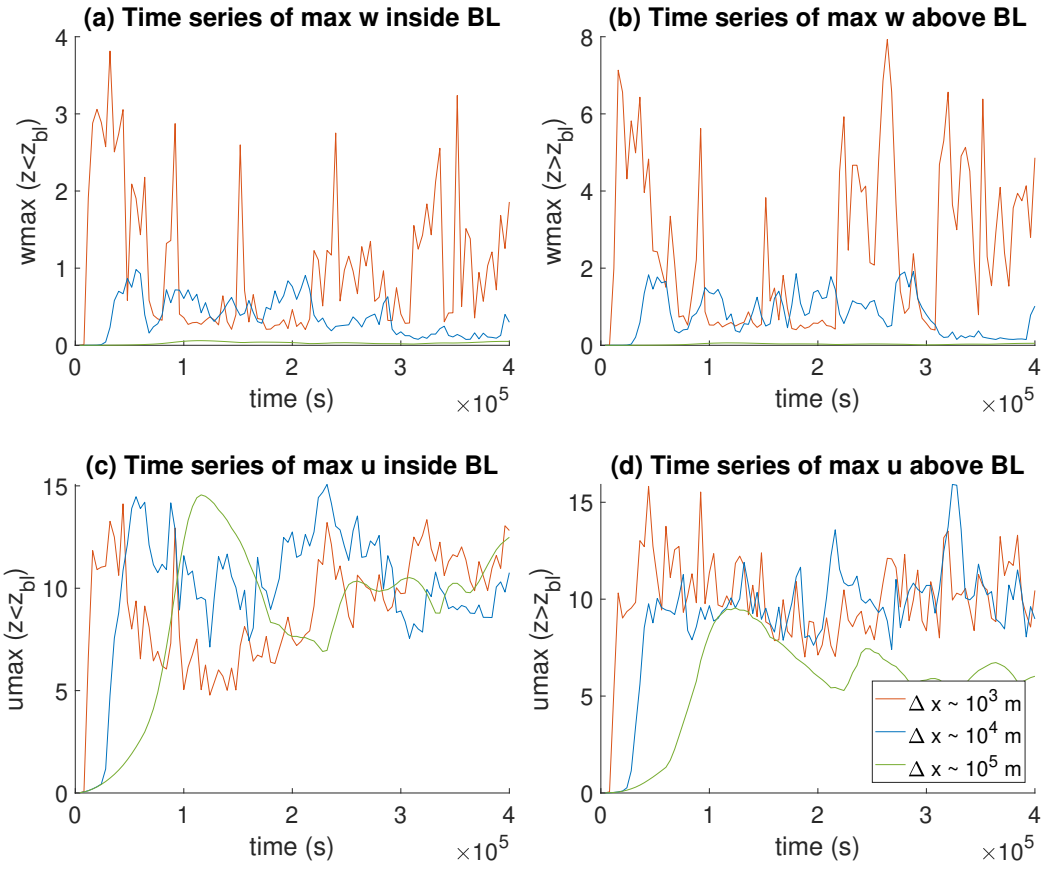

Figure 4.32: Comparison by horizontal gridlength of time series for (a) maximum vertical velocity inside the boundary layer, (b) maximum vertical velocity above the boundary layer, (c) maximum horizontal velocity inside the boundary layer, (d) maximum horizontal velocity above the boundary layer. All runs have initial specific humidity in the boundary layer 0.01 kg/kg, drag strength $\tau_0 \sim 10^4$ m and continuous heating $Q \sim 10^{-5}$ K/s. Horizontal gridlengths shown are $\Delta x \sim 10^3$ m (red),$\Delta x \sim 10^4$ m (blue), and $\Delta x \sim 10^3$ m (green).

more, we consider time series plots of runs which all have drag timescale $\tau_0 \sim 10^4$ s, specific boundary layer water content of 0.01 kg/kg or10 g/kg or and tropospheric relative humidity of 1%.

From the mass flux time series in figure 4.31, it is clear that the resolution of the model has a substantial effect on the magnitude of the mass flux at the first vertical level above the boundary layer. Although at first this may seem like it may be problematic for our results, in figure 4.32, it does not seem to affect the size of horizontal velocity u in the model, at least over the timescale represented in figure 4.32 since in all three cases for Δx, the model achieves the same magnitude for u,

with higher Δx cases starting off with larger horizontal velocities before settling, whilst lower Δx cases start off too weak in the horizontal velocity before settling.

We can explain the behaviour of the vertical velocity by reference to the mass conservation equation and anelastic/Boussinesq theory in combination with the known behaviour of moist convection.

From the anelastic/Boussinesq theory, we have

$$-\frac{\partial u}{\partial x} = \frac{\partial w}{\partial z} \implies UH = WL. \tag{4.86}$$

And from known characteristics of moist convection, we know that the horizontal lengthscale of the plume behaves as a delta function and the plume width will collapse to the smallest permissable scale unless limited by processes such as turbulence or diffusion which mitigate the collapse of scale. Here, the plume width collapses to the grid length which is the smallest persimissable horizontal scale in the model. And so by equation 4.5.3, it follows that when Δx gets smaller, L gets smaller and then W must get smaller, which means the vertical velocity w must be larger even whilst the horizontal velocity u does not change.

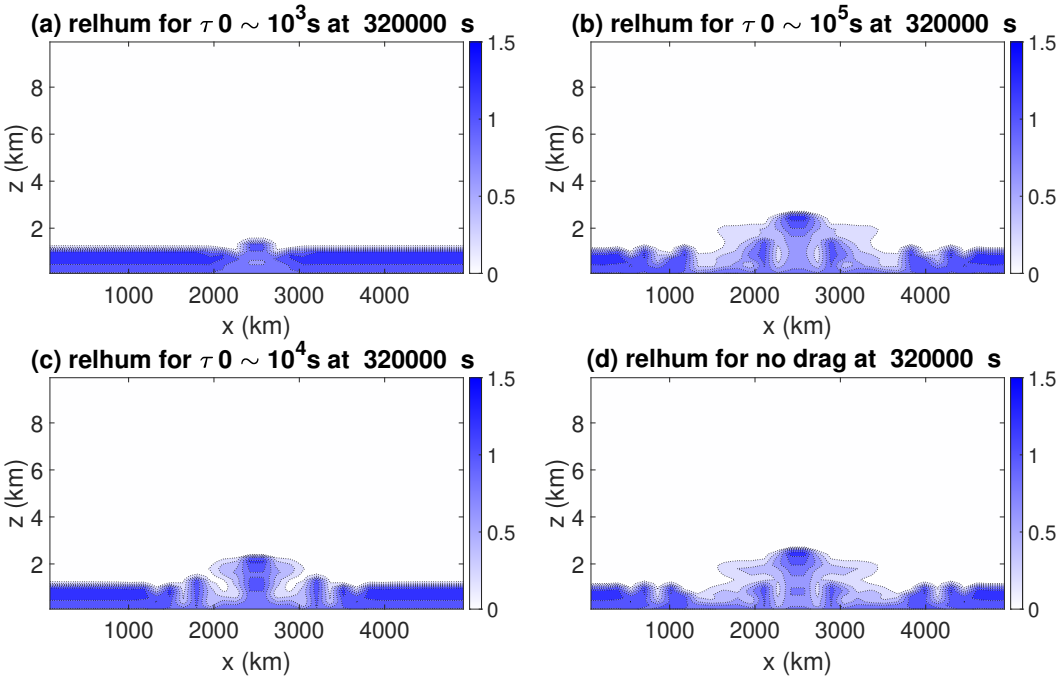

Figure 4.33: Relative humidity x-z cross sections at $t = 320,000$ s for drag strengths (a) $\tau_0 \sim 10^3$ s, (c) $\tau_0 \sim 10^4$ s, (b) $\tau_0 \sim 10^5$ s and (d) no drag with initial specific humidity in the boundary layer 0.01 kg/kg, grid length $\Delta x \sim 10^5$ m, and continuous heating $Q \sim 10^{-5}$ K/s.

In figure 4.33 where $\Delta x \sim 10^5$ m, if we compare the cross sections for relative humidity to the cross sections for relative humidity in figures 4.18 and 4.19 where $\Delta x \sim 10^4$ m, we see that when $\Delta x \sim 10^5$ m, the plumes are much broader and ascend to lower heights in the free troposphere suggesting weaker vertical velocity as expected. The plumes also take longer to trigger initially, as is evident in figure 4.31 where for each decrease in magnitude of Δx, the first peak in the relative humidity time series is delayed.

This effect is not especially surprising, but for our analysis, it is important to consider that the grid size of a given model run sets a baseline magnitude for the horizontal lengthscale L and therefore any variables in the scale analysis in section 4.3 which are dependent on L.

Thus our analysis of model behaviour in the moist case must consider that without processes to limit the collapse of the horizontal lengthscale, any results are sensitive to the choice of Δx, including at what drag value long-term balance can be achieved in the boundary layer. The triggering, sustaining and organisation of moist plumes is also substantially dependent on the horizontal gridlength of the model.

The effect of the existence or non-existence of long-term balance in the boundary layer on the model must therefore also be considered in the context of the gridlength.

4.6 Conclusions

In this chapter, we have presented a moist version of the theoretical dry framework presented in chapter 3 and we have outlined 2 additional long-term moist balance regimes as well.

We have shown that balance is achievable in the moist case, both with and without the presence of a continuous external heat source in the boundary layer.

We have shown in the case of the continuously externally heated boundary layer that ADBL is the only achievable long-term balance regime when moisture is included within the parameter space explored in this chapter. This is in stark contrast to the dry case where we saw evidence of multiple possible long-term balance regimes.

In the moist case, there is a clear strong dependence of balanced and unbalanced model runs on horizontal gridlength and as such, regimes that don't require a collapse of scales to be achieved are not viable in the moist case. The addition of moist processes causes shrinking of the horizontal lengthscale to the gridlength and

therefore moist variants of the WTG and BLWTG regimes are not achievable when moisture is included in model runs without also including other mitigating processes such as turbulence which might limit the collapse of scales. The gridlength also has a further effect on model behaviour, affecting whether or not a model run can actually achieve balance because of how it affects the horizontal lengthscale L and therefore the drag parameter D, with the link between the two affecting whether Darcy's balance can develop. The gridlength also has a substantial effect on the transient model response, with model gridlength affecting the triggering and organisation of moist plumes.

Drag strength appears to have a very minor effect on the triggering, sustaining and organisation of moist plumes in our model runs. Large difference appear to occur only when the increase in drag also causes the model boundary layer to fall into a long-term balance regime – in this case, the moist variant of ADBL in the continuously heated case or the MUBL regime in the initially heated case. Of particular note was the effect of long-term balance on the horizontal advection of moisture with model runs that were balanced showing slower triggering of plumes and organisation of plumes favouring more plumes drawing less moisture in the horizontal over fewer plumes drawing more moisture in the horizontal in the unbalanced runs.

In the initially heated runs, we also saw that as the relative humidity in the boundary layer decreases, the drag strength becomes more important in determining the model behaviour with respect to plume triggering with higher drag allowing plume triggering at a lower relative humidity in the boundary layer – provided balance is achieved. At lower but non-zero boundary layer relative humidity, the model behaved more like the dry case.

Going forwards, an investigation of transition points for boundary layer relative humidity in the continuously heated cases may provide insights into where regimes such as WTG and BLWTG become infeasible due to the presence of too much moisture and which processes and process interactions are necessary to include in models alongside moisture to limit the collapse of scales observed in the model runs in this chapter.

We may also want to consider a statistical time-average of the model runs to see whether model runs that appear unbalanced due to the presence of gravity waves could be oscillating around a balance state. Model runs which oscillate around a balance state without settling cannot be considered truly balanced, but could

nonetheless be important to understanding balance in the tropical atmosphere.

Chapter 5

Weak Temperature Gradient Adjustment with Drag Physics

Having considered balance states in the tropics in both the moist and dry cases, we now look more closely at the adjustment to balance process. In particular, we look at two different questions related to adjustment to balance.

Firstly, we consider the role of an artificial lateral sponge layer – used as a proxy for real wave dispersion and damping – in enabling a model to adjust towards a horizontally uniform Weak Temperature Gradient State. More specifically, we will investigate the interplay of resolution and damping strength. In this chapter, we derive wave solutions for the hydrostatic, Boussinesq equations with Rayleigh drag in the horizontal velocity equation. We then use a sponge layer to analyse wave behaviour in the drag damped part of the Thuburn (2017) model. We find there is a critical damping timescale indirectly dependent on the model resolution and how well-resolved the initial potential temperature perturbation is. Below the critical damping value, there can be no propagation of waves in the damped sponge layer. Above the critical value, waves propagate but decay over time. Thus, adjustment to a horizontally uniform Weak Temperature Gradient state is substantially affected by model resolution and the horizontal extent of the sponge layer.

Secondly, we will look at the role of boundary layer drag in the adjustment to balance process for the dry balance regimes outlined in chapter 3. Specifically, we will look at whether the timescales for adjustment to balance in each of the balance regimes in chapter 3 is related to the strength of boundary layer drag with respect to the resolution in the continuously heated case.

5.1 Introduction

Long-term balance is not the only kind of regime we might expect in a model and indeed there are important questions around transient behaviour prior to reaching a balanced state. Since a long-term balance state may be defined as a state in which fast motions such as waves are no longer present, the adjustment to balance is therefore the process of removing those fast motions and as such understanding the adjustment to a balanced state means understanding the process of removing those fast motions to allow balance to be established. Understanding the adjustment to a balanced state is therefore important for fully understanding how physical processes such as drag may impact the development of any balance states in the real-world or in models.

Likewise, it is particularly important to try to understand how the numerical implementation of processes such as drag may impact model results. Previous studies have considered hydrostatic adjustment (Lamb (1908), Bannon (1995)) and geostrophic adjustment (Gill et al., 1982) with numerical implementation being investigated by Winninghoff (1968) who looked at the effect of finite differencing on a one-dimensional geostrophic adjustment problem and Arakawa and Lamb (1977) who showed that grid staggering has a substantial effect on geostrophic adjustment. In this chapter, we consider the case of Weak Temperature Gradient adjustment. In particular, we look at the effect of resolution on gravity wave adjustment and the role of damping at the edges of the domain on adjustment to a horizontally uniform weak temperature gradient state.

Gravity waves are a well-documented part of the transient response in the tropics which allows the free troposphere to reach a Weak Temperature Gradient balance as well as potentially being part of the transient response before other tropical balance regimes explored in this thesis are reached as well. In the tropics, gravity waves can be triggered by processes such as convection and latent heating (Muller et al., 2018).

Gravity wave attenuation in the planetary boundary layer is also a phenomenon that has been studied in the past, especially in reference to lee-waves caused by orographic features such as mountains (Smith et al., 2002). Smith et al. (2006) show that interactions between the free troposphere flow and the boundary layer drag leads to either attenuation, reflection or no impact on gravity waves dependent

on the Reynolds number and the wavenumbers of the excited gravity waves. Jiang et al. (2006) then show that surface heat flux can have a mitigating effect on gravity wave attenuation in the boundary layer. The convective boundary layer has parallels with the ADBL regime from chapter 3 and so the boundary layer damping of gravity waves when Rayleigh drag is strong may play some part in the different adjustment to balance behaviours and properties observed in the ADBL, BLWTG and WTG regimes in chapter 3. Similarly Smith et al. (2006) note that they expect longer lee wave trains over the ocean where surface drag is weaker compared to rougher surfaces with higher surface drag. It should be noted that Smith et al. (2002) and Jiang et al. (2006) focus on gravity waves driven by orographic features whereas we concern ourselves predominantly with convectively driven gravity waves. However Smith et al. (2006) use the same theoretical analysis for both types, so parallels can be drawn between boundary layer attenuation of orographically generated gravity waves and convectively generated gravity waves.

Gravity waves in the adjustment process have been studied in the context of inertia gravity-waves for geostrophic adjustment (Arakawa and Lamb, 1977). Muller et al. (2018) show that momentum flux associated with gravity waves is substantially better resolved for fine model resolutions. It is also well-known that how well waves themselves are resolved is affected by model resolution with the largest resolvable horizontal wavenumber in any given model being $\pi/\Delta x$, where Δx is the horizontal gridlength in the model.

Our investigation in this chapter has two parts. Firstly, we provide a mathematical analysis of the effect of constant drag on gravity waves and how resolution also impacts the results from the theoretical analysis in a weak temperature gradient adjustment problem. Secondly, we will look at whether gravity wave damping via boundary layer drag strongly affects balance regimes and adjustment to balance timescales.

For our first set of experiments, where we look at weak temperature gradient adjustment with a sponge-layer, we will use the 2D semi-langrangian, semi-implicit model of Thuburn (2017) to investigate model response to initial heating and continuous damping at the edges of the horizontal domain. We implement the damping as a 'sponge-layer' at the horizontal edges of the domain to represent waves passing out of the domain as should be the case in the real-world. How well the waves are damped is then important as in the real world, there would be no reflection of waves

at the horizontal side boundaries. Sponge layer techniques are common in limited area models to prevent reflection effects at the boundaries of horizontal domains. They are also used in the top boundary of models to prevent reflection of acoustic waves. Klemp and Lilly (1978) for example use a sponge layer on the top boundary to form a more robust analysis of hydrostatic mountain waves. Klemp et al. (2008) also apply a sponge-layer to the top boundary for an analysis of gravity wave damping in split-explicit models. The use of initial heating to excite wave activity is a fairly standard setup for adjustment problems (e.g. Bannon (1995), Klemp and Lilly (1978)).

We will then vary the horizontal resolution of the model, the strength of the damping timescale and the horizontal extent of the sponge layer to check which factors have an effect on the representation of gravity waves and the adjustment to balance – here, a weak temperature gradient state. However, it should be noted that for this chapter, unlike the complexity of the WTG regimes presented earlier in this thesis, the weak temperature gradient state for our first set of experiments will be read to mean a balance state in which horizontal temperature gradients are zero or negligeably small.

We will show that the adjustment to balance is substantially affected both by the strength and the extent of the sponge layer as well as the resolution which has an effect on the highest resolvable wavenumbers in any given model.

For our second set of experiments, we will consider again the results from chapter 3 with Rayleigh drag in the boundary layer and elliptical heating to represent convective heating that can excite gravity waves in the real-world atmosphere. We will investigate whether the attenuation of gravity waves in the boundary layer due to the Rayleigh drag has an effect on the development of the ADBL and BLWTG balance regimes, and whether the absence of attenuation impacts the WTG regime. Thereby, we will also investigate whether there is any evidence that the difference in timescale for balance of the ADBL and BLWTG regimes may be a direct consequence of the attenuation of horizontally propagating gravity waves due to boundary layer drag.

5.2 Drag-Damped Gravity Waves

Let us first consider the theoretical effect of drag-damping on the reflectivity or absorption of waves in the drag-damped layer since whether waves are reflected or absorbed will affect the adjustment towards a balanced state. By considering the hydrostatic, drag-damped, Boussinesq 2D Euler equations, we can obtain a condition for gravity waves to exist within the drag-damped part of a model. Usually, the Boussinesq assumption holds only for regions where the depth of the dynamics is much less than the troposphere as in the boundary layer for example (e.g. Kosovic and Curry (2000)), but the anelastic model often gives an approximation to Boussinesq solutions which are often qualitatively correct.

5.2.1 Hydrostatic, drag-damped, Boussinesq Equations

Consider a set of simplified Euler equations with a drag term in the horizontal momentum equation (5.1) and no heating rate in the buoyancy equation (5.3). These equations are hydrostatically balanced from the vertical momentum equation (5.4) and Boussinesq in the mass conservation equation (5.2). The equations have been linearized and primes denote perturbations of the variable compared to the initial state. The equations without damping are given by Vallis (2017) and here we add damping to the horizontal momentum equation.

$$\frac{\partial \phi'}{\partial x} = -\frac{\partial u'}{\partial t} - \frac{u'}{\tau}; \tag{5.1}$$

$$\frac{\partial u'}{\partial x} = -\frac{\partial w'}{\partial z}; \tag{5.2}$$

$$\frac{\partial b'}{\partial t} = -w' N^2; \tag{5.3}$$

$$\frac{\partial \phi'}{\partial z} = b_0 + b'. \tag{5.4}$$

Here, u is the horizontal velocity, w is the vertical velocity, b is buoyancy, ϕ is a reduced pressure perturbation such that $\phi' = p'/\rho'$ and $\frac{u}{\tau}$ is a linear drag term, such as Rayleigh drag with τ a drag timescale. In this analysis, we assume τ is constant. However, in model sponge layers, τ will normally vary from the beginning of the sponge layer to the model edge. Likewise, in model boundary layers τ will vary with height. As long as τ does not vary too much in the horizontal in the sponge

layer or in the vertical in the boundary layer, then the theory should still be a good approximation. Before linearization, the thermodynamic variable b takes the form

$$b = b_0(z) + b'(x, z, t),$$

where the mean (or initial reference state b_0) is a function of height only. The reference velocities are not functions of height and before linearization are given by

$$u = \bar{u} + u'(x, z, t)$$

$$w = \bar{w} + w'(x, z, t).$$

For our purposes, we have taken $\bar{w}$ and $\bar{u}$ to be zero as there is no circulation prior to the initial potential temperature perturbation and the subsequent circulation is driven by the initial perturbation.

5.2.2 Reducing to a Single Equation

Now we reduce our linearized equation set to a single equation for a single variable. We have 4 variables and 4 equations so this should be possible. First substitute equation (5.4) into equation (5.3):

$$\frac{\partial}{\partial t}\left(\frac{\partial \phi'}{\partial z} - b_0\right) = -w'N^2 \implies \frac{\partial}{\partial t}\left(\frac{\partial \phi'}{\partial z}\right) = -w'N^2, \tag{5.5}$$

as b_0 is a function of height only and $\frac{db_0}{dt} = 0$.

We now take the derivative of equation (5.5) with respect to x in order to substitute in equation (5.1) to give

$$\frac{\partial}{\partial t}\frac{\partial}{\partial z}\left(\frac{\partial \phi'}{\partial x}\right) = -N^2\frac{\partial w'}{\partial x} \implies \frac{\partial}{\partial t}\frac{\partial}{\partial z}\left(-\frac{\partial u'}{\partial t} - \frac{u'}{\tau}\right) = -N^2\frac{\partial w'}{\partial x} \tag{5.6}$$

We take a further derivative with respect to z of equation (5.6) to give

$$\frac{\partial}{\partial t}\frac{\partial^2}{\partial z^2}\left(-\frac{\partial u'}{\partial t} - \frac{u'}{\tau}\right) = -N^2\frac{\partial}{\partial x}\frac{\partial w'}{\partial z} \tag{5.7}$$

Now we can reduce to a single equation in u:

$$-\frac{\partial^2}{\partial t^2}\frac{\partial^2 u'}{\partial z^2} - \frac{1}{\tau}\frac{\partial}{\partial t}\frac{\partial^2 u'}{\partial z^2} = N^2\frac{\partial^2 u'}{\partial x^2} \tag{5.8}$$

5.2.3 Wave solution

We take a trial wave solution of the form $u = Ue^{(i(kx+mz-\omega t))}$. This gives us a dispersion relation:

$$-\omega^2 m^2 - i\frac{\omega m^2}{\tau} = -N^2 k^2, \tag{5.9}$$

which rearranges as

$$\omega^2 + i\frac{\omega}{\tau} - \frac{N^2 k^2}{m^2} = 0. \tag{5.10}$$

We can now solve with the quadratic formula for ω to give:

$$\omega = \frac{-\frac{i}{\tau} \pm \sqrt{\frac{i^2}{\tau^2} + 4\frac{N^2 k^2}{m^2}}}{2} \implies \omega = -\frac{i}{2\tau} \pm \sqrt{\frac{-1}{4\tau^2} + \frac{N^2 k^2}{m^2}}. \tag{5.11}$$

A similar formulation for ω for molecular viscosity in Boussinesq fluid can be found in Vadas and Fritts (2005). We then obtain

$$u' = Ue^{i\left(kx+mz+\left(\frac{i}{2\tau}\pm\sqrt{\frac{-1}{4\tau^2}+\frac{N^2k^2}{m^2}}\right)t\right)}. \tag{5.12}$$

We can also derive polarization equations for the other variables w',ϕ', and b' in terms of u' by substituting our solution for u' from equation (5.12) back into equations (5.1)-(5.3).

Since all the variables will have a similar wave-like form to u', we can say that for any given variable a we have

$$\frac{\partial a}{\partial x} = ika, \quad \frac{\partial a}{\partial z} = ima, \quad \frac{\partial a}{\partial t} = -i\omega a, \tag{5.13}$$

and any higher order derivatives will follow a similar pattern.

We find ϕ' first using equation (5.1) to give

$$\frac{\partial \phi'}{\partial x} = -\frac{\partial u'}{\partial x} - \frac{u'}{\tau} \implies ik\phi' = i\omega u' - \frac{u'}{\tau}, \tag{5.14}$$

which re-arranged gives

$$\phi' = \frac{1}{ik}\left(i\omega - \frac{1}{\tau}\right)u'. \tag{5.15}$$

Likewise, we can then find w' from equation (5.2).

$$\frac{\partial w'}{\partial z} = -\frac{\partial u'}{\partial x} \implies imw' = iku', \tag{5.16}$$

which re-arranged gives

$$w' = -\frac{k}{m}u'. \tag{5.17}$$

And finally, we find b' from equation (5.3).

$$\frac{\partial b'}{\partial t} = -w'N^2 \implies -i\omega b' = \frac{k}{m}u'N^2, \tag{5.18}$$

which re-arranged gives

$$b' = -\frac{kN^2}{im\omega}u' \tag{5.19}$$

5.2.4 Low and High Friction Limits

Having outlined our equations for the variables, we can now look at the solutions in two limits. Specifically, we look at the solutions for ω in equation (5.11) in two limits:

Low friction limit: In the low friction limit, where $\tau \to \infty$, this is of course the traditional 2D Boussinesq, hydrostatic gravity waves dispersion relation i.e. $\omega = \pm\frac{Nk}{m}$ (Vallis, 2017).

High friction limit: In the high friction limit, where $\tau \to 0$ we have that $\frac{1}{4\tau} \gg \frac{N^2k^2}{m^2}$ and so we get an infinite imaginary part of ω and no real part. Thus in theory, this means no propagation of waves.

5.2.5 Small but non-zero τ

Of course, there will be some space between the two limits where τ is asymptotically neither large nor small and both terms in the square root may or may not be significant. This gives us three inequality cases and corresponding values for ω.

Case 1: If we assume $\frac{1}{4\tau^2} \gg \frac{N^2k^2}{m^2}$, we get two possible solutions for ω. The first is $\omega \approx 0$ and corresponds to the steady state, which we define to be Darcy's

balance (Beare and Cullen, 2012), a state in which there are no gravity waves and the boundary layer has achieved balance. We can see this if we substitute $\omega \approx 0$ into equation (5.15) so that we get

$$\phi' = \frac{1}{ik\tau}u'. \tag{5.20}$$

If we consider only the real part, we get $Re[\phi'] = 0$ and so ϕ' has no relation u'.

The second solution for ω is then $\omega = -\frac{i}{\tau}$. In this friction case where τ is small but not zero, $\omega = -\frac{i}{\tau}$, and if we seek a solution of the form $u' = Ue^{i(kx+mz-\omega t)}$ and substitute into equation (5.8), we will obtain a solution for the horizontal velocity of the form:

$$u' = Ue^{i(kx+mz+it/\tau)} \implies u' = Ue^{i(kx+mz)}e^{-t/\tau}. \tag{5.21}$$

In other words, in the case where drag is significant in the Boussinesq equations and $\frac{1}{4\tau^2} \gg \frac{N^2k^2}{m^2}$, waves either do not propagate i.e. $\omega \approx 0$, or the waves decay very quickly over time, decaying faster as τ decreases. In other words, waves cannot exist for long in strongly-damped parts of a model. Note also that in equation (5.21), the wave decay is approximately independent of the horizontal and vertical wavenumbers. Notably, the non-zero solution for ω is again imaginary as with the $\tau \to 0$ case, suggesting no waves can propagate even if ω is non-zero.

In this friction case with $\omega = -\frac{i}{\tau}$, we would again find that ϕ' is independent of u' as

$$\phi' = \frac{1}{ik}\left(\frac{-i^2}{\tau} - \frac{1}{\tau}\right)u' \implies \phi' = 0. \tag{5.22}$$

Case 2: If we assume $\frac{1}{4\tau^2} = \frac{N^2k^2}{m^2}$, we get only one repeated solution: $\omega = -\frac{i}{2\tau}$ or $u = Ue^{i(kx+mz)}e^{-t/2\tau}$. Again, this would mean ω has no real part and wave propagation will be impossible.

Case 3: If we assume $\frac{1}{4\tau^2} \ll \frac{N^2k^2}{m^2}$, we get the case which does provide a real part to the solutions for ω, though unlike non-damped, hydrostatic waves, the solutions also each contain an imaginary part.

The solutions for ω in the case where $\frac{1}{4\tau^2} \ll \frac{N^2k^2}{m^2}$ are

$$\omega = -\frac{i}{2\tau} + \sqrt{A}, \quad \omega = -\frac{i}{2\tau} - \sqrt{A}, \tag{5.23}$$

where A is positive and $\sqrt{A}$ is strictly real. The value of A is of course defined as $A = \frac{N^2k^2}{m^2} - \frac{1}{4\tau^2}$ from equation (5.11).

Assuming $u = Ue^{i(kx+mz-\omega t)}$, we now have two possible solutions for U:

$$u = Ue^{i(kx+mz-[-i/2\tau+\sqrt{A}]t)}; \quad u = Ue^{i(kx+mz-[-i/2\tau+\sqrt{A}]t)}. \tag{5.24}$$

Both of these can be split to give:

$$u = Ue^{i(kx+mz+\sqrt{A}t)}e^{-t/2\tau}; \quad u = Ue^{i(kx+mz-\sqrt{A}t)}e^{-t/2\tau}. \tag{5.25}$$

Note the factor $e^{-t/2\tau}$ in both solutions i.e. if waves do exist, they will be damped over time. We now give the polarization equations for case 3. For the vertical velocity, the polarization equation for w' for both solutions for ω in case 3 is the same as the other cases. ϕ' is as follows.

For $\omega = -\frac{i}{2\tau} - \sqrt{A}$, we have

$$\phi' = -\frac{1}{k}\left[\frac{i}{\tau} + \sqrt{A}\right], \tag{5.26}$$

and for $\omega = -\frac{i}{2\tau} + \sqrt{A}$, we have

$$\phi' = -\frac{1}{k}\left[\frac{i}{\tau} - \sqrt{A}\right]. \tag{5.27}$$

If we take only the real part of ϕ', both solutions give the same polarization relation e.g. $Re[\phi'] = \frac{1}{k}\sqrt{A}u'$.

From our theoretical analysis, it would seem that the key effects of the damping in the sponge layer will be either to prevent any propagation of waves and possibly therefore cause reflection at the edge of the sponge layer or to cause propagating waves to decay as they traverse the sponge layer as expected.

In particular, there will be a drag transition point as we increase the damping and therefore decrease the value of τ, but also in a model setting as we increase the resolution and increase the highest resolvable wavenumber . We will call this transition point τ_{tr} such that

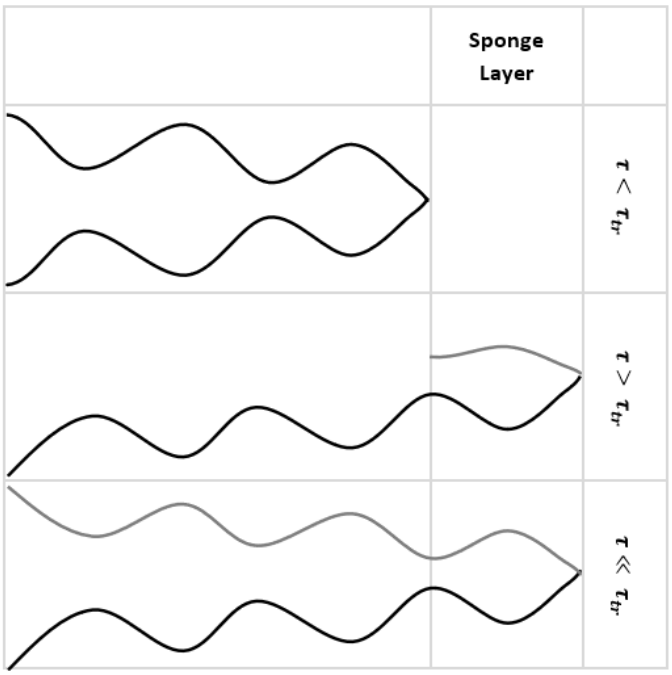

Figure 5.1: Proposed schematic of the effect of sponge layer on waves dependent on whether $\tau < \tau_{tr}$ as in case 1, $\tau > \tau_{tr}$ as in case 2 or $\tau \gg \tau_{tr}$ as in case 3. The heavy black line represents the wave at full strength whilst the grey line represents a damped wave.

$$|\tau_{tr}| = \left|\frac{m}{2Nk}\right|. \tag{5.28}$$

From there we have two separate wave behaviours in the sponge layer or boundary layer. When $|\tau| < \left|\frac{m}{2Nk}\right|$ or small τ, we have case 1 where ω is either zero or has no real part and therefore there will be no propagation of waves through the sponge layer. When $|\tau| > \left|\frac{m}{2Nk}\right|$ or larger τ, we have case 3 where ω has both imaginary and real parts and therefore waves should propagate through the sponge layer, but will decay over time with smaller values of τ causing faster decay. This is very similar to the results from Smith et al. (2006) who investigate the attenuation of convective gravity waves coming from above the boundary layer as well as orographic waves within the boundary layer as they traverse the boundary layer.

The cases do not depend on τ alone though as the values of N, k and m are also significant for determining the case and in any given model, k and m specifically will be affected by the resolution if the flow is under-resolved. The maximum resolvable horizontal wavenumber for a model with horizontal gridlength Δx will be

$\pi/\Delta x$ and the maximum resolvable vertical wavenumber will be $\pi/\Delta z$. Thus, we expect that the sponge layer damping will have different effects for different model resolutions and that the damping strength may need to be adjusted with reference to the resolution to obtain similar model behaviour at different model resolutions.

Figure 5.1 gives an idea of the effect on waves of different τ values in the sponge layer or boundary layer relative to the transition drag value. The cases here fit with the four cases outlined in Smith et al. (2006) for wave attenuation in the boundary layer based on interactions between surface friction and heat flux.

5.3 Weak Temperature Gradient Adjustment Experiments

We now look at the weak temperature gradient adjustment experiments to examine how the model resolution and the damping in the sponge layer affect the adjustment to a horizontally uniform state.

5.3.1 Model Setup

For the Weak Temperature Gradient Adjustment experiments, the model background state is set with a vertically stratified temperature field leading to vertically stratified pressure, density and entropy fields. The temperature field is again set by equation (3.73) from chapter 3. To this, we then add an initial potential temperature perturbation before the initial timestep to represent a burst of heating. We also include a sponge layer at the edges of the domain for the gravity wave experiments.

Horizontal Velocity Sponge Layer

At the edges of the model, we damp the horizontal velocity. To do this, we include a sponge layer at the edges of the domain for the gravity wave experiments. The sponge layer has form:

$$\frac{Du}{Dt} + c_p\theta\frac{\partial\pi}{\partial x} = -\frac{u}{\tau_s}F(x), \tag{5.29}$$

where τ_s is a relaxation time scale and $F(x)$ is

$$F(x) = \exp\left(-\frac{x^2}{H_r^2}\right) + \exp\left(-\frac{(x_D - x)^2}{H_r^2}\right). \tag{5.30}$$

Here, H_r is a relaxation length scale and x_D is the size of the horizontal domain. Note that $F(x) \approx 1$ at $x = 0$ m and $x = x_D$ m, provided H_r is sufficiently small that $F(x)$ is negligeably small at some point in the domain. Here, $x_D = 5,000$ km. When comparing to the theory from section 5.2, we will take $\frac{1}{\tau} = \frac{F(x)}{\tau_s}$. As τ_s is constant, we require that $\frac{\partial F(x)}{\partial x}$ is sufficiently small compared to the horizontal wavenumber k for the theory to hold.

Here, the first derivative is

$$\frac{dF(x)}{dx} = -\frac{2x}{H_r^2}\exp\left(-\frac{x^2}{H_r^2}\right) + \frac{2(x - x_D)}{H_r^2}\exp\left(-\frac{(x_D - x)^2}{H_r^2}\right). \tag{5.31}$$

and since H_r will be at least $100,000$ m, whilst x is at most $5,000,000$ m, the maximum change is $\frac{dF(x)}{dx} \sim 10^{-2}$ m^{-1}.

Damping might also be applied to the other variables in a similar fashion – for example, Klemp et al. (2008) choose to damp the vertical velocity as opposed to the horizontal velocity – but we do not examine this here as the horizontal damping is of most interest to the current study as it has more relevance to the results in the dry regimes chapter and in preliminary experiments, it was found that damping both vertical and horizontal velocity did not seem to have a large effect beyond damping only the horizontal velocity.

Initial Potential Temperature Perturbation

Heating is applied to the background state as a potential temperature θ perturbation before the first time step.

The potential temperature perturbation takes the form:

$$\theta_*(x, z) \approx 3.5K \times \cos^2\left[\frac{(z - z_0)\pi}{H_D}\right]\cos^2\left[\frac{(x - x_0)\pi}{0.1 \times x_D}\right], \tag{5.32}$$

where x_0 is the centre of the x-domain and z_0 is the centre of the z-domain. θ_* is equivalent to 3.5 K at the centre of the potential temperature perturbation and we impose $\theta_*(x, z) = 0$ at $\pm 0.005 x_D$ of the horizontal centre of the heating x_0. The

heating is elliptical in shape and stretches the entire height of the z-domain i.e. $H_D = 10$ km. The heating rate is zero at $z = 0$ m and $z = 10,000$ m.

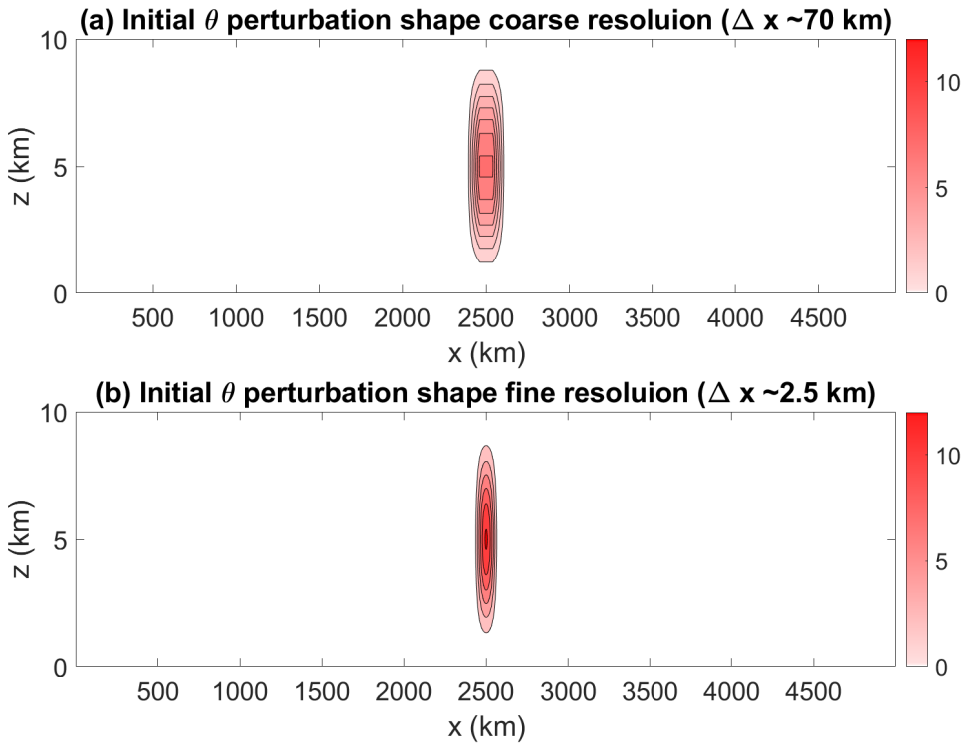

Figure 5.2: Shape of the initial θ perturbation in (a) the coarse resolution case and (b) the fine resolution case. Coarse resolution is ∼70 km and fine resolution is ∼2.5 km. Both initial θ perturbations shown in the figure are the same horizontal extent, but the fine resolution case appears thinner due to a higher number of points in the horizontal and the computer interpolation of the contour lines.

As in chapter 3, we add compensating cooling of the form:

$$S'(z) = \frac{1}{x_D} \int_0^{x_D} \theta_*(x, z) dx, \tag{5.33}$$

where x_D is the size of the x-domain and the total potential temperature perturbation is then

$$\theta'(x, z) = \theta_* - S'. \tag{5.34}$$

A potential temperature perturbation of this form should ensure no net change in entropy over the full domain i.e.

$$\int_D \frac{c_p}{\theta_{ref}} q(x, z) dx dz = 0. \tag{5.35}$$

The shape of the initial potential temperature perturbations are given in figure 5.2 for the $\Delta x \sim 2.5$ km case and the $\Delta x \sim 70$ km case. We see in figure 5.2 that the initial potential temperature perturbation is better resolved for the $\Delta x \sim 2.5$ km case, with the $\Delta x \sim 70$ km case containing only six positive points in the horizontal and having a rougher shape due the spacing of the points. The $\Delta x \sim 70$ km perturbation is also weaker than the $\Delta x \sim 2.5$ km case.

5.3.2 Experiment Outline

Our first set of experiments involves a dry troposphere setup. We use a domain size of $5,000$ km in the horizontal and 10 km in the vertical. We put an initial θ perturbation in the middle of the domain, stretching the whole length of the troposphere (10 km), but only stretching ~ 100 km in the horizontal. We will not vary the size of the horizontal domain or vertical domain in the experiments in this chapter, but we will vary the horizontal resolution Δx.

We run the test with a coarse horizontal resolution ($\Delta x \approxeq 70$ km) and a fine horizontal resolution ($\Delta x \approxeq 2.5$ km). We analyse the gravity wave response to the initial θ perturbation to understand how varying resolution and the horizontal extent of the sponge layer affects relaxation towards equilibrium, specifically how quickly the model returns to the weak temperature gradient background state and how this is affected by damping in the sponge layer.

5.3.3 Results

Results from the model are split by section. First we consider the effect of resolution, then we consider the interplay – if it exists – between resolution and damping as predicted by the theory.

Potential Temperature Adjustment to Horizontally Uniform Weak Temperature Gradient State

We begin by varying the parameters in the sponge layer to observe the effect of the damping on gravity wave activity and on the transition to a weak temperature gradient state. Within this, we will also consider the effect of resolution and we look at two different resolutions: $\Delta x \sim 2.5$ km ($\Delta x \sim 10^3$ m) and $\Delta x \sim 70$ km ($\Delta x \sim 10^4$ m).

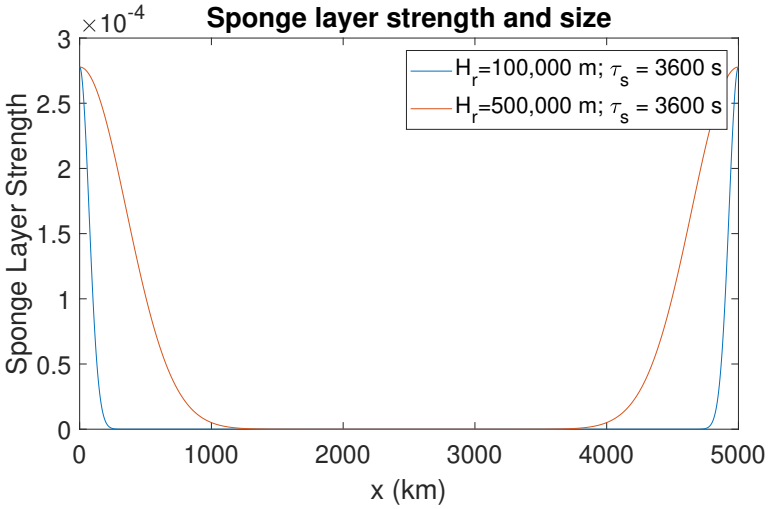

Figure 5.3: Sponge layer strength over horizontal domain for $H_r = 100,000$ m (blue) and $H_r = 500,000$ m (red) both with $\tau_s = 3600$ s.

We will also look at two cases of the sponge layer width for each resolution – one case with $H_r = 100,00$ m and one case with $H_r = 500,000$ m. The shape of the sponges are plotted in figure 5.3 with $H_r = 100,000$ m in blue and $H_r = 500,000$ m in red. These correspond to sponge layer widths at the sides of the domain of approximately 250 km and 1250 km respectively, with a much steeper gradient in τ in the $H_r = 100,000$ m case. We have plotted the sponge layers where $\tau_s = 3600$ s, but the shape will be very similar for other non-zero and non-infinite values of τ_s, except of course that the strength of the sponge layer on the y-axis will change with τ_s. It should be noted that the lines in figure 5.3 are from the $\Delta x \sim 2.5$ km runs and at $\Delta x \sim 70$ km, the $H_r = 100,000$ m cases contain few points in the horizontal within the sponge layer.

Sponge Layer with $H_r = 100$ km

The size of the sponge layer in the $H_r = 100,000$ m case is given by the blue line in figure 5.3. Using this sponge layer, but varying the strength of damping parameter τ_s, we can examine how well and how quickly the model settles to a weak temperature gradient state – that is to say a state where the horizontal temperature gradients are zero. Figure 5.4 shows the coarse version of the model ($\Delta x \sim 70$ km) with the different strengths of damping parameter τ_s ranging from $\tau_s = 360$ s to $\tau_s = 36000$ s. In figure 5.4, we look at the L2 norm of potential temperature θ with respect to the horizontal mean $\bar{\theta}$ at the same timestep to check adjustment towards

a horizontally uniform state in θ.

The L2 norm of θ with respect to the horizontal mean $\bar{\theta}$ at the same timestep is given by

$$\theta_{norm} = \frac{1}{x_D H_D} \int_{H_D} \int_{x_D} \left(\theta - \bar{\theta}\right)^2 dxdz \tag{5.36}$$

where

$$\bar{\theta} = \frac{1}{x_D} \int_0^{x_D} \theta(x, z) dx \tag{5.37}$$

and where θ is the current potential temperature field. Again, x_D represents the size of the x-domain.

When $\Delta x \sim 10^4$ m, the smoothest damping of gravity waves occurs when $\tau_s = 3600$ s as evidenced in figure 5.4. For larger τ_s and smaller τ_s, the results are more chaotic with peaks in the green and blue lines in figure 5.4 suggesting reflection of waves occurring for the first time at approximately $50,000$ s. This implies there is some value for τ_s that is optimal for giving the fastest adjustment to a weak temperature gradient state by preventing unphysical reflection of waves at the side boundaries of the model. Klemp and Lilly (1978) also found reflection of waves when the strength (or viscosity) of the sponge layer was too strong as well as when the strength of the sponge layer was too weak. They looked specifically at acoustic waves and top boundary sponge layers.

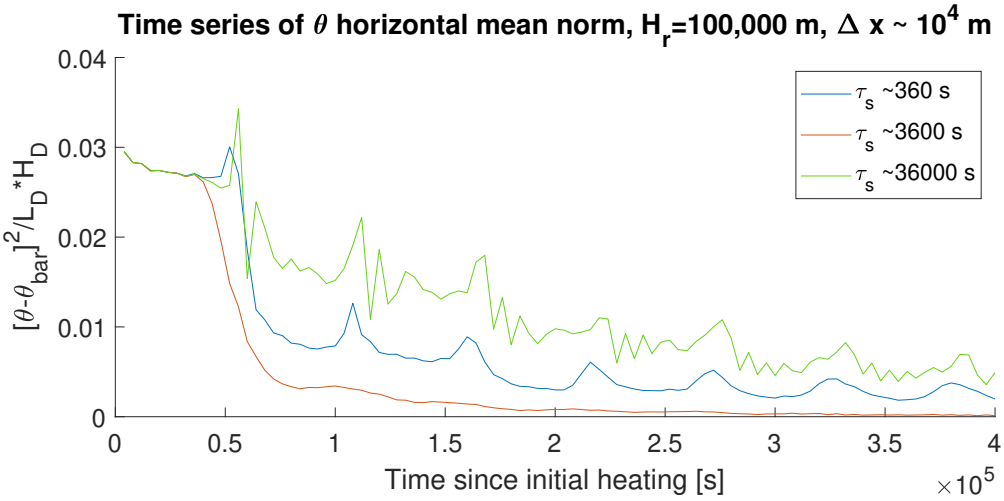

Figure 5.4: Coarse resolution model runs ($\Delta x \sim 10^4$ m) with initial θ perturbation and $\tau_s = 360$ s (blue), $\tau_s = 3600$ s (red), $\tau_s = 36000$ s (green). L2 norm of θ profile against mean θ profile at each timestep. $H_r = 100,000$ m.

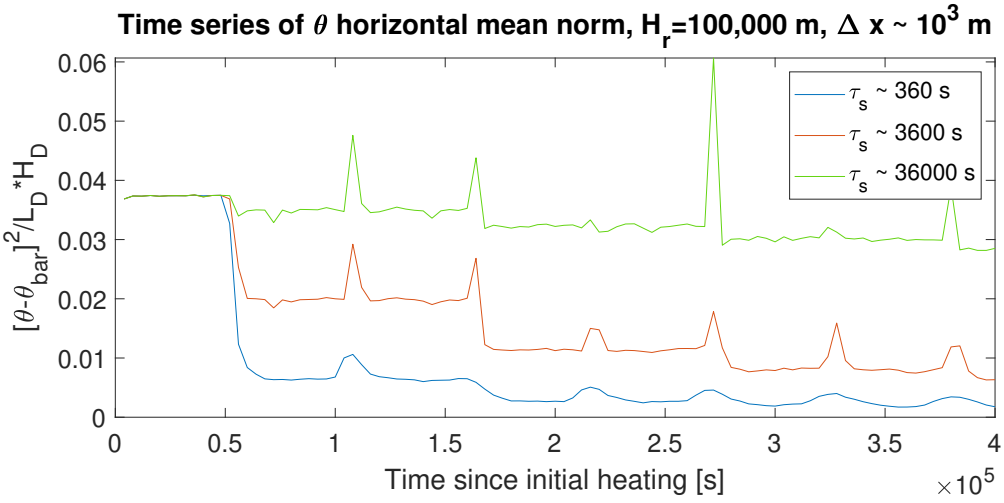

Figure 5.5: Fine resolution model runs ($\Delta x \sim 10^3$ m) with initial θ perturbation and $\tau_s = 360$ s (blue), $\tau_s = 3600$ s (red), $\tau_s = 36000$ s (green). L2 norm of θ profile against mean θ profile at each timestep. $H_r = 100,000$ m.

In the fine resolution case where $\Delta x = 10^5$ m, the strongest damping with $\tau_s = 360$ s is the most effective at returning the model to a weak temperature gradient state with minimal evidence of wave reflection at the side boundaries.

Note that for any resolution Δx, the highest resolvable horizontal wavenumber is $\pi/\Delta x$ so for the coarse resolution model runs where $\Delta x \sim 10^4$ m, the highest resolvable horizontal wavenumbers will be in the region $\pi/10^4$ or 10^{-4} m^{-1}. Considering again the theory and specifically the drag transition point in equation (5.28), we should also consider the dominant wavenumber in the vertical which should be $\pi/H_D \sim 10^{-4}$ m^{-1} or a wavenumber corresponding to half a wavelength over the full vertical domain H_D due to the shape of the heating. The largest resolvable vertical wavenumber would be of course $\pi/\Delta z$. We take also $N^2 \sim 10^{-4}$ s^{-2} to give a drag transition point $\tau_{tr} \sim 10^2$ s (see table 5.1). This means if $\tau \leq \tau_{tr}$ for $\tau = \tau_s/F(x)$, we fall into case 1 or case 2 from section 5.2 where waves should be incapable of propagating through the sponge layer and therefore might be reflecting as though the sponge layer is a solid boundary.

When $\tau > \tau_{tr}$, the waves should be able to propagate through the sponge layer as in case 3 of section 5.2, but of course, as τ increases, the damping gets weaker and so the waves might be insufficently damped by the sponge layer. As with $\tau \leq \tau_{tr}$, values of τ that are much larger than τ_{tr} will also demonstrate reflective behaviour, though the reflections are likely to be occurring at the boundary edge as opposed to the sponge layer edge as should be the case for $\tau \leq \tau_{tr}$.

Resolution Δx	**10^3**	**10^4**	**10^5**	[m]
$\max(k)$	10^{-3}	10^{-4}	10^{-5}	[m^{-1}]
m	10^{-4}	10^{-4}	10^{-4}	[m^{-1}]
N	10^{-2}	10^{-2}	10^{-2}	[s]
$\tau_{tr} = \left\lvert \frac{m}{2Nk} \right\rvert$	10	10^2	10^3	[s]

Table 5.1: Table of maximum resolvable wavenumbers by resolution, the buoyancy frequency and the transition point at which waves will no longer be able to propagate in the sponge layer.

In the fine resolution case, where $\Delta x \sim 10^3$ m, the highest resolvable horizontal wavenumbers will be in the region $\pi/10^3$ or 10^{-3} m^{-1} whilst the values of N and m remain unchanged (see table 5.1). This means that the drag transition point is $\tau_{tr} = 10$ s and therefore $\tau_s/F(x) > \tau_{tr}$ is satisfied when $\Delta x = 10^3$ m for all values of τ_s in figure 5.5 and the damping is at least partially effective for all the runs.

Sponge Layer with $H_r = 500$ km

The size of the sponge layer in the $H_r = 500,000$ m case is given by the red line in figure 5.3 and again we will vary the strength of damping parameter τ_s. Figures 5.7 and 5.8 show potential temperature norm plots for coarse and fine resolution runs for $H_r = 500,000$ m and for each value of τ_s. With the larger sponge layer size, we can see that $\tau_s = 360$ s performs best for both the $\Delta x \sim 10^4$ m and $\Delta x \sim 10^3$ m runs.

Given what we saw with the $H_r = 100,000$ m case and the optimum $\tau = \tau_s/F(x)$ needing to be above a certain threshold, it is pertinent to discuss now the behaviour of the $\Delta x \sim 10^4$ m, $\tau_s \sim 10^3$ m and $H_r = 500,000$ m case that performed best for our coarse resolution run. Since $\tau_s = 360$ s should give us a sponge layer where we have $\tau \leq 10^2$ s at peak strength, we might expect reflection of the waves as in the $H_r = 100,000$ m case. However, it is evident from figure 5.6 that in the $H_r = 500,000$ m, $\tau_s \sim 10^3$ s case, the sponge layer is less than 10^{-3} s in strength for 500 km in the horizontal before reaching the 10^{-3} s threshold, a region which is similar to the $H_r = 100,000$ m layer width. So it is possible that the majority of the damping of the coarse resolution run is occurring in the portion of the sponge layer where the strength of the sponge layer is weaker than 10^{-3} s.

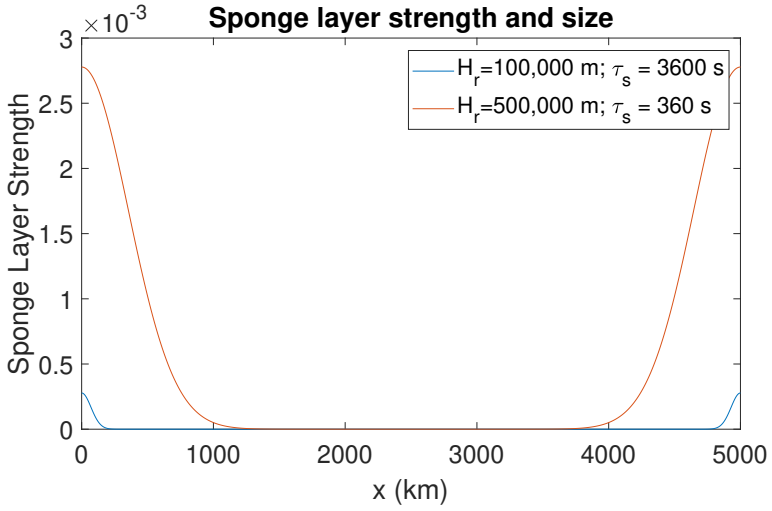

Figure 5.6: Sponge layer strength over horizontal domain for $H_r = 100,000$ m (blue) with $\tau_S = 3600$ s and $H_r = 500,000$ m (red) with $\tau_s = 360$ s.

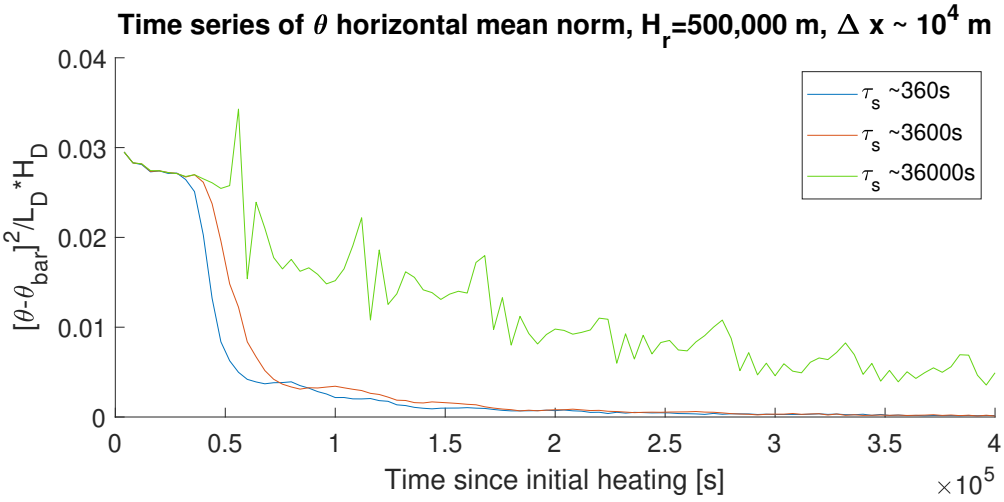

Figure 5.7: Coarse resolution model runs ($\Delta x \sim 10^4$ m) with initial θ perturbation and $\tau_s = 360$ s (blue), $\tau_s = 3600$ s (red), $\tau_s = 36000$ s (green). L2 norm of θ profile against mean θ profile at each timestep. $H_r = 500,000$ m.

We now look at Hovmoller plots (or x-t cross-sections) in figure 5.9 to check if reflection is occurring in the first 500 km of the sponge layer in the coarse resolution $H_r = 500,000$ m, $\tau_s = 10^3$ s case. Firstly, in figure 5.9, we can see evidence of at least two distinct wave patterns in both the $H_r = 100,000$ m and the $H_r = 500,000$ m cases. One wave crosses from the centre of the horizontal domain to the edge in approximately $50,000$ s with a speed of ~ 50 m/s. The second slower wave is approximately three times slower, reaching the edge of the domain at approximately $150,000$ s with a speed of ~ 16 m/s, both speeds are consistent with possible gravity waves. We can see that the damping of waves in subplot (a) of figure 5.9 where

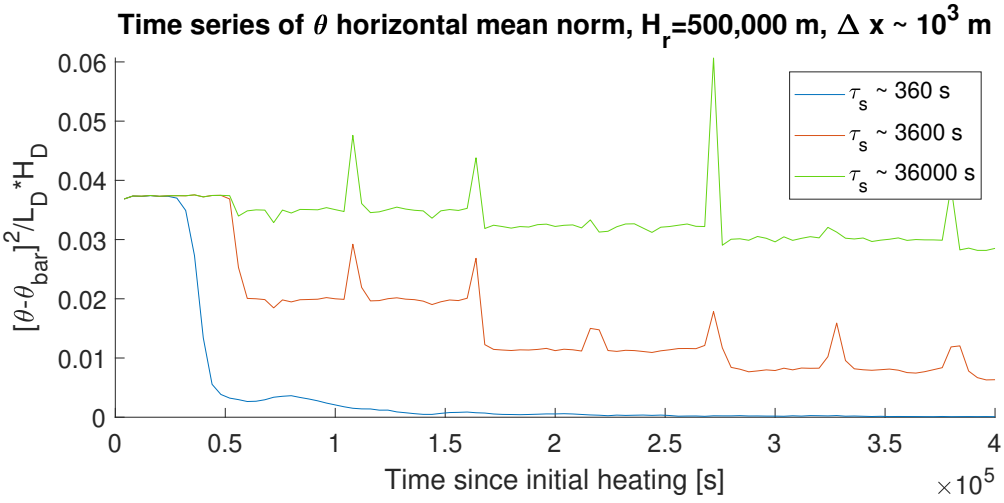

Figure 5.8: Fine resolution model runs ($\Delta x \sim 10^3$ m) with initial θ perturbation and $\tau_s = 360$ s (blue), $\tau_s = 3600$ s (red), $\tau_s = 36000$ s (green). L2 norm of θ profile against mean θ profile at each timestep. $H_r = 500,000$ m.

$H_r = 100,000$ m and $\tau_s = 3600$ s is occurring in the full sponge layer which is weaker than τ_{tr} .

In figure 5.9 subplot (b), we can see that in the $H_r = 500,000$ m, $\tau_s = 360$ s case, waves are being damped in the portion of the sponge layer that is weaker than τ_{tr} and there also appears to be reflection of waves within the sponge layer as the waves get damped before reaching the edge of horizontal boundary in figure 5.9 subplot (b). Indeed they get damped at ~ 500 km from the boundary, close to where the sponge layer in theory transitions to a value of τ that is greater than the transition point $\tau_{tr} \sim 10^2$ s in figure 5.6.

We now look at Hovmoller plots of the fine resolution runs with $H_r = 100,000$ m, $\tau_s \sim 10^4$ s and $H_r = 500,000$ m, $\tau_s \sim 10^4$ s. However the plots in figure 5.10 do not seem to show any remarkable differences. This is to be expected as there was little difference in the θ norm plots for $H_r = 500,000$ m, $\tau_s \sim 10^4$ s and $H_r = 100,000$ m, $\tau_s \sim 10^4$ s in figures 5.5 and 5.8 and in both cases, the resolution is fine enough that the heating is well-resolved. In figure 5.10, both cases have waves traversing the sponge layer and although the waves in the $H_r = 100,000$ m case spend less time in the sponge-layer due to the horizontal structure, the peak damping rate remains the same at $1/3600$ s^{-1} in figure 5.10. Each time waves traverse the sponge layer, they loose a little less than half their θ variance in figures 5.5 and 5.8 and so it takes multiple boundary reflections for waves to fall below detection level.

Thus, waves are not as efficiently damped in the fine resolution case when $\tau_s \sim 10^4$ s. When the heating is well-resolved, we will see waves with larger horizontal wavenumbers than in the under-resolved case. Since τ_{tr} depends on the value of k, if the heating is under-resolved, damping is affected by the maximum resolvable horizontal wavenumber of the model. When the heating is well-resolved, the dominant horizontal wavenumber will depend more on the structure of the heating and not so much on the resolution constraints.

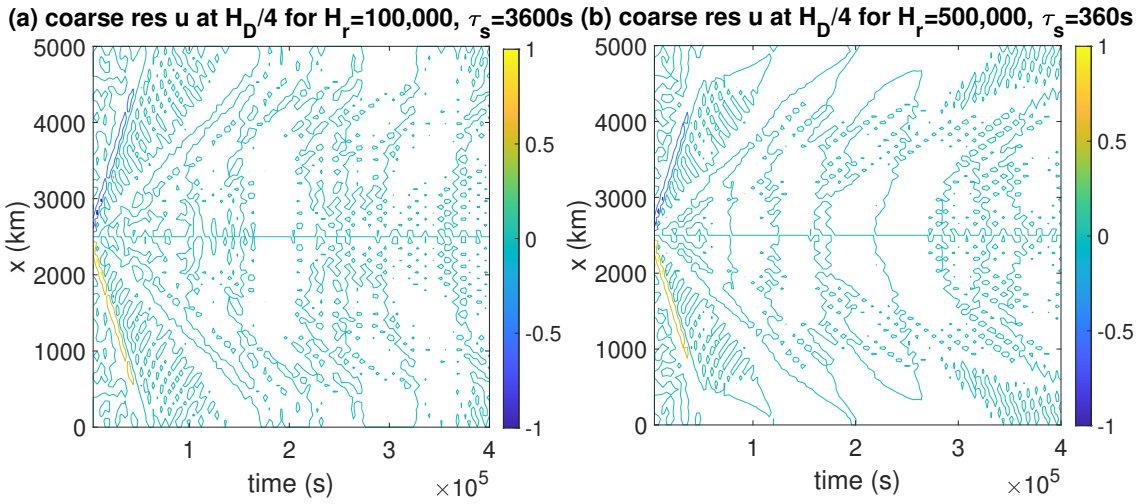

Figure 5.9: Hovmoller plots of horizontal velocity (u) in coarse resolution runs (approx 70 km) at height $H_D/4$. Subplot (a) has $H_r = 100,000$ m, $\tau_s = 3600$ s and (b) has $H_r = 500,000$ m, $\tau_s = 360$ s.

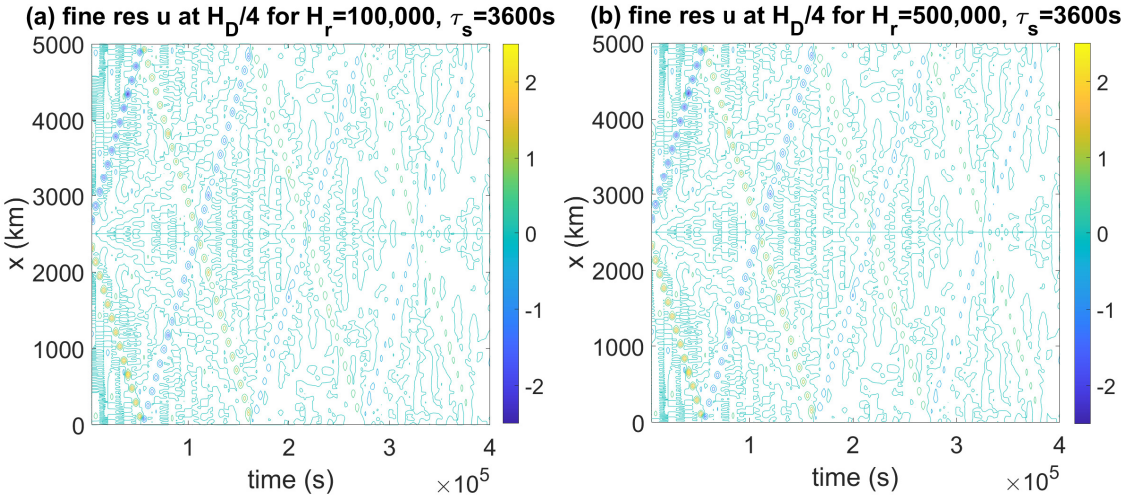

Figure 5.10: Hovmoller plots of horizontal velocity (u) in fine resolution runs (approx 2.5 km) at height $H_D/4$. Subplot (a) has $H_r = 100,000$ m, $\tau_s = 3600$ s and (b) has $H_r = 500,000$ m, $\tau_s = 3600$ s.

5.4 Gravity Waves in the Dry Continuously Heated Case

For our second set of results, we look again at the dry model runs in chapter 3 to analyse the presence of gravity waves during the adjustment to balance process. We look at the L106drag720, L106drag7200, L106drag72000, and L106nodrag cases in table 3.2, for heating $Q \sim 10^{-5}$ K/s since there is a clear distinction of regime after 7 days with resolution $\Delta x \sim 10^4$ m. The L106drag720 should be ADBL, whilst the L106drag7200 and L106drag72000 should be BLWTG, and the L106nodrag should be WTG. We will also look at results for $Q \sim 10^{-6}$ K/s and $Q \sim 10^{-4}$ K/s as well for a broader view of the model runs. In this section, it will be read that τ_s in the theory in section 5.2 is equivalent to τ_0 in the dry cases from chapter 3.

We recall that the heating in the dry case in chapter 3 was continuous and only in the boundary layer, stretching $\approx 1,000$ km in the horizontal (figure 3.2) and should be well-resolved when $\Delta x \sim 10^4$ m as in the dry case runs we re-investigate in this chapter. Thus, we do not expect reflection of waves to be a problem as observed in the under-resolved coarse resolution case in the weak temperature gradient adjustment experiments when the damping was very strong ($\tau_s \sim 10^2$). Instead, we would expect waves to be damped continuously as they traverse the boundary layer with different rates of attenuation dependent on the strength of the damping in the boundary layer (case 3: $\tau \gg \tau_{tr}$).

In particular, we expect the dry case runs from chapter 3 that have stronger boundary layer drag to damp waves faster than the runs that have weaker boundary layer drag. And we theorise that that the difference in damping efficiency of waves has an effect on how long the it takes for the different dry regimes in chapter 3 to be achieved. In other words, we expect dry regimes where there is typically stronger drag to have faster balance timescales.

5.4.1 Results

For our analysis, we look at Hovmoller plots for three heating rates: $Q \sim 10^{-4}$ K/s; $Q \sim 10^{-5}$ K/s; and $Q \sim 10^{-6}$ K/s. For each of the heating rates, we then look at four boundary layer drag strengths: $\tau_0 \sim 10^3$ s; $\tau_0 \sim 10^4$ s; $\tau_0 \sim 10^5$ s; and $\tau_0 \sim \infty$ (or no drag).

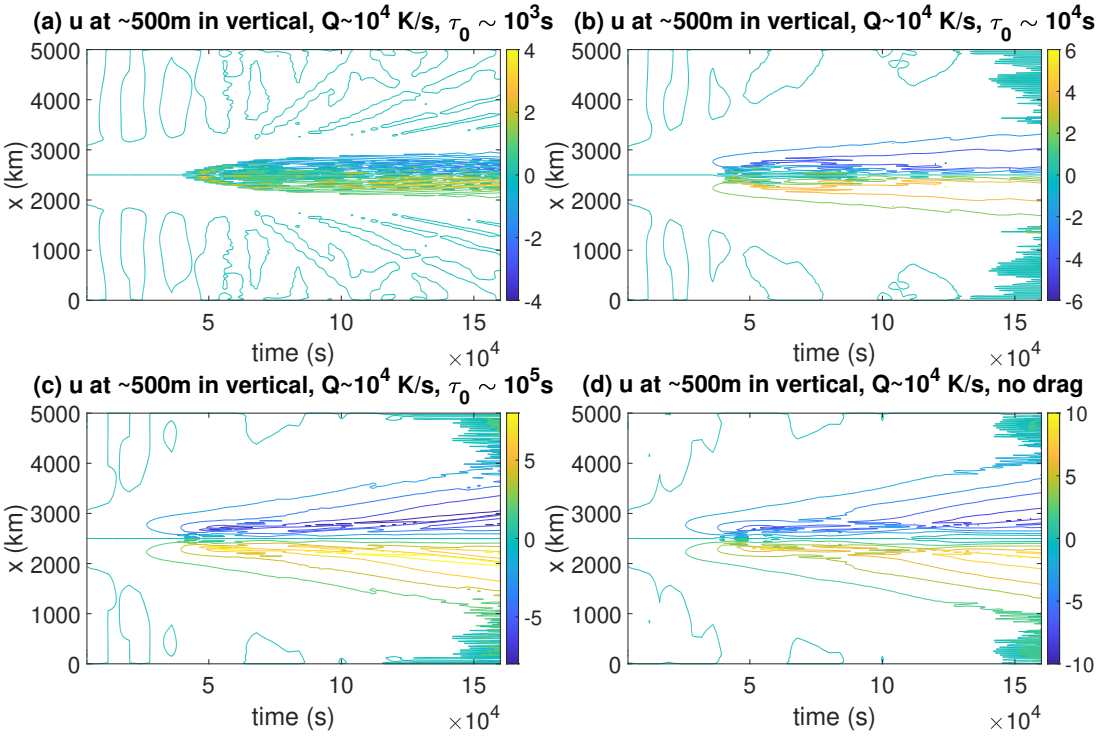

Figure 5.11: Hovmoller plots of horizontal velocity (u) in dry regime runs from chapter 3 at approximately 500 m in the vertical (middle of the boundary layer) with heating rate $Q \sim 10^{-4}$ K/s and horizontal resolution $\Delta x \sim 10^4$ m. Drag timescales in the boundary layer are (a) $\tau_0 \sim 10^3$ s, (b) $\tau_0 \sim 10^4$ s, (c) $\tau_0 \sim 10^5$ s, and (d) no drag.

In chapter 3, these were classed into regimes and here, we can see the different features of those regimes. Subplot (a) in figures 5.11, 5.12, and 5.13 shows that the $\tau_0 \sim 10^3$ s runs show clear evidence of circulation being confined in the ADBL regime, whilst the circulation moves outwards from the heating over time in subplots (b), (c), and (d), corresponding to BLWTG ($\tau_0 \sim 10^4$ s and $\tau_0 \sim 10^5$ s runs) and WTG ($\tau_0 \sim \infty$) regimes.

Figure 5.11 (a) also shows further evidence that the $\tau_0 \sim 10^3$ s, $Q \sim 10^{-4}$ K/s runs may not have been fully balanced as there is strong evidence of gravity waves in the middle vertical level of the boundary layer after around $t = 60,000$ s. The other runs however do appear to be balanced, especially in figures 5.12 and 5.13, where all the Hovmoller plots are smooth over the times depicted.

However, whether there are gravity waves before balance is reached is less clear, There is some evidence of the circulation fanning out in the horizontal from the start time onwards with higher drag runs fanning out more slowly. In figure 5.12,

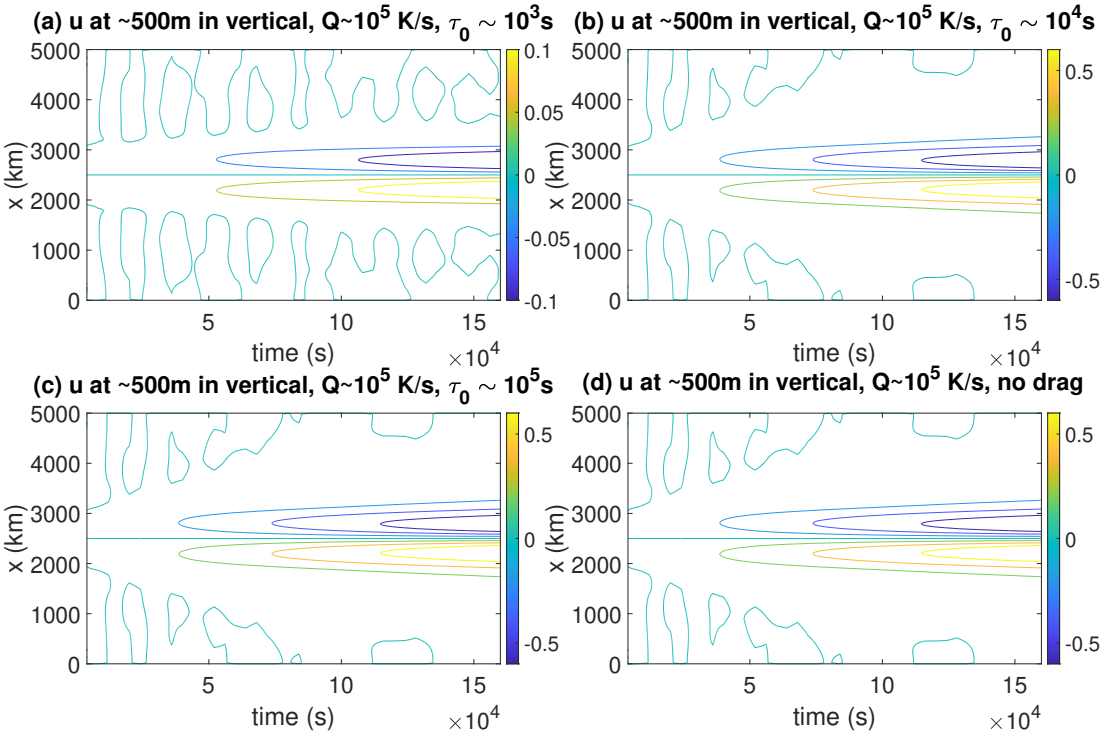

Figure 5.12: Hovmoller plots of horizontal velocity (u) in dry regime runs from chapter 3 at approximately 500 m in the vertical (middle of the boundary layer) with heating rate $Q \sim 10^{-5}$ K/s and horizontal resolution $\Delta x \sim 10^4$ m. Drag timescales in the boundary layer are (a) $\tau_0 \sim 10^3$ s, (b) $\tau_0 \sim 10^4$ s, (c) $\tau_0 \sim 10^5$ s, and (d) no drag.

it is very clear that subplots (b), (c) and (d) are behaving similiarly whilst subplot (a) shows much more confined horizontal behaviour. As balance is not reached until $T > 10^4$s in ADBL, and $T > 10^5$ s for BLWTG or WTG for $Q \sim 10^{-5}$ K/s (for $Q \sim 10^{-6}$ K/s, the balance timescales are shorter by at most an order of magnitude) we can assume that the behaviour of the model before the balance timescale might show transient behaviour such as gravity waves.

To better determine the existence or not of waves, we look at Hovmoller plots for the horizontal velocity minus some time-averaged horizontal velocity. The equation is below:

$$[u - u_{av}]_t\,; \quad u_{av} = \frac{1}{2t_{av}} \int_{t-t_{av}}^{t+t_{av}} u dt \tag{5.38}$$

where u_{av} is the time-averaged horizontal velocity and t_{av} is half of the total time we will be averaging over. Here, we take the time-averaging over $\approx 50,000$ s or $t_{av} = 25,000$ s as this was approximately the time taken in the weak temperature

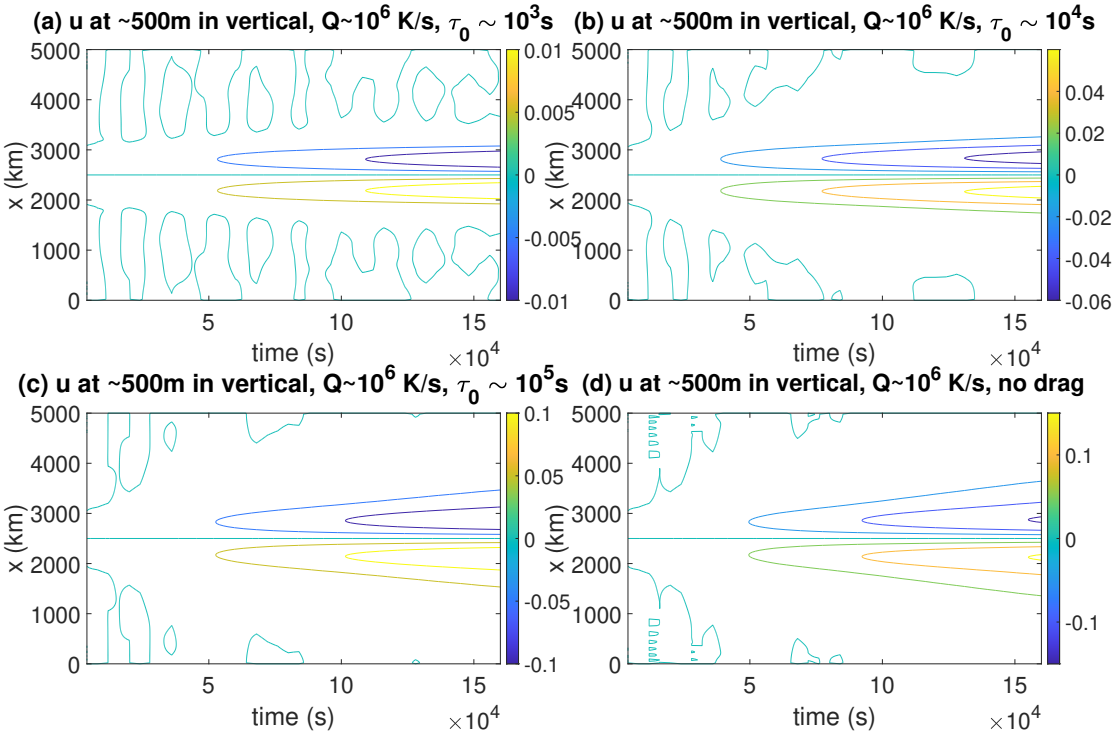

Figure 5.13: Hovmoller plots of horizontal velocity (u) in dry regime runs from chapter 3 at approximately 500 m in the vertical (middle of the boundary layer) with heating rate $Q \sim 10^{-6}$ K/s and horizontal resolution $\Delta x \sim 10^4$ m. Drag timescales in the boundary layer are (a) $\tau_0 \sim 10^3$ s, (b) $\tau_0 \sim 10^4$ s, (c) $\tau_0 \sim 10^5$ s, and (d) no drag.

gradient adjustment experiments for the gravity waves to traverse from the centre of the heating to the edges of the horizontal domain. We choose not to use the balance timescale in the averaging as the circulation is still developing before balance is reached.

Using the time-averaged calculation, we get Hovmoller plots for $u - u_{av}$ in figures 5.14, 5.15, and 5.16. Since these plots should look at the model settling to balance, we would expect a large wave signal initially which fades over time as balance is achieved.

Figure 5.14 shows evidence of waves in all the runs, with waves actually appearing to be most prominent in the $\tau_0 \sim 10^3$ s case. In the weaker and no drag cases, there is some evidence of the waves fading out or becoming less important to the circulation over time with any spokes getting replaced by what looks like very horizontally confined horizontal velocity circulations with a horizontal lengthscale corresponding to the horizontal gridlength. The waves in the $\tau_0 \sim 10^3$ s case appear more stable

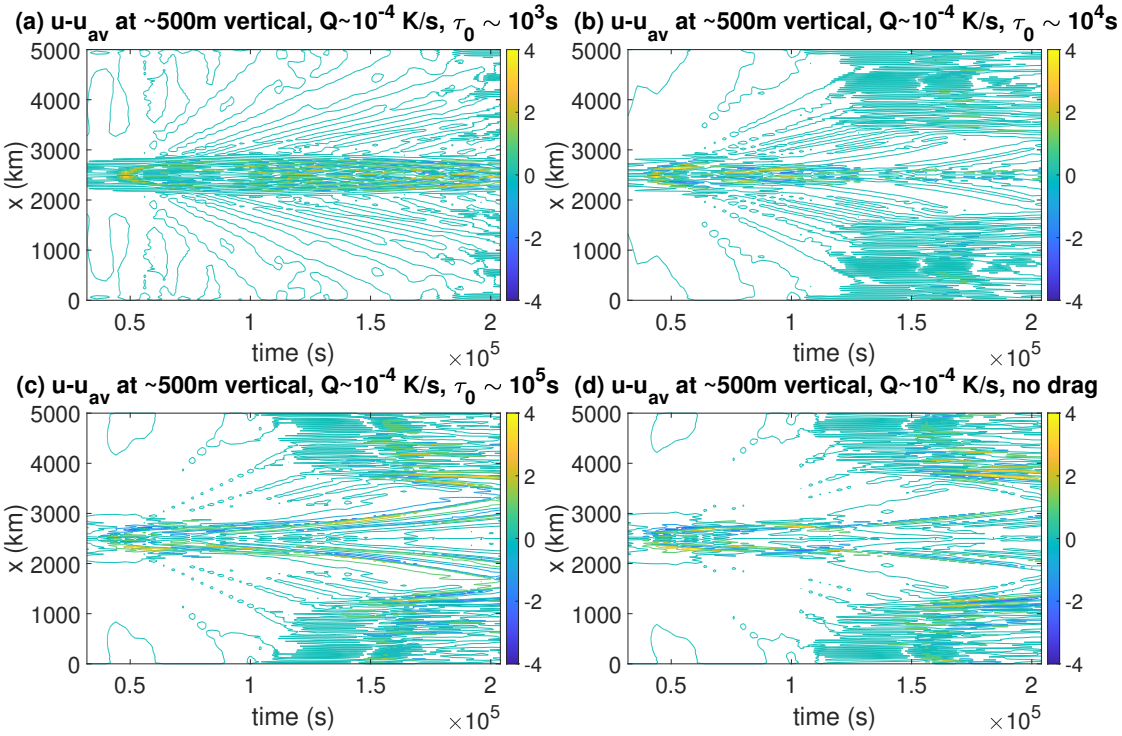

Figure 5.14: Hovmoller plots of horizontal velocity minus a time average of the horizontal velocity over $\sim 50,000$ s ($u - u_{av}$) in dry regime runs from chapter 3 at approximately 500 m in the vertical (middle of the boundary layer) with heating rate $Q \sim 10^{-4}$ K/s and horizontal resolution $\Delta x \sim 10^4$ m. Drag timescales in the boundary layer are (a) $\tau_0 \sim 10^3$ s, (b) $\tau_0 \sim 10^4$ s, (c) $\tau_0 \sim 10^5$ s, and (d) no drag.

than any of the other runs.

In figure 5.15, where $Q \sim 10^{-5}$ K/s, there is muted evidence of waves in subplots (b), (c) and (d) for waves with speeds of ~ 30 m/s and ~ 20 m/s, but very little evidence of waves in subplot (a). In figure 5.16 where $Q \sim 10^{-6}$ K/s, subplots (c) and (d) show some evidence of possible gravity wave structures with both subplots showing a significant area where the circulation fans out from the centre of the horizontal domain at a speed of approximately 10 m/s which is consistent with gravity waves. Subplot (b) in figure 5.16 shows muted potential gravity wave behaviour and subplot (a) shows even less with no obvious diagonal spokes denoting waves at time $t = 40,000$ s fanning out as time goes on. The lack of waves in subplot (a) in figures 5.15 and 5.16 could be due to the balance timescale already being reached at this point as we have $T > 10^4$ s which would mean balance could have been achieved if the model run falls into the ADBL regime.

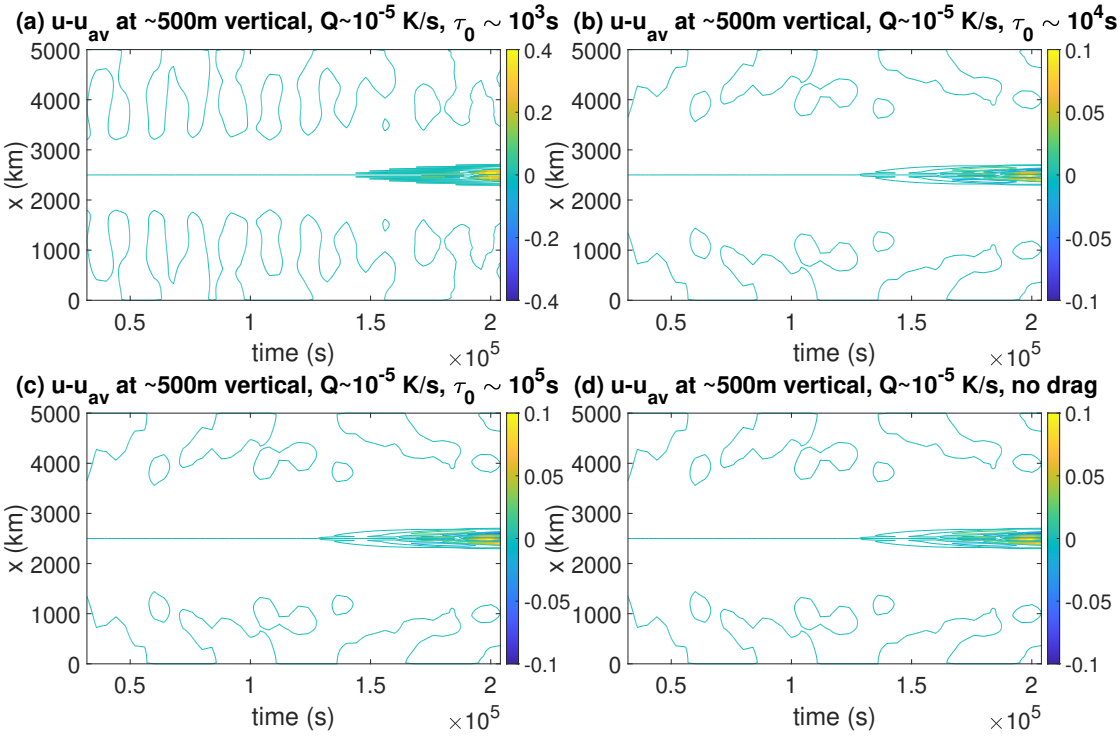

Figure 5.15: Hovmoller plots of horizontal velocity minus a time average of the horizontal velocity over $\sim 50,000$ s $(u - u_{av})$ in dry regime runs from chapter 3 at approximately 500 m in the vertical (middle of the boundary layer) with heating rate $Q \sim 10^{-5}$ K/s and horizontal resolution $\Delta x \sim 10^4$ m. Drag timescales in the boundary layer are (a) $\tau_0 \sim 10^3$ s, (b) $\tau_0 \sim 10^4$ s, (c) $\tau_0 \sim 10^5$ s, and (d) no drag.

5.5 Conclusions

Part of understanding balances in the tropics is understanding adjustment to balance. We have investigated the ability of the Thuburn (2017) model to return to a horizontally uniform Weak Temperature Gradient state after either a resolved or under-resolved initial potential temperature perturbation.

In this chapter, we derived wave solutions for the 2D dry hydrostatic, Boussinesq equations with Rayleigh drag in the horizontal momentum equation. We show that there is a critical damping timescale of drag above which waves cannot propagate at all. The critical damping timescale is dependent on the model horizontal and vertical resolution as well as how well-resolved the heating is. The adjustment to a horizontally uniform weak temperature gradient state is therefore substantially affected by the strength and extent of damping in the sponge layer.

We have also looked at the boundary layer behaviour in the dry balance runs in chapter 3 to ascertain whether strong drag relative to resolution has an effect on

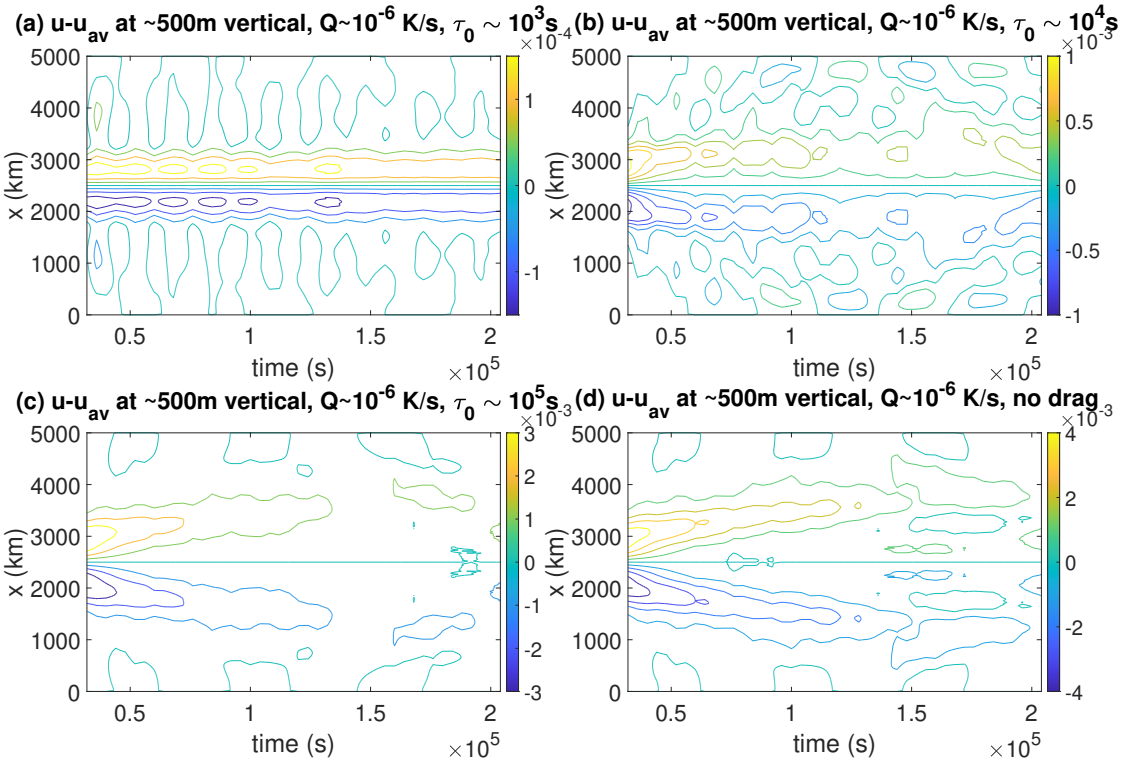

Figure 5.16: Hovmoller plots of horizontal velocity minus a time average of the horizontal velocity over $\sim 50,000$ s ($u - u_{av}$) in dry regime runs from chapter 3 at approximately 500 m in the vertical (middle of the boundary layer) with heating rate $Q \sim 10^{-6}$ K/s and horizontal resolution $\Delta x \sim 10^4$ m. Drag timescales in the boundary layer are (a) $\tau_0 \sim 10^3$ s, (b) $\tau_0 \sim 10^4$ s, (c) $\tau_0 \sim 10^5$ s, and (d) no drag.

boundary layer balance regimes. Specifically, we wanted to look at whether increasing drag strength in the boundary layer can inhibit the formation and propagation of waves and thereby whether wave activity is actually an important contributing factor to whether a model run falls into the ADBL or BLWTG regime and whether it affects for example the collapse of scale in the horizontal lengthscale. We found clear evidence of gravity waves in the dry balance runs investigated here before balance is achieved in the BLWTG and WTG regimes. We also re-established that there was a difference in the shape of the horizontal velocity circulation in the Hovmoller plots for the ADBL regime and that balance appears to be achieved faster. However, there is no conclusive answer to whether it is the damping of gravity waves which causes the difference in balance timescale between the regimes from the results investigated here so further investigations may be necessary. In particular, we may want to look at decreasing the model resolution to see if it might have an effect.

Chapter 6

Conclusions and Discussion

In this thesis, we have examined the effect of drag and heating in the tropical atmosphere as well as the interactions between them in the dry and moist cases.

We have used theoretical frameworks to outline long-term balance regimes and tested the existence of said regimes as well as how well model results fit into the predicted framework. We have also considered adjustment to balance and the effect of damping on gravity waves.

In the dry balance regime experiments in chapter 3, we found that theoretical boundary layer balance regimes were replicable in a model and so could form the basis of a test case for dynamical cores coupled to physics. We also found that the theoretical balance regimes had fairly good explanatory power for the behaviour differences observed in the model.

In the moist regime experiments in chapter 4, we found that the onset of plumes and organisation of plumes was affected by whether or not the the boundary layer was balanced. We also found that the existence or not of long-term balance in the boundary layer had a greater impact on model behaviour than drag strength alone particularly with respect to the triggering and organisation of moist convective plumes.

In the gravity wave adjustment experiments in chapter 5, we saw how drag strength affected damping of waves relative to resolution when the heating was not well-resolved. We found that there was a critical value at which waves get damped based on the highest resolvable wavenumbers and the damping strength.

At the start of this thesis, we set out to answer a few key questions in the sphere of physics-dynamics coupling in the tropics. Firstly, we wanted to better

understand the effect of tropical processes and specifically boundary layer processes such as surface drag and convective heating as well as moist processes. We also wanted to better understand the interactions between them.

We approached the question by examining the effect of each process on long-term circulations in the tropics via attempting to determine the existence or non-existence of long-term balance states. In chapter 3, we outlined a theoretical regime space, taking account of surface drag and heating in the 2D Euler equations for the dry tropical atmosphere. We then tested the ability of a 2D model to replicate the regimes and found at least three different regimes were identifiable in the model and displayed different behaviours based on the strength of the drag and the strength of the heating.

In chapter 4, we outlined moist versions of the dry regimes in chapter 3 as well as regimes we could not obtain in the dry case due to the absence of latent heating. We found again that balance states were achievable in the moist boundary layer in the 2D model runs, however only two balance states appeared feasible this time. Unlike in the dry case, most moist runs failed to achieve any of the balance states outlined in the moist theory – at least over the timescales considered in our study.

Our second question related to the effect of imposed parameters and specifically horizontal resolution on whether long-term balance is achievable or not and whether the balance state of a given model run is dependent on the grid resolution.

In chapter 3, we saw that the horizontal grid size impacted the horizontal length-scale in the model for some regimes, and therefore affected the threshold at which the model moved from one regime another. We found that increasing the drag beyond a certain point in particular caused a collapse of horizontal scales to the grid scale.

In chapter 4, we also observed a dependence on horizontal gridlength in the moist case with some model runs only achieving balance for a given gridlength. However, the collapse of horizontal scales to the horizontal gridlength was present in nearly all model runs suggesting the presence of moisture alone caused the collapse. Increasing the drag was therefore less important and had an effect only on the existence or not of balance in model runs.

Finally, we asked a third question about gravity waves and the importance of drag-damping on the ability of a model to adjust to a balance state. In chapter 5, we looked specifically at adjustment to a weak temperature gradient state and

found that drag-damping did affect the adjustment to balance dependent on parameters such as the resolution and the strength and size of the damped layer. We also looked again at the dry experiments from the perspective of analysing the presence of gravity waves and damping from the drag timescale. For the re-investigated dry experiments in chapter 5, we found inconclusive results. There was no strong evidence of the damping of gravity waves when the drag timescale increased. However we see clearly again the difference in timescales for achieving the different balances, especially the difference between the ADBL and BLWTG/WTG balance timescales.

The work presented in this thesis also raises further questions. For the dry case, it would be interesting to run the test case in other models to see whether the behaviours we observed in the Thuburn (2017) model are replicated and whether other models also fit well with the predictions for output variables. There is also some scope for trying to understand why the thermodynamic variables in particular diverged from the theory.

For the moist case, we might want to explore in more detail which processes limit the collapse of scale in the horizontal lengthscale and how those processes interact with the drag and possible long-term balance regimes. Inclusion of processes that might limit the collapse of scale would be an interesting addition as well as further investigation into balance timescales. For example, we might want to know whether the timescale over which the moisture returns to the boundary layer causes the lack of formation of balance or whether it is caused by other processes.

For the gravity wave adjustment chapter, we might also want to look at how the drag strength affects the damping of waves in the moist cases explored in this thesis as this may help us better understand the mechanisms which affect the adjustment to balance timescales in the moist case and why some model runs don't reach balance at all. Better understanding the adjustment to balance in the moist case may also help us identify differences from the adjustment to balance in the dry case which are associated specifically with the addition of moisture to the problem.

The tropical atmosphere is a complicated part of the Earth System, but this thesis has shed some light on process interactions between surface drag, convective heating and moisture and outlined long-term balance regimes and theoretical frameworks which may help improve our understanding of specific process interactions.

Bibliography

(2021, 10). *IFS Documentation CY47R3 - Part III Dynamics and numerical procedures*. Number 3 in IFS Documentation. ECMWF.

Arakawa, A. and V. R. Lamb (1977). Computational design of the basic dynamical processes of the ucla general circulation model. In J. CHANG (Ed.), *General Circulation Models of the Atmosphere*, Volume 17 of *Methods in Computational Physics: Advances in Research and Applications*, pp. 173–265. Elsevier.

Back, L. E. and C. S. Bretherton (2009). On the relationship between sst gradients, boundary layer winds, and convergence over the tropical oceans. *Journal of Climate 22*(15), 4182–4196.

Bannon, P. R. (1995). Hydrostatic adjustment: Lamb's problem. *Journal of Atmospheric Sciences 52*(10), 1743 – 1752.

Beare, R. J. and M. J. P. Cullen (2012). Balanced models of boundary-layer convergence. *Quarterly Journal of the Royal Meteorological Society 138*(667), 1452–1464.

Beare, R. J. and M. J. P. Cullen (2019). A simple model of a balanced boundary layer coupled to a large-scale convective circulation. *Journal of the Atmospheric Sciences 76*(3), 837–849.

Beljaars, A., G. Balsamo, P. Bechtold, A. Bozzo, R. Forbes, R. J. Hogan, M. Kohler, J.-J. Morcrette, A. M. Tompkins, P. Viterbo, and N. Wedi (2018). The numerics of physical parametrization in the ecmwf model. *Frontiers in Earth Science 6*.

Birch, C. E., M. J. Roberts, L. Garcia-Carreras, D. Ackerley, M. J. Reeder, A. P. Lock, and R. Schiemann (2015). Sea-breeze dynamics and convection initiation: The influence of convective parameterization in weather and climate model biases. *Journal of Climate 28*(20), 8093–8108.

Bony, S., B. Stevens, D. M. W. Frierson, C. Jakob, M. Kageyama, R. Pincus, T. G. Shepherd, S. C. Sherwood, A. P. Siebesma, A. H. Sobel, M. Watanabe, and M. J. Webb (2015). Clouds, circulation and climate sensitivity. *Nature Geoscience 8*, 261–268.

Bretherton, C. S. and A. H. Sobel (2002). A simple model of a convectively coupled walker circulation using the weak temperature gradient approximation. *Journal of Climate), publisher = American Meteorological Society, doi = 10.1175/1520-0442(2002)015¡2907:ASMOAC¿2.0.CO;2 15*(20), 2907–2920.

Bretherton, C. S. and A. H. Sobel (2003). The gill model and the weak temperature gradient approximation. *Journal of the Atmospheric Sciences 60*(2), 451–460.

Buckingham, E. (1914, Oct). On physically similar systems; illustrations of the use of dimensional equations. *Phys. Rev. 4*, 345–376.

Charney, J. G. and N. A. Phillips (1953). Numerical Integration of the quasi-geostrophic equations for barotropic and simple barotropic flows. *Journal of Meteorology 10*(2), 71–99.

Chen, S. S., R. A. Houze, and B. E. Mapes (1996). Multiscale variability of deep convection in realation to large-scale circulation in toga coare. *Journal of Atmospheric Sciences 53*(10), 1380–1409.

Cullen, M. (2018). The use of semigeostrophic theory to diagnose the behaviour of an atmospheric gcm. *Fluids 3*(4).

Dennis, J. M., J. Edwards, K. J. Evans, O. Guba, P. H. Lauritzen, A. A. Mirin, A. St-Cyr, M. A. Taylor, and P. H. Worley (2012). Cam-se: A scalable spectral element dynamical core for the community atmosphere model. *The International Journal of High Performance Computing Applications 26*(1), 74–89.

Diamantakis, M., N. Wood, and T. Davies (2006). An improved implicit predictor corrector scheme for boundary layer vertical diffusion. *Quarterly Journal of the Royal Meteorological Society 132*(616), 959–978.

Donahue, A. S. and P. M. Caldwell (2018). Impact of physics parameterization ordering in a global atmosphere model. *Journal of Advances in Modeling Earth Systems*.

Dubos, T., S. Dubey, M. Tort, R. Mittal, Y. Meurdesoif, and F. Hourdin (2015). Dynamico-1.0, an icosahedral hydrostatic dynamical core designed for consistency and versatility. *Geoscientific Model Development 8*(10), 3131–3150.

Dukowicz, J. K. (2013). Evaluation of various approximations in atmosphere and ocean modeling based on an exact treatment of gravity wave dispersion. *Journal of the Atmospheric Sciences*.

ECMWF-TIGGE-Skill-forecasts (accessed-2022). Tigge skill forecasts.

Emanuel, K. A., M. Fantini, and A. J. Thorpe (1987). Baroclinic instability in an environment of small stability to slantwise moist convection. part i: Two-dimensional models. *Journal of the Atmospheric Sciences 44*(12), 1559–1573.

Emmanuel, K. (1994). *Atmospheric Convection* (1 ed.). Oxford University Press.

Gill, A., A. E, and A. P. (Londyn) (1982). *Atmosphere-Ocean Dynamics*. Number v. 30 in Atmosphere-ocean Dynamics. Elsevier Science.

Gill, A. E. (1980). Some simple solutions for heat–induced tropical circulation. *Quarterly Journal of the Royal Meteorological Society 106*(449), 447–462.

Good, P., R. Chadwick, C. E. Holloway, J. Kennedy, J. A. Lowe, R. Roehrig, and S. S. Rushley (2021). High sensitivity of tropical precipitation to local sea surface temperature. *Nature 589*, 408–414.

Gross, M., H. Wan, P. J. Rasch, P. M. Caldwell, D. L. Williamson, D. Klocke, C. Jablonowski, D. R. Thatcher, N. Wood, M. Cullen, B. Beare, M. Willett, F. Lemarie, E. Blayo, S. Malardel, P. Termonia, A. Gassmann, P. H. Lauritzen, H. Johansen, C. M. Zarzycki, K. Sakaguchi, and R. Leung (2018). Physics-dynamics coupling in weather, climate, and earth system models: Challenges and recent progress. *Monthly Weather Review 146*(11), 3505–3544.

Hartmann, D. L. and K. Larson (2002). An important constraint on tropical cloud - climate feedback. *Geophysical Research Letters 29*(20), 12–1–12–4.

Held, I. M. and A. Y. Hou (1980). Nonlinear axially symmetric circulations in a nearly inviscid atmosphere. *Journal of Atmospheric Sciences 37*(3), 515 – 533.

Held, I. M. and M. J. Suarez (1994). A proposal for the intercomparison of the dynamical cores of atmospheric general circulation models. *Bulletin of the American Meteorological Society 75*(10), 1825–1830.

Holdaway, D., J. Thuburn, and N. Wood (2013). Comparison of lorenz and charney-phillips vertical discretisations for dynamics-boundary layer coupling. part i: Steady states. *Quarterly Journal of the Royal Meteorological Society 139*(673), 1073–1086.

Honnert, R., G. A. Efstathiou, R. J. Beare, J. Ito, A. Lock, R. Neggers, R. S. Plant, H. H. Shin, L. Tomassini, and B. Zhou (2020). The atmospheric boundary layer and the "gray zone" of turbulence: A critical review. *Journal of Geophysical Research: Atmospheres 125*(13), e2019JD030317.

Honnert, R., V. Masson, and F. Couvreux (2011). A diagnostic for evaluating the representation of turbulence in atmospheric models at the kilometric scale. *Journal of the Atmospheric Sciences 68*(12), 3112 – 3131.

Jiang, Q., J. D. Doyle, and R. B. Smith (2006). Interaction between trapped waves and boundary layers. *Journal of the Atmospheric Sciences 63*(2), 617 – 633.

Kalnay, E. and M. Kanamitsu (1988). Time schemes for strongly nonlinear damping equations. *Monthly Weather Review 116*(10), 1945 – 1958.

Klein, R. (2005). Multiple spatial scales in engineering and atmospheric low mach number flows. *ESAIM: Mathematical Modelling and Numerical Analysis 39*(3), 537–559.

Klemp, J. B., J. Dudhia, and A. D. Hassiotis (2008). An upper gravity-wave absorbing layer for nwp applications. *Monthly Weather Review 136*(10), 3987 – 4004.

Klemp, J. B. and D. K. Lilly (1978). Numerical simulation of hydrostatic mountain waves. *Journal of Atmospheric Sciences 35*(1), 78 – 107.

Kosovic, B. and J. A. Curry (2000). A large eddy simulation study of a quasi-steady, stably stratified atmospheric boundary layer. *Journal of the Atmospheric Sciences 57*(8), 1052 – 1068.

Lamb, H. (1908). On the theory of waves propagated vertically in the atmosphere. *Proc. London Math. Soc 136*(7), 122–141.

Lean, H. W., P. A. Clark, M. Dixon, N. M. Roberts, A. Fitch, R. Forbes, and C. Halliwell (2008). Characteristics of high-resolution versions of the met office unified model for forecasting convection over the united kingdom. *Monthly Weather Review 136*(9), 3408 – 3424.

Lindzen, R. S. and S. Nigam (1987). On the role of sea surface temperature gradients in forcing low-level winds and convergence in the tropics. *Journal of the Atmospheric Sciences 44*(17), 2418–2436.

Lock, A. P., A. R. Brown, M. R. Bush, G. M. Martin, and R. N. B. Smith (2000). A new boundary layer mixing scheme. part i: Scheme description and single-column model tests. *Monthly Weather Review 128*(9), 3187 – 3199.

Lorenz, E. N. (1960). Energy and numerical weather prediction. *Tellus 12*(4), 364–373.

Maher, P., E. P. Gerber, B. Medeiros, T. M. Merlis, S. Sherwood, A. Sheshadri, A. H. Sobel, G. K. Vallis, A. Voigt, and P. Zurita-Gotor (2019). Model hierarchies for understanding atmospheric circulation. *Reviews of Geophysics 57*(2), 250–280.

Morcrette, J.-J., G. Mozdzynski, and M. Leutbecher (2008). A reduced radiation grid for the ecmwf integrated forecasting system. *Monthly Weather Review 136*(12), 4760 – 4772.

Muller, C. and S. Bony (2015). What favors convective aggregation and why? *Geophysical Research Letters 42*(13), 5626–5634.

Muller, S. K., E. Manzini, M. Giorgetta, K. Sato, and T. Nasuno (2018). Convectively generated gravity waves in high resolution models of tropical dynamics. *Journal of Advances in Modeling Earth Systems 10*(10), 2564–2588.

Neale, R. B. and B. J. Hoskins (2000). A standard test for agcms including their physical parametrizations: I: the proposal. *Atmospheric Science Letters 1*(2), 101–107.

PaiMazumder, D. and J. M. Done (2016). Potential predictability sources of the 2012 u.s. drought in observations and a regional model ensemble. *Journal of Geophysical Research: Atmospheres 121*(21), 12,581–12,592.

Park, S.-B., S. Boing, and P. Gentine (2018). Role of surface friction on shallow nonprecipitating convection. *Journal of the Atmospheric Sciences 75*(1), 163 – 178.

Park, Y.-Y., R. Buizza, and M. Leutbecher (2008). Tigge: Preliminary results on comparing and combining ensembles. *Quarterly Journal of the Royal Meteorological Society 134*(637), 2029–2050.

Putman, W. M. and S.-J. Lin (2007). Finite-volume transport on various cubed-sphere grids. *Journal of Computational Physics 227*(1), 55–78.

Qaddouri, A. and V. Lee (2011). The canadian global environmental multiscale model on the yin-yang grid system. *Quarterly Journal of the Royal Meteorological Society 137*(660), 1913–1926.

Randall, D. A., C. M. Bitz, G. Danabasoglu, A. S. Denning, P. R. Gent, A. Gettelman, S. M. Griffies, P. Lynch, H. Morrison, R. Pincus, and J. Thuburn (2019, 07). 100 years of earth system model development. *Meteorological Monographs 59*, 12.1–12.66.

Ringler, T. D., D. Jacobsen, M. Gunzburger, L. Ju, M. Duda, and W. Skamarock (2011). Exploring a multiresolution modeling approach within the shallow-water equations. *Monthly Weather Review 139*(11), 3348 – 3368.

Robert, A. (1982). A semi-lagrangian and semi-implicit numerical integration scheme for the primitive meteorological equations. *Journal of the Meteorological Society of Japan. Ser. II 60*(1), 319–325.

Romps, D. M. (2012). Weak pressure gradient approximation and its analytical solutions. *Journal of the Atmospheric Sciences 69*(9), 2835–2845.

Smith, R. B., Q. Jiang, and J. D. Doyle (2006). A theory of gravity wave absorption by a boundary layer. *Journal of the Atmospheric Sciences 63*(2), 774 – 781.

Smith, R. B., S. Skubis, J. D. Doyle, A. S. Broad, C. Kiemle, and H. Volkert (2002). Mountain waves over mont blanc: Influence of a stagnant boundary layer. *Journal of the Atmospheric Sciences 59*(13), 2073 – 2092.

Sobel, A. H., J. Nilsson, and L. M. Polvani (2001). The weak temperature gradient approximation and balanced tropical moisture waves. *Journal of the Atmospheric Sciences 58*(23), 3650–3665.

Staniforth, A. and J. Thuburn (2012). Horizontal grids for global weather and climate prediction models: a review. *Quarterly Journal of the Royal Meteorological Society 138*(662), 1–26.

Stevens, B., J. Duan, J. C. McWilliams, M. MÃ$\frac{1}{4}$nnich, and J. D. Neelin (2002). Entrainment, rayleigh friction, and boundary layer winds over the tropical pacific. *Journal of Climate 15*(1), 30–44.

Sukhatme, J., A. J. Madja, and L. M. Smith (2012). Two-dimensional moist stratified turbulence and the emergence of vertically sheared horizontal flows. *Physics of Fluids 24*(3), 0366021–03660214.

Swinbank, R., M. Kyouda, P. Buchanan, L. Froude, T. M. Hamill, T. D. Hewson, J. H. Keller, M. Matsueda, J. Methven, F. Pappenberger, M. Scheuerer, H. A. Titley, L. Wilson, and M. Yamaguchi (2016). The tigge project and its achievements. *Bulletin of the American Meteorological Society 97*(1), 49–68.

Thatcher, D. R. and C. Jablonowski (2016). A moist aquaplanet variant of the held–suarez test for atmospheric model dynamical cores. *Geoscientific Model Development 9*(4), 1263–1292.

Thorpe, A. J. and T. H. Guymer (1977). The nocturnal jet. *Quarterly Journal of the Royal Meteorological Society 103*(438), 633–653.

Thuburn, J. (2017). Use of the gibbs thermodynamic potential to express the equation of state in atmospheric models. *Quarterly Journal of the Royal Meteorological Society 143*(704), 1185–1196.

Ullrich, P. A., C. Jablonowski, J. Kent, P. H. Lauritzen, R. Nair, K. A. Reed, C. M. Zarzycki, D. M. Hall, D. Dazlich, R. Heikes, C. Konor, D. Randall, T. Dubos,

Y. Meurdesoif, X. Chen, L. Harris, C. Kühnlein, V. Lee, A. Qaddouri, C. Girard, M. Giorgetta, D. Reinert, J. Klemp, S.-H. Park, W. Skamarock, H. Miura, T. Ohno, R. Yoshida, R. Walko, A. Reinecke, and K. Viner (2017). Dcmip2016: a review of non-hydrostatic dynamical core design and intercomparison of participating models. *Geoscientific Model Development 10*(12), 4477–4509.

Vadas, S. L. and D. C. Fritts (2005). Thermospheric responses to gravity waves: Influences of increasing viscosity and thermal diffusivity. *Journal of Geophysical Research: Atmospheres 110*(D15).

Vallis, G. K. (2017). *Atmospheric and Oceanic Fluid Dynamics: Fundamentals and Large-Scale Circulation* (2 ed.). Cambridge University Press.

Vallis, G. K. (2021). Distilling the mechanism for the madden-julian oscillation into a simple translating structure. *Quarterly Journal of the Royal Meteorological Society 147*(738), 3032–3047.

Walters, D., I. Boutle, M. Brooks, T. Melvin, R. Stratton, S. Vosper, H. Wells, K. Williams, N. Wood, T. Allen, A. Bushell, D. Copsey, P. Earnshaw, J. Edwards, M. Gross, S. Hardiman, C. Harris, J. Heming, N. Klingaman, R. Levine, J. Manners, G. Martin, S. Milton, M. Mittermaier, C. Morcrette, T. Riddick, M. Roberts, C. Sanchez, P. Selwood, A. Stirling, C. Smith, D. Suri, W. Tennant, P. L. Vidale, J. Wilkinson, M. Willett, S. Woolnough, and P. Xavier (2017). The met office unified model global atmosphere 6.0/6.1 and jules global land 6.0/6.1 configurations. *Geoscientific Model Development 10*(4), 1487–1520.

Wan, H., P. J. Rasch, M. A. Taylor, and C. Jablonowski (2015). Short term time step convergence in a climate model. *Journal of Advances in Modeling Earth Systems 7*(1), 215–25.

Wan, H., P. J. Rasch, K. Zhang, J. Kazil, and L. R. Leung (2013). Numerical issues associated with compensating and competing processes in climate models: an example from echam-ham. *Geoscientific Model Development 6*(3), 861–874.

Williamson, D. L. (2013). The effect of time steps and time-scales on parametrization suites. *Quarterly Journal of the Royal Meteorological Society 139*(671), 548–560.

Winninghoff, F. J. (1968, jan). *On the Adjustment Toward a Geostrophic Balance in a Simple Primitive Equation Model with Application to the Problems of Initialization and Objective Analysis.* Ph. D. thesis, UNIVERSITY OF CALIFORNIA, LOS ANGELES.

Wood, N., A. Staniforth, A. White, T. Allen, M. Diamantakis, M. Gross, T. Melvin, C. Smith, S. Vosper, M. Zerroukat, and J. Thuburn (2014). An inherently mass-conserving semi-implicit semi-lagrangian discretization of the deep-atmosphere global non-hydrostatic equations. *Quarterly Journal of the Royal Meteorological Society 140*(682), 1505–1520.

Wu, Z., D. S. Battisti, and E. S. Sarachik (2000). Rayleigh friction, newtonian cooling, and the linear response to steady tropical heating. *Journal of the Atmospheric Sciences 57*(12), 1937–1957.

Wyngaard, J. C. (2004). Toward numerical modeling in the terra incognita. *Journal of the Atmospheric Sciences 61*(14), 1816 –1826.

Zangl, G., D. Reinert, P. Ripodas, and M. Baldauf (2015). The icon (icosahedral non-hydrostatic) modelling framework of dwd and mpi-m: Description of the non-hydrostatic dynamical core. *Quarterly Journal of the Royal Meteorological Society 141*(687), 563–579.